Resolution Studies for the Micro Vertex Detector of the $\overline{\mathsf{P}}$ANDA Experiment and the Reconstruction of Charmed Mesons for Specific Hadronic Channels

Dissertation
zur Erlangung des akademischen Grades
Doctor rerum naturalium
(Dr.rer.nat)

vorgelegt
der Fakultät Mathematik und Naturwissenschaften
der Technischen Universität Dresden

von
Dipl.-Phys. René Jäkel
geboren am 02.07.1977 in Bautzen

2009

1. Gutachter : Prof. Dr. H. Freiesleben (TU Dresden)

2. Gutachter : Prof. Dr. K.Th. Brinkmann (Universität Bonn)

Datum der Einreichung : 06.04.2009

Datum der Verteidigung: 17.07.2009

Kurzdarstellung

Das $\overline{\text{P}}$ANDA Experiment wird Teil der geplanten Ausbaustufe FAIR als Erweiterung zur GSI und wird die Untersuchung von hadronischen Reaktionen in Antiproton-Proton Annihilationen ermöglichen. Durch die zu erwartende exzellente Strahlqualität und hohe Luminosität ergeben sich vielfältige Möglichkeiten zur Untersuchung von Hadronenwechselwirkungen, wie beispielsweise die genaue Spektroskopie des Charmoniumsystems. Um vielfältige Untersuchungen verschiedenster hadronischer Systeme zu gewährleisten, wurde der Aufbau eines universellen Detektors geplant, des $\overline{\text{P}}$ANDA Detektors. Dazu ist ein hochauflösender Vertexdetektor (MVD) eine wichtige Komponente, um im Zusammenspiel mit weiteren Detektorkomponenten zur Spur- und Vertexrekonstruktion beitragen zu können.

Im Rahmen dieser Arbeit wurden detaillierte Simulationen durchgeführt, die das Auflösungsvermögen des Vertexdetektors charakterisieren, ganz besonders im Hinblick auf die Rekonstruktion verschiedener physikalischer Kanäle. Dafür war die Entwicklung und Implementierung von Algorithmen zur Rekonstruktion der zu erwartenden Detektordaten und deren Integration in den Spurfit zur Teilchenrekonstruktion eine Grundvoraussetzung. Dadurch ist es möglich das Auflösungsvermögen des MVD und des gesamten experimentellen Aufbaus unter realistischen Bedingungen zu testen und zu optimieren. Die Spur- und Vertexrekonstruction wird anhand der Kanäle $\overline{p}p \to \pi^+\pi^-$ und $\overline{p}p \to J/\psi\gamma$ evaluiert.

Der zu erwartende hadronische Untergrund stellt hohe Anforderungen an die Selektionskraft des experimentellen Aufbaus, bezüglich der physikalischen Observablen, dar. Dies ist besonders für die Untersuchung des Charmoiumsystems oberhalb der $D\overline{D}$-Schwelle von Bedeutung, wofür kaum experimentelle Untersuchungen vorliegen und der $\overline{\text{P}}$ANDA Detektor zukünftig einen entscheidenden Beitrag zum Verständnis gebundener mesonischer Systeme beitragen kann. Zuständen im Charmoniumsystem ist es erlaubt in Open-Charm-Kanäle ($D\overline{D}$) zu zerfallen, die eine eindeutige experimentelle Signatur $\overline{p}p \to D\overline{D}$ mittels der D-Zerfälle in geladene Teilchen im Detektor erlauben. Im Rahmen dieser Arbeit konnte anhand zweier grundlegender Reaktionen gezeigt werden, dass selbst unter ungünstigen Annahmen über den zu erwartenden Wirkungsquerschnitt, der noch nicht schwellennah vermessen wurde, das stark unterdrückte Signal gegenüber Untergrundereignissen hinreichend angereichert werden kann. Dies erlaubt eine klare Identifizierung des $D\overline{D}$ Ausgangskanales, wobei die wesentlichen Untergrundbeiträge identifiziert und diskutiert werden.

Contents

Introduction **1**

1 The $\overline{\text{P}}$ANDA Physics Program **5**
1.1 Introduction . . . 5
1.2 Charmonium Spectroscopy . . . 7
1.2.1 Charmonium below the $D\overline{D}$ Threshold . . . 8
1.2.2 Charmonium above the $D\overline{D}$ Threshold . . . 10
1.3 Gluonic Excitations - Search for Glueballs and Hybrids . . . 13
1.3.1 Glueballs . . . 14
1.3.2 Hybrid States . . . 16
1.4 Other Physics Options . . . 19
1.4.1 Open Charm Spectroscopy . . . 19
1.4.2 Charm in Medium . . . 21
1.4.3 Hypernuclear Physics . . . 22

2 The $\overline{\text{P}}$ANDA Detector **25**
2.1 Introduction . . . 25
2.2 Target Spectrometer . . . 26
2.2.1 Target Options . . . 28
2.2.2 Micro Vertex Detector . . . 29
2.2.3 Central Tracking System . . . 31
2.2.4 Barrel Time Of Flight Detector . . . 33
2.2.5 Cherenkov Detectors . . . 34
2.2.6 Electromagnetic Calorimeter . . . 34
2.2.7 Magnet System and Muon Chambers . . . 36
2.3 Dipole Spectrometer . . . 37
2.3.1 Forward Tracking . . . 37
2.3.2 Particle Identification . . . 38
2.4 Detector Concept for Hypernuclear Physics . . . 39
2.5 Data Acquisition and Trigger Concept . . . 40

3 The Micro Vertex Detector **43**
3.1 Overview . . . 43
3.1.1 Hadronic Environment . . . 44

3.1.2 Consequences on the MVD Design . . . 46
3.2 Physics Requirements . . . 47
3.2.1 Detection of Low Momentum Particles . . . 47
3.2.2 Determination of the Vertex Position . . . 51
3.2.3 High Rate Environment . . . 55
3.3 Design Aspects . . . 57
3.3.1 Current Design . . . 59
3.3.2 Detector Technologies . . . 60
3.3.3 Design Iterations . . . 62
3.3.4 MVD in the Simulations . . . 63

4 Performance of the MVD 65
4.1 Overview . . . 65
4.2 Single Hit Resolution . . . 67
4.2.1 Cluster Hit Reconstruction . . . 67
4.3 Single Track Resolution . . . 73
4.3.1 Track Model . . . 74
4.3.2 Momentum Resolution . . . 75
4.3.3 Vertex Resolution . . . 76
4.4 Contribution to Particle Identification . . . 80
4.4.1 Calculation of the Energy Loss Information . . . 80
4.4.2 Separation of Different Particle Species . . . 84
4.4.3 Discussion of the PID Information . . . 86

5 Vertex Reconstruction Performance for Specific Benchmark Channels 89
5.1 Overview . . . 89
5.1.1 Definition of the Primary Interaction Point . . . 90
5.2 Vertex Resolution for the Channel $\bar{p}p \rightarrow \pi^+\pi^-$ . . . 91
5.2.1 $\pi^+\pi^-$ Event Selection . . . 91
5.2.2 Resolution of the $\pi^+\pi^-$ Production Vertex . . . 93
5.3 Vertex Resolution of the J/ψ Leptonic Decay . . . 97
5.3.1 $J/\psi\gamma$ Event Selection . . . 98
5.3.2 Resolution of the J/ψ Decay Vertex . . . 100
5.4 Vertex Resolution for Different Readout Structure Sizes . . . 101
5.4.1 Variation of the Pixel Cell Size . . . 103
5.4.2 Variation of the Strip Sensor Readout Pitch . . . 106

6 Physics Performance for Charmed Meson Channels 109
6.1 Motivation . . . 109
6.2 Definition of the $D\overline{D}$ Benchmark Channels . . . 111
6.2.1 Reaction Cross Sections . . . 112
6.2.2 Hadronic Background Reactions . . . 115
6.3 Reconstruction of Signal Events . . . 117

6.3.1 The Signal Channel $\bar{p}p \to D^+D^-$ . . . 117
6.3.2 The Signal Channel $\bar{p}p \to D^{*+}D^{*-}$ . . . 122
6.4 Suppression of Hadronic Backgrounds . . . 126
6.4.1 Simulation Demands . . . 126
6.4.2 Background Analysis for the $\bar{p}p \to D^+D^-$ Channel . . . 127
6.4.3 Background Analysis for the $\bar{p}p \to D^{*+}D^{*-}$ Channel . . . 135
6.5 Expected $D\overline{D}$ Data Rates . . . 138

Conclusive Remarks **141**

A Structure of the Reconstruction Software of the Micro Vertex Detector **143**
A.1 Overview . . . 143
A.2 Detector Implementation . . . 145
A.3 Generation of the Digitized Data Formats . . . 146
A.4 Cluster Reconstruction . . . 149

Bibliography **150**

Figures **163**

Tables **165**

Danksagung **167**

Versicherung **169**

Introduction

The $\overline{\text{P}}$ANDA experiment will operate in the antiproton storage ring HESR at the future FAIR facility [1] in Darmstadt. This enables the study of antiproton-proton and antiproton-nucleus interactions at low and intermediate beam momenta between 1.5 GeV/c and 15 GeV/c. The HESR will provide a high resolution antiproton beam, which allows the investigation of a broad variety of different physics topics in hadron physics.

At low energies only the three light quarks (u,d,s) take part in hadronic reactions. Basic properties such as the mass of confined QCD objects are determined by dynamic processes and not by the basic properties of quarks. Up to now it is not theoretical understood, how the masses of hadrons can be explained by fundamental principles.

The QCD [2] provide a theoretical framework based on a field theory approach and can describe many aspects of elementary particle physics in detail. However, at energies where hadronization takes place the theoretical description is much weaker. The theory becomes exceedingly difficult, because the gluon as force carrying boson is strongly self-interacting. The processes are not longer describable in approximative ways and become in principle multi-body problems.

From 1983 to 1996 the LEAR experimental program [3] at CERN allowed to investigate $\overline{\text{p}}$p interactions up to a beam momentum of 1.94 GeV/c. Many different aspects have been studied by the LEAR experiments, such as baryon physics with a focus to hyperon channels and the investigation of scalar and vector mesons. The later was connected to the search for exotic hybrid or entirely gluonic states, which are not forbidden by QCD and for which first evidences were found.

Therefore the idea was formulated [4] to use the advantages of an antiproton beam to investigate $\overline{\text{p}}$p annihilation processes at higher energies, were channels with charm content can be addressed. Since the charm quark is much heavier than the three light quarks, resonances are more likely narrow and exotic states might be easier to be found, while mixing between conventional states is less strong compared to the light sector [5]. Hadrons with charm content can be described theoretically in a approximative way, e.g. the charmonium system ($c\overline{c}$) can be explained in non-relativistic potential models, which are quite succesfull to describe basic properties of $c\overline{c}$ states. The use of antiproton-proton interactions allow the direct formation of charmonium states. In these investigations the resolution of the produced state is in principle only limited by the uncertainty of the beam energy, which is much

better compared to the resolution of the detector system. Up to now only at high incident antiproton energies data about the charmonium system are present, but with much smaller systematic uncertainties compared to experiments performed at e^+e^- colliders [6].

Chapter 1 will discuss many of these aspects in connection to the planned physics program for the $\overline{\mathsf{P}}$ANDA experiment. In this context the $\overline{\mathsf{P}}$ANDA experiment can be interpreted as successor experiment of the LEAR experiments at higher beam energies and with a qualitatively and quantitatively improved antiproton beam.

In Chapter 2 the main concepts of the experimental setup for the $\overline{\mathsf{P}}$ANDA apparatus are introduced. The $\overline{\mathsf{P}}$ANDA design focus on a high quality electromagnetic calorimeter and a precise tracking system. The conceptional design of $\overline{\mathsf{P}}$ANDA has two major parts, a central tracker around the beam-target interaction zone within a superconducting solenoid and a forward spectrometer for small-angle trajectories based on a dipole magnet.

The first sub-detector which surrounds the interaction zone is the Micro Vertex Detector (MVD). The MVD will provide precise space point measurements as basis for charged particle tracking. The detector concept of the MVD is based on silicon semiconductor detectors, which provide a sufficient granularity for high resolution vertex measurements. In recent years silicon detectors became the standard technology for particle tracking in HEP experiments. $\overline{\mathsf{P}}$ANDA will use silicon detectors as first detector layers close to the interaction point. Due to the rather low momenta of the particles in the final state the small angle scattering in the material of the tracking detectors becomes a limiting factor in terms of vertex resolution. Chapter 3 introduces the MVD and requirements on its design are discussed.

In Chapters 4 and 5 the performance of the planed MVD design is discussed. The major task for the silicon tracker is to allow the reconstruction of the particle trajectory with high precision. Furthermore, the frontend electronics of the MVD may provide information which can contribute to particle identification. For low-energetic particles the energy loss in silicon becomes particle dependent, which allows the separation of different particles species. Results of these basic studies for the MVD are presented in Chapter 4.

The MVD is only one part of the tracking system. The combination of the MVD and the outer tracking detectors is very important for vertex and momentum reconstruction, since the MVD can provide only around four space point measurements. To evaluate the combined tracking two basic channels have been investigated. The channel $\overline{p}p \to \pi^+\pi^-$ was analyzed at the highest $\overline{\mathsf{P}}$ANDA beam momentum of 15 GeV/c. This allows the test of the forward disc part of the MVD in combination with the forward tracking detectors. The high Lorentz boost to the final state confines the pions to a rather narrow cone around the beam pipe. As second channel the reaction $\overline{p}p \to J\!/\!\psi\gamma$ has been investigated at a medium momentum of 5.55 GeV/c. The $J\!/\!\psi$ can decay into a pair of charged leptons which gives a clean signature in the detector. Chapter 5 discusses qualitatively the influence of the spatial resolution of the MVD

on the vertex resolution. This is of particular importance in order to define the optimum for basic parameters for the development of the silicon sensors. The size of the sensitive structures implemented on the sensor surface defines the spatial resolution of the hit position on the sensor surface and different alternatives for structure sizes are discussed.

In Chapter 6 two open-charm channels like $\overline{p}p \rightarrow D\overline{D}$ are discussed in the context of the investigation of higher charmonium states. In $\overline{\mathrm{p}}$p interactions $c\overline{c}$ states can be produced in formation experiments, but the hadronic background is many orders of magnitudes larger than the expected physics signal. Although there are only estimates for the relevant production cross sections, the reconstruction ability of the whole $\overline{\mathsf{P}}$ANDA apparatus is discussed for the $D\overline{D}$ benchmark channels. The analysis focus on the suppression of major background components, for which a good vertex resolution provided by the MVD is essential.

To investigate these complex questions different detailed simulations have been performed. A major part of this work was the development of sophisticated simulation and reconstruction software. This includes the MVD as a major part of the $\overline{\mathsf{P}}$ANDA simulation framework and is a prerequisite to obtain realistic physics results and important for further optimizations and development of the inner vertex detector.

1 The $\overline{\text{P}}$ANDA Physics Program

1.1 Introduction

The Quantum Chromo Dynamics (QCD) [2] is quite successful to describe the structure and interactions of hadrons. But not all aspects of the strong force can be understood in detail, e.g. the mass of the hadrons can only be calculated by using phenomenologic models, but not derived from first principles like the QCD Lagrangian. In QCD in analogy to QED the force between QCD objects can be described by the exchange of a boson, the gluon. The gluons bind the quarks, which are the building blocks of any QCD object, either mesons ($q\overline{q}$) or baryons (qqq). The quark and the gluon are carrying a strong charge, which was called "color". In nature there is no colored object and a single quark or gluon cannot be observed freely in an experiment. This property of the QCD is called confinement and a consequence of the gluon self interaction. This self interaction makes the theory difficult to solve and approximations have to be made. The strength of the strong coupling is not constant and varies with energy, or analog with the distance between strong-interacting object. This is reflected by the dependence of the strong coupling constant as function of the distance shown in Figure 1.1.

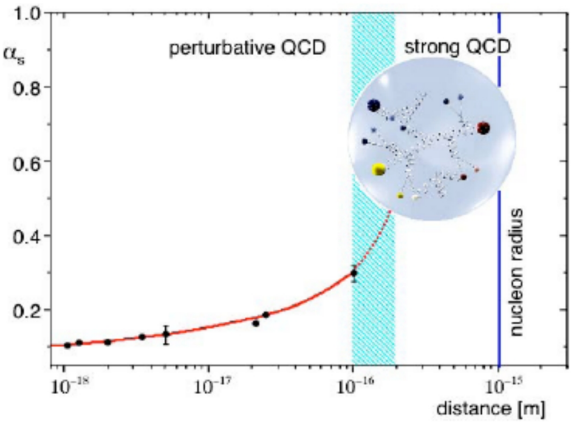

Figure 1.1: Coupling constant of the strong interaction as function of the distance (figure from [7]).

At low energies (or at longer distances) where the constituents are confined in hadrons the theory can be approximated in expansions of the pion mass (Chiral Perturbation Theory χPT). At high energies the constituents become quasi-free particles

in scattering experiments. The theory can therefore be expanded with perturbative methods to approximate the scattering processes. In the transition region, where perturbation theories starts to fail to describe physics processes, the quarks can not longer be treated as free particles and confinement to hadronic objects takes place (Figure 1.1, shaded region). In this energy domain the mass difference between light and heavy quark flavors becomes relevant. For some systems theory can be expanded in terms of the inverse heavy quark masses and is called Heavy Quark Effective Theory (HQET).

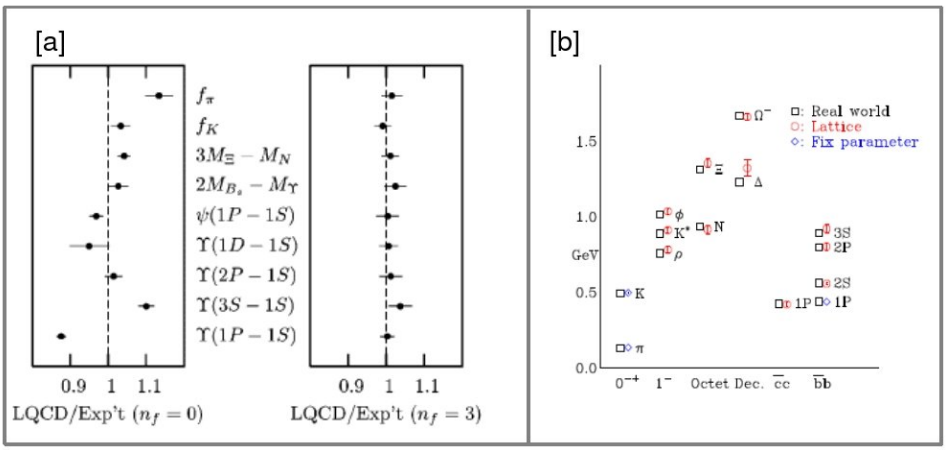

Figure 1.2: Results from lattice QCD calculations compared to experimental data: a) mass differences between baryons and higher quarkonia with (right) and without (left) quark vacuum polarization [8]. b) shows hadron masses obtained on the lattice by the MILC collaboration [9].

In recent years lattice calculations became more and more detailed to describe specific systems. The continuous space time is reduced to discrete values of the lattice grid spacing which causes a natural cut off value $\sim 1/a$, with a as the spacing dimension. Calculations on the lattice are model dependent but became predictive, e.g. in the calculation of glueball or hybrid systems (see Section 1.3.1 for details). In the last years lattice calculations became more and more precise and Figure 1.2 summarizes some results.

Although much progress has been made in recent years to improve the understanding of the strong force in general and in particular of bound systems, such as the charmonium system, precise experiments in the intermediate energy region are necessary to understand the under-laying concepts and dynamics of hadronic reactions.

The $\overline{\text{P}}$ANDA experiment can address many of these questions using antiproton-

proton interactions as a high precision tool. In the following sections some of the main aspects of the physics program of the $\overline{\mathrm{P}}$ANDA experiment will be briefly discussed. Since the experimental program is very wide, only major aspects are discussed here and a more detailed discussion can be found in Ref. [10].

1.2 Charmonium Spectroscopy

Charmonium is a bound system of two charmed quarks, the c-quark and its antiquark $\bar{c}$. Similar to the the electromagnetical bound e^+e^- system, the $c\bar{c}$ system is confined by the strong force. The charmonium system, and in general the investigation of heavier quarkonia, provide a fundamental system for the study of QCD bound systems. The c quark is with a mass of $m_c = 1.27^{+0.07}_{-0.11}$ GeV/c^2 is much heavier than the light u, d and s quarks. This allows the use on non-relativistic quark potential models, which predict bound and mostly very narrow states. The spectrum is shown in Figure 1.3 [11].

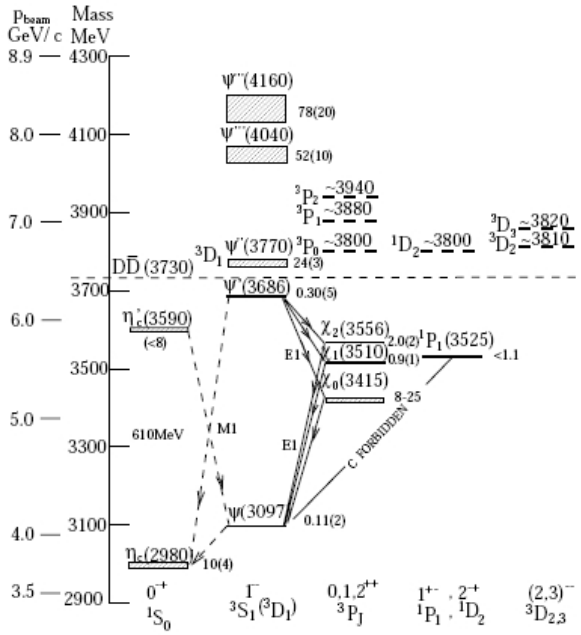

Figure 1.3: View of the charmonium spectrum [11].

The first observation of a charmonium state in 1974 [12],[13] confirmed the existence of the c quark, which was previously predicted [14]. The later called J/ψ state was found via its decay into e^+e^- and because of its narrow width. Currently, the

best experimental knowledge exist for the narrow ψ states, the $J/\psi(1S_1)$[1] and its first excited state $\psi'(2S_1)$, which have the same quantum numbers like the photon. Theses states can directly be produced in e^+e^- annihilation, because they have exactly the same quantum numbers like the photon and the reaction process is shown in Figure 1.4 (left graph).

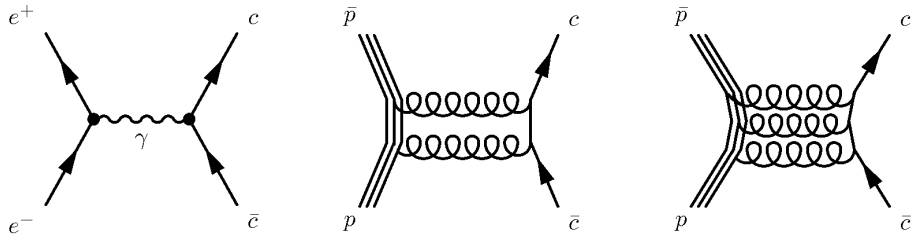

Figure 1.4: Formation of charmonium in e^+e^- (left graph) and in $\overline{\text{p}}$p annihilations.

An complementary approach is to investigate $c\bar{c}$ states in $\overline{\text{p}}$p annihilation (Figure 1.4, middle+right graph), which provide a tool for precise width measurements of these states. The direct formation of all charmonium states would provide higher event yields, compared to e^+e^- experiments. At e^+e^- colliders only those $c\bar{c}$ states can directly be formed which have the same quantum numbers like the photon. Other states can only be investigated in production experiments which mostly suffer in statistics. In $\overline{\text{p}}$p formation experiments the energy resolution of the produced states is basically limited only by the total beam energy uncertainty, which is much smaller than the resolution of the experimental setup.

1.2.1 Charmonium below the $D\overline{D}$ Threshold

Although all the states below the $D\overline{D}$ threshold are confirmed, for some states basic properties are still partly known with high uncertainties. For the $J/\psi(1S_1)$ or the $\psi(2S_1)$ states the best knowledge comes from e^+e^- experiments and their properties have been measured with very high accuracy [15],[16]. At the CLEO-c experiment the formation of the $2S$ state in $e^+e^- \rightarrow \psi(2S_1)$ allows also the investigation of lower charmonium states through transitions of the $\psi(2S_1)$. Data from the B-factories[2] provide information about $c\bar{c}$ states as well. Other $c\bar{c}$ states except the 1^{--} states

[1]The spectroscopic notation $^{2S+1}L_J$ is often used to classify a quarkonium system in analogy to the formalism to describe the states of the hydrogen atom.

[2]The BaBar and Belle experiments are using e^+e^- colliders to produce large samples of B mesons which can decay to $c\bar{c}$ states.

can be investigated in e^+e^- scattering via radiative decays of higher resonances, B meson decays, initial state radiation or double charmonium production [6]. These second order processes usually suffer in statistics and small cross sections and are hard to detect.

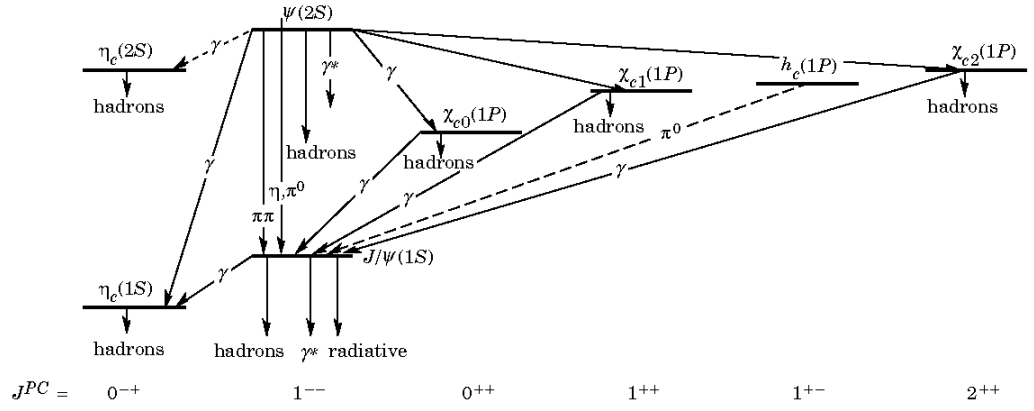

Figure 1.5: Level scheme for the eight charmonium states below the $D\overline{D}$ threshold and their allowed radiative decays [15].

But not all details can be addressed with e^+e^- colliders, e.g. the total width of the $\eta_c(2S_0)$ is known with an uncertainty of only 50 % [15]. This state has been investigated e.g. at BaBar in B meson decays and found the decay $\eta_c(2S) \rightarrow K\bar{K}\pi$ [17]. Belle has seen this state in two-photon fusion [18].

E835 and CLEO-c have reported her recent findings of the long missing charmonium state below the $D\overline{D}$ threshold called h_c which was identified as the $^1P_1$ state [19],[20]. This state was first reported by the E760 experiment in a $\overline{\text{p}}$p formation experiment, but not clearly identified by its successor experiment E835 [6],[19]. In 2005 this state was confirmed by CLEO [20] with a mass of $m(h_c) = 3525.93 \pm 0.27$ MeV/c^2 as a narrow state with a total width of less than $\Gamma_{tot} \leq 1$ MeV. The charmonium state $h_c(1P)$ is of particular importance in the determination of the spin-dependent component of the $q\overline{q}$ confinement potential [6]. The measurement of this resonance allows the fine-tuning of theories like lattice QCD or NRQCD predictions, which are important in order to provide a consistent picture of the charmonium system from the theoretical side. The h_c was identified via its decay $h_c \rightarrow \eta_c + \gamma$ by E835 [19] and by CLEO-c in the process $e^+e^- \rightarrow \psi(2S) \rightarrow h_c\pi^0 \rightarrow \eta_c + \gamma\pi^0$ [20]. Both experiments report a statistical significance of only 3σ and 5σ, respectively. Only an upper limit for the width of the h_c was given to $\Gamma_{tot} < 1$ MeV. Recent investigation by CLEO-c [21] gave a mass value of $M(h_c) = 3525.28 \pm 0.19 \pm 0.12$ MeV/c^2 and a hyper-fine splitting using the centroid χ_{cJ} state to $\Delta M_{hf} = 0.02 \pm 0.19 \pm 0.13$, which

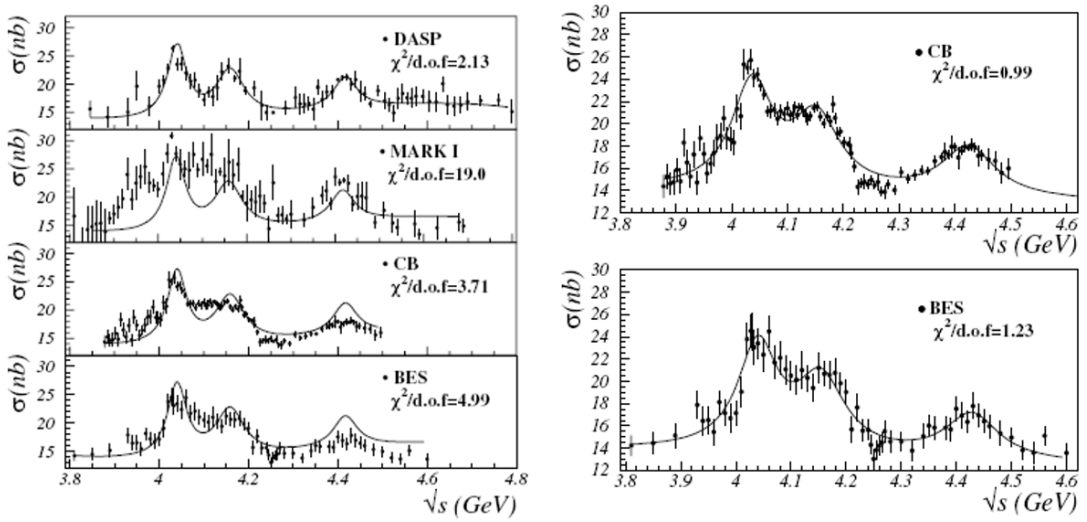

a) b)

Figure 1.6: Cross section of hadron production in e^+e^- collision above the $D\overline{D}$ threshold: a) comparison from various experiments and b) best fit to the experimental data from Crystal Ball and BES (figures from [22]).

is consistent with zero, but with relatively large errors compared to the small width of the h_c.

1.2.2 Charmonium above the $D\overline{D}$ Threshold

The knowledge of charmonium states above the open charm threshold is much less compared to the narrow states below the $D\overline{D}$ threshold. The $1D$ states are predicted to be close to the open-charm threshold, but only one state have been positively identified, the $\psi'(3770)$ as $^3D_1$ state. Furthermore, the excited S and P states are predicted to have masses above the open charm threshold. The experimental situation is rather poor, since only the $\psi'(3770)$ has been identified, which decays predominantly into $D\overline{D}$ (BR($\psi'(3770) \rightarrow D\overline{D}$) $> 85\,\%$ [15]).

The states $\psi'(4040)$, $\psi'(4160)$ and $\psi'(4415)$ have been seen in e^+e^- formation experiments by several experiments, but the different measurements do not show a consistent picture [22]. Figure 1.6 shows a comparison of the measured cross section $e^+e^- \rightarrow hadrons$ over a wide energy range by various experiments. Clearly visible are three resonant contributions in the spectra. In the lower part of the spectrum the MARC-I measurement sees only a broad structure, where DASP, Crystal Ball and BES can distinguish two states . The Crystal Ball and BES data sets agree reasonable well (Figure 1.6 right part), both cannot reproduce the dip in the cross section between the two lower states in the DASP data. Furthermore, the total

cross sections obtained by DASP and especially by MARK-1 differ from the other experiments.

The mass region above the $D\overline{D}$ threshold is in different aspects of interest. Not only for the search of predicted $c\bar{c}$ states, but also the investigation of new physics. Above the $D\overline{D}$ threshold new resonances have been found, which fit only partly in the charmonium scheme. The nature of these states is still controversially discussed, whether these resonances are charmonium states, $D\overline{D}$ molecules or charmed hybrid states. A brief discussion about $c\bar{c}g$ hybrid candidates will be given in Section 1.3.2.2.

state	M [MeV/c^2]	Γ [MeV]	decay	comment
$X(3872)$	$3872 \pm 0.6 \pm 0.5$	< 2.3	$\pi^+\pi^- J/\psi$	$D^0\overline{D}^{*0}$ molecule
			$\nrightarrow D\overline{D}$, $D^0\overline{D}^0\pi^0$	2^3D_2 possible
$Z(3930)$	3929 ± 5	29 ± 10	$D\overline{D}$ dominant	2^3P_2 (χ'_{c2})
$X(3940)$	$3943 \pm 6 \pm 6$	< 52	$D\overline{D}^*$ dominant	3^1S_0 (η''_c)
			$\nrightarrow D\overline{D}$	2^3P_1 (χ'_{c1})
$Y(3940)$	$3943 \pm 4 \pm 13$	$87 \pm 22 \pm 26$	$\omega J/\psi$, $\nrightarrow D\overline{D}$	2^3P_1 (χ'_{c1})
				($c\bar{c}g$) hybrid
$\psi(4040)$	4039 ± 1	80 ± 10	$D\overline{D}$ dominant	3^3S_1
$Y(4260)$	4263^{+8}_{-9}	95 ± 14	$\pi\pi J/\psi$	$\psi(4S)$,
				($c\bar{c}g$) hybrid

Table 1.1: Recently found states above the $D\overline{D}$ threshold and their observed mass and width parameters [15]. In addition, main decay channels and possible scenarios about their nature are given [23],[24] (see text for details).

Table 1.1 gives an overview about some recently found resonances above the $D\overline{D}$ threshold which are discussed in the context of charmonium. For some states an assignment to a charmonium state seems to be plausible, for others different explanations are still controversially discussed and this unclear situation has lead to the name of the so-called XYZ-puzzle in the charmonium system.

In 2003 the Belle collaboration observed a resonance in the exclusive B-decay $B^\pm \rightarrow K^\pm X(3872) \rightarrow K^\pm\pi^+\pi^- J/\psi$ [25], which was later confirmed by BaBar in the same channel [26] and in $\overline{\text{p}}$p annihilation at high energies by CDF [27] and D0 [28] via the same decay. The $X(3872)$ is rather narrow with a total width of about $\Gamma_{tot} = 3.0^{+2.1}_{-1.7}$ MeV [15]. If the $X(3872)$ is a $c\bar{c}$ state which cannot decay into $D\overline{D}$, than the transition into the χ_{cJ} states would be favored[3]. These transitions were

[3]The decay to open charm $c\bar{c} \rightarrow D\overline{D}$ opens further decay channels and the particular resonance will be observed with a larger width.

not observed so far [15]. Recent analysis by CDF [29] suggest the quantum numbers $J^{PC} = 1^{++}$ or 2^{-+}, which are consistent with their data. The $c\bar{c}$ candidates which are close enough in mass are the 2^3P_1 and the 1^1D_2 states.

Belle has reported the finding of a resonance, called $Z(3930)$ [30], which can be associated with the 2^3P_2 charmonium state [15]. This state was observed in two-photon fusion and decays predominantly into $D\overline{D}$. Its width is in the order of expectations for a $c\bar{c}$ states, which can decay to open charm. If the $X(3872)$ is the associated 2^3P_1 state, than the mass difference to the $Z(3930)$ would be in the order of $\Delta M \approx 60$ MeV/c^2, which appears to be too large. Therefore the suggestion was made to identify the narrow $X(3872)$ to be a loosely bound $D^0\overline{D}^{*0}$ molecule [31] with the quantum numbers 1^{++} and the possible decay channel to $D^0\overline{D}^{*0}\pi^0$, recently observed by the Belle collaboration [32]. The $Z(3930)$ can be interpreted as the missing χ'_{c2} charmonium state.

Belle found in double-charmonium production $e^+e^- \to J\!/\!\psi X(3940)$ a new resonance called $X(3940)$ [33] via its dominant $D\overline{D}^*$ decay mode with a mass of $M(X(3940)) = 3936 \pm 14$ MeV/c^2 and a width about $\Gamma < 52$ MeV. The $X(3940)$ is a good candidate for the missing 2^3P_1 (χ'_{c1}) charmonium state. Although the statistical significance is low, a 5σ $X(3940)$ signal has been reported in the $J\!/\!\psi$ recoil mass spectrum for events identified from the corresponding process $e^+e^- \to J\!/\!\psi D\overline{D}^*$, whereas the signal was not observed in the $e^+e^- \to J\!/\!\psi D\overline{D}$ channel. The absence of the $D\overline{D}$ decay channel suggest the possible assignment to η''_c (3^1S_0) [23].

Another finding was made by Belle called the $X(3945)$[4] [34] in the B-decay $B \to K\omega J\!/\!\psi$, where a signal was found in the $\omega J\!/\!\psi$ subsystem. The mass of this state has been given to $M(X(3945) = 3943 \pm 11 \pm 13$ MeV/c^2 with a 8σ significance. The state has been reported by BaBar [35], but with a smaller mass of $M(X(3945) = 3911.6^{3.8}_{-3.4} \pm 1.9$ MeV/c^2.

The heavier $X(4260)$ has been seen in initial state radiation by BaBar [36] in the $\pi^+\pi^- J\!/\!\psi$ mass spectrum and was later confirmed by CLEO [37] and Belle [38]. Belle observes an additional enhancement around $M \approx 4050$ MeV/c^2, which was not reported by the first BaBar observation using only a one-resonance fit to their data. Both experiments have seen evidence for a $X(4260)$ in the $\pi^+\pi^- J\!/\!\psi$ subsystem. These states have been explained as $c\bar{c}$ $(4S)$ state [39] and would be supported by the Belle observation of a lower enhancement, which could than be interpreted as $\psi(4040)$ charmonium state[5]. Theoretical efforts were done to explain this enhancement as charmed hybrid state. In lattice-gauge theory [41] and in flux-tube model calculations [42] the lowest hybrid states is expected at a mass around $M = 4200$ MeV/c^2, which would than dominantly decay into $D\overline{D}_1$. The absence of a $D\overline{D}$ signal would support this. Furthermore, the $X(4260)$ is very close to higher $D\overline{D}^*$ thresholds and a possible

[4]The Particle Data Group has named this state $X(3945)$, whereas Belle call the same resonance $Y(3940)$ (not to mistaken this state for the $X(3940)$).

[5]For the $\psi(4040)$ the decay to $\pi^+\pi^- J\!/\!\psi$ has been reported in a direct scan $e^+e^- \to$ *hadrons* performed by CLEO [40].

explanation could be a bound molecular-like state $D\overline{D}_1$ instead, which would than decay to $D\pi\overline{D}^*$ [23].

Additional evidence for a state $X(4360)$ have been reported by BaBar [43] and Belle [44]. The Belle enhancement was best explained by taking a further resonance with the mass around $M = 4.66$ GeV/c^2 into account, which was not seen by BaBar [15]. Similar to the discussion of the $X(4260)$ the nature of these two heavier states is not clear. Possible assignments are a $c\bar{c}$ state (5^3S_1) for the $X(4660)$ and a possible hybrid nature of the $X(4360)$ [23].

The experimental situation for most of the states above the $D\overline{D}$ threshold is rather poor, and partly controversially discussed. The information about theses states have been obtained from e^+e^- colliders. The experimental programs of BaBar and CLEO-c have ended and only Belle continuous the e^+e^- program. In the near future the BES-III experiment starts after an upgrade of the previous BES-II experiment at the BEPC e^+e^- collider [45] and may contribute to the investigations of charmonium with a precision comparable to CLEO-c and BaBar.

Therefore, the study of this particular mass region above the $D\overline{D}$ threshold via $\overline{\mathrm{p}}\mathrm{p}$ annihilation would provide information from a different system. The high accuracy of the antiproton beam is of importance for precise mass and width measurements to clearly identify certain states to the charmonium system. Some of these states are close to $D\overline{D}$ threshold, e.g. the $X(3872)$ is very close to the $D^0\overline{D}^{*0}$ threshold. The investigation of higher $c\bar{c}$ states in $\overline{\mathrm{p}}\mathrm{p}$ annihilation and in particular their decays into open charm $\overline{\mathrm{p}}\mathrm{p} \to c\bar{c} \to D\overline{D}$ can help to clarify the nature of the recently observed states.

1.3 Gluonic Excitations - Search for Glueballs and Hybrids

The spectroscopy of hadrons has shown that mesonic states can be described in relatively simple quark models as bound $q\bar{q}$ object. For a deep understanding of QCD bound objects it is important to understand in detail the role of the gluons and how the binding of the constituents is realized. Beside the simple $q\bar{q}$ states QCD allows the formation of states with excited glue. The gluonic component may be excited and contributes to the quantum number of the bound object. The additional degree of freedom allows quantum numbers, which are not possible with conventional $q\bar{q}$ states and therefore these object are referred to as hybrid[6] states ($q\bar{q}g$). Identifying a QCD object in a hadronic reaction with those exotic quantum numbers would be a direct evidence for a gluonic excitation beside ordinary quark matter. The finding of an exotic state would help to get insight in the mechanisms and nature of the QCD and the development of theoretical models in the description of QCD bound states.

[6]Hybrid states may be seen not as simple excitations of a single gluon, but as excited flux tube carrying orbital momentum.

It might be even possible to excite states of bound colorless gluon mixtures (ggg), so called glueballs.

The speculations about non-conventional states are supported by experimental findings in the light meson sector. There are more candidates found as expected in the scalar sector. Furthermore the recent findings in the charm sector can be interpreted as partly caused by hybrid states, in particular in the mass region above the $D\overline{D}$ threshold.

1.3.1 Glueballs

Glueballs may be produced in all kinds of gluon rich processes, like radiative decays of hadrons, in pomeron collisions[7] or $\overline{\text{p}}$p annihilation. Unfortunately there is no complete theory describing the dynamic interactions of quarks and gluons at energies, where hadronization of the constituents takes place. A good approach to describe the interactions between the constituents are lattice calculations [47]. A calculated spectrum of predicted glueball states from this calculations is shown in Figure 1.7.

In this framework the lightest glueball 0^{++} is expected at a mass around 1.7 GeV/c^2. Up to now no candidate of the predicted spectrum has been clearly identified. Other model calculations allow lighter glueballs even below the 1 GeV/c^2 mass threshold [46]. However, in the light sector the glueball candidate will mix with mesons with the same quantum numbers. This mixing effect would result in rather broad structures which are experimentally difficult to observe.

1.3.1.1 Glueball Candidates

The hadronic decays of the narrow J/ψ charmonium state into hadrons may be a promising source of glueball production. The decay is a gluon rich process involving three gluons or a photon and two gluons. The later, the radiative decay of the J/ψ may be a good candidate to search for a state which is formed by gluonic interactions. The photon can be detected as recoil partner and evidence for a candidate was observed and called $\eta(1440)$ [48]. It is still controversially discussed, whether this state can be seen as evidence for a glueball. Other experiments were not able to reproduce this finding, but have reported signals at somewhat smaller or higher masses [49]. These observations support the interpretations that the $\eta(1440)$ is a mixture of two states, the η_L and η_H, with the masses of $m_{\eta_L} = 1405$ MeV/c^2 and $m_{\eta_H} = 1475$ MeV/c^2, respectively [49]. The lower state η_L is dominantly decaying into $a_0\pi$ whereas the heavier η_H decays into $K^*\overline{K} + \overline{K}^*K$ [15]. Other interpretations argue that the $\eta(1440)$ is just the radial excitation of the η', similar to the $\eta(1295)$, which can be interpreted as radial excitation of the η [50]. The PDG group assigns the quantum numbers $J^{PC} = 0^{-+}$ [15] to the $\eta(1440)$. This does not correspond

[7] A pomeron process is the exchange of gluons between hadrons in a scattering process. The valence quarks are not effected and only the gluonic parts of the hadrons are interacting. This may be a possible source of glueball production [46].

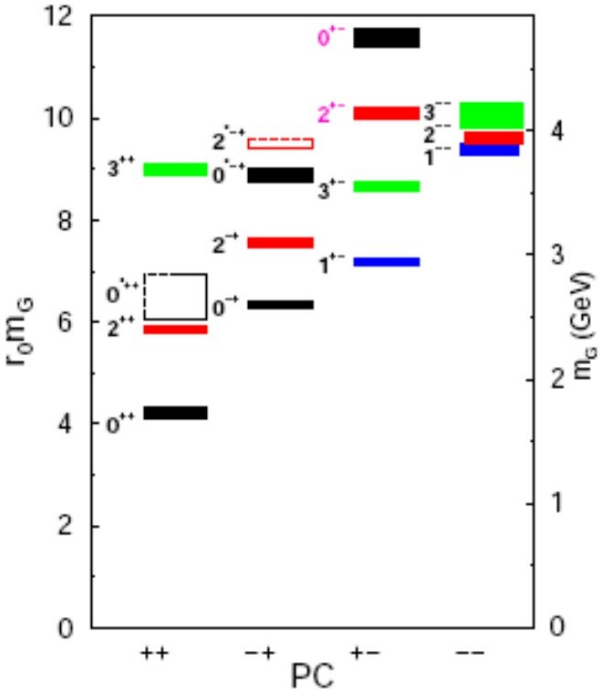

Figure 1.7: Spectrum of glueball states obtained by lattice calculations (from [47]).

to the state predicted in lattice calculations, since this predictions does not favor a light glueball with quantum numbers 0^{-+} and expect this state to appear at a mass of $M \approx 2.5$ GeV/c^2 [51], [47]. But there are other prediction using a flux tube model [52] which predict a glueball at the mass of the $\eta(1440)$. This gives room for the interpretation of the lighter component η_L to be indeed the glueball, whereas the heavier η_H is a member of the 0^{-+} nonet.

The axial meson $f_1(1510)$[8] may be a candidate for a glueball or a gluon rich state in the 1^{++} axial meson sector [53]. The PDG group omits this state from the particle listings although its decay into $K^*\overline{K}$ was seen and competes with the $f_1(1420)$ to be the $s\bar{s}$ member of the axial nonet [15].

There is another resonance, the $f_0(1710)$, which was found in this gluon rich environment, namely in the radiative J/ψ decay: $J/\psi \rightarrow \gamma f_0(1710)$. The decays into 2η and $K\overline{K}$ have been reported and for this state the quantum numbers $I^G J^{PC} = 0^+ even^{++}$ have been assigned [15], but the nature of this state is far from being confirmed. The $f_0(1710)$ is a candidate for a glueball which fits into the predicted glueball spectrum. Others speculate that if this state is a glueball, a signal in radiative charmonium production can be expected [54]. The cross section for this process

[8] The Particle Data Group has excluded this state from the particle listings since it needs further confirmation, more informations available online:[15].

may be in the same order of magnitude compared to double-charmonium production via the process $e^+e^- \rightarrow J/\psi X$, where $X = \eta_c, \chi_{c0}, \eta_c(2S)$ and predicted to be in the order of a few fb. It is obvious that these second order processes are difficult to address in e^+e^- collisions, although the Belle collaboration reported a signal in the region around $M_x \approx 1.7 GeV/c^2$ [55], which may be interpreted as partly caused by glueball formation.

Recent lattice calculations does not favor a light glueball candidate (Figure 1.7), but there are more experimental findings in the scalar meson sector than expected by simple quark models, e.g. there are 7 f_0 states as candidates for the 1^{++} nonet, for which the pure $q\overline{q}$ states are still not clearly identified. The glueball nature of some barely confirmed states is far from being settled and there are different explanations for their nature, either being a $q\overline{q}$ state, a glueball or hybrid state, a molecular like $q\overline{q}q\overline{q}$ state or simply a mixing effect with some nearby resonance.

1.3.2 Hybrid States

The excitation of a gluonic component of a hybrid states provides a further degree of freedom. This allows the states to have exotic quantum numbers, which are not possible for normal $q\overline{q}$ states. In the bag model the gluon can be excited in two different modes [56]. The lower energetic mode is the transverse-electric mode (TE) which has axial vector quantum numbers $J^{PC} = 1^{+-}$, whereas the transverse-magnetic mode (TM) has vector quantum numbers $J^{PC} = 1^{--}$. Adding a gluonic excitation to a $q\overline{q}$ ground state ($^1S_0$=0^{-+}, $^3S_1$=1^{--}) without angular momentum results in eight possible states, for which three of them are exotic and cannot be formed by a pure $q\overline{q}$ state:

$$\begin{array}{lcll} & & (TE) & (TM) \\ 0^{-+} & \rightarrow & 1^{--} & 1^{++} \\ 1^{--} & \rightarrow & (0,1,2)^{-+} & (0,1,2)^{+-} \end{array} \tag{1.1}$$

The finding of a state with one of the exotic quantum numbers 0^{+-}, 1^{-+} or 2^{+-} (color-marked in Equation (1.1)) would be a clear evidence for a hybrid state. These states are often referred to as *Exotics*.

1.3.2.1 Light Hybrid Candidates

In the light meson sector, where only the u, d and s quarks contribute to the formation of bound states, hybrid states may be rather broad and mix with conventional $q\overline{q}$ states of the same quantum numbers. The Crystal Barrel collaboration at CERN-LEAR reported on a resonance called $\pi_1(1400)$ in antiproton proton annihilations $\overline{\text{p}}\text{p} \rightarrow \pi^0\pi^0\eta$ [57] and in antiproton neutron reactions $\overline{p}n \rightarrow \pi^-\pi^0\eta$ [58]. The observed mass was $M = 1360 \pm 25$ MeV/c^2 and $M = 1400 \pm 20 \pm 20$ MeV/c^2, respectively. The same state was observed by the E852 experiment using a 18 GeV pion beam in the

reaction $\pi^- p \to \eta\pi^0 n$ [59]. E852 reports a mass, which is about ≈ 100 MeV/c^2 smaller $M = 1257 \pm 2 \pm 25$ MeV/c^2, but obtained a much larger event sample compared to the Crystal Barrel experiment. They confirm the observation of exotic quantum numbers $J^{PC} = 1^{-+}$ to the observed states via a partial wave analysis in the $\eta\pi^0$ subsystem and found a width of $\Gamma = 354 \pm 64 \pm 58$ MeV.

The E852 experiment reported another evidence for a hybrid state in the light sector. The signal was seen in the reaction $\pi^- p \to \pi^+\pi^-\pi^- p$ at a mass of $M = 1593 \pm 8^{-47}_{+29}$ in the $\rho\pi$ subsystem after a partial wave analysis, which favors the exotic quantum number $J^{PC} = 1^{-+}$ to this state called $\pi_1(1600)$ [60]. Evidence for the $\pi_1(1600)$ has also been reported by the Crystal Barrel collaboration in a reaction by using stopped antiprotons in a hydrogen target $\overline{\mathrm{p}}\mathrm{p} \to \omega\pi^+\pi^-\pi^0$ [61].

A later reanalysis of a much larger data set[9] from the E852 experiment [62] did not confirm the $\pi_1(1600)$ as $J^{PC} = 1^{-+}$ contribution to the $\pi^+\pi^-\pi^-$ subsystem. There are other speculations [63] which suggest the $\pi_1(1400)$ may be a $q\bar{q}q\bar{q}$ molecule, rather than a hybrid states, whereas the $\pi_1(1600)$ might be indeed a hybrid candidate. This is supported by the stronger $\eta'\pi$ coupling of the heavier state, which could be an evidence for the hybrid nature of the state [64].

The broad resonances in the light meson sector are experimentally difficult to investigate. Both promising candidates have a relatively large width of $\Gamma(\pi_1(1400)) = 313 \pm 40$ MeV and $\Gamma(\pi_1(1600)) = 234 \pm 50$ MeV, respectively. A clear identification of their quantum numbers is difficult, since in the light sector several broad states can overlap and mix. The example of the $\pi_1(1600)$ which was excluded by later reanalysis of the data shows the difficulties in the partial wave analysis, especially if only small data samples are available. Only high statistic data sets can help clarify the question whether light hybrid mesonic states exist or can help to give possible other explanations.

1.3.2.2 Charmed Hybrid Candidates

Hybrid states with charm quark contributions, in particular charmonium-like states ($c\bar{c}g$), are predicted to be narrow compared to the proposed hybrid candidates in the light sector (see Section 1.3.2.1 for details). If the mass of a charmed state is below certain $D\overline{D}^*$ thresholds, this states would have a narrow width and the decay to open charm would be forbidden.

Beside the description of heavy quarkonia the existence of heavy hybrid states including b and c quarks have been proposed in lattice calculations [65],[66]. Figure 1.8 shows the predicted hybrid potential (left) and the associated level scheme compared to the predicted charmonium bound states.

Lattice calculations predict the lowest laying hybrid state with a mass around $M = 4250$ MeV/c^2. The recently found $Y(4260)$ resonance by BaBar [36] and Belle

[9] The earlier data set contained 2.5×10^5 events [60], whereas the later analysis contained 3×10^6 events [62].

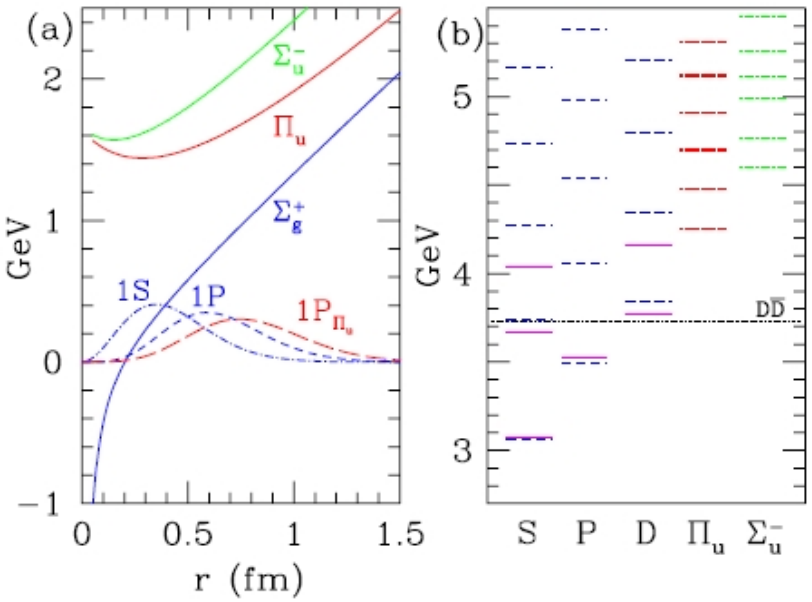

Figure 1.8: (a) Heavy quarkonium potentials and wave functions (dashed) for different excitation levels from LQCD. Σ denotes normal one gluon exchange while the excited Π potentials are the lowest lying hybrid potentials. (b) Charmonium spectrum from LQCD. The conventional charmonium states are on the right while the hybrids are found in column Π_u and Σ_u^- (figure from [10] and model details can be found in [66]).

[38] could therefore be a charmed hybrid candidate. A possible explanation of an ordinary $c\bar{c}$ state could not been excluded so far (see discussion in Section 1.2.2 for information about charmonium in the mass region above the $D\overline{D}$ threshold). Since the reported width to the e^+e^- final state is very small compared to the $\psi\pi\pi$ channel, this can be interpreted as either a $c\bar{c}$ state or a strong coupling to excited glue and therefore an indirect hint to a charmed hybrid state [67]. It is still under debate whether the $Y(4260)$ is a real hybrid state or even a $c\bar{s}\bar{c}s$ molecule.

Several other evidences have been reported in e^+e^- collision in the mass region above the $D\overline{D}$ threshold. Another candidate, the $X(4360)$ seen by BaBar [43] have been discussed in the same context as the $Y(4260)$. Experimentally in this region, where different thresholds are accessible, it is important to establish the source of a signal clearly from being not simply a threshold effect. The $\overline{\text{P}}$ANDA experiment can investigate the charmonium mass region and can contribute to the search of proposed $c\bar{c}$ and hybrid states in $\overline{\text{p}}$p interactions. Except hybrid states with exotic quantum numbers all states can be investigated in direct formation experiments, which would allow very precise width and mass measurements due to the very low initial beam

momentum and energy uncertainty as the limiting factor.

1.4 Other Physics Options

Beside high precision spectroscopy in the charmed meson sector many different physics applications will be addressable in $\overline{\text{p}}$p interactions. In the following sections only a brief overview about further highlights of the rich $\overline{\text{P}}$ANDA physics program. Further information about the $\overline{\text{P}}$ANDA physics program can be found in Refs. [68][10].

1.4.1 Open Charm Spectroscopy

The investigation of mesonic open-charm states allow the investigation of a bound QCD system comparable to hydrogen, which can be described in the framework of QED. High precision spectroscopy of D and D_s states[10] become possible with the high precision antiproton beam within $\overline{\text{P}}$ANDA. The combination of a c quark and a light u or d quark leads to the well established D mesons and their radial excitations D^*. The Particle Data Group list the four $J^P = 0^-$ ground states :

$$\begin{array}{ll} D^+(c\bar{d}) & D^-(\bar{c}d) \\ D^0(c\bar{u}) & \bar{D^0}(\bar{c}u) \end{array}$$

and the corresponding first excited D^* states with $J^P = 1^-$. Four states with $L = 1$ are well established [15]:

	J^P
$D_0^*(2400)^0$	0^+
$D_1^*(2420)^0$	1^+
$D_1^*(2430)^0$	1^+
$D_2^*(2460)^0$	2^+

The study of these states provides information about the spin-structure of the quark-antiquark potential in QCD at relatively large distances. The charged counter parts $D_0^*(2400)^\pm$ and $D_1^*(2420)^\pm$ have been observed but need further investigations in order to confirm the quantum numbers of these states [15].

In general the description of the non-strange D-meson spectrum agrees well with theoretical predictions [69]. For bound systems of D_s mesons[11] the situation is different. Although the mass of the lighter constituents is not so much different compared to the heavy c quark, the spectrum of the D^0 mesons revealed some surprises. The

[10] D mesons are the combinations of a *charm* quark with the light *up* or *down* quarks, whereas the D_s mesons contain a *strange* quark instead.

[11] This is heavy-light abound system where the u or d quarks are replaced by a strange quark s.

ground state $D_s^{\pm}$ with $J^P = 0^-$ and the first excited state $D_s^{*\pm}$ with $J^P = 1^-$ have been observed in e^+e^- collisions in the via their decay to $\phi\pi$ [70],[71]. Additionally two states above the D^*K threshold were known, the $D_s(2536)$ observed by the ARGUS collaboration [72] in the late 1980's and the $D_s(2573)$ found by CLEO-2 [73], respectively.

The observation of two new states of the $c\bar{s}$ system, the $D_s^{\pm}(2317)$ and the $D_s^{\pm}(2460)$, respectively, show a large disagreement to model calculations. The $D_s^{\pm}(2317) \rightarrow D_s^{+}\pi^0$ was found by BaBar [74] and shortly after this state was confirmed by Belle and CLEO-c. CLEO-c found the second new resonance via its decay $D_s^{\pm}(2460) \rightarrow D_s^{*+}\pi^0$ [75]. Both resonances are very small $\Gamma < 4$ MeV, because the mass is little below the DK and D^*K threshold, respectively. Figure 1.9 shows the disagreement of the newly found states (marked as red dots) and other states of the D_s spectrum predicted by theory. Additional, the corresponding DK thresholds are indicated.

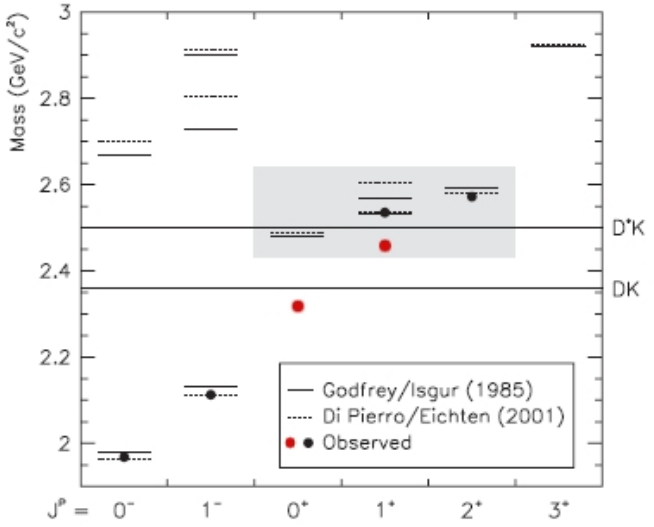

Figure 1.9: Predicted mass spectrum for the heavy-light $c\bar{s}$ system. The experimental findings of D_s states are marked as black dots. The red dots symbolize the recently found new states $D_s^{\pm}(2317)$ and $D_s^{\pm}(2460)$, which do not fit in the picture (figure from [74]).

The mass shift of the $D_s^{\pm}(2317)$ appears to be low for predictions [76],[69] of the $c\bar{s}$ system, around $\Delta M \approx 150$ MeV/c^2 and for the $D_s^{\pm}(2460)$ $\Delta M \approx 100$ MeV/c^2, respectively. The observed decay $D_s^{\pm}(2317) \rightarrow D_s^{+}\pi^0$ violates isospin conservation and no electromagnetic channel has been observed [74]. The lack of a further strong decay channel results in a very narrow resonance, for which BaBar and Belle could give only upper limits. The large deviation from the model predictions and the mass

below certain DK thresholds give room for speculations about the nature of these states or the possible reaction mechanisms. Since both states are slightly below a DK threshold an explanation as a molecular bound $D-K$ system has been proposed [77]. To disentangle different scenarios a precise width determination and the search for possible decay channels like $D_s^+\gamma$ or $D_s^+\gamma$ vs their counterparts including D_s^{*+} would help to pin down the nature of these narrow resonances. $\overline{\text{P}}$ANDA offers a unique possibility to study e.g. the reaction $\overline{\text{p}}\text{p} \rightarrow D_s^{\pm} D_{s0}^{*}(2317)^{\mp}$ in a threshold scan in order to measure the width of the resonance [10]. Furthermore, the determination of the decay branching ratios are needed.

1.4.2 Charm in Medium

QCD is spontaneously broken in chiral symmetry by massive fermions. The restauration of the symmetry is expected at high nuclear densities and temperatures. The study of in-medium processes, such as hadron production in nuclei, might occur under partly restored chiral symmetry due to the finite nuclear density ρ. As observables reduced masses and coupling constants have been predicted, e.g. for vector mesons ρ or ω produced in heavy nuclei [78]. The mass shift may be caused by a change of the quark condensate at higher densities.

In recent years the experimental investigation of chiral restoration has been studied in elementary processes in pp and γp collisions at low densities or in heavy ion collisions at high energies and densities. At FAIR the CBM collaboration plans to investigate the change of properties of charmed hadrons in nuclear densities in heavy ion collisions. The $\overline{\text{P}}$ANDA detector provides the opportunity to replace the hydrogen target by a nuclear target, which would allow the investigation of antiproton-nucleus collisions ($\overline{\text{p}}$N) and therefore the investigation of the change of basic properties of open and hidden charm states at lower densities.

In-medium effects are expected to occur at low energies, where hadrons produced in nuclear medium are at rest or have only a small relative momentum. For charmed mesons a mass shift for D mesons have been predicted up to $\Delta M = 100$ MeV/c^2 for densities of $3\rho_0$ within a quark-meson coupling model in symmetric nuclear matter [79]. Figure 1.10 shows the result of model calculation in comparison to the expected nucleon mass shift. Furthermore, this model predicts a deeply bound charmed meson state within ^{208}Pb. The calculated binding energies are different for D^0 (≈ 100 MeV) and $\overline{D}^0$ (≈ 10 MeV) [79]. The experimental observation of in-medium effects of heavy-light systems ($c\overline{q}$) if exist, would help to understand the role of chiral restoration and the understanding of QCD in dense matter.

Furthermore, a long standing question is the dissociation of charmonium in medium. The $J/\psi N$ cross section is so far unknown [10], except from indirect information from J/ψ cross section measurements, e.g. from pA collisions at high momenta of 450 MeV/c [80] by the NA50 collaboration, which finds a cross section of $\sigma_{abs} J/\psi = 4.6 \pm 0.6$ mb. At $\overline{\text{P}}$ANDA the dissociation of charmonium states can occur via the

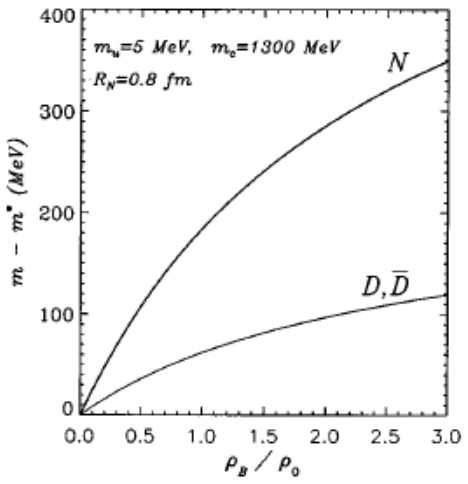

Figure 1.10: Predicted in-medium modification of the D meson and nucleon mass in symmetric nuclear matter and its density dependence. (figure from [79]).

processes $J/\psi N \to \overline{D}\Lambda_c$ or $J/\psi N \to D\overline{D}N$. The $J/\psi N$ cross section measurements in hadronic reactions, or in reactions which involve light nuclei, are closely related to the understanding of charmonium production in heavy ion collisions and may help to understand QCD processes at high densities and temperatures.

1.4.3 Hypernuclear Physics

The production of deeply bound hyperons in nuclei provides a tool to study the binding of nuclei and in particular the spin-dependent part of the nuclear potential. This can be obtained by measuring the level scheme of bound hyperons within the nuclear potential [10]. Furthermore the investigation of strange hadrons in matter is for other fields in physics of interest, such as the evolution of neutron stars or in heavy-ion collisions. The theoretical description of hypernuclei remains rather difficult, since this problem is a multi-body problem, which can only be handled in approximative ways [81]. Figure 1.11 shows a nuclear chart of experimentally found single- and double-hypernuclei (left). The determination of the level scheme of single- and double-hypernuclei may provide unique information about hyperon-nucleon and hyperon-hyperon interactions [10].

The right-hand side of Figure 1.11 shows schematically the expected experimental signature. Antiprotons interact with the light nuclear target material and a pair of e.g. $\Xi^-\overline{\Xi}^+$ is produced at rest. The re-scattered Ξ^- gets stopped in the second nuclear target, where it will be eventually captured and the formed Ξ-hypernuclei will be transformed to a double Λ hypernucleus [10]. As secondary targets beryllium, boron and carbon are foreseen. The double Λ hypernucleus can be detected by γ-rays from the de-excitation of the bound Λs within the nuclear potential.

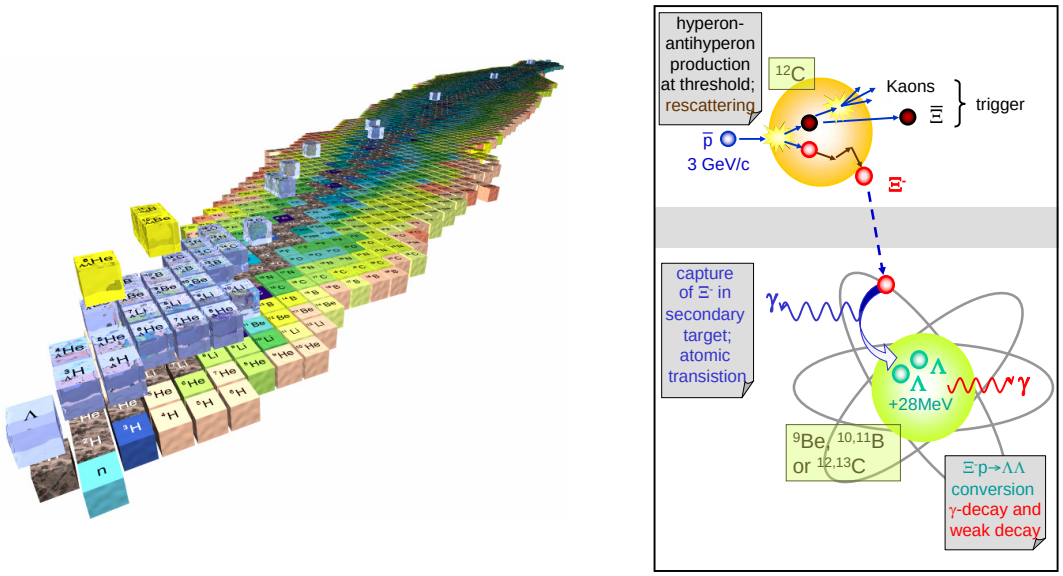

a) b)

Figure 1.11: a) Nuclear chart superimposed with a chart of hypernuclei (blue) and double-hypernuclei (yellow). b) Production of double-hypernuclei with a secondary target at $\overline{\text{P}}$ANDA (see text for details, figures from [10]).

2 The $\overline{\text{P}}$ANDA Detector

2.1 Introduction

The $\overline{\text{P}}$ANDA detector will be located in the antiproton storage ring HESR as part of the new FAIR facility [1] extending the GSI at Darmstadt. The HESR will be part of a large scale construction of an accelerator complex for antiproton and ion beams. As fixed-target experiment the $\overline{\text{P}}$ANDA detector makes use of an antiproton beam in the momentum range from 1.5 GeV/c up to 15 GeV/c. A high luminosity up to $L = 2 \cdot 10^{32}$ cm^{-2} s^{-1} can be achieved with up to 10^{11} antiprotons in the beam and a target thicknesses of $4 \cdot 10^{15}$ atoms cm^{-2}. To increase the beam lifetime, which is limited by beam losses due to interactions with the relatively thick target material, two operational modes are foreseen. A high luminosity mode, which provides the highest possible luminosity up to the envisaged $L = 2 \cdot 10^{32}\text{cm}^{-2}\text{s}^{-1}$ and a mean momentum spread of the antiproton beam of $\Delta p/p = 10^{-4}$. This would be useful for survey experiments, e.g. in the charmonium region above the $D\overline{D}$ threshold. A second mode delivers the best momentum resolution of $\Delta p/p = 10^{-5}$, at the cost of a factor of ten reduced luminosity. The later mode would make high precision measurements such as resonance width measurements possible.

The following parts will introduce the proposed $\overline{\text{P}}$ANDA apparatus as a unique tool to investigate QCD processes in $\overline{\text{p}}$p annihilation reactions. The $\overline{\text{P}}$ANDA apparatus will be a fixed target setup located at a straight section of the HESR. Figure 2.1 gives an overview of the planed detector setup.

To provide a good momentum resolution the detector setup is split up into two parts. The target spectrometer surrounds the interaction point and is mainly built by detectors inside a super-conducting solenoid. The second major part is a dipole magnet in down-stream direction. Behind the dipole the forward detectors deliver tracking and particle identification information. The forward spectrometer covers small angle tracks with respect to the beam pipe up to $\pm 10°$ in horizontal and $\pm 5°$ in vertical direction, respectively. Both parts are equipped with tracking detectors and components for particle identification, such as Cherenkov counters, electromagnetic calorimeters and muon detectors.

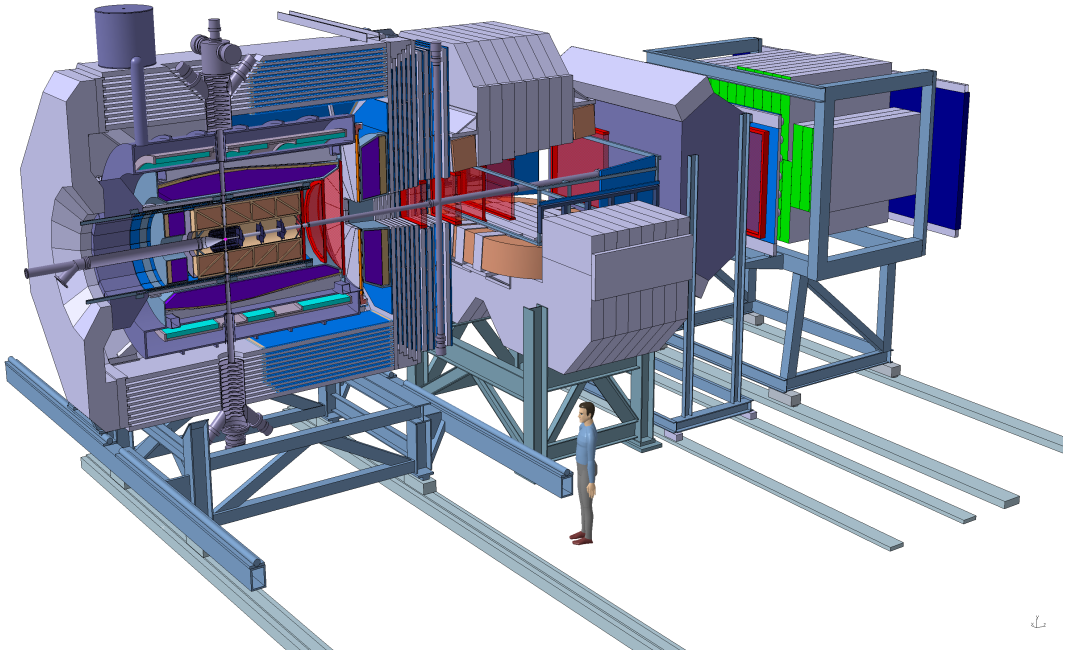

Figure 2.1: Schematic view of the $\overline{\text{P}}$ANDA apparatus with a solenoid magnet surrounding the target region and a forward spectrometer part for low angle particle reconstruction.

2.2 Target Spectrometer

Figure 2.2 gives a close view of the target spectrometer which includes pipes for the target material and the circulating beam, where the beam enters from the left side. The primary interaction region, defined by the cross point of the beam and the hydrogen target, will be surrounded by the inner tracking detector, the Micro Vertex Detector (MVD). This detector component is composed of silicon pixel and strip detectors for high precision track and vertex reconstruction. The outer tracking system follows directly behind the MVD. There are two options for the realization of this device, either a Time Projection Chamber (TPC), or a Straw Tube Tracker (STT).

After the tracking detectors other components for particle identifications are foreseen. A Direct Imaging Ring Cherenkov (DIRC) detector provides information about different particle species via its different amount of produced Cherenkov light at the same incident momentum. The Electromagnetic Calorimeter (EMC) is designed to reconstruct the shape of an electromagnetic shower produced in the optical sensitive crystals. The shape and amount of the collected light delivers information about the energy and direction of mainly photons and leptons. These detector components are placed inside a super-conducting solenoid, which provides a magnetic field parallel

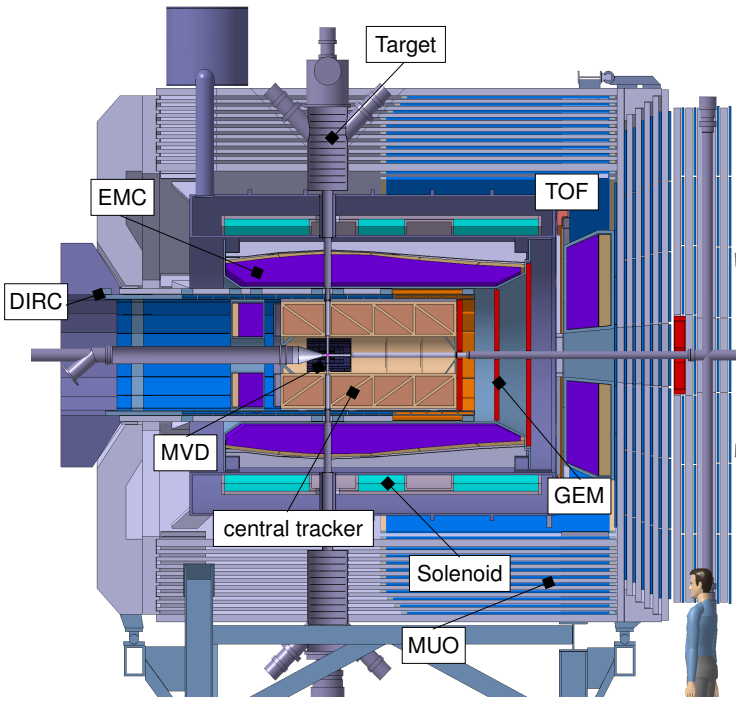

Figure 2.2: Side view of the $\overline{\text{P}}$ANDA target spectrometer. The beam enters from the left side.

to the beam direction of maximal 2 T. The iron return yoke of the solenoid will be instrumented with Muon Counters (MUO).

Additional to the barrel-shaped structure of the target spectrometer two endcap structures close the gap to the forward spectrometer and in addition in upstream beam direction. The backward hemisphere is mainly covered by the backward EMC and the readout of the barrel DIRC, whereas in forward direction additional tracking stations and an endcap Cherenkov detector, as well as a forward EMC endcap, complete the target spectrometer setup.

The barrel section of the target spectrometer will mainly measure lower energetic particles. If the momentum is larger than 800 MeV/c, the barrel DIRC and endcap Cherenkov detectors are able to identify the nature of a particular trajectory. To provide particle identification for slower particles, the tracking detectors, in particular the central tracker, can deliver energy loss information of the reconstructed trajectory . Furthermore a time-of-flight system is currently under investigation in the barrel section which can contribute in the low momentum region.

2.2.1 Target Options

Two basically different hydrogen target options are under investigation for use in $\overline{\text{P}}$ANDA. A cluster jet target and a pellet target. The luminosity can be given to:

$$L = f_{rev} N_{\overline{p}} \frac{\langle N \rangle}{A} \tag{2.1}$$

where f_{rev} is the revolution frequency of the antiproton beam. With $N_{\overline{p}} = 10^{11}$ antiprotons in the ring a luminosity of larger than $L = 10^{32}$ cm^{-2}s^{-1} at medium antiproton beam momentum can only be reached with a target density of at least $\langle N \rangle / A = 4 \cdot 10^{15}$ atoms per cm^{-2}. Both target options would be able to fulfill this requirement, but under different circumstances. Both alternatives would fit into the compact design of the central part of the $\overline{\text{P}}$ANDA detector and show specific advantages and disadvantages, which will be briefly discussed.

2.2.1.1 Clusterjet Target

Cold hydrogen gas is ejected through a nozzle which leads to the formation of a homogeneous stream of hydrogen clusters. The size of the clusters can be adjusted by the gas pressure and varies between 10^3 and 10^6 molecules per cluster. The main advantage of this target type is the homogeneity of the cluster stream at the interaction point and over the interaction time with the circulating antiproton beam. Over the beam spill[1], where almost the complete antiproton beam will be consumed, the density of the cluster jet can be adjusted to keep the luminosity as large as possible while the number of antiprotons decreases over time.

Currently there are some applications running with an internal cluster jet target, e.g. the ANKE [82] experiment located as an internal experiment at the COSY beam facility. For the use in $\overline{\text{P}}$ANDA the distance between target nozzle and interaction point has to be increased to 2 m compared to 60 cm in case of the ANKE target.

A disadvantage of this target type will be the large uncertainty of the beam-target interaction zone due to the lateral spread of the cluster jet. The uncertainty in beam direction will be in the order of a few millimeter. The interaction point (IP) will be defined in the transverse plane reasonable well by the emittance of the beam of, which can be adjusted to be smaller than $\epsilon < 1$ mm mrad. The reconstruction of the longitudinal component of the IP has to rely on the precision of the tracking system.

2.2.1.2 Pellet Target

This target type provides a stream of frozen hydrogen droplets, the so-called pellets, with dimensions between 25-40 μm. The distance between individual pellets can be

[1] A spill is the time of operation of an experiment with only one filling of the HESR ring with antiprotons. The length of this time period depends mainly on the antiproton loss rate due to beam target interactions, the beam cooling and the production rate of antiprotons.

adjusted that only one pellet at once will interact with the antiproton beam. The lateral spread of the pellet stream will be in the order of one millimeter and therefor reduced to the cluster jet target alternative. Furthermore, the interaction time with the beam is long enough to reconstruct the position of each individual pellet. This would result in a very good knowledge of the primary interaction point not only in transverse direction, which will be predominantly defined by the beam emittance.

A major disadvantage will be the non-uniform luminosity over the interaction time of an individual pellet with the beam. Since the $\overline{\text{P}}$ANDA experiment will be a high luminosity an use a continuous beam, the readout of the individual detector components has to be fast and continuously. A strong variation of the luminosity would result in an additional challenge to cope with high data rates.

Currently a pellet target is in operation at the WASA-COSY experiment [83], located in Jülich, which can provide the needed target thickness of 10^{15}-10^{16} atoms per cm^{-2} [84], but with larger pellet sizes than aspired for the use in $\overline{\text{P}}$ANDA. Furthermore, the distance between the target nozzle and the IP will be much larger, which would increase the lateral spread of the pellets. To track the pellets individually, a optical tracking system for the use in $\overline{\text{P}}$ANDA is under development. With such a device an absolute position determination of 50 μm could be reached.

2.2.1.3 Other Target Options

For the hypernuclear part of the $\overline{\text{P}}$ANDA physics program (see Section 1.4.3) a modification of the upstream endcap of the $\overline{\text{P}}$ANDA apparatus will be necessary. This includes a modified primary and secondary target. For the investigation of antiproton-nucleus reactions a wire target can be used.

2.2.2 Micro Vertex Detector

The Micro Vertex Detector (MVD) will be an important part of the tracking system. The MVD surrounds the interaction point and delivers the first hit measurements. This is of importance for the reconstruction of delayed decay vertices from charmed D mesons or hyperons. For this purpose the MVD make use of silicon semiconductor devices with high granularity and fast readout capabilities. The MVD reflect the two-folded design of the $\overline{\text{P}}$ANDA apparatus in its design. It consists out of a barrel section with four layers and six forward disc stations. Moreover, the target pipe has to cross the MVD in the middle, which is an additional difficulty to provide a good coverage of the solid angle and stability of the detector structures. The MVD will be placed in the central tracking device, which defines the maximum available space for the inner tracking detector to be only 15 cm and results in a very compact design of the detector. The services for support like cooling of the frontend electronics and the routing of the readout cables has to be done mainly in upstream direction. Detailed studies are under way in order to exploit possible solutions for such a compact inner

tracking detector. Figure 2.3 illustrate the design of the MVD and shows additionally the pipes for the antiproton beam and target material.

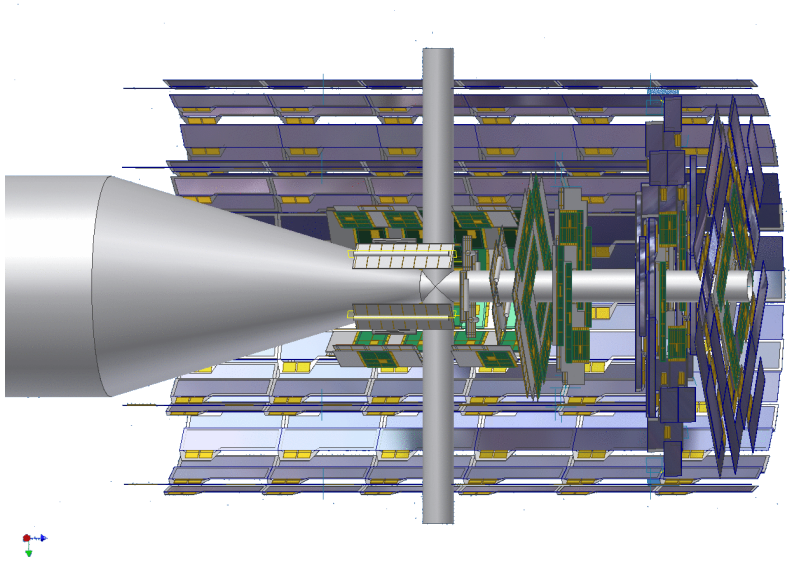

Figure 2.3: The inner tracking detector of the target spectrometer, the Micro Vertex Detector, surrounding the interaction point. Additionally the pipe cross for the circulating antiproton beam and the target material is shown.

The innermost layers of this design consists of silicon pixel detectors, similar to the detector types used in the large LHC experiments [85]. Pixel detectors are radiation hard and provide very accurate space point measurements close to the interaction point (IP). The size of the pixel will be $100 \times 100\ \mu\text{m}^2$. The outer two layers of the barrel section will be built of double-sided silicon strip detectors, which have less readout channels per sensor compared to the pixel detectors. The readout of the individual sides will be done independently. Later in the reconstruction phase of the track fit, both sides are combined to calculate space point information comparable to the pixel detector information.

In the high reaction rate environment, were PANDA will operate, a fast readout of the sensor elements is under development. For the pixel part of the MVD a new frontend is under development using 130 μm technology[2] [86]. This allows the use of smaller pixel cells and their coupled readout electronics keep the full functionality compared to larger readout cells. Contrary to the large LHC experiments, which will

[2]The size of the structures, which can be used to implement electronic components for circuitry is limited by a lithographic process. At present semiconductor technology structure sizes down to 130 μm are available.

have collisions of protons every 25 ns and a trigger available in this time period, in $\overline{\text{P}}$ANDA the event building will be done in a later stage. This is a direct consequence of the continuous beam-target interactions. The development of a readout strategy based on a global time reference and for every hit individually is necessary for the operation in $\overline{\text{P}}$ANDA.

The readout of the strip detectors will be done with a new frontend, which is developed at GSI together with the CBM collaboration. A low power consumption and a free running readout are the major development directions. Section 3.3 provides a detailed discussion about the basic requirements of the MVD.

2.2.3 Central Tracking System

The central tracker follows behind the MVD and will be a gas based system. There are two different concepts for building the central tracking detector. Either a Time Projection Chamber (TPC) will be used, or a Straw Tube Tracker (STT). The central tracker covers a cylindrical volume with the inner radius of 15 cm up to an outer radius of 50 cm and will have a length of 1.5 m. After this cylindrical volume several stations of Gas Electron Multiplier (GEM) detectors will provide hit measurements of low angle tracks towards the dipole tracking and the target spectrometer downstream endcap. The relatively long distance of about one meter between the last MVD forward disc station and the first GEM detector plane will be covered by additional silicon strip discs. This is especially important in a polar angle range below $\theta = 20°$, since the resolution of the central tracker starts to decrease at this point due to the relatively small volume traversed by the particle trajectory.

2.2.3.1 Time Projection Chamber

The Time Projection Chamber consists of two half cylinders, which enclose the MVD and the beam and target pipes. Figure 2.4 shows schematically the technical layout. The inner radius is defined by the size of the MVD, which is about 15 cm and the outer radius less than 50 cm. The device has a length of 150 cm. Charged particles which enters the gas volume of the TPC ionize the chamber gas and the electrons drift toward the readout plane in the upstream direction of the chamber. The readout will be realized by GEM detectors, which are advantageous for the readout in a high rate environment. The GEM readout provides a good spacial resolution of the measured track in the transverse plane, whereas the horizontal component is reconstructed by the simultaneous drift time measurement. Since the electrons drift with constant velocity toward the backward plane, the track position in z direction can be calculated. Additionally the deposited energy of the charged track will be measured and delivers together with the reconstruction of the trajectory a dE/dx information, which is especially important for low momentum particles. The good resolution of the TPC will be helpful to reconstruct short-lived particles containing strangeness, which may decay outside of the MVD.

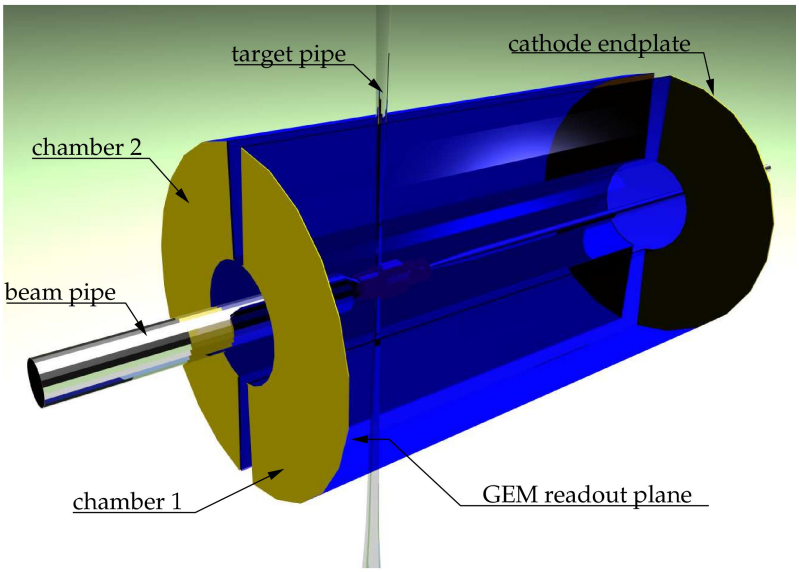

Figure 2.4: Schematic view of the Time Projection Chamber. The beam and target pipes are also indicated.

Since the electron drift is rather slow and no dedicated trigger can be used, several thousand tracks will be in the gas volume at the same time. Therefor additional information from other detector components are important to reconstruct individual events. For this purpose especially the MVD can contribute fast information from the readout of the last MVD layer in front of the TPC.

2.2.3.2 Straw Tube Tracker

The second option currently under investigation for the central tracker is the Straw Tube Tracker. The building block of the STT is the so-called straw, which is a metal-coated mylar foil rolled up to a tube with an inner wire. The tube is self supporting due to the high inner gas pressure and in general this concept provide a very light detector concept. A traversing particle ionizes the gas and the charge carrier move to the inner wire due to the electric field induced by a high voltage between tube and wire. The small diameter of the tube of 1 cm defines a very small drift volume and therefor the readout of the deposited charge can be accomplished much faster compared to the TPC. The combination of all individual energy measurements allows the reconstruction of an energy loss which is comparable to the expected signal from the TPC.

The straw tubes will be grouped in layers and will contain in total 24 layers, which are arranged in a hexagonal shape to fit best into the cylindrical volume. Figure 2.5 shows the STT volume together with a stiff outer support frame, which connects the STT to the adjacent detector components. Additionally, the beam and target pipes are visible. Eight layers in the middle of the volume are skewed by an angle

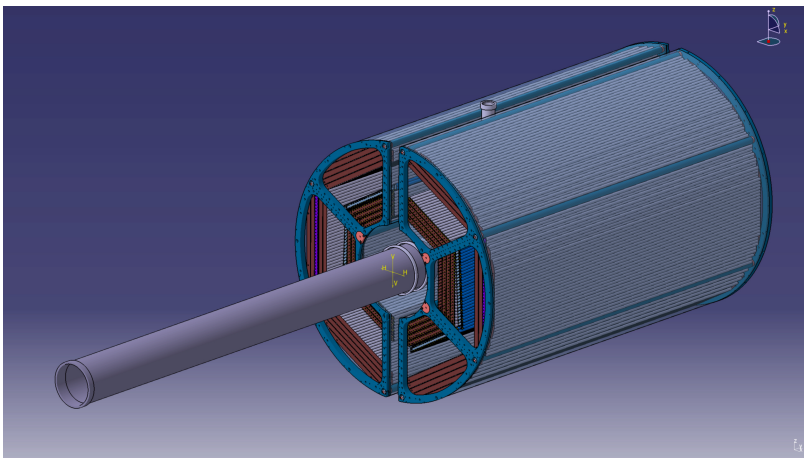

Figure 2.5: Schematic view of the Straw Tube Tracker, which consists of small tubes separated in different layers. The pipe for the incoming beam is shown in addition.

of 3° with respect to each other. This allows the determination of the longitudinal coordinate with a precision of a few millimeter.

2.2.3.3 Gas Electronic Multiplier Stations

The heart of a GEM detector is an insulating layer, which is metallized on both sides. The foil is pierced by microscopic holes with a typical size of 70 μm and a distance of 150 μm. The GEM foil is placed in a gas volume between a cathode and a readout anode, where the holes act as amplifier of the electric field. Within this very strong field, electrons from the ionization process of charged tracks traversing the detector, get amplified by the strong local fields. Several layers of GEM foils can be placed after another to form an amplifying cascade of electrons to the readout anode.

GEM detectors can be operated in high rate environments and can be read out relatively fast compared to other gaseous detectors. Only the electron component of the free charges generated by ionization in the chamber gas is transfered to the readout anode, which is much faster than the slower ion drift. The positive ions are evacuated at the GEM holes [87] and do not contribute to the readout signal.

2.2.4 Barrel Time Of Flight Detector

A barrel TOF between 22° and 140° polar angle would be suited to contribute to particle identification, because this region is often populated by slow particles, depending on beam energy and target material. Below approximately 800 MeV/c particle momentum the DIRC cannot contribute to the particle identification. Since there is no possibility to introduce a start detector close to the IP, only relative timing can be used. For this a time resolution of better than 100 ps would be needed.

The barrel TOF information for higher energetic tracks could be used to simplify the readout of the adjacent DIRC detector. The time measurement of the TOF would serve as reference for the DIRC readout. In this scenario only the arrival time of the photons produced as Cherenkov photons in the DIRC has to be measured. This would drastically reduce the cost of the DIRC readout, which is the large fraction of the cost budget of $\overline{\text{P}}$ANDA.

2.2.5 Cherenkov Detectors

Particles with very high momenta emit light in a medium, if the particle velocity exceeds the speed of light within the used detector medium. This effect is known as Cherenkov effect and the light can be detected by using a transparent medium, such as e.g. quartz glass. The emission angle Θ_c of the Cherenkov light with respect to the particle trajectory is given as:

$$\Theta_c = arccos(1/n\beta) \tag{2.2}$$

and depends on the particle velocity[3] β. Since the momentum of the particle depends on the mass and velocity, a combination of the emission angle measurement and the momentum reconstruction from the tracking system is able to identify the mass and therefore its particle type.

The choice of fused silica as radiator material for the detector slabs allows a separation of pions and kaons down to a particle momentum of around 800 MeV/c and up to a maximum momentum of 5 GeV/c. The produced light is totally reflected in the quartz slab to the back end and a focusing lens projects the light to Micro-Channel Plate Photomultiplier Tubes (MC-PMT). These detectors can operate in a magnetic field and no light guide system and no large water tank as imaging system, like used for the BaBar detector [88], has to be used. This simplifies the handling of the readout system and reduces the costs drastically. A modified readout concept could further reduce the costs for the light-readout by using the barrel TOF detector right in front of the DIRC. The combination of the arrival time of the Cherenkov light and the time information of the TOF detector can substitute the two-dimensional light readout of the Cherenkov light.

2.2.6 Electromagnetic Calorimeter

Behind the central Cherenkov detector follows the barrel EMC. The aim is to provide a good energy resolution for a wide dynamic range of photon energies, which is essential for many aspects of the $\overline{\text{P}}$ANDA physics program. If a photon enters the EMC an electromagnetic shower is produced, which is fully detected by the crystals of the calorimeter. The dimensions of the calorimeter crystals are chosen to cover

[3] A usual declaration for the particle velocity is the relative velocity to the speed of light $\beta = v/c$.

the full particle shower by minimizing the length of the crystals. This results in a compact design of the EMC. As crystal material an improved version of lead-tungstate[4] (PWO), which was originally developed for the CMS experiment, will be used [89]. This material provides a higher light yield from the shower products, which allows to detect very low energetic photons. The design value for the lowest cluster threshold energy is around 10 MeV. This requires a cooling of the whole calorimeter to an operation temperature of $-25°C$ and increases the light yield of the crystals further by a factor of four.

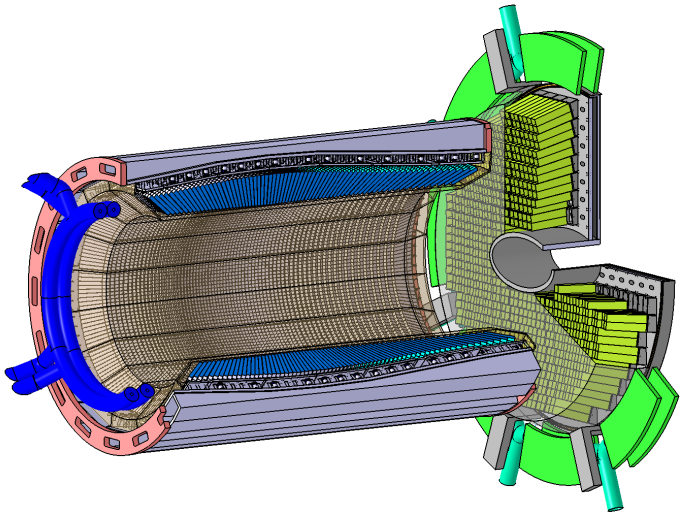

Figure 2.6: Schematic view of the electromagnetic calorimeters in the target spectrometer section. Additionally to the barrel EMC (blue) the forward endcap is shown (green). The smaller backward EMC endcap and the inner detector components are excluded. The beam enters from the left.

Figure 2.6 shows a schematic view of the central barrel EMC (blue crystals) and the forward EMC endcap (green crystals), which is the major part of the forward endcap structure of the target spectrometer. The crystals have a quadratic front surface with an edge size of 2.1 cm and a crystal length of 20 cm, which corresponds to $22X_0$. The barrel section contains more than 11000 crystals, the forward endcap 3600 and the backward endcap nearly 600. The crystals are special aligned to point to the interaction point.

The EMC will operate in a magnetic field of about 2 T, which excludes the use of photomultipliers for the light readout, which cannot be operated in a strong magnetic field. Additionally, the sensor should be less sensitive to ionizing radiation to

[4]PWO is the short form of $PbWO_4$, which is an inorganic scintillator material.

allow the very low photon energy threshold. For this purpose a large area avalanche photodiode (LAAPD) has been developed for the crystal readout in the barrel section. Compared to ordinary APDs the size of the sensor surface, which connects the sensor to the crystal, has been increased to 10×10 mm^2 [89]. Two of these photo sensors are attached to the same crystal to increase the signal to noise ratio and gives redundancy in the readout. The photo sensors and the crystals are radiation hard.

The forward endcap will operate in a region with higher event rate due to the fixed-target topology of $\overline{\text{P}}$ANDA. The expected event rate will be up to five times higher compared to the barrel EMC and about 5×10^5 s^{-1}. For the readout of the crystals in the forward endcap vacuum phototriodes (VPT) will be used. These sensors resists a higher radiation dose and can operate in a high rate environment.

2.2.7 Magnet System and Muon Chambers

A super-conducting solenoid magnet provides a uniform horizontal field in beam direction within the inner radius of 90 cm and a length of 2.8 m. In the region of the MVD and the central tracker a field divergence of less than two percent is envisaged. The central tracker will cover tracks down to 10° in the horizontal and 5° in the vertical plane. The target pipe has to cross the magnet system and the cryostat of the coil will have two bore holes for the target material passage.

The solenoid will be surrounded by an return yoke, which will be instrumented in the downstream direction with muon chambers (MUO). The iron yoke will be sandwich-like segmented with tracking detectors. Monitored Drift Tubes (MDTs) like used for ATLAS experiment [90],[91] could be used as detectors.

The detection of muons, e.g. from the leptonic decay of the J/ψ or semi-leptonic decays of open charm, is important for many physics aspects of the $\overline{\text{P}}$ANDA physics program. The muons have to be clearly identified over a wide momentum range and moreover the separation from background, mainly coming from the high cross sections of hadronic channels which includes pions in the final states, is essential to clearly separate pion decay muons from signal muons.

In the return yoke of the solenoid magnet a range tracking system for muons will be implemented. A sandwich-like concept is foreseen composed of absorber material and tracking detectors. This staggered system allows the tracking of pion decays and the clear identification within the muon system. The thickness of the muon system have to be increased in the endcap due to the higher momentum of the particles in this region. To reach the same separation power an additional muon filter will be introduced in the gap between the endcap of the target spectrometer and the dipole magnet.

As tracking detectors between the absorber layers aluminum drift tubes are foreseen similar the the COMPASS muon detection system [92]. These rectangular drift tubes are capacitively coupled with strip read out on both ends of the detector to reconstruct the longitudinal coordinate and the thickness will be 1 cm, which allows the high segmentation and a good spacial resolution.

2.3 Dipole Spectrometer

A 2 Tm dipole magnet for momentum reconstruction of charged particles covers the opening in the target spectrometer. The dipole will cover a solid angle for tracks up to ±5° in vertical and ±10° in horizontal direction. Figure 2.7 shows a schematic view of major detector components in the forward detector part.

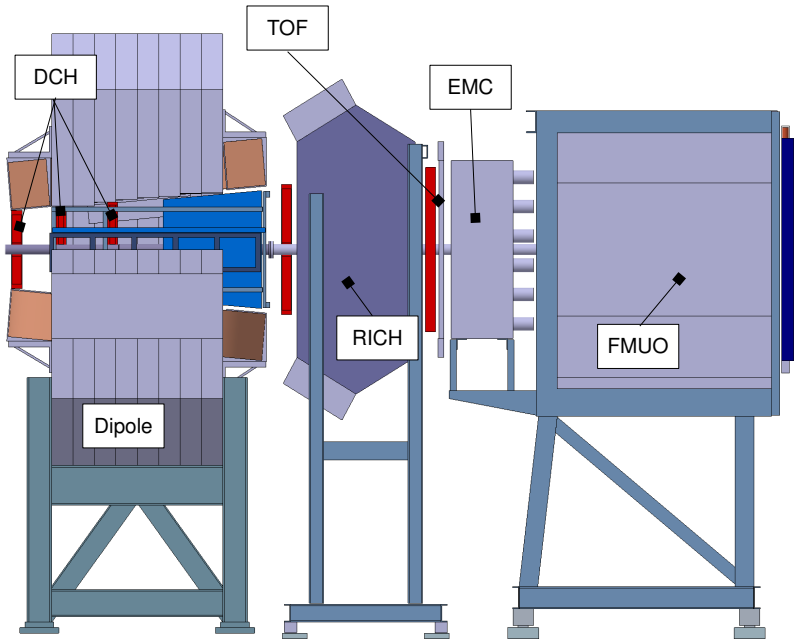

Figure 2.7: Side view of the $\overline{\text{P}}$ANDA forward spectrometer including the dipole magnet. The beam direction is from left to right.

2.3.1 Forward Tracking

After the target spectrometer the 2 Tm dipole magnet allows the momentum reconstruction of fast charged particles. The dipole magnet is equipped with tracking detectors of three times two layers, two layers in front of the magnet, two within the large dipole gap and the last two layers right after the magnet. Each individual layer will consist of four double-layers of straw tubes, two aligned horizontally and the other two layers are inclined by few degree with respect to the horizontal axis (similar to the inclination between individual straw layers in the central tracker). Alternatively, drift chambers are an option to be used instead. The width of the drift chambers will be 1 cm. Currently both options are discussed for the use as

forward tracking detector components and would allow a lightweight tracking system. The expected momentum resolution for particles around 3 GeV/c will be only $\Delta p/p = 0.2\,\%$ and is basically driven by multiple scattering in the gas and wire materials [10].

2.3.2 Particle Identification

Particle identification in the forward part of $\overline{\text{P}}$ANDA is realized by two complementary detector concepts. A RICH detector covers the intermediate and high momentum range between 2–15 GeV/c. For particles below 2 GeV/c a system of TOF detectors will be used. This allows efficient π/K and K/p separation. Behind the last TOF wall an electromagnetic calorimeter and the forward muon detector will follow. A Shashlyk-type calorimeter based on lead-scintillator sandwiches will allow to separate electrons from photons. Afterwards the muon detection system (FMUO) will be of similar type compared to the muon chambers in the target spectrometer.

2.3.2.1 Ring Imaging Cherenkov Counter

The forward RICH detector will be able to cover a momentum range of 2–15 GeV/c and allows the π/K and K/p separation. The basic concept was developed for the HERMES RICH [93] using two different radiator types. A silica aerogel (2.8% X_0) array is followed by an additional radiator volume filled by freon gas (C_4F_{16}, 5% X_0) in front of the mirror array. This lightweight mirror will be used to focus the light on an array of photo tubes placed at the outside of the RICH [10]. The RICH detector of the HERMES experiment has proven that this detector concept allows the separation of pion, kaons and protons in a momentum range of 2–15 GeV/c with very high efficiencies [93].

2.3.2.2 Time of Flight Detector

For low momentum particles a TOF detector system will allow the separation of π/K up to momenta of ≈ 3 GeV/c and K/p separation up to ≈ 5 GeV/c, respectively with an estimated time resolution of about 50 ns [10]. The detector components will consist of plastic scintillators and will be read out at both ends. There will be two walls of scintillator slabs with varying width from 5–10 cm. The first wall will be located in the dipole opening especially for the detection of very low momentum particles, which will not exit the dipole magnet. A second wall for higher energetic particles will be placed in front of the electromagnetic calorimeter.

2.3.2.3 Electromagnetic Calorimeter

The forward electromagnetic calorimeter will make use of lead-scintillators and will be of Shashlyk-type as e.g. used by the LHCb experiment [94], for which a pion

misidentification probability below 1 % have been achieved over a wide momentum range. The readout is realized with length shifting fibers coupled to photomultipliers. To cover the acceptance 26 rows and 54 columns are required with an individual cell size of 55 mm [10]. The forward EMC will be located around 7 m behind the interaction zone.

2.3.2.4 Muon Detectors

Similar to the muon system in the target spectrometer section the forward muon detector will composed of aluminum drift tubes [92]. The FMUO is designed to allow the separation of muons and pion for the highest momenta at $\overline{\text{P}}$ANDA. Additionally, the setup allows the detection of neutrons and antineutrons with moderate resolution [10].

2.4 Detector Concept for Hypernuclear Physics

The investigation of hypernuclei requires a modification of the backward endcap of the $\overline{\text{P}}$ANDA detector. The heart of the hypernuclear physics program is a system of specially designed primary and secondary targets. As introduced in Section 1.4.3 a nuclear target will be needed to produce strange particles, e.g. a pair of strange baryons of the type $\bar{\text{p}}\text{p} \rightarrow \Xi^{-}\overline{\Xi}^{+}$, where one Ξ is used to tag the production event in the $\overline{\text{P}}$ANDA spectrometer and the other Ξ gets absorbed in the secondary target. Figure 2.8 shows the modified experimental setup of the backward part (left) with included germanium array (right).

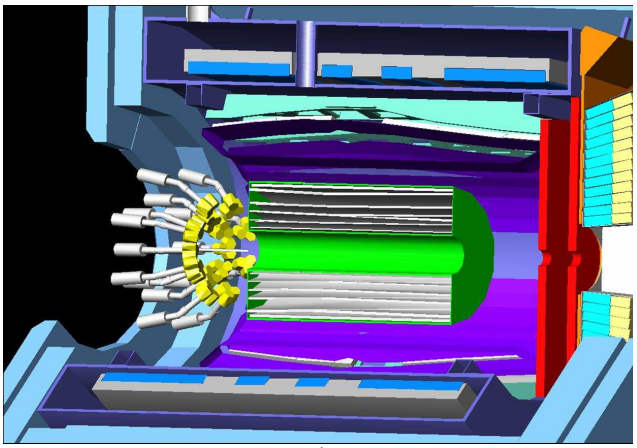

a)

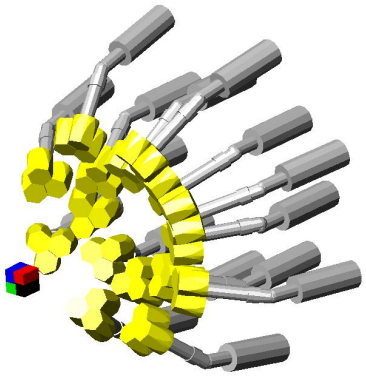

b)

Figure 2.8: a) Modification of the backward $\overline{\text{P}}$ANDA endcap with inserted germanium detector array. b) Close view of the germanium detector array arrangement and indicated nuclear target (figures from [10]).

The antiproton beam interacts with a primary nuclear target, e.g. ^{12}C. The beam energy is optimized to produce a pair of hyperons at rest or with very low excess energy, Around the beam pipe a system of silicon tracking detectors with alternating layers of absorber material provides tracking information of the decay products and serves as secondary target. A similar setup is used by the FINUDA group [95] for the investigation of light hypernuclei.

A set of germanium detectors allow the detection of photons from the deexcitation of the produced hypernuclei from the target position. An arrangement of 15 triple-germanium detectors (Figure 2.8 left) covers the backward hemisphere. A major challenge is the operation of germanium detectos in the high rate environment at $\overline{\text{P}}$ANDA.

2.5 Data Acquisition and Trigger Concept

The data acquisition system is a really challenging task. Not only a high beam current and high data rates have to be handled in the detector, but also the $\overline{\text{P}}$ANDA detector has to be able to investigate many different physics aspect. This multi multi-purpose detector relies on the reconstructions of different physics event patterns.

At $\overline{\text{P}}$ANDA a continuous antiproton beam interacts with the target material. In many other experiments, like e.g. in colliders experiments, a bunched beam structure can be used to time the occurrence of physics events to a well defined time window. At the LHC experiments the bunch crossing interval is 25 ns. This allows the development of a hierarchic trigger concept, which allows to process data from fast detector components in a first selection stage, before other parts of the detector are read out and processed in a later stage.

At $\overline{\text{P}}$ANDA a continuous readout of all sub-detector components in parallel has to be realized. This allows a high flexibility in the event selection, but also the data processing of a large amount of collected data. This is only possible, if at sub-detector level the front-end electronics is able to perform first filtering, such as noise and zero suppression, or clustering, e.g. in the calorimeter or the MVD on a very short time scale.

A precise timing system and the consistency of the global time reference is extremely important in this autonomous sub-detector scheme. All time information has to be derived from a global reference in order to keep the consistency of the data processing. At a later stage the sub-detector data are buffered and a data collection process allows the combination of different sub-sets of detector data. This process can be configured very flexible in order to filter relevant information for selected physics topics. Large computing nodes connected with fast optical links with a high bandwidth have to process algorithms for feature extraction and event selection.

Currently more specialized solutions for data processing are under development to be used in the $\overline{\text{P}}$ANDA experiment. FPGAs can be used close to individual detector components for preselection, e.g. in the MVD readout to perform the cluster search.

This specialized solutions allow a very fast processing of the collected data and a early reduction of the large amount of collected data.

A high speed network is essential to provide fast communication between certain detector components. This can be realized via a network fabric, which is flexible enough to be re-configured to meet different physics requirements [10]. For interaction rates of around $2 \cdot 10^7$ s^{-1} a high bandwidth around 200 GB/s is needed, which has to be processed and filtered to an event information of about 100–200 MB/s.

Very important is the accuracy of sub-detector data in terms of calibration stability. Additional calibration runs are foreseen between measurement cycles. For a later control a small amount of raw detector data and calibration constants from various detectors are stored besides physics data to large storage systems.

3 The Micro Vertex Detector

3.1 Overview

The Micro Vertex Detector (MVD) is the first detector component, which surrounds the interaction zone of the $\overline{\text{P}}$ANDA experiment. The primary interaction region is defined by the circulating antiproton beam and the crossing target material. The aim of the MVD is to provide precise space point measurements as close as possible to the primary reaction region. The measurement of the particle trajectory close to its origin allows the determination of the reaction position with a resolution of better than $\Delta x_i = 100$ μm. This is of particular importance for the detection of delayed decays, caused by the under-laying weak decay of strange or charmed quarks within the confined hadrons. The reconstruction of the secondary vertex allows the clear identification of the weak decay process and is of major interest for many physics aspects of the $\overline{\text{P}}$ANDA physics program.

Hadrons with strange quark content have decay lengths in the order of a few centimeters, whereas charmed mesons and baryons decay typically after some tens to few hundreds of micrometers and usually remain in the beam pipe. Additionally, most reaction particles will have a larger longitudinal momentum component in comparison to their transverse component, which arises from the relatively high beam momentum transfered to the particles in the final state. This is a direct consequence of the fixed-target topology of the experimental setup. To provide a good coverage of the solid angle and to ensure a good spatial resolution, the MVD is based on a set of barrel layers for high angle tracks and several disc-like structures to detect tracks under small angles. The transition region between both parts will be around 45° in polar angle, which is the optimum in order to minimize the material budget of the MVD. Due to the compactness of the $\overline{\text{P}}$ANDA apparatus the overall space for the inner tracking detector is limited and has to fit in a barrel with a radius of 15 cm only. Furthermore, due to the high luminosity the innermost detector layers, in particular the forward disc-like structures, have to operate in a high rate environment. The usage of a fixed target causes an increased particle flux towards smaller angles and requires a high readout speed of the forward silicon detectors in order to avoid efficiency losses of the tracking system.

$\overline{\text{P}}$ANDA cannot use an event based trigger for the selection of different physics events, since the circulating antiproton beam will be continuous and several physics

events have to be reconstructed in parallel. At a later stage, information from the individual sub-detector components are combined in the event building phase. The silicon detectors of the MVD will be of similar type to state-of-the-art silicon detectors, which are widely used in HEP experiments, such as in the large LHC experiments. These detectors can deliver a fast hit information, because the drift time of the deposited charge in the sensor material is very small[1]. For the operation in $\overline{\text{P}}$ANDA a new readout scheme has to be developed to operate these detectors in a continuous beam environment. Detector components with fast readout like the MVD will be important for early decisions in the event building to reduce the amount of data to be processed further on to the analysis stage.

In this chapter, basic characteristics and design aspects of the MVD will be discussed. Section 3.3 gives a summary of the current design of the MVD, which was the basis for the resolution studies presented in Chapter 4 and Chapter 5. The physics performance of the complete detector setup, including a detailed description of the MVD, is exemplified in detail for the reconstruction of charmed meson channels in Chapter 6.

3.1.1 Hadronic Environment

The PANDA detector will use a stationary target within the antiproton storage and accelerator ring HESR. The beam momentum of the antiprotons will be in the range from 1.5 GeV/c to 15 GeV/c and for higher beam momenta the reaction particles will have a prominent longitudinal momentum component coming from the momentum transfer to the particles in the final state. A large fraction of the particle flux traverses the MVD mainly under small angles with respect to the beam pipe. The available phase space is illustrated in Figure 3.1 for antiproton-proton (left) and antiproton-nucleus (right) collisions, respectively.

In $\overline{\text{p}}$p collisions at low incident antiproton momentum the trajectories in the final reaction channels are almost uniformly distributed over the full solid angle[2] (Figure 3.1, upper left). Additionally, two intensity maxima are visible at small angles and almost maximum momentum and of low momentum tracks, which traverse the MVD almost perpendicular to the beam axis. This is caused by elastic $\overline{\text{p}}$p scattering, where the antiprotons stay at low angles and the protons are scattered at larger angles. With increasing beam momentum the elastic cross section drops down and the maximum of the particle flux gets shifted toward smaller angles due to the larger beam boost transfered to the final state. Hadronic reactions in $\overline{\text{p}}$p collisions can be reasonably well described by the DPM [96] model, which was the basis for simulations of the hadronic background shown in Figure 3.1.

[1] The readout time for an individual pixel can be less than 25 ns, e.g. as achieved for pixel detectors by the ATLAS collaboration [85].

[2] The display of the phase space in Figure 3.1 comprehends the azimuthal information of the particle trajectory, which is uniform over the full MVD except small openings for the target pipe.

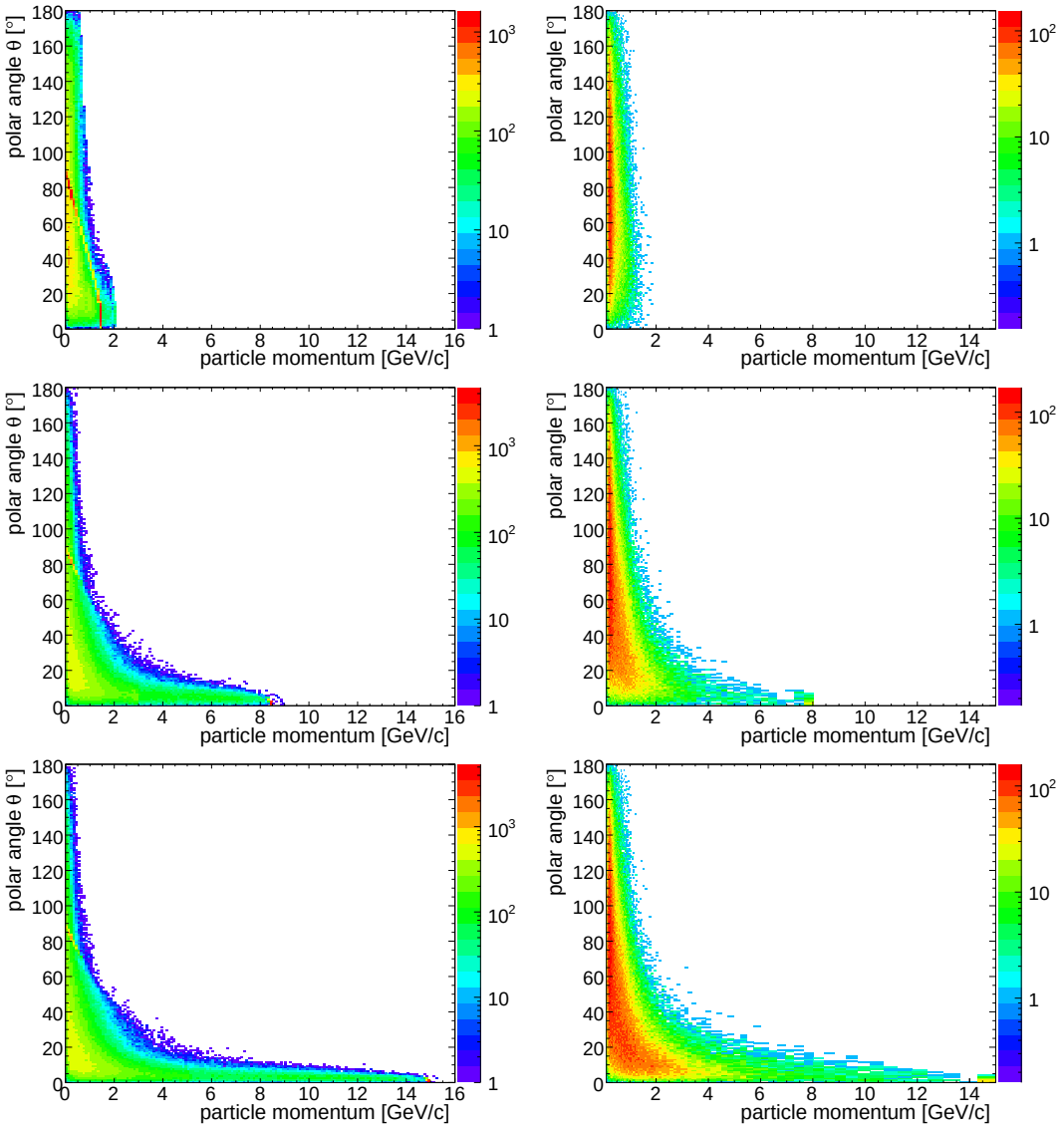

Figure 3.1: Phase space distribution of all promoted tracks in the detector for $\overline{\mathrm{p}}$p (left) and $\overline{\mathrm{p}}$–gold (right) collisions. The beam momenta are 1.5 GeV/c, 8 GeV/c and 15 GeV/c, respectively (from top to bottom, intensity scale drawn logarithmically).

The right column of Figure 3.1 shows the track distributions for antiproton-gold collisions at beam energies of 1.5 GeV/c, 8 GeV/c and 15 GeV/c, respectively. At low incident beam momentum the maximum of the particle flux is almost uniformly distributed over the full MVD acceptance. Most particles have only small momenta of only a few hundreds of MeV/c. This low energetic contribution remains rather constant at intermediate and highest $\overline{\mathsf{P}}$ANDA beam momenta. Additionally, a shift of the maximum to lower angles becomes visible, but not dominant, compared to $\overline{\mathrm{p}}$p

collisions. The UrQMD model [97] provides a model based on Monte Carlo techniques to calculate the cross sections of antiproton collisions with heavier nuclei [98]. This model was originally used to describe heavy ion collisions for a large range of energies from 1 AGeV/c up to several hundreds of AGeV/c at high energy collider, such as RHIC and ALICE. This model was adopted by the $\overline{\mathsf{P}}$ANDA collaboration to the relevant energy range [10]. The highest hit rates in the MVD are expected to occur in experiments which use heavy nuclear targets and at highest beam momentum. The hit rates in the MVD silicon detectors especially in the forward disc layers will be very high at the maximum luminosity and can exceed 10^6 hits per second for individual front-end chips and 10^3 hits per second for individual pixel cells.

3.1.2 Consequences on the MVD Design

As discussed in the previous paragraph, the particle flux in the $\overline{\mathsf{P}}$ANDA detector is not uniform and changes with incident beam momentum. To provide the best coverage of the solid angle, especially very close to the interaction zone, the MVD will be defined by two major parts. The large angle component will be best covered by several barrel-like structures, which fill all the space between the beam pipe and the adjacent outer tracking detectors in the target spectrometer. Additionally, disc-like structures will close the gap towards the beam pipe for small polar angles. The two-folded design of the MVD is illustrated in Figure 3.2. Additionally, the pipes for the circulating antiproton beam (entering from the left side) and the target material are shown. The maximum radius for the whole MVD volume is only 15 cm, where the outer tracking device follows up. Six disc-like structures are foreseen to provide measurements of the particle trajectory close to the interaction point down to angles of a few degree with respect to the beam pipe. The outer radius of the beam and target pipes will be limited to only 1 cm within the MVD volume. To reduce the effect of multiple scattering in the beam pipe wall material, a light-weight material, such as an alloy made of aluminum and beryllium, is envisaged as pipe material. The thickness of the wall can be thinned down to 250 μm.

The reduction of the material budget of the MVD, including materials for holding structures, cooling and readout cables is one of the major interests of the ongoing R&D projects for the development of the MVD. The connection of the inner part can only be realized in upstream beam direction. Technically difficult will be the operation of the disc part to the outside, which is located further downstream and has to be realized also in upstream direction. An optimized solution has to be found in order to avoid areas with increased material in the MVD barrel section to realize the readout of the forward MVD part. This is of interest, since the barrel section measures predominantly the lower energetic component of the particle flux, depending on the incident beam energy and reaction channel. To much material would negatively influence the resolution of the MVD.

Connected to the coverage of the solid angle is the reduction of overlapping regions

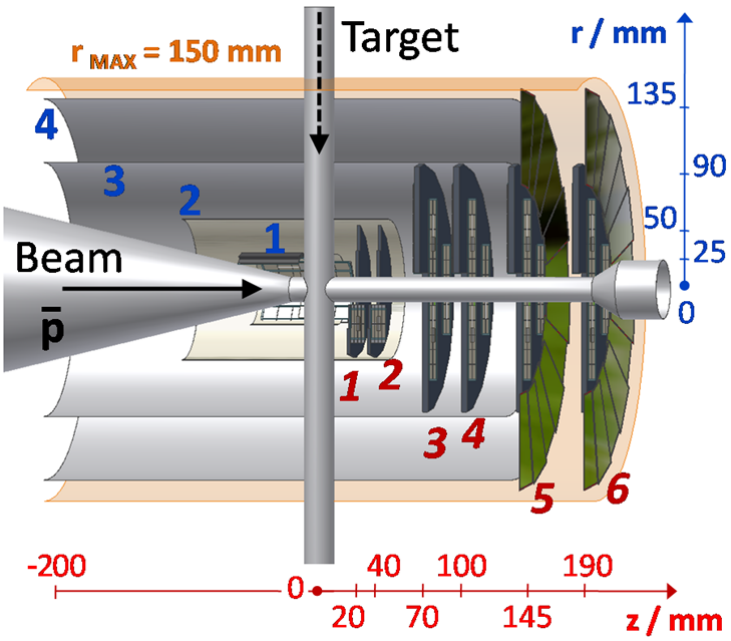

Figure 3.2: Artists view of the MVD and the target and beam pipe cross which defines the primary interaction region.

of detector modules in the barrel and the disc sections of the MVD. Currently, different arrangements of barrel and disc structures are under investigations, which are similar to the setup shown exemplarily in Figure 3.2. Section 3.3 will give a short overview of some design aspects.

3.2 Physics Requirements

3.2.1 Detection of Low Momentum Particles

For different reactions, particles in the final state might have a strong low energetic component, even at highest or intermediate $\overline{\text{P}}$ANDA beam energies. Figure 3.3 illustrates the available phase space for the products of the three-body $D^{\pm} \rightarrow K^{\mp}\pi^{\pm}\pi^{\pm}$ decay at an intermediate beam momentum of 6.73 GeV/c for the reaction $\overline{\text{p}}\text{p} \rightarrow D^{+}D^{-}$. For pions a prominent maximum at low longitudinal momenta is clearly visible. For kaons the maximum is less dominant and shifted towards higher momenta. To cover the full phase space of this reaction, a high reconstruction efficiency for low-momentum particle tracks is needed to increase the signal yield. This is of particular importance for channels with low production cross sections, such as expected in the search for exotic states in the charmed sector or high precision measurements of charmonium resonances.

For low energetic particles the momentum and vertex resolution will be limited

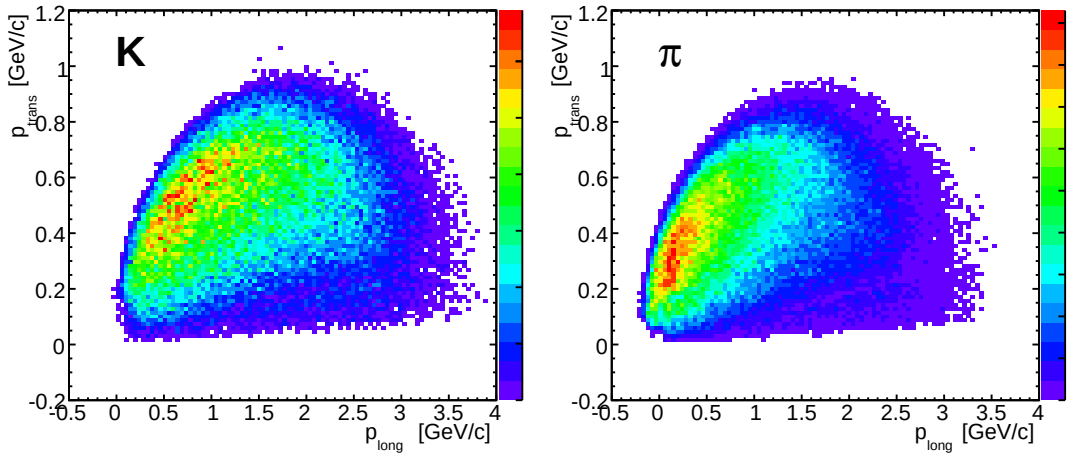

Figure 3.3: Momentum components for kaons (left) and pions (right) from the decay $D^{\pm} \rightarrow K^{\mp}\pi^{\pm}\pi^{\pm}$ of the reaction $\overline{\mathrm{p}}\mathrm{p} \rightarrow D^{+}D^{-}$ close to the production threshold.

by small angle scattering caused by the interactions of charged particles with the detector material. The relative low momentum spectrum of the reaction particles demands an optimized solution of the MVD material budget, which has to be minimized, especially for trajectories reconstructed in the target spectrometer, which are measured with the MVD barrel section for polar angles larger than approximately 45°. Figure 3.4 shows the momentum dependence of the mean deflection angle for various particle types after traversing 800 μm silicon, which is in the order of the thickness of two layers of silicon pixel detectors.

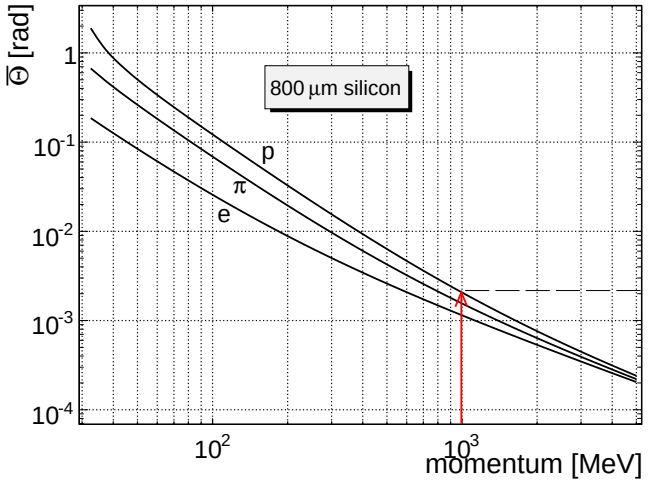

Figure 3.4: Momentum dependent distribution of the mean deflection angle $\bar{\Theta}$ for different particle species caused by small angle scattering.

The lateral deflection of a proton with momentum of about 1 GeV/c will be in the order of 2 mrad (marked by the arrow in Figure 3.4). This can be translated in a lateral displacement of approximately 20 μm per centimeter flight length after distortion. The distance to the following detector layer will be in the order of a few centimeters, depending on the direction of the track. The abberation of the hit position in the next layer is therefore in the same order compared to the uncertainty of the hit position measurement, which is defined by the size of the readout structure on the sensor surface. The resolution of the hit position measured by the silicon sensors is mainly defined by the pixel cell size or the width of the readout strips in the case of strip detectors, respectively. The position measurement obtained by the pixel detector can be reconstructed with a precision of better than 30 μm on the sensor surface, which is in the same order compared to the uncertainty introduced by small angle scattering. The intrinsic hit resolution of the MVD will be discussed more in detail in Section 4.2.

This estimate demonstrates, that a minimum of material of the inner tracking system is important in order to obtain a good vertex resolution. Therefore, a compromise between the number of hit measurements per track in the MVD and a minimized material budget has to be found. Usually materials for mechanical stability, cables for readout and power supply and cooling of the electronics is the major parts of the material budget, which altogether account for up to three-quarters of the inner tracker material budget, as e.g. used for current application in the field of HEP experiments [99]. Therefore a lightweight support structure and low power consumption of the front-end electronics, which reduces the cooling needs, is essential to reach the envisaged vertex resolution of better than 100 μm.

It is foreseen to build four barrel layers between beam pipe and outer tracking system and six disc-like structures to cover the space towards the beam axis. This two-folded design allows the measurement of mostly four space points for a wide polar angle region between 5° and 160°.

Figure 3.5 shows the mean number of hit points per track for pions with a beam momentum of $p_\pi = 1GeV/c$ tracked in the magnetic field in the solenoid part of $\overline{\mathsf{P}}$ANDA. The blue histogram in Figure 3.5 corresponds to tracks in the barrel section, whereas the red distributions shows only tracks measured by the forward disc part. For this simulation an idealized track generator was used to distribute trajectories equally over the full MVD coverage in a polar angle range between 0°–160°. The situation in $\overline{\mathsf{P}}$ANDA experiments will be different since the beam boost would favor higher energetic particles in the forward direction.

Figure 3.6 show a two-dimensional map of the mean hit number for the full solid angle. Looking from the interaction point most tracks will have four hits in the MVD. For trajectories, which traverse the forward discs section of the MVD, the mean hit number per track will be slightly increased due to the larger overlap of sensors within the same detector layer and the higher number of disc structures.

The MVD will have a polar angle coverage between $5 - 160°$ and covers the full

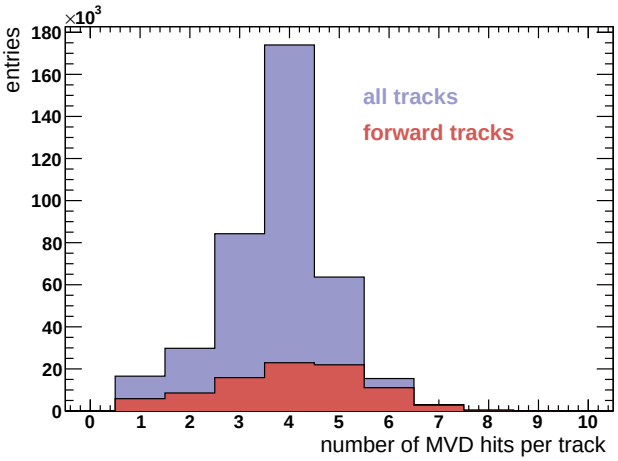

Figure 3.5: Distribution of the number of MVD hits per track from the IP, for tracks measured with the MVD barrel part (blue) and for trajectories going through the MVD forward discs (orange) separated.

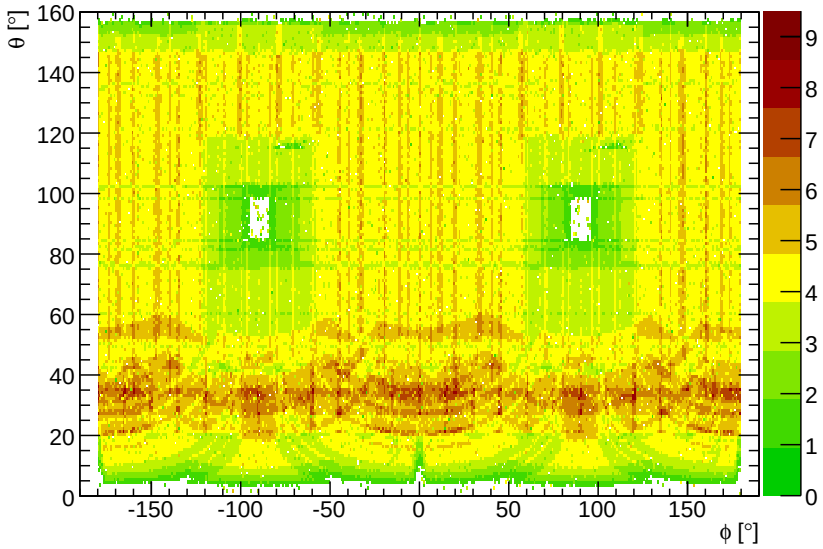

Figure 3.6: Mean number of hit points measured by the MVD per track (colored scale). The azimuthal vs the polar angle is shown. Except the necessary target pipe openings at $\phi = \pm 90°$ there are no further acceptance losses over the MVD range.

azimuth almost uniform, except the small opening in the MVD for the target pipe around 90° (see Figure 3.5). In the barrel section the overlap of sensors of different layers is minimized and the mean hit number per track is mostly four as expected. In the disc section more overlapping regions have to be tolerated. The inner pixel layers will make use of the same rectangular-shaped sensors which are used to build the barrel layers. Therefor more overlap in the disc structures has to be accepted

to assure a sufficient coverage in forward direction. In the larger forward discs the outer ring of sensor elements can be replaced by strip sensors, which allow the same coverage but with less overlap. The design of the MVD will be discussed more in detail in Section 3.3.

3.2.2 Determination of the Vertex Position

For many aspects of the $\overline{\text{P}}$ANDA physics program it is essential to detect the delayed decays of resonances with strange or charm quark content. The resolution of the decay position has to be obtained better than the typical decay length of the particular particles. Furthermore, the separation of the decay position from the reaction origin is important to separate background reactions from the physics channel. Typical decay lengths of strange particles, e.g. the well known Λ^0, are in the order of a few centimeter, whereas particles with charm quark content decay typically within a few hundreds of micrometers. Table 3.1 gives an overview of short-lived hadronic states and some of their prominent decay modes.

Since the reaction process occurs in flight, the incident beam momentum is transfered to the reaction particles in the outgoing channel. Due to the boost to the decaying particle the observed flight length L gets elongated by a relativistic factor and can be given as:

$$L = \beta\gamma c\tau \tag{3.1}$$

L depends on the relativistic velocity $\beta = v/c$ and the γ factor, which is defined as $\gamma = (1-\beta^2)^{-1}$. τ is the mean decay time in the particle rest frame. Due to the beam boost the velocity of short-lived particles might be relatively high, e.g. a K_s^0 with momentum of $p = 1$ GeV/c will have a mean decay length in the detector, which is elongated by a factor of $\beta\gamma \approx 3.2$, whereas Table 3.1 lists only the decay length $c\tau$.

To detect charged hadrons with strange quark content, the combination of the MVD and the outer tracking detectors is essential. Charged strange hadrons decay often into a pair of a neutral and a charged daughter, which leaves a typical signature marked by a kink in the tracking system. The decay position might be inside or even behind the MVD volume, since the flight length of the particular resonance can be in the order of the dimensions of the MVD. The additional identification of the neutral partner from the decay outside the tracking system would enhance the signal reconstruction ability. Double-strange charged baryons, such as Ω^- and Ξ^-, Ξ^0 decay most-likely subsequently into a Λ^0, which can be detected via its large branching ratio into a pair of a proton and a pion.

Particles with charm content decay usually within the beam pipe diameter of two centimeter and therefor in front of the first MVD layer. Since the incident antiproton momentum is at least around 6.5 GeV/c in order to overcome the charm production threshold, the hadrons containing charm are boosted in the forward direction. Especially for low excess energies above the $c\bar{c}$ threshold the phase space for those

particle		decay length $c\tau$	prominent decay channels (BR)
mesons	$(q\bar{q})$		
K_s^0	$(d\bar{s})$	2.684 cm	$\pi^+\pi^-$ (69.20 ± 0.05) %
D^+	$(c\bar{d})$	311.8 μm	$K^0 + anything + \bar{K^0} + anything$ (61 ± 5) %
			$e^- + anything$ (16.0 ± 0.4) %
			$K^- + anything$ (25.7 ± 1.4) %
			$K^+ + anything$ (5.9 ± 0.8) %
			e.g. $K^-\pi^+\pi^+$ (9.22 ± 0.21) %
D^0	$(c\bar{u})$	122.9 μm	$K^0 + anything + \bar{K^0} + anything$ (47 ± 4) %
			$K^- + anything$ (54.7 ± 2.8)%
			$K^+ + anything$ (3.4 ± 0.4)%
			e.g. $K^+\pi^-\pi^0$ (13.9 ± 0.5) %
			e.g. $K^+\pi^-$ (3.89 ± 0.05)%
D_s^+	$(c\bar{s})$	149.9 μm	$K^0 + anything + \bar{K^0} + anything$ (39 ± 28) %
			$K^- + anything$ (13^{-12}_{+14}) %
			$K^+ + anything$ (20^{-18}_{+14}) %
			e.g. $K^+K^-\pi^-$ (5.50 ± 0.28) %
baryons	(qqq)		
Λ^0	(uds)	7.890 cm	$p\pi^-$ (63.9 ± 0.5) %
			$n\pi^0$ (35.8 ± 0.5)%
Σ^+	(uus)	2.404 cm	$p\pi^0$ (51.57 ± 0.30) %
			$n\pi^+$ (48.31 ± 0.30) %
Σ^-	(dds)	4.434 cm	$n\pi^-$ (99.848 ± 0.005) %
Ω^-	(uss)	2.461 cm	ΛK^- (67.8 ± 0.7) %
Ξ^-	(dss)	4.91 cm	$\Lambda\pi^-$ (99.887 ± 0.035) %
Ξ^0	(uss)	8.71 cm	$\Lambda\pi^0$ (99.525 ± 0.012) %
Λ_c^+	(udc)	59.9 μm	p (or n) $+anything$ (50 ± 16) %
			$\Lambda + anything$ (35 ± 11) %
			$\Sigma^\pm + anything$ (10 ± 5) %
			$pK^-\pi^+$ (5.0 ± 1.3) %
Ξ_c^+	(ucs)	132.0 μm	$\Xi^-\pi^+\pi^+$ (*seen*)
Ξ_c^0	(dcs)	33.6 μm	$\Xi^-\pi^+$ (*seen*)

Table 3.1: Decay length of various short-lived particles and some of their prominent decays (values from [15]).

reactions is limited and the particles remain under small angles with respect to the beam axis. For a clear separation of the decay position from the $\overline{\text{p}}$p interaction point the determination of the longitudinal component of the decay position is essential.

As discussed in the previous section the material budget of the tracking system has to be minimized in order to reduce the small angle scattering, which rises from interactions of the reaction particles with the materials. A very thin aluminum-

beryllium alloy with a wall thickness of 230 μm is foreseen to construct the beam and target pipes in order to keep the distortion of the particle trajectory in front of the MVD as low as possible.

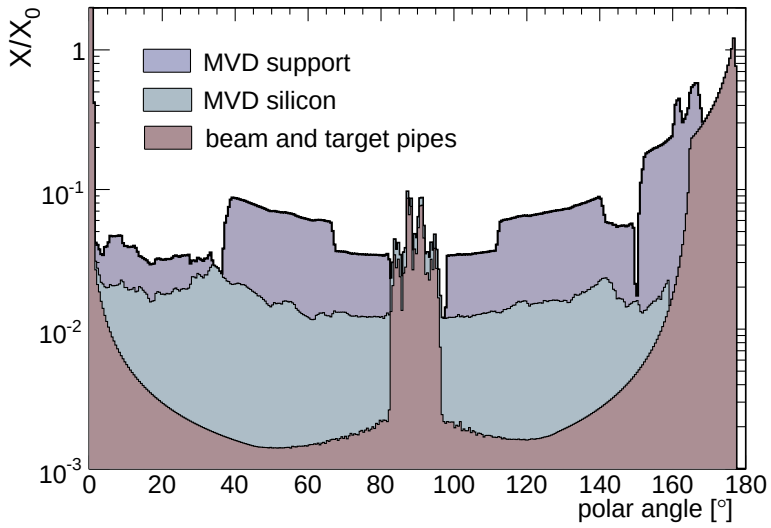

Figure 3.7: Part of the radiation length X/X_0 for materials within the MVD volume as function of the polar angle. Additionally the beam and target pipes are incorporated.

The thickness of the walls of the pipe system becomes important only for trajectories with very low polar angles. This can be seen in Figure 3.7, which shows the fraction of the radiation length for all materials within the volume defined by the MVD dimensions and additional the beam and target pipe system of the whole $\overline{\text{P}}$ANDA setup in the target spectrometer section. The contribution of the pipe material budget (purple area) to the total X/X_0 distribution, which is the superposition of all individual contributions, is the smallest, although the distribution arises toward very low and very high trajectory angles with respect to the beam pipe. For those trajectories, the particle traverses the multiple of the particular wall thickness, which causes the drastic increase of the material budget in this region. This is of particular interest for the dipole magnet section of $\overline{\text{P}}$ANDA (note that the y-coordinate in Figure 3.7 is drawn logarithmic).

The largest contribution to the material budget of the MVD comes from the support structures, whereas the silicon detectors (turquoise area) contribute only up to three percent of the radiation length in total to the overall material budget. Recent applications in HEP experiments, e.g. the silicon tracking detector of the ZEUS experiment [99], have shown that the support structures make the largest contribution to the material budget. Support structures include not only holding structures,

but also materials for cooling pipes and cables for data readout and all operational services. Altogether, this makes up to three-quarter of the full material budget of the MVD. The design value for the MVD is envisaged to stay below 2 % radiation length per layer, which is a challenging task and can only be achieved by using only very light-weighted materials.

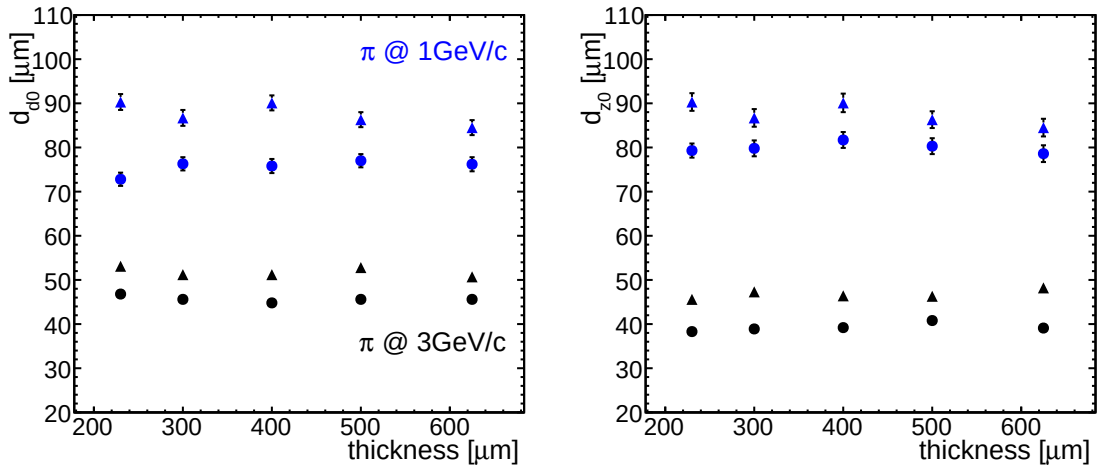

Figure 3.8: Resolution of the primary vertex position for single pion tracks for different thicknesses of the beam pipe (x-coordinate) and different amount of support material. Only tracks reconstructed in the barrel section of the MVD for polar angles between 60° and 65° have been used.

At $\overline{\text{P}}$ANDA energies, the resolution of of the production vertex and the momentum reconstruction are predominantly limited by small angle scattering, rather than the resolution of the trajectory hit position measured by the silicon detectors. This is demonstrated exemplarily in Figure 3.8 for pions reconstructed in the barrel section of the MVD for two different momenta: at $p_\pi = 1$ GeV/c (blue symbols) and at $p_\pi = 3$ GeV/c (black symbols) incident momentum, respectively. As production position an idealized vertex position has been defined at the interaction point and only tracks in the barrel section between 60° and 65° in polar angle have been used. The reconstructed distance of closest approach to this position is a direct measure of the tracker resolution, which is predominantly defined by the MVD, rather than the outer tracking detectors[3]. The vertex resolution is shown separately for the lateral (left figure) and the longitudinal (right figure) component in beam direction, respectively. The filled dots represents the standard MVD material budget as given in Figure 3.7, whereas the rectangular symbols show the resolution with estimated doubled amount

[3]In this simulations the STT was chosen as outer tracker option.

of support material in the considered barrel region. The resolution differs almost by a factor of two for low momentum pions at 1 GeV/c incident momentum from the 3 GeV/c momentum case, which is directly caused by the different strength of small angle scattering. The axis of abscissae shows the wall thickness of the beam pipe, which varies almost up to a factor of three compared to the design value of 230 μm of aluminum-beryllium alloy. Within the statistics this does not have a significant influence on the vertex position, whereas an increase in the material budget has a direct impact on the resolution, in particular in the barrel section, where most-likely low momentum particles have to be measured.

3.2.3 High Rate Environment

The high luminosity of up to $L = 2 \times 10^{32}$ cm^{-2}s^{-1} causes a high interaction rate and therefore a high count rate in the MVD. As discussed in Section 3.1.1, the maximum of the particle flux is shifted toward small angles especially at higher beam momenta due to the fixed-target topology. The MVD disc part has to deal with the highest hit rates in the readout electronics. Although the number of particles per event remains rather small compared to HEP experiments, the count rates in the detectors may be largely due to the anisotropic particle flux. Figure 3.9 shows the number of particles per event for $\overline{\text{p}}$p (left) and $\overline{\text{p}}$-Au collisions at the maximum $\overline{\text{P}}$ANDA beam momentum of 15 GeV/c.

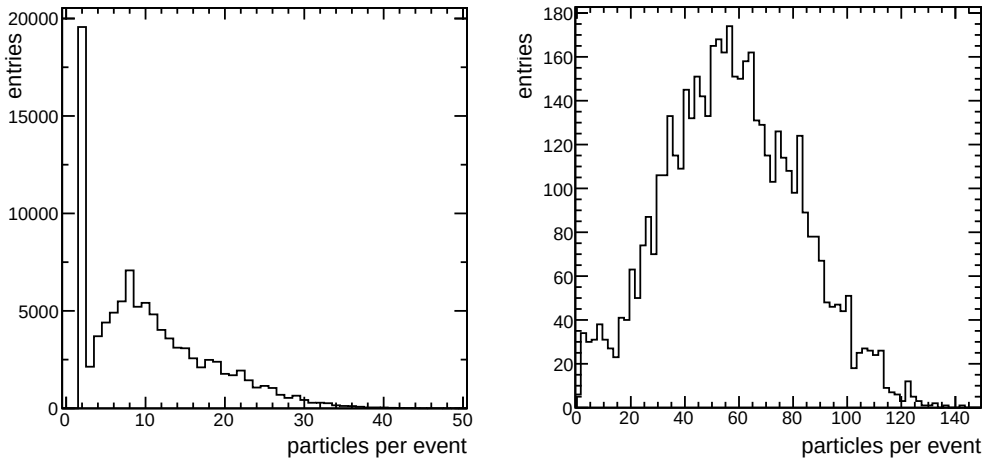

Figure 3.9: Number of particles per event for $\overline{\text{p}}$p (left) and for $\overline{\text{p}}$-Au collisions (right) at maximum $\overline{\text{P}}$ANDA beam momentum.

Table 3.2 lists the mean number of tracks per event for $\overline{\text{p}}$p and $\overline{\text{p}}$-Au collisions at different incident beam momenta of 1.5 GeV/c, 8 GeV/c and 15 GeV/c, respectively.

momentum [GeV/c]	particle multiplicity	charged particle multiplicity (only stable)	$\frac{(\overline{p}p)_{el}}{(\overline{p}p)_{total}}$ [in %]
		$\overline{p}p$	
1.5	5.9	2.4	49.1
8.0	8.9	3.4	22.2
15.0	10.6	4.0	19.6
		$\overline{p}$-Au	
1.5	30.8	13.8	-
8.0	51.1	22.2	-
15.0	57.3	23.9	-

Table 3.2: Particle multiplicity per event for $\overline{p}p$ and $\overline{p}$-Au collisions at different incident beam momenta. Relevant for the MVD is the charged track multiplicity. Additionally, the fraction of elastic $\overline{p}p$ part to the total cross section is given.

These numbers were obtained by use of the DPM model [96], which describes annihilation processes in $\overline{p}p$ interactions and includes hadronic elastic scattering[4]. Elastic scattering events are the source of low momentum protons, which traverse the detector almost perpendicular to the beam axis and produce a large energy deposit in the sensor material, which contributes to the process of radiation damage. The relative strength of the elastic scattering decreases with higher beam momenta and the relevant strength for different incident beam momenta is given also in Table 3.2.

The $\overline{p}$-Au data were obtained by using the UrQMD model [97],[98]. The mean number of charged particles in the final state is much larger, compared to $\overline{p}p$ interactions. Many particles will be low-energetic (see Figure 3.1) and especially light nuclear fragments from the antiproton collisions with the heavy gold target can cause material damage of the silicon detectors.

For the development of the front-end electronics for the sensor readout the knowledge of the expected data rate is important. In a previous attempt [100] the expected data rates in the detector were estimated on the basis of only the track density and with much less statistics. For the following estimates of the expected maximum count rates the digitized detector data format has been used (see Section A.3 for details). This allows an estimate based on a realistic readout concept for the silicon detectors.

Table 3.3 summarizes the maximum count rates at different levels. The rate on sensor level is important for the dimension of the module controller chip as part of the ATLAS pixel detector which is the basis for the $\overline{\text{PANDA}}$ pixel detector design.

[4] A newer version of this model is now available in the simulation framework, which includes elastic Coulomb-interactions.

reaction	sub-detector	hit rate [per second]		
		per sensor	per front-end	per channel
$\overline{\mathrm{p}}$p	pixel	5.7×10^6	0.8×10^6	0.1×10^3
$\overline{\mathrm{p}}$p	strip	1.6×10^6	1.2×10^6	7.0×10^3
$\overline{\mathrm{p}}$N	pixel	38.4×10^6	7.1×10^6	0.8×10^3
$\overline{\mathrm{p}}$N	strip	7.5×10^6	5.1×10^6	$9.0. \times 10^3$

Table 3.3: Expected maximum count rates at different reactions at the maximum $\overline{\mathsf{P}}$ANDA beam momentum. The rates are calculated with respect to the sensor, the front-end with the maximum rate on the sensor and the maximum channel.

The rate on front-end level defines the size of the bus, which transfers the data to the next level. The pixel or strip count rate defines the minimum time, which is needed in order to guarantee the readout of the particular cell to avoid double hits from different events in the same time interval.

The values presented in Table 3.3 show that the MVD has to operate in a high rate environment. The values are in good agreement with previous calculations for the pixel part [100] and additional values for the strip detector part of the MVD were given. The front-end electronics for the pixel detector are able to deal with even higher track densities, as e.g. at the ATLAS experiment at the LHC [100]. The readout concept of the MVD cannot be realized with a first-level trigger like in the ATLAS pixel detector case. Currently, new developments for a $\overline{\mathsf{P}}$ANDA pixel detector front-end chip are in progress.

The count rates in the strip detector part of the MVD depends on the size of the used sensor. For the simulation presented above a size of 2.2×6.2 cm^2 has been used. Different dimensions would increase the length of the strips implemented on the surface of the sensor and directly affect the front-end count rate. Nonetheless, the front-end electronics of state-of-the-art strip detector applications will be able to realize the needed high speed readout of the detector data. For this purpose, the $\overline{\mathsf{P}}$ANDA collaboration contributes to new developments of a new strip detector front-end chip for experiments at the FAIR facility.

3.3 Design Aspects

The $\overline{\mathsf{P}}$ANDA spectrometer will be a compact apparatus operating with a stationary target and will use an circulating antiproton beam. The layout of the apparatus is split into two major parts, a central solenoid spectrometer and a dipole spectrometer, which covers small angle tracks with respect to the beam axis. A summary of the experimental setup is given in Section 2. The general two-folded design is reflected

by the innermost tracking detector. A barrel section with four layers and a number of disc-like structures around the beam pipe are foreseen to close the gap towards further tracking stations, provided either by GEM detectors or drift chambers in the endcap of the target spectrometer. The crossover between barrel and forward part of the MVD is chosen around 45° in polar angle to minimize the effective path length of the particle trajectory through the detector materials. An overview of the present layout of the MVD is given in Figure 3.10 together with the beam and target pipe cross.

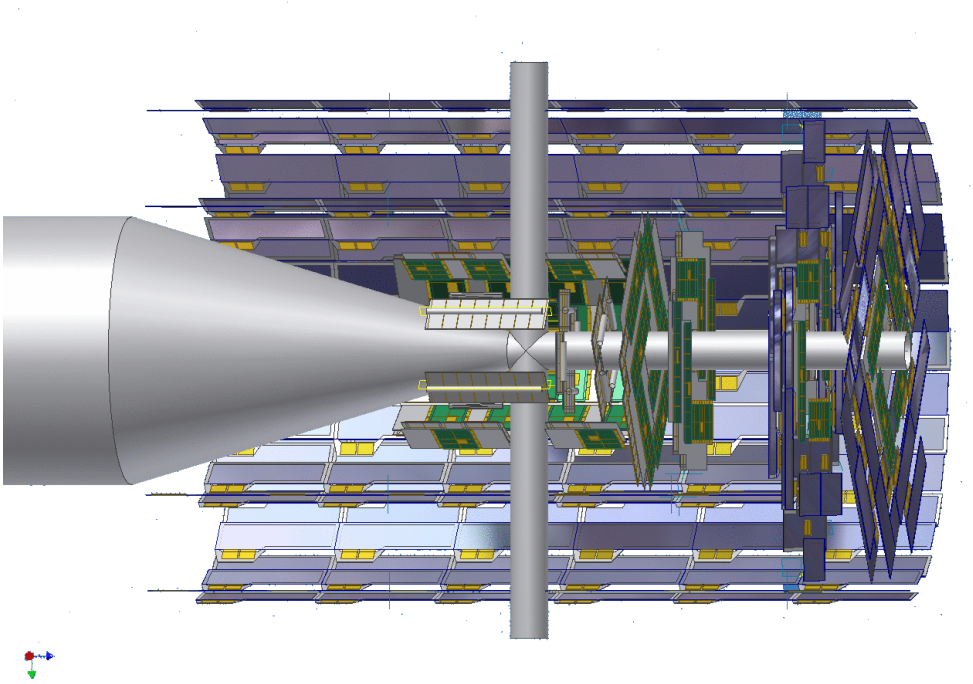

Figure 3.10: Inside view of the Micro Vertex Detector. There will be four layers in the barrel section and six forward disc structures. Additional the beam and target pipes are shown, where the beam enters from the left.

In this paragraph the layout of the MVD is introduced. The general layout of the MVD is fixed, which includes the number of layers and the outer dimensions. Currently different modifications of the setup are under investigations. Section 3.3.3 provides further information about current developments. The implementation of the MVD in the simulations used for most investigations presented in Section 4–6 is explained more in detail in Section 3.3.4.

3.3.1 Current Design

The aim of the MVD is to deliver four hit point measurements close to the interaction zone, which is defined by the beam target interaction. Four layers in the barrel section will fill the gap between the beam axis and the outer tracking device, which starts at an outer radius of 15 cm. The forward region below 45° in polar angle is covered by six disc-like structures. Table 3.4 summarizes the dimensions of all barrel layers and disc structures as shown in Figure 3.10.

barrel MVD		
structure	mean radius [cm]	length [cm]
barrel 1	2.5	6.5
barrel 2	5.0	13.0
barrel 3	9.0	32.0
barrel 4	13.5	39.0
forward MVD		
structure	outer radius [cm]	z position [cm]
disc 1	9.3	2.0
disc 2	9.3	4.0
disc 3	12.7	7.0
disc 4	12.7	9.0
disc 5	24.0	16.0
disc 6	24.0	18.0

Table 3.4: Summary of the MVD barrel and disc structure dimensions.

The innermost two layers of the barrel section consist entirely of hybrid pixel detectors, comparably to those used in the LHC experiments [85],[101]. Since the environment in which the silicon detectors have to operate are different from the LHC experiments, certain detector aspects have to be adapted for the use in $\overline{\text{P}}$ANDA (see Section 3.3.2.1 for details). The two outermost layers of the MVD barrel part will be constructed of double-sided silicon strip detectors, which give an advantage in the material budget. Strip detectors do not require a second silicon wafer bonded on the detector surface, like for the hybrid pixel detectors. The front-end ASICs are connected at the sensor edge via bonds and the signals are further on transfered to the outside. The expected particle flux in the outer barrel layers is sufficiently low to operate strip detectors in this particular area. The combination of the hit information from both sides of the strip sensor allows the reconstruction of a point-like information comparable to the pixel detector measurement. The use of strip detec-

tors reduces the amount of readout channels drastically compared to pixel detectors with the same surface.

The four disc stations, which are closest to the IP, to be seen as inner part in Figure 3.10 (green colored elements) and also the inner elements of the larger two outer discs are pixel detectors. Pixel detectors were produced so far only in rectangular-shaped, which represents not an ideal building block to form small disc-like structures close to the interaction point. As indicated in Figure 3.10, the first four discs layers are arranged as two double-layers, with a minimal spacing in between. In the double-layer, the individual sensor planes can be tilted by a certain angle with respect to each other, in order to compensate acceptance gaps, which results from the non-uniformly coverage of the disc by rectangular-shaped sensors. The holding structure for these double-layers can be made very light in weight, since the number of sensors is small. A concept is currently under investigation, which provides the stability for both individual layers at the same time [102].

The last two disc structures of the MVD will be of mixed type. The innermost detector elements will be pixel detectors, whereas the outer laying sensors are strip detectors. Currently various concepts are under investigation for the construction of these mixed type discs. In the current layout rectangular-shaped sensors are used (see Figure 3.10). Silicon strip detectors can be produced wedge-shaped, which makes it easier to cover the disc surface. Section 3.3.3 gives and idea how this structures might look like.

3.3.2 Detector Technologies

Many experiments in particle and nuclear physics use an advanced vertex detector for particle tracking. For the precision needed only semiconductor detectors are flexible enough to operate in very different environments and energy domains in experiments to investigate different physics aspects. Two different approaches using semiconductor technologies are standard up to date: silicon pixel and strip detectors. In pixel detectors the sensitive detector region is divided in individual cells providing directly a three dimensional spacial information. The active area of strip sensors is read out by individual strips on the surface and deliver therefore only a two dimensional information. The other side can be read out independently and the combination of both signals provides also a three-dimensional information.

For both detector concepts the realization of continuous readout is currently under development. In the following sections the different detector concepts are introduced and discussed for the use in the $\overline{\text{P}}$ANDA experiment.

3.3.2.1 Hybrid Pixel Detectors

As high resolution detectors pixel sensors are foreseen to deliver the first hit points measured with the MVD close to the interaction point. The advantages are the intrinsic good spatial resolution and the good radiation tolerance of the standard

250 μm production process. The latest developments of pixel detectors were mainly driven by the construction of the inner tracking detectors for the large LHC experiments, e.g. the ATLAS experiment [85]. These large multi-purpose detectors have to handle high event rates and have to tolerate a large radiation dose during their lifetime and are an ideal candidate for the MVD of the $\overline{\mathsf{P}}$ANDA experiment. Although, some modifications are necessary to operate these detectors in the $\overline{\mathsf{P}}$ANDA environment. The proposed pixel dimension for $\overline{\mathsf{P}}$ANDA is different and will be of quadratic shape with a size in the order of 100×100 μm^2 rather than 50×400 μm^2 as designed for the ATLAS experiment. The readout concept of the front-end ASICs will be different, since in the HESR where $\overline{\mathsf{P}}$ANDA will be located the beam current will be continuous and contrary to the bunched beam structure of the LHC[5]. Therefore, the trigger concept for the detector readout has to be modified for the use in $\overline{\mathsf{P}}$ANDA. For this purpose the development of a new front-end chip is planed [86]. This project is using the new 130 μm production process, which allows the implementation of smaller feature sizes in the semiconductor material. This will be advantageous to reach smaller pixel dimensions and the needed radiation tolerance level for the operation of the detector close to the interaction point. The estimated radiation dose during ten years of $\overline{\mathsf{P}}$ANDA operation will be in the order of two magnitudes less compared to the LHC radiation environment in case of $\overline{p}p$ collisions and at least a factor of ten less in case of $\overline{p}N$ collisions. By using a radiation hard technology the effect of radiation damage to the detectors can be reduced and longer operation times can be achieved.

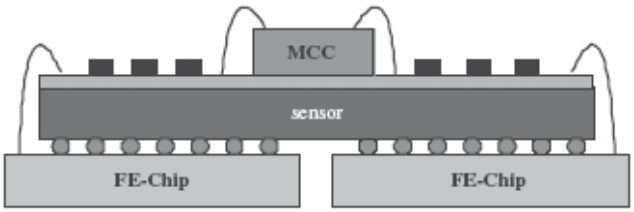

Figure 3.11: Readout concept of the ATLAS pixel detector with two rows of front-end chips bonded on the sensor surface. The module controller chip (MCC) combines the collected data from all front-ends and provides the communication to the DAQ system.

The material budget of the pixel layers is of special interest since the integrated material budget of the MVD will not only cause γ background via conversion for the sensitive electromagnetic calorimeter, but also increases the multiple scattering in

[5]The LHC provides two beams of protons with a maximum energy of 7 TeV each, which will collide at well defined interaction points, where the large detectors are operating.

the materials of different layers, which limits the track and vertex resolution. Pixel detectors need the readout chip directly bonded on the surface of the sensor wafer in order to realize the readout of the pixel matrix. The concept is shown schematically in Figure 3.11 This additional silicon layer cannot be thinned significantly below 200 μm and adds to the material budget. Additional cooling services are needed in the sensor area to remove the heat produced by the readout electronics during operation.

3.3.2.2 Silicon Strips

Since two decades silicon strip detectors are used in many nuclear and particle physics experiments [103]. These flexible detectors are radiation resistant, fast in readout speed and are nowadays comparably cheap, in contrast to pixel detectors.

The readout electronics does not need a wafer of the same size of the sensor area like for pixel detectors. Usually the front-end is connected via bonds directly at the ends of the strips on the sensor surface. The analog signals can be further transfered via flexible kapton[6] cables, e.g. to the end of a barrel stave. This is of advantage, since the front-end electronics should not operate in a region of a high radiation dose.

Strip detectors can be produced flexible in dimensions and shapes. The CMS experiment at the LHC uses different sensor shapes for different regions of the large inner tracking detector [101]. Wedge-shaped sensors may be used for the $\overline{\text{P}}$ANDA MVD for the forward discs and rectangular shaped sensors for the barrel section. The same front-end electronics can be used easily for different dimensions. Since the strips are implemented on the sensor surface, the signal to background noise ratio will be therefore lower compared to pixel detectors.

The use of strip detectors reduces the number of readout channels drastically compared to the same sized pixel detector. To obtain a three dimensional spatial information from the particle trajectory the combination of independent strip information is necessary. This can be done either by combining different layers of strip detectors or to enable the same sensor to be read out on both sides. The direction of the readout structures have a relative angle of 90° in maximum which is often called stereo angle. This readout scheme enables the device to reach comparable hit resolution like pixel detectors.

3.3.3 Design Iterations

In the layout of the MVD as introduced in Section 3.3.1 regions with increased overlaps of sensors in the discs cannot be avoided, since the sensors are simply of rectangular shape. To minimize the overlap between sensors in the same layer, wedge-shaped detector elements can be used instead. The CMS collaboration uses in the

[6]Kapton cables provide a good electronic shielding with a minimum of material needed for insulation. Furthermore they are very robust and flexible and widely used in HEP detector construction.

ring sections of the inner tracking detector also silicon strip detectors of wedge-shape [101].

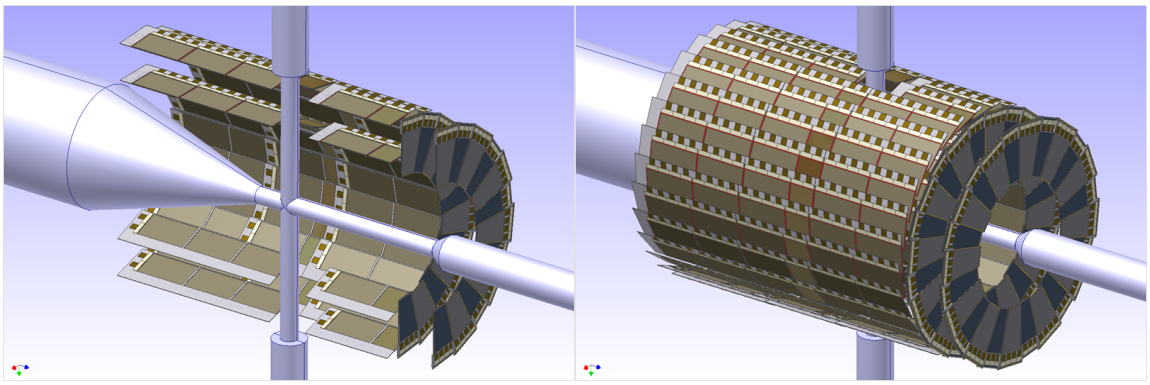

Figure 3.12: Design study of the outer MVD strip detector layers. In this study the forward discs are built of wedge-shaped strip detectors and the last two discs are shifted outside of the barrel section (pixel detector elements excluded, beam enters from the left).

Figure 3.12 shows an adopted concept study with changed strip detector elements in the forward discs. Only the strip elements are shown and the two last layers are located further downstream. Additional space is needed for the readout of the strip detectors at the outer edge of the disc. The staves in the barrel layers are designed to provide the readout on both sides of the stave for the double sided strip detectors. The presence of the target pipe is an additional difficulty in the construction of the barrel section. The layers are split into two halves, which are connected at the outside to the outer tracking system.

3.3.4 MVD in the Simulations

Based on the MVD layout described in Section 3.3.1 the performance of the proposed setup was analyzed within a full $\overline{\text{P}}$ANDA detector simulation. Within the simulation framework a detailed description of the inner vertex detector was realized. This includes not only the sensor material but also major components of the non-sensitive material budget, in particular the mounting structure, equivalent material for the cables and cooling. The largest part of the material budget results from support structures for holding the sensors and for cooling needs. The amount of material was estimated and introduced in the detector description. An overview of the MVD as it appears in the simulations is given in Figure 3.13. The support structures are only visible for the forward discs. In the barrel section the support is represented

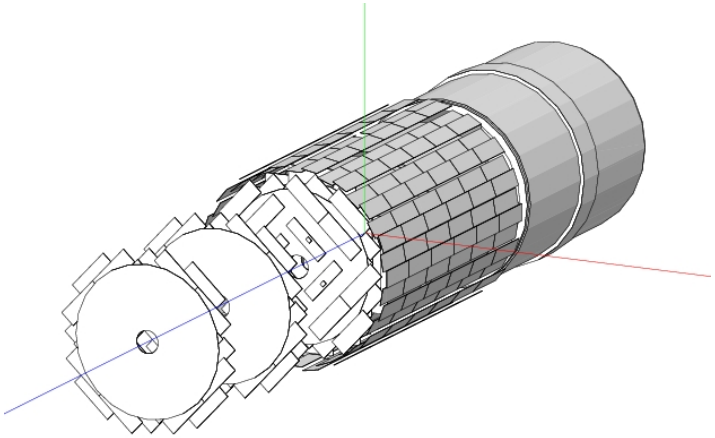

Figure 3.13: Overview of the MVD implementation within the software framework. Apart from the sensors and readout elements the major components of the support are included as well (see text for details).

by two tubes of carbon between the layers. The material budget per MVD layer[7] is in the order of 2% of the radiation length (see Figure 3.7). In the upstream region an additional support structure representing mainly cabling and cooling support was introduced. A realistic material budget representation in the detector simulation is not only important for track reconstruction, but also of interest for production of conversion photons as possible background source for the backward endcap of the electromagnetic calorimeter.

The detector description is done via the XML[8] script language. This has the advantage of a clear definition standard for different applications. The geometry definition is not only used by the simulation, but also for reconstruction and particle identification. This allows a consistent use of basic parameters such as sensor thickness and dimensions. Together with the use of a sophisticated database system [105], even a chronological evolution of parameters can be realized. The simulation of the detector and the physics processes of particle interactions with materials is done with the GEANT4 transport code [106]. Further information about the structure of the simulation code and the digitization formalism, which is a prerequisite of the reconstruction algorithm, can be found in Section A.1.

[7] Value obtained by other experiments, e.g. the ZEUS silicon detector [99] show a material budget including all services in the order of $3\%X_0$ per layer.

[8] Extensible Markup Language is a general specification language to define a common standard for various applications. The tools used within the PANDA framework have been originally developed by the CMS collaboration [104].

4 Performance of the MVD

4.1 Overview

The Micro Vertex Detector is an integral part of the $\overline{\text{P}}$ANDA experiment and crucial for a good track reconstruction. As already discussed in Section 3.2.2 the limiting factor for the resolution is the material budget of the MVD rather than the hit resolution. This will be discussed in detail in Section 4.2. Figure 4.1 shows a comparison between the momentum resolution of the track fit with the full tracking system and without the MVD. The full tracking includes information of the MVD, STT[1], GEM detectors and the forward dipole tracking and the analysis was done for pions with a fixed momentum of $p_\pi = 1$ GeV/c. Altogether omitting the MVD in the track

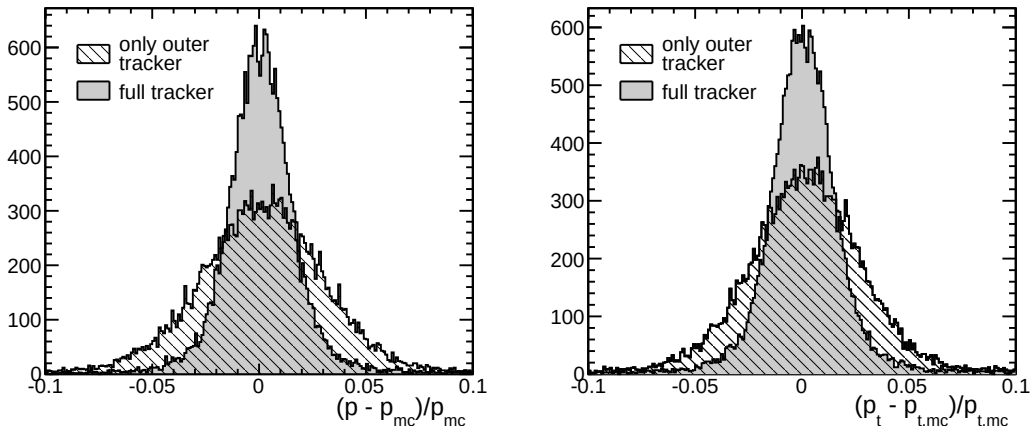

Figure 4.1: Comparison of the momentum error obtained by the full $\overline{\text{P}}$ANDA track fit (grey) and without MVD in the fit procedure (hatched). The right frame shows the deviation of the fitted transverse momentum from the Monte Carlo value and the left frame shows the corresponding total momentum distribution.

[1]Here, the tracking system version with the Straw Tube Tracker in the target spectrometer has been used.

building degrades the momentum resolution by almost a factor two. Values for the error distribution shown in Figure 4.1 are given in Table 4.1. Although this design

		momentum		transverse momentum	
		mean	σ [%]	mean	σ [%]
1 GeV/c	full tracking	6.7×10^{-4}	1.40	6.80×10^{-4}	1.42
	without MVD	1.5×10^{-3}	2.60	1.29×10^{-3}	2.90

Table 4.1: Mean and σ values for the error distribution of the transverse and total momentum for the full $\overline{\text{P}}$ANDA tracking and without MVD in the track fit as shown in Figure 4.1.

would not be realistic for an efficient tracking system this simple comparison shows that the influence of the MVD on the momentum resolution is about a factor two.

Silicon strip and pixel detectors provide very precise space point measurements, which are crucial for high resolution vertex reconstruction. Due to the beam boost in a fixed target experiment, most particles traversing the detector will have a larger longitudinal than transverse momentum component. To measure the primary vertex, the MVD is essential as illustrated in Figure 4.2 in a comparison of the primary vertex resolution for the full tracking system (grey distribution) and without the MVD in the track fit (hatched distribution). In a plane transverse to the beam axis, which

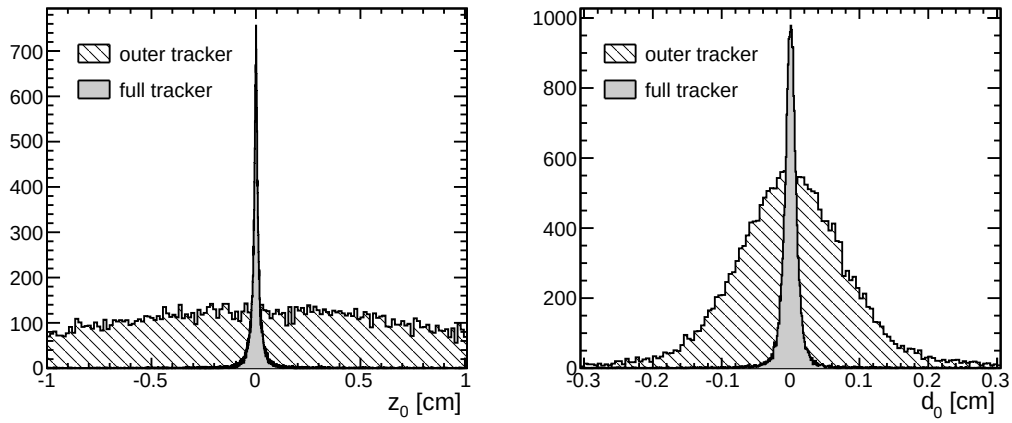

Figure 4.2: Track parameter z_0 (left) and d_0 (right) for pions with momentum $p = 1$ GeV/c reconstructed with the $\overline{\text{P}}$ANDA tracking system (grey) and without MVD in the track fit (hatched).

corresponds to the d_0 track parameter, the resolution gets worse but is still better than one millimeter. This comes about mainly from the forward tracking for particles with small angle with respect to the beam axis. The corresponding z_0 information is practically lost.

4.2 Single Hit Resolution

For short-lived particles, e.g. D mesons with typical decay lengths of a few hundred micrometers, it is important to measure the decay products as closely as possible to the interaction point. As introduced in Section 3.3.1 the MVD makes use of two different detector technologies. Hybrid pixel detectors are used in the first layers and silicon strip detectors in the outer layers. The resolution of the decay position depends on the uncertainty of the hit measurement, which is defined by the piercing point of the trajectory through the detector.

In general the resolution can be expressed as deviation from the expectation value written as [107]:

$$\begin{aligned} \sigma^2_{geom} &= \left\langle (x_0 - x)^2 \right\rangle = \int_{-p/2}^{+p/2} x^2 dx \Big/ \int dx \\ &= \frac{1}{3}\frac{p^3/4}{p} = \frac{p^2}{12} \end{aligned} \tag{4.1}$$

and depends directly on the spacing p of the readout structures[2]. x is the sensitive coordinate on the surface of the device. For strip detectors of the MVD with a strip pitch of $p = 100$ μm the geometric resolution would be according to Equation (4.1) $\sigma_{geom} = 28.9$ μm. If more than one pixel cell or more than one strip contributes to the hit information from a single track, the position of the hit point can be interpolated by using the measured energy information provided by the front-end electronics. The collected charge per channel is used to calculate a weighted position informations.

4.2.1 Cluster Hit Reconstruction

The resolution of the reconstructed vertex position depends on the ability to measure the flight path of a particle through the detector. Depending on the momentum of the particle its path gets distorted by multiple scattering in the materials, as discussed in Section 3.2. Nonetheless, the reduction of the uncertainty of the hit measurement at the sensor surface increases the vertex resolution, especially for higher energetic particles.

[2]The spacing, often referred as pitch, is defined e.g in case of strip detectors as distance between active neighboring conductor strips, which collect the deposited charge in the sensor material.

In order to find an optimum solution for the size of the pixels and the spacing between conductive strips, different sets of readout sizes have been simulated. All generated channels are processed to the cluster finding procedure, which is the basis for the track finding and track fitting. The software description of the MVD in the simulations allows a variation of basic parameters at run-time by using the digitized data format (see Section A.3 for details).

In the MVD design used for this simulations, pixel detector modules were utilized based on the original ATLAS sensor design, where asymmetric pixels were used with as size of 50×400 μm^2 [85]. The digitization procedure in the simulation, which generates the expected detector response, used the ATLAS front-end chip as a model chip. The size of the pixel cell is a free parameter in the simulation and can be varied. For $\overline{\text{P}}$ANDA different dimensions of pixels would be favored. The ATLAS standard pixel size was selected for the need in a collider experiment and the longer coordinate points in beam direction. At $\overline{\text{P}}$ANDA especially the resolution in beam direction is of interest and smaller pixel dimension increase the hit resolution.

The strip sensors will be read out independently on the front and back side of the sensor module. The direction of the metalization on the sensor surface defines the coordinate for which the side is sensitive. If the strip points in z direction, e.g. in a stave in the barrel section of the MVD, then the strip number, which was hit by the particle, measures the ϕ angle in the transverse plane. These strips are called $r\phi$ strips[3]. The z strips are aligned perpendicularly to the $r\phi$ strips and are therefore sensitive to measure the z coordinate of the hit position. The orientation of the pixels and strips with respect to the beam axis is shown schematically in Figure 4.3. Table 4.2 lists dimension parameters for different settings.

	area [μm^2]		$r\phi$ [μm]	z [μm]
	100×100		43	50
pixel cells	200×50	strip spacing	85	98
	50×200		-	160

Table 4.2: Defined sets of readout dimensions within the digitization phase of the simulation.

[3]The sensors in the barrel section are arranged on the surface of a cylinder. The strips which points to the barrel surface in beam direction along the middle axis of the barrel, can be described in cylindrical coordinates with the product of the radius r and the the angle in the xy plane ϕ, assuming the middle axis points in z direction.

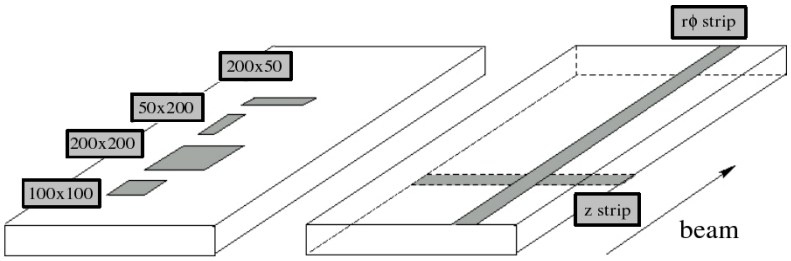

Figure 4.3: Visualization of the pixel sizes and their orientation with respect to the beam direction (arrow, in case of barrel modules). The long strips point in beam direction and measure the ϕ angle in the barrel section. The short z strips are shown in addition, which would be read out at the back side of the sensor.

The numbers for the $r\phi$ and z pitch are caused by the size of the strip sensor modules, which were predefined by the CAD design and input to the simulations. Due to the fixed number of 128 channels per front-end used for the readout of the strip sensor, the numbers given in Table 5.1 can only be approximate values in contrast to the pixel dimensions. The readout dimensions for the strip detectors were defined to stay as close as possible to a pitch of approximately 50 μm, 100 μm and 150 μm, respectively.

For the different pixel dimensions the size of the corresponding clusters are shown in Figure 4.4. Only hits in the barrel section have been considered to allow a direct comparison. For quadratic 100×100 μm^2 pixels the mean cluster size is $\overline{N} = 2.56$. In general the mean size of the cluster depends on the direction of the particle with respect to the sensor surface. Usually the size of the readout structure is smaller than the thickness of the detector layer and therefore the probability to excite more than one channel rises with increasing trajectory angles with respect to the sensor surface. A thickness of $d = 200$ μm for pixel and $d = 250$ μm for strip detectors was used.

For rectangular pixel dimensions the mean cluster size changes depending on the orientation of the pixel with respect to the beam axis. If the shorter dimension points in beam direction (blue distribution, Figure 4.4) the cluster size rises. In that case more than one channel contributes to the hit cluster. If the longer dimension of the rectangular pixel points in beam direction (red distribution) the mean number of pixel cells per cluster remains rather constant compared to the standard case of quadratic 100×100 μm^2 pixels.

The readout on either side of the double-sided strip sensors was modeled to be independent on both sides. A stereo angle of 90° was assumed, which is a natural value for rectangular sensors. For the defined settings from Table 4.2 the size of the strip hit clusters are shown in Figure 4.5.

For double-sided strip detectors the readout is realized independently on both

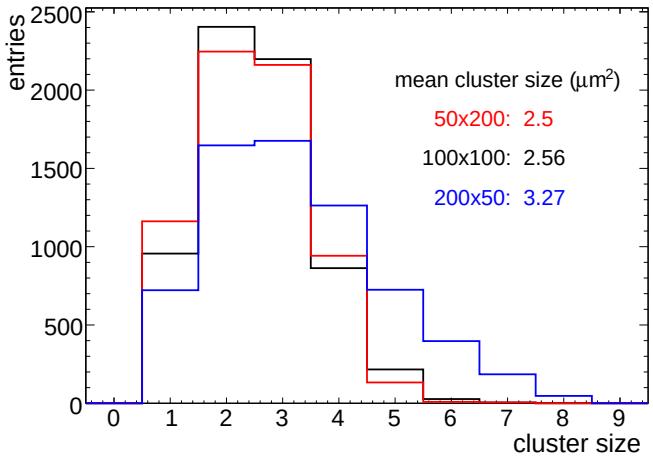

Figure 4.4: Distribution and mean size of reconstructed pixel clusters for various pixel dimensions.

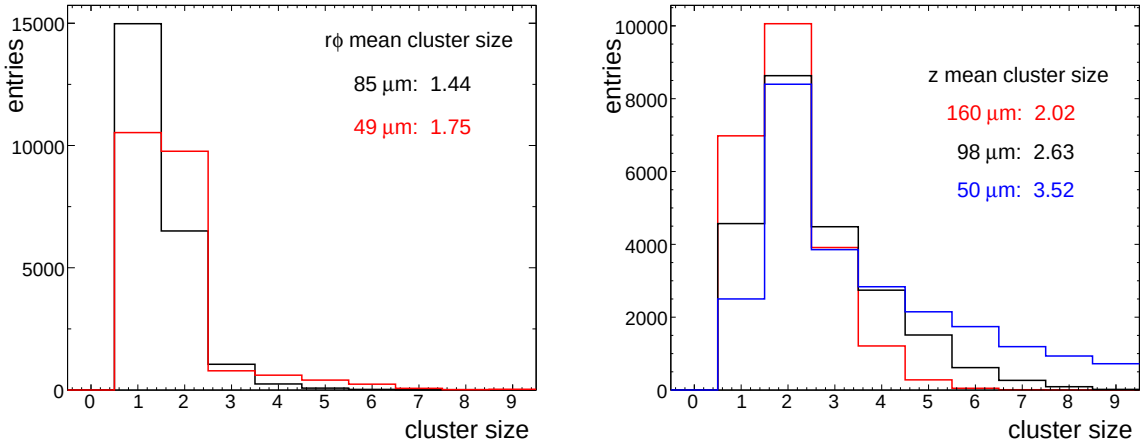

Figure 4.5: Size of the reconstructed strip hit cluster for $r\phi$ strips (left) and z strip clusters (right).

sides of the sensor and both measurements are combined in a second step to a three-dimensional hit information. Therefore, Figure 4.5 shows the $r\phi$ and z clusters independently on the cluster level. The $r\phi$ cluster size is in general smaller and for larger strip widths there is only one channel contributing. Reducing the strip width, the mean cluster size increases, which is advantageous for position measurement. The shorter strips are sensitive to measure the z position of the track on the sensor surface. Therefore the mean cluster size increases with smaller strip dimensions.

After the cluster is found the weighted position on the sensor is calculated. A comparison between the reconstructed hit position and the Monte Carlo value for

the track position is shown in Figure 4.6 for pixel sensor hits. The deviation is

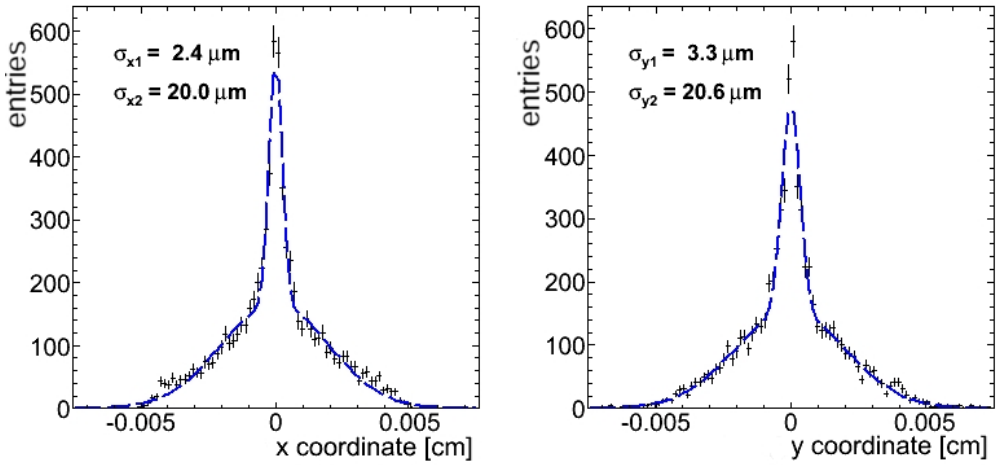

Figure 4.6: The resolution of the reconstructed pixel hit position after clustering determined through a comparison with the simulated value.

shown for the x and y coordinate separately. The broader component comes from clusters with a width of one for the corresponding direction, whereas the needle-like structure on top of the resolution distribution comes from clusters with more than one channel. Additional charge weighting between adjacent pixel cells improves the resolution further.

Figure 4.6 was obtained for a pixel size of 100×100 μm^2. A cluster for pixel hits delivers a two-dimensional hit information on the sensor. Therefore the radial deviation from the original hit gives a measure for the hit resolution. This is shown for different cluster sizes in Figure 4.7.

The hit resolution for one-pixel clusters is equal to the geometric resolution defined by Equation (4.1), which corresponds to the black distribution in Figure 4.7. If two pixels contribute to a cluster the resolution improves from $\hat{r} = 27.7$ μm to $\hat{r} = 21.1$ μm and further to $\hat{r} = 18.6$ μm in case of clusters with more than two pixels (green distribution).

Table 4.3 summarizes the hit resolution for pixel sensors for different pixel sizes. For 50×200 μm^2 large pixels the longer pixel dimension points in the z direction, whereas for 200×50 μm^2 large pixels the short dimension measures the z coordinate. In both cases the hit resolution is in general always worse compared to quadratic 100×100 μm^2 large pixels. The hit resolution is then limited by the longer pixel dimension, for which only one pixel contributes in this direction. In these cases the resolution suffers by a broader contribution from the longer pixel dimension.

For strip sensors the cluster information is obtained independently from both sides

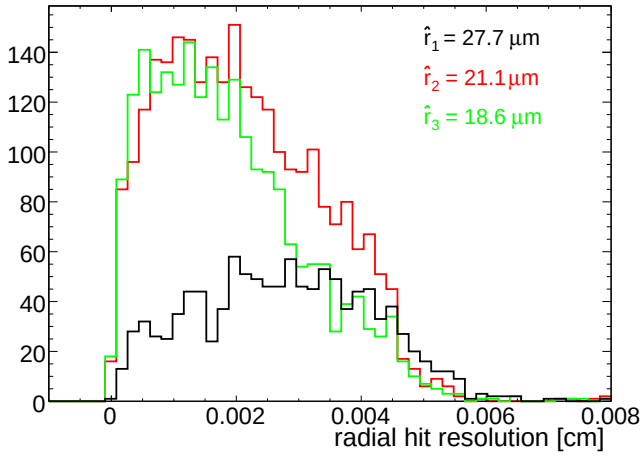

Figure 4.7: Two dimensional deviation of the reconstructed hit position on the pixel sensor for different cluster sizes (see text for details).

pixel size	2-dim deviation [μm]		
[μm^2]	cluster size 1	cluster size 2	cluster size 3
100×100	27.7	21.1	18.6
50×200	35.8	22.2	30.6
200×50	36.7	36.0	35.3

Table 4.3: Two-dimensional uncertainty of the reconstructed hit position on the pixel sensor compared to the Monte Carlo value.

of the sensor. The left side of Figure 4.8 shows the difference between the reconstructed $r\phi$ coordinated and the Monte-Carlo value, whereas the right figure shows the difference of the z coordinates on the sensor. The black distributions were obtained by modeling 85 μm broad $r\phi$-strips and 98 μm broad z-strips. The red distributions assumes 43 μm broad strips in the $r\phi$ direction and relatively broad strips with 160 μm in z direction. For the long strips on the sensor in $r\phi$ direction the hit resolution perpendicular to the beam increases by decreasing the strip dimension. This is simply caused by the increase of two-strip clusters in this direction, for which charge sharing can be used to improve the hit resolution. In case of 85 μm wide strip spacing the resolution is dominated by single-channel clusters. This can be compared to the cluster sizes for different settings given in Figure 4.5. In that case the width of the error distribution is not much better compared to the geometrical resolution defined by Equation (4.1). Only much smaller $r\phi$-strips of 43 μm would improve the hit resolution.

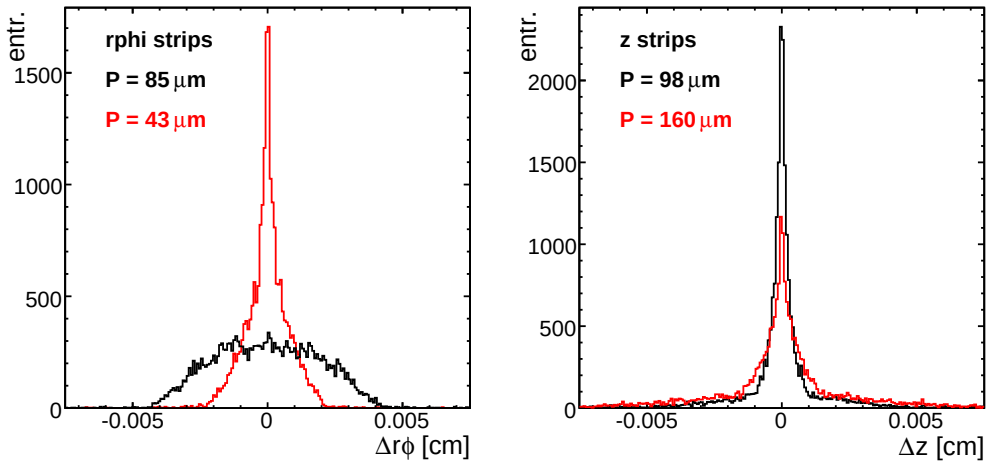

Figure 4.8: Deviation of the cluster position from the Monte-Carlo value on the strip detectors for different strip sizes. The deviation from the z and $r\phi$ side are shown separately

Broader strips in z direction do not much worsen the resolution since most likely in the majority of hits the cluster is reconstructed by two or more channels (see Figure 4.5). The distribution for 50 μm large z strips has been omitted in Figure 4.8 since the deviation from the Monte-Carlo value was not further improved.

4.3 Single Track Resolution

The MVD is an integral part of the tracking system and crucial for a precise vertex resolution. The MVD provides the first measurements of detector hits with a precision of only a few tens of μm or better, as discussed in the previous section. In order to reconstruct the whole track the information from different sub-detector components has to be combined. For the track model used for the investigations discussed here the MVD, STT, DCH and GEM detectors have been employed and combined with the dipole tracking for particles entering the dipole section. The BaBar tracking formalisms and techniques have been adopted for the $\overline{\text{P}}$ANDA experiment within the simulation framework. The MVD represents a major component to realize a realistic particle tracking and the implementation of the reconstruction algorithms and the adoption of the track finding and fitting formalism was the basis for the following investigations of the tracking with the $\overline{\text{P}}$ANDA detector.

4.3.1 Track Model

In the target spectrometer a constant field along the beam axis

$$\vec{B} = (0,\, 0,\, B_z) \tag{4.2}$$

with $B_z = 2$ T will be used. A moving charged particle then follows a trajectory which can be described by a helix. A common description can be obtained in a five-dimensional parameter space [108],[109]

$$P = \begin{pmatrix} d_0 \\ \phi_0 \\ \omega \\ z_0 \\ \tan\lambda \end{pmatrix}. \tag{4.3}$$

For a given point on the orbit the projection of the distance to the origin in the $x-y$ plane defines d_0 and the angle of this projection is given by ϕ_0. d_0 gets a sign by the curvature of the orbit, which can be related to an angular momentum $\vec{r} \times \vec{p}$ [108]. The distance of the point to the origin projected to the beam direction defines z_0. ω is proportional to $1/p_t$ and a measure of the track curvature in the $x-y$ plane and $\tan\lambda$ is the tangent of the track dip angle in the $\rho - z$ projection, defined by cylindrical coordinates. The position of the particle as a function of the $x-y$ plane projection of the flight length l from the point of closest approach l can be given as [108]:

$$\vec{F}(P,l) = \begin{cases} \left(\sin\dfrac{\phi_0+\omega l}{\omega} - (1/\omega + d_0)sin\phi_0\right) & \vec{e_x} \\ \left(-\cos\dfrac{\phi_0+\omega l}{\omega} + (1/\omega + d_0)cos\phi_0\right) & \vec{e_y} \\ (z_o + \tan\lambda) & \vec{e_z} \end{cases} \tag{4.4}$$

Equation (4.4) describes a helix with the additional free parameter l. All reconstructed hits from the tracking detectors are combined and a Kalman filter technique [110] is used together with a smoothing function in order to find the best orbit. This treatment of the trajectory allows the correction of physical distortions, like effects from magnetic field inhomogeneity, material effects and the uncertainty of the hit measurements to some extent [108].

The effect of these corrections are illustrated in Figure 4.9, which shows a comparison of the track parameter z_0 for single pion tracks with momentum $p = 1$ GeV/c over the full MVD coverage. An ideal vertex position of $IP = (0, 0, 0)$ has been used in this simulation as reference point. Then z_0 is a direct measure of the vertex resolution along the beam axis.

The distributions are well described by a superposition of two Gaussian components. The widths of the individual contributions to the corrected histogram (red)

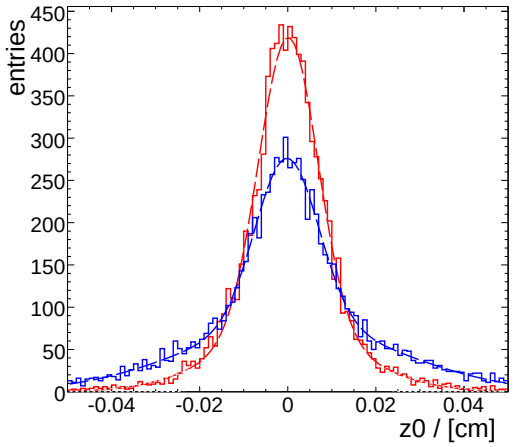

Figure 4.9: Influence of the material dependent corrections on the primary vertex resolution along the beam axis with (blue) and without (red) energy loss corrections.

are $\sigma_1 = 66$ μm and $\sigma_2 = 163$ μm, whereas for the relative strength of both contributions a ratio of $\approx 7:1$ can be given. For the uncorrected case (blue histogram) the distribution becomes wider and the relative contribution of the broad component is stronger and result in a relative ratio of only $\approx 3:1$. The individual widths are $\sigma_1 = 71$ μm and $\sigma_2 = 240$ μm, respectively.

4.3.2 Momentum Resolution

The Micro Vertex Detector as part of the tracking system has direct influence on the momentum resolution, for which a reconstruction of the curvature of the trajectory in the magnetic field is crucial. Although the number of hits in the MVD is small (~ 4) compared to the central tracker (> 20) the influence was already approximated and shown in Figure 4.1 with an effect of $\approx 50\%$ resolution drop in a scenario without the MVD. To obtain a good momentum resolution the amount of material of the tracking system has to be minimized in order to reduce the error in the momentum reconstructed caused by multiple scattering and energy loss. The curvature of the track is basically measured by the ω parameter of the helix parameterization, which is the inverse of the radius in the $x - y$ plane

$$\omega = \frac{1}{r} \tag{4.5}$$

The transverse momentum

$$p_t = \sqrt{p_x^2 + p_y^2} = \frac{qa}{w} \tag{4.6}$$

directly depends on the curvature measurement. q is the charge of the particle in units of the elementary charge and a is related to the magnetic field strength: $a = -eB_z$. The longitudinal momentum component is defined by the dip angle of the helix and the transverse momentum component:

$$p_z = p_t \tan \lambda \tag{4.7}$$

Figure 4.10 shows the momentum resolution for pions reconstructed with a combined fit with the MVD and the STT in the target spectrometer. Since the material

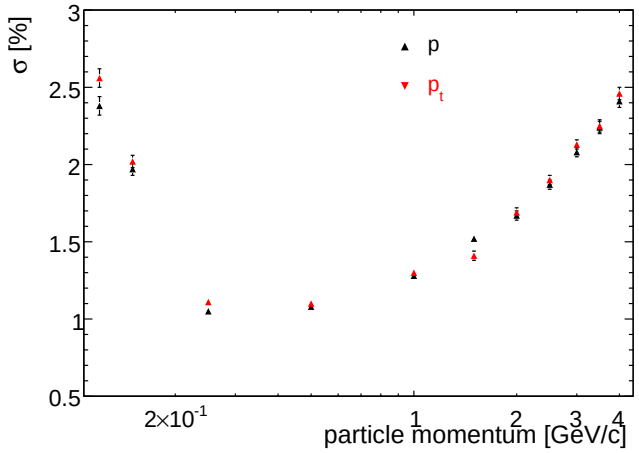

Figure 4.10: Momentum resolution for pions reconstructed in the target spectrometer section in a combined fit using the MVD and STT for polar angles between $\theta = 60°$ and 80°.

budget of the tracking system, and in particular of the MVD, is not uniform for all particle directions, as can be seen in Figure 3.7, only tracks within a rather narrow polar angle window of $\theta = 60°$ to 80° have been selected for a direct comparison. The momentum resolution is between 50 MeV/c and 2 GeV/c well below 2% and has its minimum between 300 . . . 500 MeV/c. Note that the momentum scale in Figure 4.10 is drawn logarithmic. Up to particle momenta of 4 GeV/c the momentum resolution is still better than 2.5%.

4.3.3 Vertex Resolution

The MVD is designed to reconstruct the decay vertex of a short-lived particles over a wide momentum range and over the full detector coverage. Figure 4.11 shows the resolution of the primary vertex for pions with a momentum of $p = 1$ GeV/c. A single-particle generator has been used in the detector simulation over the full

$\overline{\text{P}}$ANDA coverage assuming an ideal interaction point position of $IP = (0, 0, 0)$. The distributions for the transverse vertex parameter d_0 and the longitudinal vertex

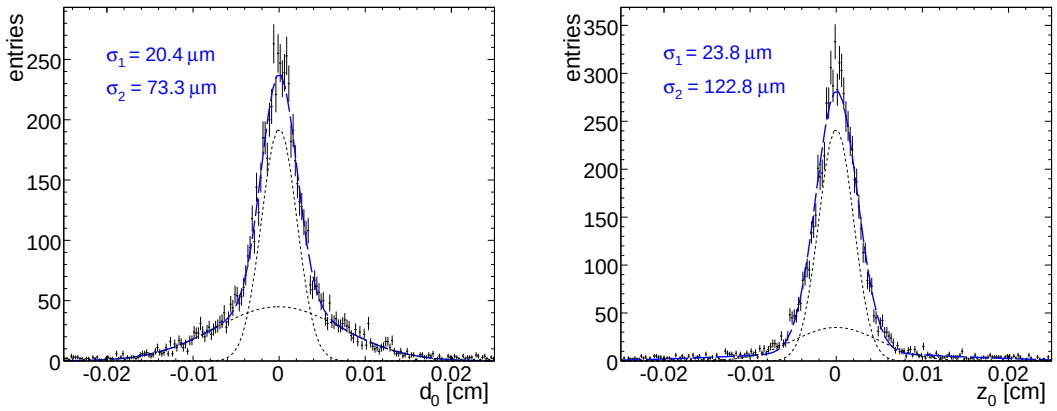

Figure 4.11: Vertex resolution for pions with momentum of $p = 1$ GeV/c. An isotropic single-track generator has been used for selected tracks in the barrel section.

component z_0 can be described by two Gaussian components. Tracks in the barrel section of the tracker in a polar angle window of $\theta = 60°$ and $80°$ have been selected. The narrow component of the vertex parameters come from tracks with a pixel hit in the first layer, whereas for the smaller, broader component the first hit is missing. In general the coverage very close to the interaction point by the first pixel layer is essential for a good vertex resolution. In that respect, the design of the pixel part utilized in this simulations is not optimized, as can be seen in Figure 3.10, where gaps between the individual sensors are still present and further optimization is needed.

For small particle momenta multiple scattering and energy loss in the detector materials will dominate the track resolution and therefore the vertex uncertainty. Figure 4.12 shows the quality of the vertex reconstruction for pions traversing the detector with different momenta.

For momenta larger than $p = 1.5$ GeV/c the vertex resolution is around $\sigma \approx 50$ μm. Figure 4.12 shows a superposition of all tracks with a MVD contribution between 5° and 140° in polar angle. Since the distributions for individual momentum bins are a superposition of different Gaussian components a weighted error was calculated taking the area of the individual Gaussians fit contributions into account.

The material budget of the tracking system will be different for particles traversing the detector at different angles. The resolution of the decay vertex strongly depends on the direction of the daughter particle. The transverse vertex resolution $\sigma(d_0)$ and its dependence on the polar angle is shown in Figure 4.13 for pions with a momentum of $p = 3$ GeV/c.

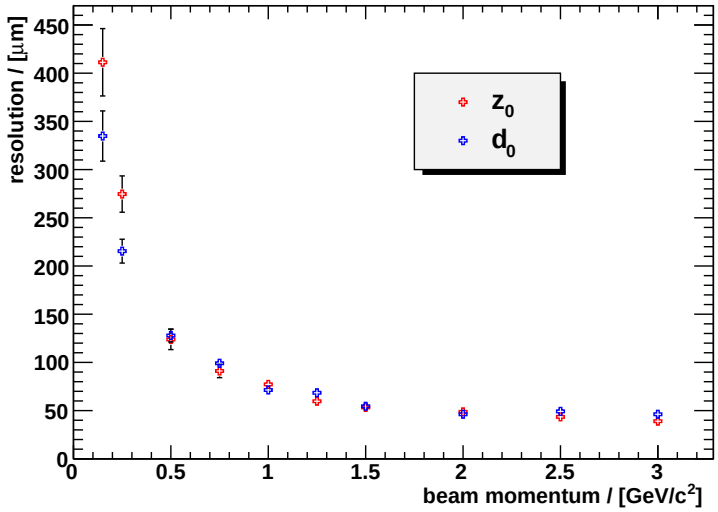

Figure 4.12: Momentum dependence of the vertex components d_0 and z_0 for tracks traversing the full MVD coverage in the polar angle range between 5° and 140°.

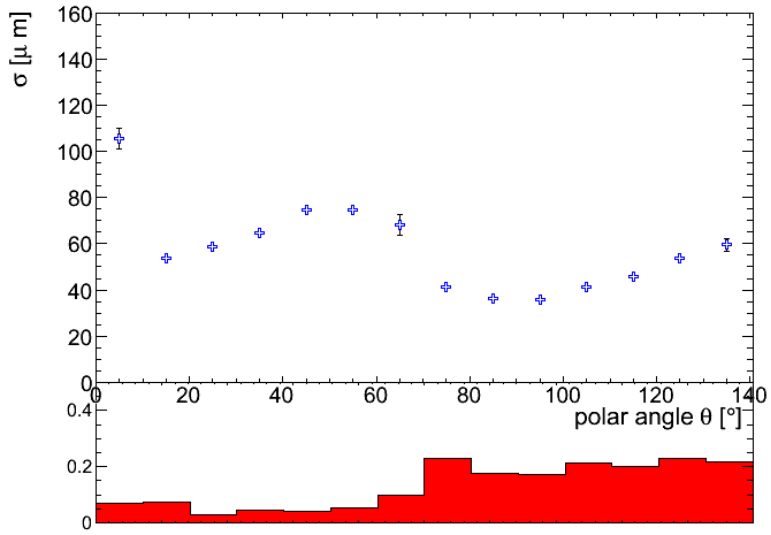

Figure 4.13: Angular dependence of the transverse vertex resolution $\sigma(d_0)$. The underlying histogram shows the contribution of a broader error component.

The resolution of the transverse vertex parameter shows a local maximum between $\theta = 40°$ and 60°, which is caused by the enhanced material budget from additional overlaps from detectors of the barrel and disc section. The histogram below the polar

angle dependence of the transverse resolution shows the contribution of a broader error source in the corresponding polar angle bin. An example was already given in Figure 4.11 for a larger angular bin of $\Delta\theta = 20°$. The higher fraction of the larger component in the barrel section of the MVD comes again from trajectories missing the first pixel layer. To give a qualitative comparison of the reconstructed vertex parameter resolution, the widths of both distributions have been added to a total width by scaling the individual components. The rise in the upstream direction for polar angles larger than 90° is then given by the rising material budget for tracks coming from the primary interaction point.

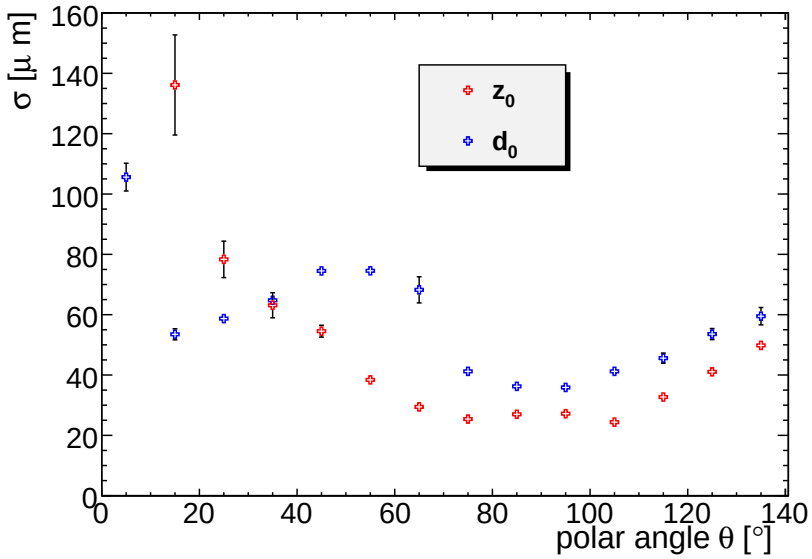

Figure 4.14: Vertex resolution with polar angle dependence.

Figure 4.14 shows additionally the longitudinal vertex resolution $\sigma(z_0)$ and its polar angle dependence. For angles larger than $\theta = 40°$ the distribution follows a parabola with its minimum at 90°, as expected by following the θ dependence of the material budget (see Figure 3.7). For small polar angles the uncertainty perpendicular to the trajectory causes a large uncertainty in the determination of the longitudinal vertex position and causes the strong increase in Figure 4.14 for $\sigma(z_0)$ towards small angles. There is no further constraint to reconstruct the vertex component along the beam direction. In the limit $\theta \to 0$ the longitudinal information would vanish completely. In a physics event there are usually more constraints, e.g. for a particle decay into several daughters. In Chapter 5 the vertex resolution for two physics channels is discussed more in detail.

4.4 Contribution to Particle Identification

Although the number of reconstructed MVD hit points per track is limited to four in the barrel section and five to six in the forward domain, the energy loss information provided by the readout electronics can be used as part of the particle identification decision. The ability of separating different particle species relies on an accurate energy loss information and a good knowledge of the track inclination with respect to the sensor surfaces.

4.4.1 Calculation of the Energy Loss Information

The energy-loss distribution follows the well known Bethe-Bloch formula at higher particle momenta [111] omitting the corrections for low energies:

$$\overline{S} = \left.\frac{dE}{dx}\right|_{mean} = K\frac{\rho Z}{A}\frac{z^2}{\beta^2}\left\{\ln\left[\frac{2m_e\gamma^2v^2W_{max}}{I^2}\right] - 2\beta^2\right\} \tag{4.8}$$

whereas the constant K can be given as:

$$K = 2\pi N_a r_e^2 m_e c^2 = 0.1535\,\mathrm{MeVcm^2/g} \tag{4.9}$$

The excitation potential for silicon can be set to $I = 140$ eV. The variables and constants are defined as follows:

m_e	...	electron mass
r_e	...	classical electron radius
c	...	speed of light
N_A	...	Avogadro constant
ρ	...	material density
Z, A	...	atomic number and weight of absorbing material
z	...	atomic number of particle
β, γ	...	relativistic velocity and factor
v	...	particle velocity
W_{max}	...	maximum energy transfer in single collision

Contrary to the usual method of summing the individual hit measurements dE_i/dx_i to an energy loss information $dE/dx = \sum_i^n dE_i/dx_i$ all hit measurements can be combined in a merged method to a total quantity

$$\left(\frac{dE}{dx}\right)_{total} = \frac{\sum dE_i}{\sum dx_i} \tag{4.10}$$

The dE_i are the energy information from the reconstructed hits and the dx_i are obtained by calculating the length of the corresponding track, which traverses the sensor material. This method treats the MVD as a single volume rather than the sum of individual measurements and reduces slightly the spread within a band compared to the usual truncated mean method ($\sum dE_i/dx_i$).

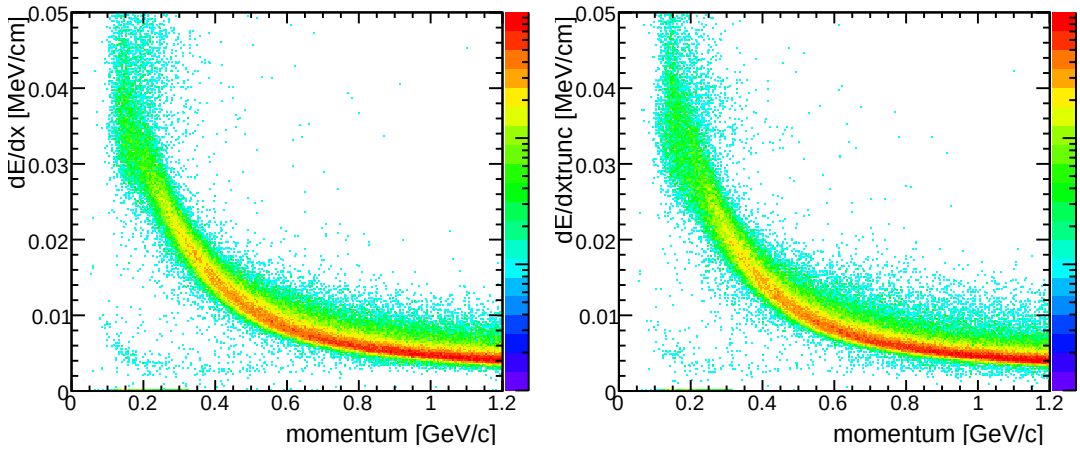

Figure 4.15: Comparison of the energy loss signal obtained for two different methods, the merged method used in the MVD reconstruction (left, Equation (4.10)) compared to the truncated mean method (right).

Figure 4.15 shows a comparison of both methods for protons. The left figure shows the energy loss and its dependence with increasing track momentum calculated with Equation (4.10). The right figure shows the calculated energy loss using the truncated mean method, by summing the individual dE_i/dx_i information for a track and omitting the highest value. This should reduces the strength of the Landau tail. Nonetheless the left proton band appears to be slightly narrower.

To reproduce the distribution in a fit, all uncertainties are merged into a single Gaussian error, which is added to the Landau-distributed energy loss information. The convolution of both distributions is defined as

$$w(s) = \int L(x)\, G(s-x)dx \tag{4.11}$$

and the parameterizations used are

$$G_\sigma(x) = \frac{1}{\sqrt{2\pi}\sigma} e^{-x^2/\sigma^2} \tag{4.12}$$

for the Gauss distribution and

$$L_\tau(x) = \frac{1}{\pi\tau} \int_0^\infty e^{-t(\ln t - x/\tau)} \sin(\pi t)dt \tag{4.13}$$

for the scaled Landau distribution. The parameters are σ_G for the Gauss width, σ_τ for the Landau width, respectively. s is the most probable value of the Landau distribution. A typical fit result is shown in Figure 4.16 and the corresponding fit parameters can be found in Table 4.4. Additionally, the fit results from the convolution integral with the truncated mean method are given (right column).

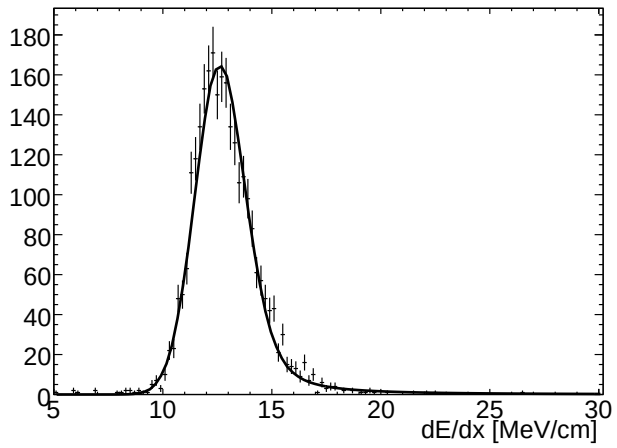

Figure 4.16: Energy loss distribution for protons with $p = 400$ MeV/c reconstructed with the MVD.

parameter	$\overline{S}_{total}$ [MeV/cm]	$\overline{S}_{trunc}$
σ_L	0.15 ± 0.02	0.21 ± 0.02
σ_G	1.05 ± 0.03	1.03 ± 0.04
s	12.37 ± 0.04	12.06 ± 0.04

Table 4.4: Fit parameters for the convolution integral of the energy loss distribution for the example given in Figure 4.16. The values are compared to the truncated mean method (right column).

The best fit result to the energy loss distribution is given by the merged method: $(dE/dx)_{total}$ compared to the truncated mean method, for which the Landau width is in the order of 30% smaller. Therefore this methods was chosen to calculate the

momentum dependent probability for all different particles species. Furthermore, it was demanded that at least three reconstructed hits per track have to contribute in order to provide a sufficient energy loss information from the MVD.

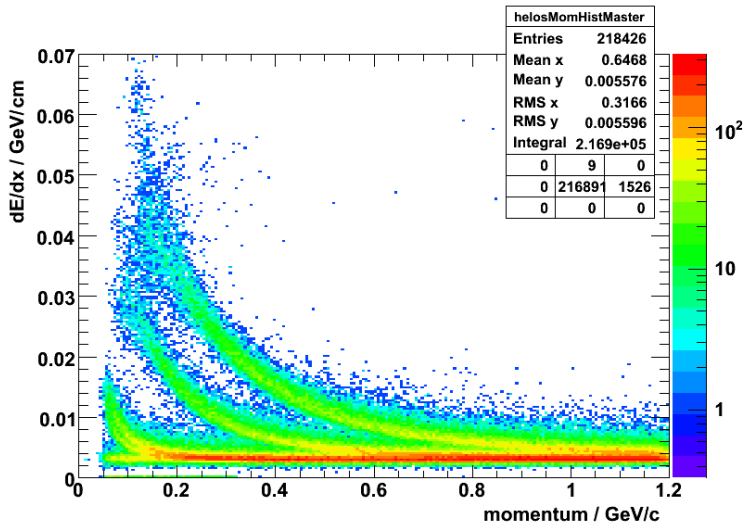

Figure 4.17: dE/dx information from the MVD versus track momentum for protons (upper band), kaons (middle) and pions/muons/electrons (lower).

Figure 4.17 illustrates that the MVD can contribute to the particle identification, but separation might be possible only for protons (upper band) and kaons (middle) from the lowest band which is a superposition of pions, muons and electrons.

The smearing of the energy loss information for low-momentum particles comes from the uncertainty of the track momentum itself rather than the energy information from the MVD. For these investigations the track fitter used the pion hypothesis for all different particle types. The additional systematic momentum uncertainty can be seen in Figure 4.17 for kaons and protons, whereas for pions (lowest band) the band at lower momenta appears almost constant in width down to small momenta. Figure 4.18 shows the deviation from the Bethe-Bloch expectation, which starts for momenta smaller than $p = 300$ MeV/c for protons and $p = 200$ MeV/c for kaons. A relatively small deviation of the reconstructed track momentum results in a large difference to the expected Bethe-Bloch value and is caused by the very steep rise of the Bethe-Bloch formula in the limit towards low momenta.

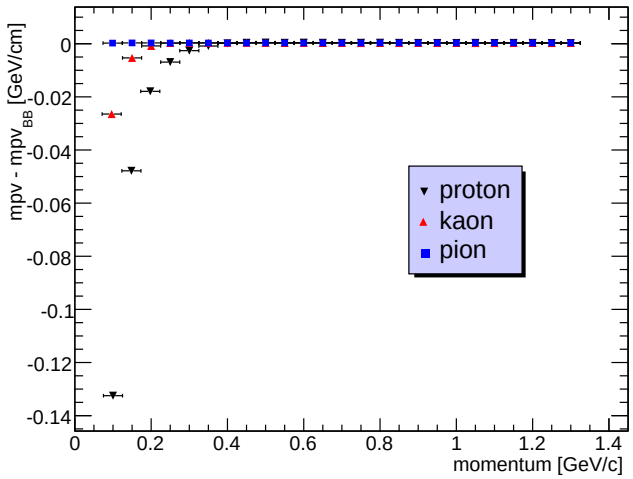

Figure 4.18: Deviation of the calculated mean value of the energy loss distribution from the Bethe-Bloch expectation.

4.4.2 Separation of Different Particle Species

For each particle species the parametrizations were obtained independently by generating 3×10^5 single particle events each, over a momentum range from 50 MeV/c to 2.0 GeV/c. The energy loss distribution was fitted in 25 MeV/c wide momentum bins to get the parameters s_i, σ_{G_i} and σ_{L_i} at any given momentum interval p_i. The dependence of the parameters can be described by polynomial functions [112] and is the basis of the calculation of the particle probability for a given track in the reconstruction.

A common method to estimate the quality of the particle identification information for two different particle species is the separation power P

$$P = \frac{s_1 - s_2}{\sigma_G}, \tag{4.14}$$

which can be calculated under the assumption that for all particle types the width of the energy loss distribution will be the same and the errors are of Gaussian type. Since the width of the dE/dx signal from the MVD is not constant for different particle types over the considered momentum range, the sum of both widths of the individual bands is used and Equation (4.14) can be modified to

$$P' = \frac{s_1 - s_2}{\sigma_{G_1}/2 + \sigma_{G_2}/2}. \tag{4.15}$$

The s_i and σ_{G_i} are the fitted parameters for the convolution given in equation 4.11. The separation power is a measure for the quality of a particular property. Assuming

that the energy loss distributions from both particle types are best separated at a value κ between this distributions, then the probability to find the particle follows directly from the integral over one of the distributions

$$p_i = \int_{-\infty}^{\kappa} G_{\sigma_i}(x)dx. \tag{4.16}$$

The separation power P expresses the probability in terms of the width of the distribution itself[4].

For particle momenta below 400 MeV/c the Gauss width is much larger than the Landau width, e.g. for protons with 400 MeV/c momentum; see Table 4.4 for the corresponding fit parameters. As can be seen in Figure 4.19 the width of both contributions to the dE/dx signal is comparable for medium and higher momenta.

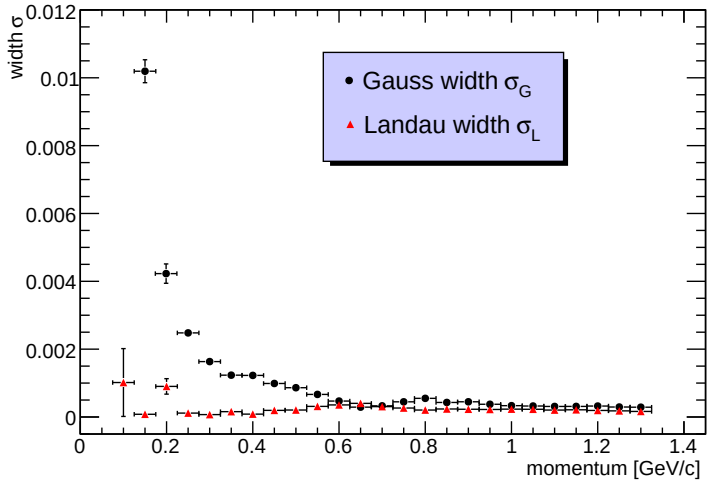

Figure 4.19: Momentum dependence of the Gaussian and Landau component of the energy loss.

Since the Gaussian width is dominant for small particle momenta the separation power given in Equation (4.15) can be calculated and is shown in Figure 4.20. In order to compensate the Landau tail especially for higher momenta the Gaussian widths have been multiplied by a factor of two. The separation power computes for the momentum bin of $p = 400$ MeV/c to $P = 5.26$.

The additional systematic momentum uncertainty at lower momenta causes a widening of the energy loss band. The separation power decreases below $p = 300$ MeV/c for K/p and p/π separation for which the separation would be expected to

[4]One can say P expresses the number of Gaussian sigmas for the given separator.

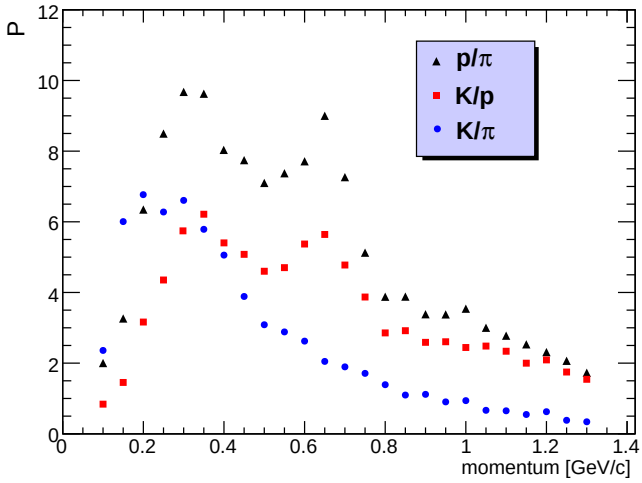

Figure 4.20: Separation power for p/π (black triangles), K/p (red squares) and K/π (blue circles) separation and its dependence on momentum.

be largest. For K/π separation the loss of separation power is smaller since the pion momentum is much better defined at very low momenta. The best separation can be obtained between $p = 200$ MeV/c and $p = 800$ MeV/c for p/π and K/p, and up to $p = 600$ MeV/c for K/π separation demanding at least a separation power $P = 3$.

There is a second maximum in the separation power for p/π and K/p between 500 MeV/c and 800 MeV/c. This is not a real maximum and caused by a slight shift of the Gaussian width with respect to the Landau component. This shift is only small, as can be seen already in Figure 4.19, as a small dent in the Gaussian width curve. The fit of the convolution integral to the reconstructed energy loss data has some freedom to vary the Gaussian against the Landau width with the same fit quality. For pions and kaons this behavior was not observed and it is probably caused by still not sufficient statistics for protons.

4.4.3 Discussion of the PID Information

Based on the investigations discussed in the previous sections, the MVD can contribute to the particle identification at low momenta. This is of interest since only the TPC (or alternatively the STT) can contribute to PID of charged particles in the momentum range around a few hundreds of MeV/c.

The momentum dependence of the three parameters σ_G, σ_L and s was input to calculate a probability for each particle type [112]. For each reconstructed track the probability can be calculated to belong to a specific type based on the obtained parameterizations. This is done for all possible particle types in parallel and a

momentum dependent likelihood can be calculated

$$L(p) = \prod_{i=1}^{5} f_i(p) \tag{4.17}$$

whereas all particle types (e, μ, π, K, p) are considered.

The normalized likelihood for proton tracks is shown in Figure 4.21. The upper picture shows the calculated proton probability and its dependence on momentum. The lower left picture shows the corresponding kaon misidentification probability

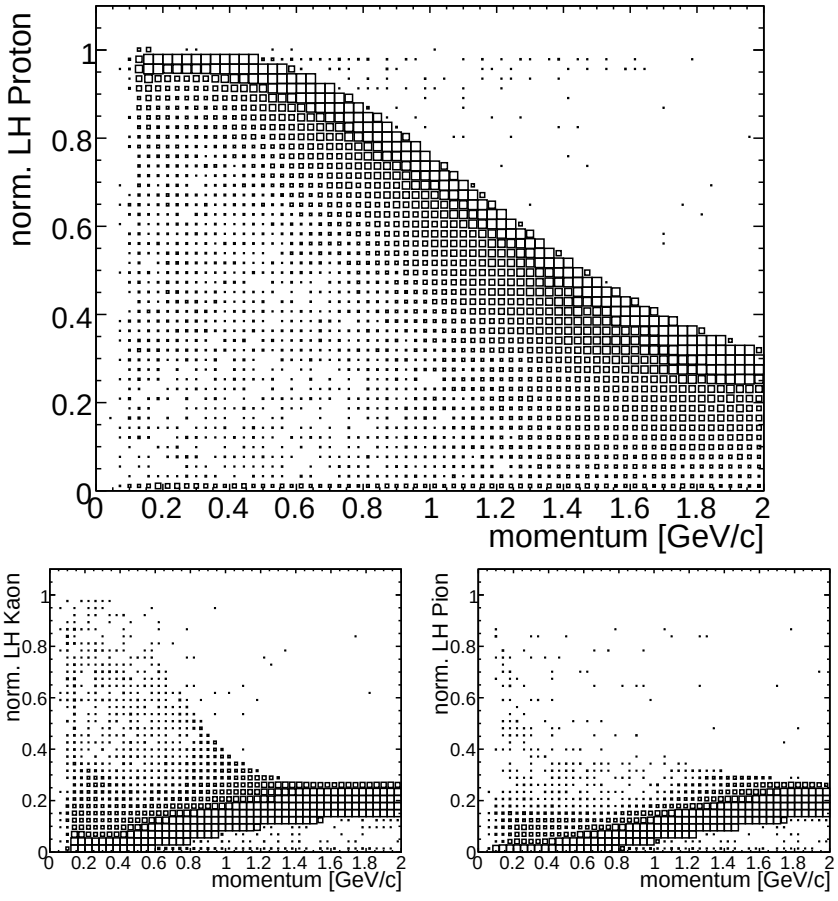

Figure 4.21: Normalized likelihood from the energy loss information for proton tracks up to 2 GeV/c momentum. The figure to the lower right shows the corresponding kaon misidentification probability, and the lower right the probability to identify these tracks as pions, respectively.

and the picture in the lower right part the pion misidentification. Below $p = 1$ GeV/c the protons can be separated with a probability of higher than 70%. The misidentification probabilities for the other particle types are rising and above $p = 1.5$ GeV/c the proton probability is below 40% and therefore protons cannot be separated from the other particle species.

The calculation of the likelihood takes the full dE/dx distribution into account and the influence of the Landau tail can be seen in Figure 4.21 as smearing of the probability to smaller values. The smearing becomes stronger with higher momentum since the relative influence of the Landau contribution in the description of the energy loss signal becomes stronger with rising momentum. The calculation of the individual probabilities assumes equally abundance of all particles types, which was done for a direct comparison. This is not the case for most of the physics channels, e.g. the strangeness production at $\overline{\mathsf{P}}\mathsf{ANDA}$ energies is strongly suppressed. This would reduce further the ability to separate kaons from pions, because the Landau contribution would potentially contaminate the kaon region depending on the relative abundance of kaons and pions for a given sample. In this context the separation power shown in Figure 4.20 seems to be too optimistic, since the Landau contribution was neglected for its calculation.

Some other possible error sources could not be included in these calculations. For a good separation an accurate energy measurement of the collected charge in the MVD sensors is essential. Since the frontend electronics are not fully defined, its influence was excluded. The collected charge can be obtained with an error of usually only a few % and would therefore contribute as an additional Gaussian factor but smaller as the systematic uncertainty coming from the track fit. The error of the charge measurement is connected to the gain of the charge measurement with the frontend itself, e.g. the envisaged TOPIX frontend for the MVD pixel part can measure signals containing up to 8×10^5 electrons[5]. This range in the energy measurement is sufficient to reconstruct the full proton band down to very small momenta.

The knowledge of the path length of the track through the sensitive detector material is also very important. For this investigation the assumption was made, that the MVD is perfectly aligned, which will result in an additional alignment error in the real experiment. Further calibration studies have to prove that the position information will be sufficiently accurate to retain the separation of the individual energy loss bands.

[5] A charged track causes an ionization in the depletion zone of the sensor material which is detected and its charge is proportional to the deposited energy. The ionizing energy for silicon is $E_{ion} = 3.6$ eV.

5 Vertex Reconstruction Performance for Specific Benchmark Channels

5.1 Overview

The Micro Vertex Detector is an integral component of the $\overline{\text{P}}$ANDA tracking system. The performance of the inner tracking detector is determined by the ability to reconstruct the production and decay vertex positions of short-living particles with high precision. In this section the vertex reconstruction ability of the tracking system will be discussed for two different channels. The channel $\bar{p}p \rightarrow \pi^+\pi^-$ was studied at the highest beam momentum of $p_{beam} = 15$ GeV/c. Due to the fixed target topology the pions share the beam momentum and are mostly restricted to a cone around the beam axis. This channel allows the study of the two-pion production vertex at higher particle momenta and focuses on the forward part of the tracking system, in particular the MVD, which delivers the very first track measurements.

The second channel presented here is the leptonic decay of the charmonium resonance J/ψ. In order to investigate the vertex resolution, the reaction $\bar{p}p \rightarrow J/\psi\gamma \rightarrow \mu^+\mu^-\gamma$ has been studied at a beam energy, that corresponds to the χ_{c1} resonance, for which the radiative decay to $J/\psi\gamma$ has a branching ratio of $BR = 35.6\%$ [15]. The focus of this analysis is to investigate the vertex reconstruction ability of the two-muon J/ψ decay. In the event reconstruction usually the restriction on the χ^2 of the decay vertex position is used. A good vertex resolution of the tracking system would therefore directly influence the efficiency of the J/ψ reconstruction and not dominantly influence the resolution of the mass signal.

For both channels the effect of the hit resolution on the vertex resolution will be discussed. At $\overline{\text{P}}$ANDA energies the track resolution is limited by small angle scattering caused by particle interactions with detector materials, especially at low particle momenta. Nonetheless, a better hit resolution in the pixel layers of the MVD close to the interaction point could improve the vertex reconstruction. The influence of various readout schemes, which define the quality of hit resolution, will be discussed.

5.1.1 Definition of the Primary Interaction Point

The ability to constrain the primary interaction point strongly depends on the target type. As introduced in Section 2.2.1 two basically different target options for the $\overline{\text{P}}$ANDA experiment are currently discussed. The cluster pellet target would in principle allow to define the primary vertex within the very small dimensions of the frozen hydrogen droplet, with typical dimensions of a few tens of μm. To reach this resolution it is necessary to determine the absolute position of the droplet itself with respect to the $\overline{\text{P}}$ANDA coordinate system. This turns out to be rather challenging, since the interaction time due to the small beam diameter and small radius will be short. In addition, the spread of the droplet train might be in the order of a few millimeter [113] and the luminosity may change over the interaction time of the droplet with the circulating antiproton beam.

In case of the cluster jet target the interaction zone is by far more extended in beam direction compared to the spread of the individual pellets. Furthermore the target density varies along the beam axis. Perpendicular to the beam axis the interaction zone is defined by the emittance of the beam. The transverse emittance of the beam will be smaller than $\epsilon = 1$ mm·mrad for $N(\overline{p}) = 3.5 \cdot 10^{10}$ antiprotons [10]. The emittance represents the available phase space for the antiproton beam and can be reduced by the magnetic system down to a diameter much below a millimeter. This will be compensated by an increase of the transverse momentum of the incoming beam.

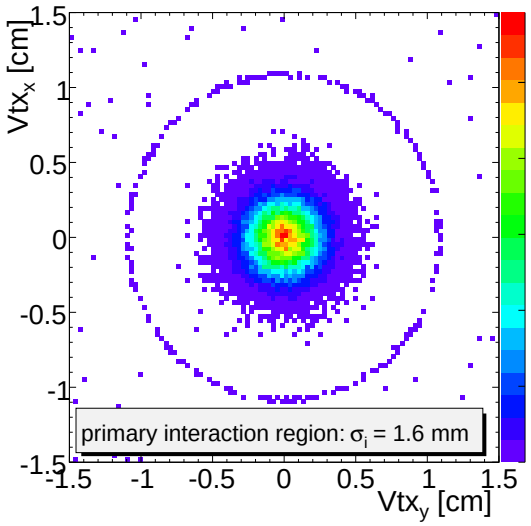

Figure 5.1: Definition of the primary vertex region by the event generator. Only the transverse components are shown. In beam direction the same beam spot resolution was assumed.

Figure 5.1 shows the definition of the primary interaction region used for event generation. The spread of the beam-target interaction zone was set to a value of $\sigma_i = 1.6$ mm for all three spacial dimensions $i = (x, y, z)$. The ring structure in the transversal plane in Figure 5.1 comes from interactions of the reaction products with the beam pipe, which has a radius of 1 cm. The target definition was used for all physics simulations presented in this work.

5.2 Vertex Resolution for the Channel $\bar{p}p \to \pi^+\pi^-$

The channel $\bar{p}p \to \pi^+\pi^-$ has been analyzed at the highest $\overline{\text{PANDA}}$ beam momentum of $p = 15$ GeV/c in order to evaluate the vertex reconstruction at high particle momenta. This is of interest not only for the forward dipole tracking, but also of relevance for the forward disc part of the MVD. Of special interest is the resolution of the primary vertex along the beam axis.

5.2.1 $\pi^+\pi^-$ Event Selection

At least two charged tracks were demanded in the analysis with different PID cuts for each particle. For one pion the information from the particle identification has been used and a pion identification probability of at least 55% has been set as minimum value. For the other pion no further restriction has been made. The pion candidates were fitted to a common vertex and an additional kinematic fit applied in order to meet the beam four-momentum. These selections are able to suppress the combinatorial background completely and provide a clear event sample to study the production vertex position. Table 5.1 gives an overview of the cuts used and their influence on the efficiency. The last row gives the probability to reconstruct more than one initial system in the event and is a measure of the combinatorial background. This can happen, if secondary particles are produced in the detector and misidentified as one of the reaction pions.

cut	efficiency [%]	combinatorics [%]
only geometric constraints	42.0	2.0
pion probability $> 55\%$	37.1	1.4
pion probability $> 55\%$, 4C-fit	30.9	-

Table 5.1: Influence of various cuts on the two pion reconstruction efficiency at maximum beam energy.

Only a few selection criteria were used to combine the pions to the initial beam-target system. The geometric constraints mean, that a common production vertex has been fitted using both trajectories from the pion candidates. For one pion a likelihood probability of larger than 55% was demanded. Additionally, a four-constraints kinematical fit was used to refit the two-pion four-momentum to meet the beam energy and momentum (in total four constraints). The efficiency drops down from 42% to 30.9% according to Table 5.1. For this analysis only a clean sample of two pion events was of interest in order to study the resolution of the production vertex.

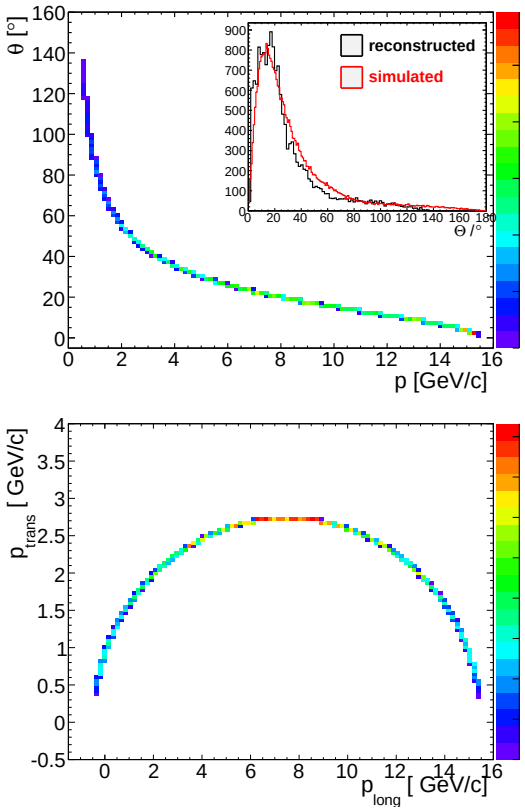

Figure 5.2: Angular distribution of the reconstructed pions with respect to their momentum (upper) and transverse vs. longitudinal pion momentum component (lower). The smaller picture in the upper frame shows the distribution of pion angles with respect to the beam axis in the laboratory frame. The bands appear very narrow, which is a direct consequence of the four-constraints kinematic fit.

Figure 5.2 shows the relevant phase space for the pions. The upper histogram shows the pions polar angle versus its total momentum. The smaller inset at the upper right corner shows the polar angle distribution of the pions. Most particles are moving in forward direction and stay in a cone around $\theta \approx 50°$, which corresponds to the MVD forward disc region. The red histogram in the upper frame in Figure 5.2 shows the simulated pion angular distribution and was scaled to the angular distribution of the reconstructed pions (black histogram). Both distributions agree almost perfectly. This shows the good coverage for this reaction in forward direction.

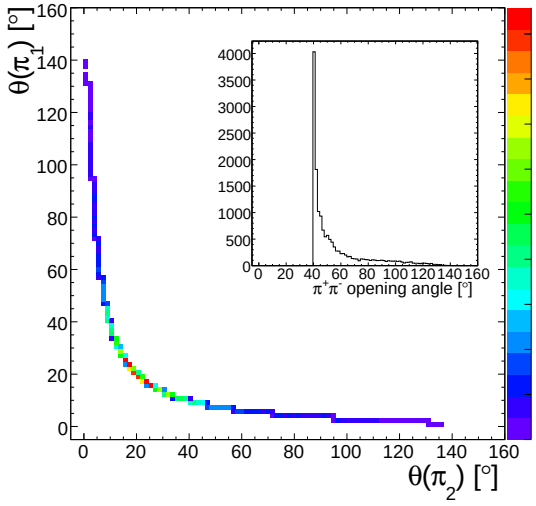

Figure 5.3: Relation of the pion angles from the reaction $\bar{p}p \rightarrow \pi^+\pi^-$ and the corresponding opening angle between both pion tracks in the laboratory frame (small inset).

Figure 5.3 shows the corresponding angular distribution of one of the pions with respect to the direction of its partner. The smaller histogram shows the opening angle between both tracks in the laboratory system. Due to the high beam boost to both pions the tracks are mostly restricted to the forward hemisphere of the detector.

5.2.2 Resolution of the $\pi^+\pi^-$ Production Vertex

As discussed in Section 4.3.3 the vertex resolution projection on the beam axis for single tracks depends strongly on the direction of the particle. For two tracks originating from the same production point the vertex position of one track will be constrained by both trajectories. In order to calculate the resolution of the tracking system and to obtain the primary vertex position, the two pion tracks have been constrained to a common vertex and the total momentum has been kinematical refitted to meet the beam four-momentum. The difference vector

$$\vec{r} = \vec{r}_{reco} - \vec{r}_{sim}, \tag{5.1}$$

where $\vec{r}_{reco}$ is the reconstructed decay position of the initial $\bar{p}p$ system and $\vec{r}_{sim}$ is the Monte Carlo truth information, has been projected to the $x - y$ plane. This projection corresponds to the resolution lateral to the beam direction. The projection on the beam axis gives the resolution in beam direction. The upper row of Figure 5.4 shows the deviation of the reconstructed vertex position from the generated one with respect to the transverse momentum of the pion track and the lower row with respect to the total momentum, respectively.

The transverse component d_0 has been calculated from the projection of the vector given in Equation (5.1) to the transverse plane and is a positive quantity. Nonetheless the width of the distribution can be compared to the resolution of the single

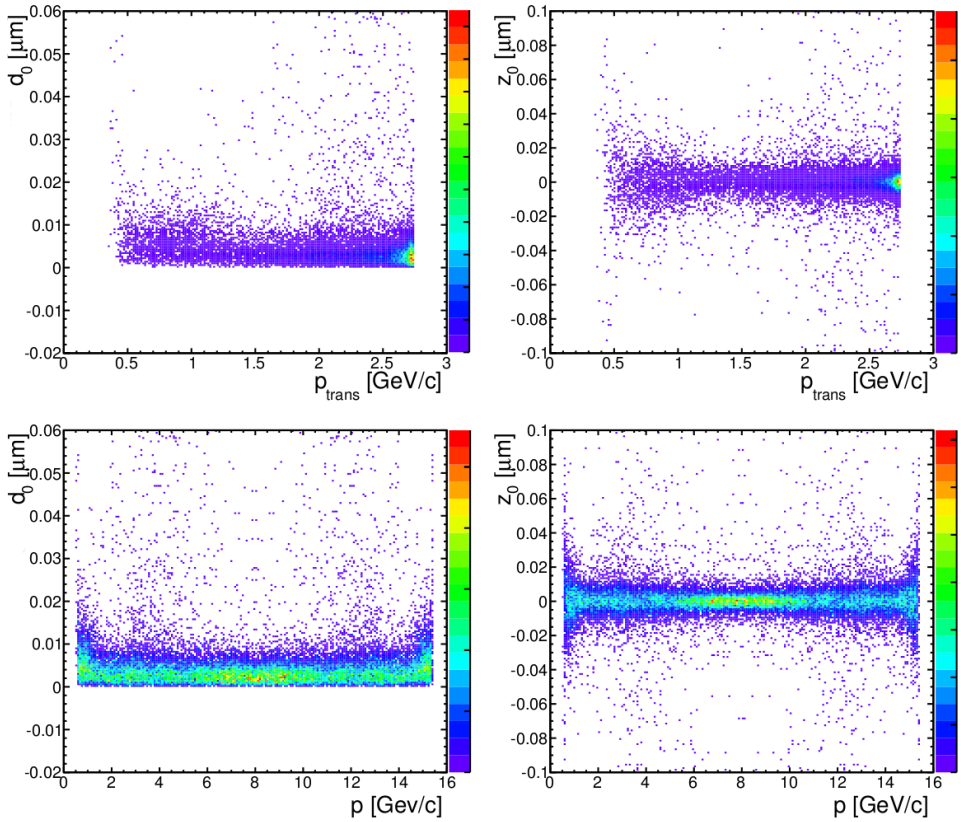

Figure 5.4: Two-dimensional view of the difference of reconstructed and generated vertex position as a function of particle momentum. The left side shows the projection on the $x - y$ plane and the right side the projection onto the beam axis. The upper row shows the vertex resolution versus transverse momentum, whereas the second row shows the same as a function of total momentum.

track studies presented in Section 4.3. The helix fit gives directly the signed track parameter d_0, which preserves the sign by taking the track direction into account [114]. Since the momentum transfer to the pions is large due to the high beam momentum the transverse momentum component remains rather small. It shows a maximum at the largest possible transverse momentum, which corresponds to half the beam momentum transfered to one pion. The resolution transverse to the beam and along the beam axis appears to be rather constant with momentum.

Figure 5.5 shows the two-pion production vertex resolution for all reconstructed events over the full MVD coverage and for all particle momenta. More than 90% of all events have a smaller lateral displacement of less than 100 μm and a longitudinal displacement of less than 150 μm. The width of the d_0 distribution as shown in

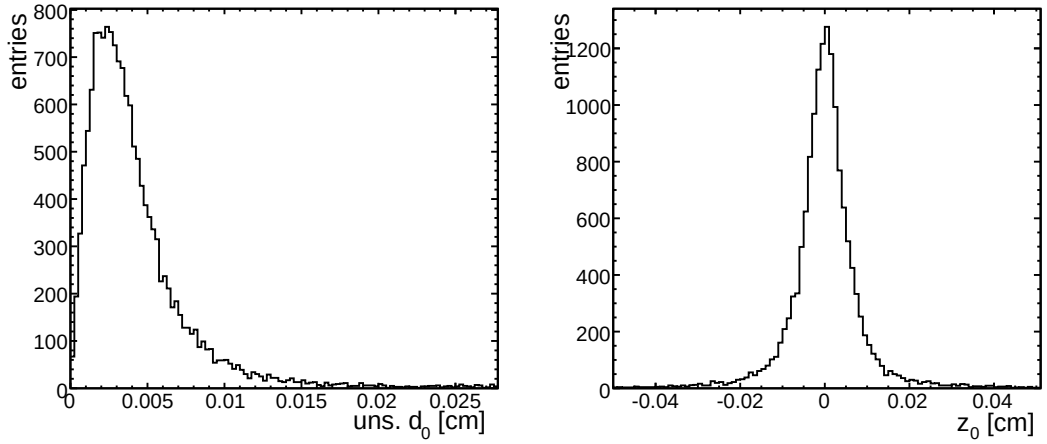

Figure 5.5: Transverse (left) and longitudinal (right) impact parameter resolution for pions from the reaction $\bar{p}p \to \pi^+\pi^-$.

Figure 5.5 (left) has been obtained by calculating the standard deviation

$$\sigma_{d0} = \sqrt{\frac{1}{N}\sum_i (d_i - d_{mean})^2} \tag{5.2}$$

over the given range. The resolution $\sigma(z_0)$ in beam direction can be directly compared to the helix parameter from the single track studies, presented in Section 4.3. The longitudinal resolution is slightly worse compared to the transverse component. The values are obtained by taking all reconstructed $\pi^+\pi^-$ events into account over the full MVD coverage and for all particle momenta.

To get a quantitative picture the momentum axis was divided into $p_i = 800$ MeV/c wide bins and the resolution for each bin was calculated. Figure 5.6 shows the evolution of the vertex resolution along the beam pipe with respect to the particle momentum. Again, the figure to the left show the lateral resolution $\sigma(d_0)$ and the figure to the right the resolution in beam direction $\sigma(z_0)$.

The vertex resolution along the beam direction shows a symmetric behavior with a minimum at half the total momentum of the system. The best resolution corresponds to the case where each pion has half of the total momentum and the transverse momentum component becomes largest. Then the opening angle between both pion tracks can be calculated via

$$\alpha_{\pi^+\pi^-} = 2 \cdot \arctan \frac{p_{\perp,max}}{p_{\parallel,max}/2} \tag{5.3}$$

Using the values $p_{\perp,max} = 2.75$ GeV/c and $p_{\parallel,max} = 7.5$ GeV/c the minimum opening angle is $\alpha_{\pi^+\pi^-} = 40.3$ °. In this case both pion tracks are reconstructed in the

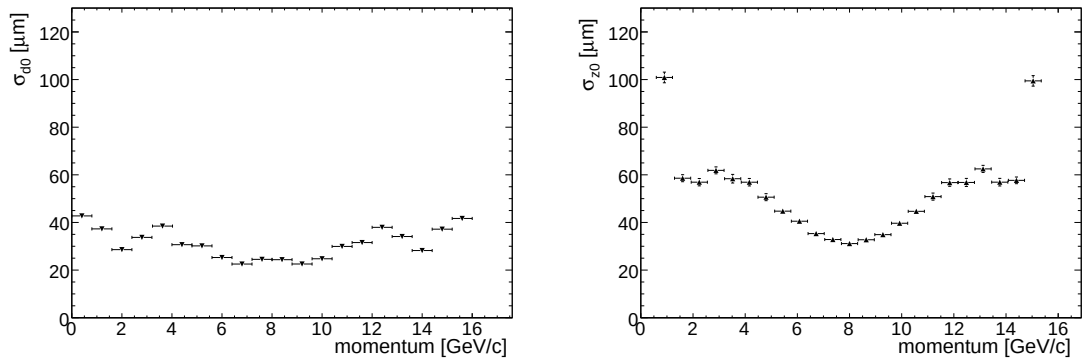

Figure 5.6: Dependence of the primary vertex resolution on momentum. The left side shows the transverse resolution and the right side the resolution in beam direction.

forward disc part of the MVD and stay in the target spectrometer of $\overline{\mathsf{P}}$ANDA. The distribution of the opening angle in the two-pion system was given in Figure 5.3.

The first and last bin of the longitudinal resolution $\sigma(z_0)$ in Figure 5.6 shows a resolution which is almost a factor of two larger than the other bins. This corresponds to the case where one pion carries almost the total beam momentum and has a very small transverse momentum component. At the same time the corresponding low momentum partner is identified with the MVD. The high momentum track stays close to the beam pipe and most of these tracks do not intersect the MVD and the vertex resolution is then defined by only a few MVD measurements for the low momentum track and the forward tracking in the dipole section for the high momentum partner.

The resolution of the two-pion vertex position with respect to the polar angle of the pion trajectory is shown in Figure 5.7. The resolution $\sigma(d_0)$ in the plane perpendicular to the beam axis at the reconstructed production vertex is shown in the upper figure. The small inset shows the distribution of the lateral component of the difference vector given by equation (5.1). The figure in the lower part shows the component $\sigma(d_0)$ in beam direction, respectively. Only events with pion tracks with a polar angle up to 70° have been taken into account. Higher pion angles are suppressed by kinematical constraints due to the large beam boost to the pion system and this region suffers from low statistics. The angular distribution was divided into $\Delta\theta = 3.5°$ wide bins.

The transverse resolution $\sigma(d_0)$ is almost constant over the full angle. The resolution in z direction is best when both pions have the largest momentum. For other kinematic solutions the resolution is degraded by multiple scattering of the less energetic pion and becomes up to a factor two worse. According to Figure 5.2 a pion track at $\theta = 40°$ corresponds to a momentum of $p \approx 3$ GeV/c. The resolution will then suffer from the increase in multiple scattering caused by the interaction of the pions with the detector elements. At very small angles below $\theta < 3.5°$ the MVD can no longer contribute to the track reconstruction for the high momentum partner close

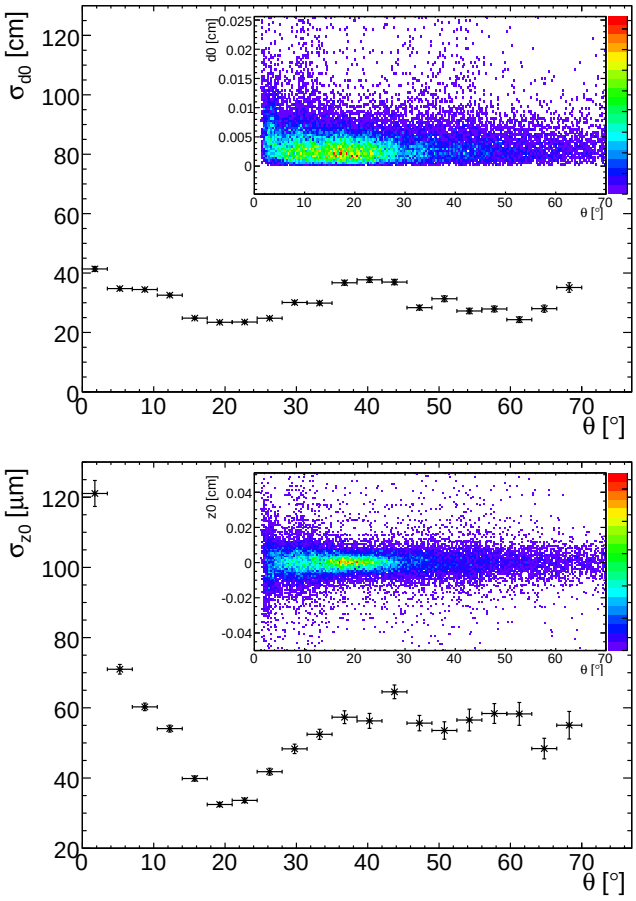

Figure 5.7: Resolution of the $\pi^+\pi^-$ production vertex transverse (upper) and longitudinal (lower) to the beam direction as function of the pion polar angle.

to the beam axis and only the low momentum pion track is reconstructed with the MVD barrel section. The resolution along the beam degrades then to $\sigma(z0) \approx 120$ μm.

5.3 Vertex Resolution of the J/ψ Leptonic Decay

The investigation of the charmonium system is of interest to understand the binding of heavy quarks within a strong potential and important for the development of QCD potential models. The radiative decay of higher charmonium states into $J/\psi\gamma$ can be detected via the prominent two-lepton decay of the J/ψ and the gamma, which carries the transition energy and can be reconstructed in the electromagnetic calorimeter. The charged decay of the J/ψ is a good test for the tracking system, since the leptons cover a wide momentum and polar angle range in the detector.

5.3.1 $J/\psi\gamma$ Event Selection

Figure 5.8 shows the allowed phase space of the muons from the decay $J/\psi \rightarrow \mu^+\mu^-$. The upper row shows the angle of the muons with respect to each other (left) and the opening angle between both charged tracks. Most likely one track is going in the forward direction, while at the same time the corresponding muon track stays in the barrel section of the MVD. The reconstruction of the two-lepton decay vertex of the J/ψ is therefore a good performance test for the tracking system, and in particular the MVD.

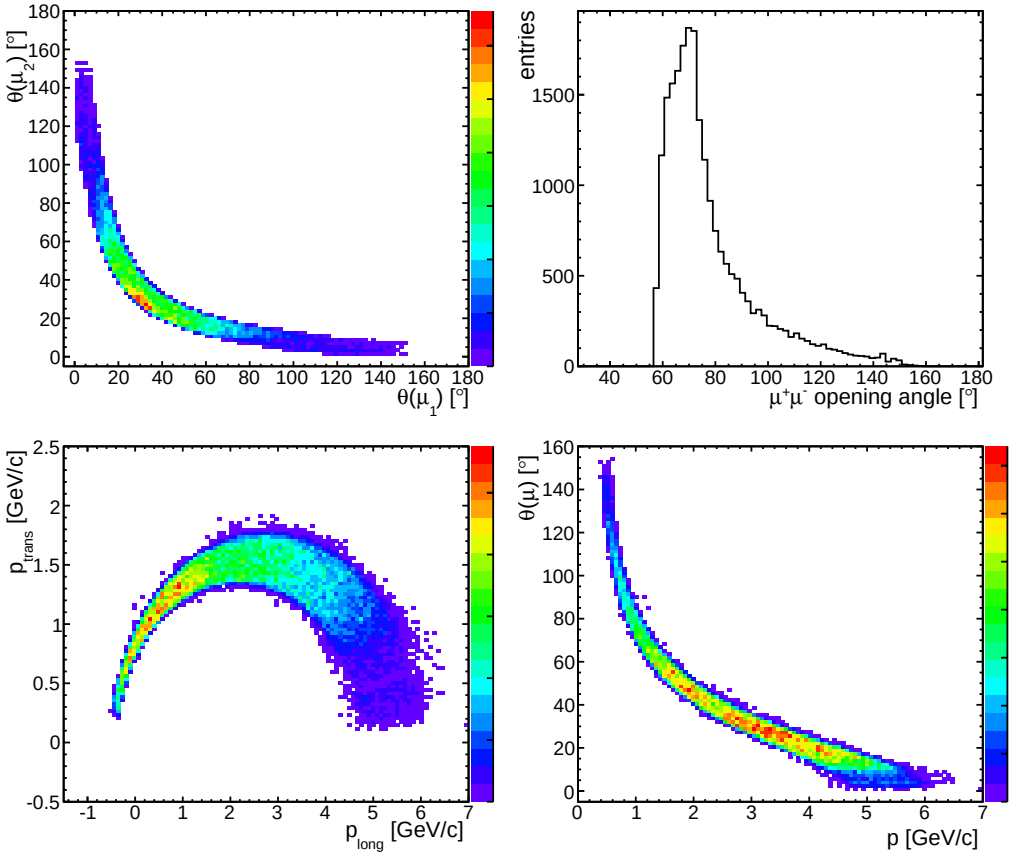

Figure 5.8: Illustration of the allowed phase space for the two muons coming form the J/ψ decay.

In order to reconstruct the J/ψ state, at least two muon candidates are requested in the reconstruction. Both of them have to come from a common vertex with a vertex probability χ^2 of larger than 0.001. The total momentum of the event has to meet

the four-momentum of the beam-target system. The analysis has been performed at a nominal beam momentum of $p_{beam} = 5.5502$ GeV/c, which corresponds to the mass of the (^1P) charmonium state χ_{c1}, for which the radiative decay $\chi_{c1} \rightarrow J/\psi\gamma$ has a relative branching of $BR = 35.6\%$ [15]. Since the phase space for the leptonic decay was of interest, the simulation was performed without generating the (^1P) charmonium state explicitly.

For one of the two muons from the J/ψ decay a particle identification probability of $LH > 55\%$ has been demanded. For the other one no additional PID cut was set. This reduces the combinatorial background to zero and only one J/ψ candidate per reconstructed event was found. Figure 5.9 shows the invariant mass of the two-muon system. The FWHM of the invariant two-muon mass is $\sigma_{FWHM} = 8.5$ MeV/c^2. The

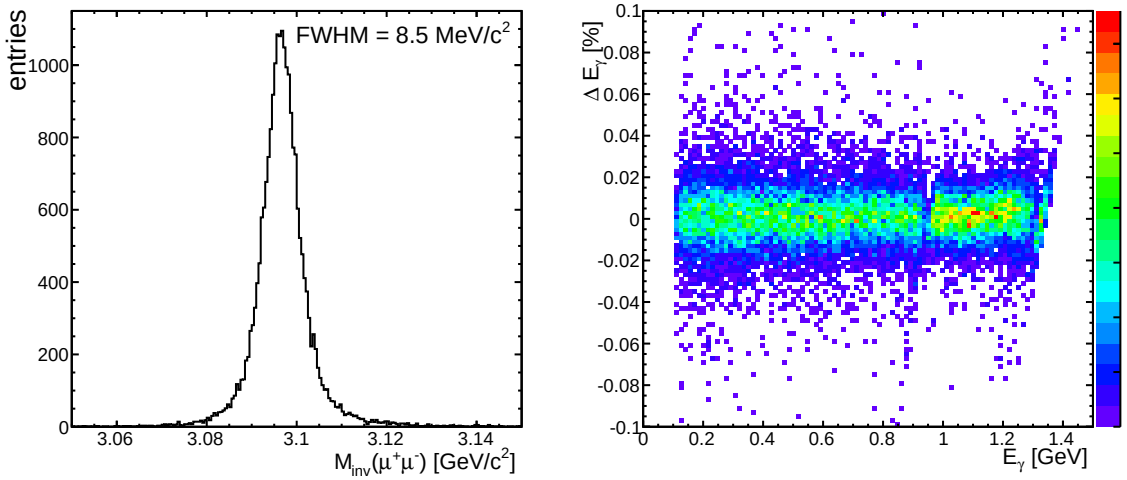

Figure 5.9: Invariant mass of the two-muon J/ψ candidates (left) and the error of the corresponding γ (right).

right hand side of Figure 5.9 shows the relative error of the photon energy, which can be calculated by comparing the reconstructed photon energy to its generated value $E_{\gamma,mc}$

$$\Delta E_\gamma / E = \frac{E_{\gamma,reco} - E_{\gamma,mc}}{E_{\gamma,mc}}. \tag{5.4}$$

The relative error stays almost constant over the allowed γ energy range. The width of the error distribution gives a relative error of $\Delta E_\gamma / E = 1.1\%$. The resolution of the J/ψ is defined by the uncertainty of the muon momentum, for which the relative error is in the order of $\Delta p_\mu / p \approx 1.8\%$.

5.3.2 Resolution of the J/ψ Decay Vertex

The spacial resolution of the decay position of the charmonium resonance is expected to be slightly worse compared to the primary vertex resolution of the channel $\bar{p}p \rightarrow \pi^+\pi^-$ discussed in Section 5.2. The vertex resolution and its dependence on the muon momentum is shown in Figure 5.10 (upper row). Additional, the angular dependence on the vertex resolution is shown below.

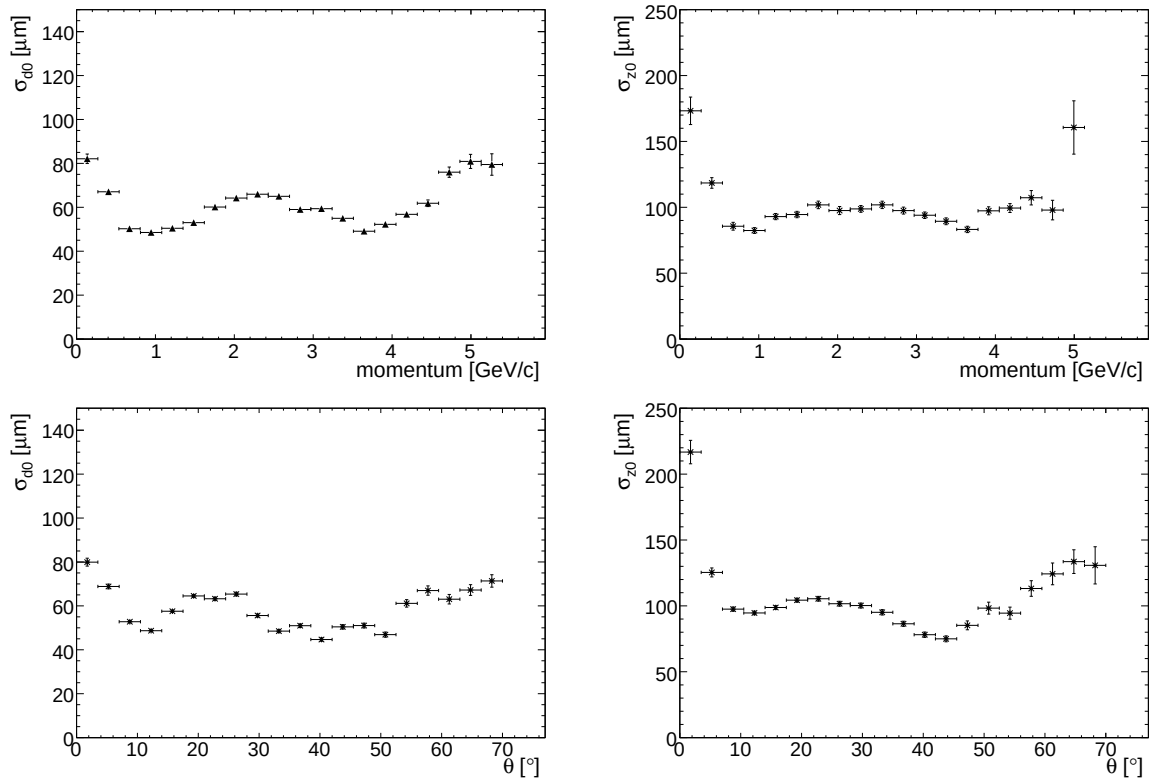

Figure 5.10: Uncertainty of the reconstructed J/ψ decay vertex position as a function of muon momentum (upper row) and as function of the muon direction (lower row). The figure on the left side shows in each case the lateral resolution, whereas the right to the right shows the vertex resolution in beam direction.

The best resolution of $\sigma(d_0) = 50$ μm and $\sigma(z_0) = 80$ μm is obtained for relatively large muon momenta of $p_{mu} \approx 3.5$ GeV/c. In that case the particle trajectory is measured in forward direction with the MVD discs between 20° and 30° polar angle. The corresponding lower-energetic partner leaves hits in the barrel section of the MVD. For those combinations the opening angle becomes relatively large and the vertex position can be constrained in both directions reasonably well. For the

symmetric solution, where both tracks have approximately the same momentum, the trajectories are most likely in the overlap region of barrel and disc structures in the MVD. This increases the effective material budget for these particular particle trajectories and causes a worsening in resolution of ≈ 20 μm in both directions. The increase in the vertex uncertainty at lower and higher particle momenta is caused by combinations where one partner is confined to small angles and high momentum and the other track to low momentum and large angles. The trajectories are cover almost the full backward solid angle up to polar angles of $\theta = 140°$.

5.4 Vertex Resolution for Different Readout Structure Sizes

In this section the influence of various readout structure sizes on the vertex resolution will be discussed with particular emphasis on the pixel cell dimensions. The pixel sensors will provide the very first hits for the track reconstruction and their hit precision will determine the reconstruction of the vertex position. This was already discussed in the context of the single track reconstructed in Section 4.3.3. Table 5.2 lists all considered setups and gives an overview of dimensions of the readout structures modeled in the digitization phase of the detector simulation (see Section A.3).

setup	pixel cell size [μm^2]	strip pitch [μm]	
		z	$r\phi$
A1	100×100	98	86
A2	200×200	98	86
A3	200×50	98	86
A4	50×200	98	86
B1	100×100	49	57
B2	100×100	98	86
B3	100×100	164	172

Table 5.2: Defined sets of readout dimensions within the digitization phase in the simulations. The geometric sizes defines the resolution of the hit measurement on the sensor.

The default solution for the size of the pixel cell features 100×100 μm^2 large pixels

and roughly 100 μm wide spacing of the strips on the strip detector surface, which corresponds to option A1 in Table 5.2. For the simulation of the influence of the pixel size on the vertex resolution the strip readout pitch were kept constant for all settings A1-A4. This allows the direct comparison of various pixel dimensions. The settings A2 and A3 have the same pixel cell area, but the orientation of the pixel on the sensor is different. A pixel size of 50×2000 μm^2 defines the long side to point in the direction, in which the module is larger (see Figure 4.3 for an illustration). If the module is located in a barrel layer of the MVD the long side would point in beam direction, as Figure 4.3 indicates. For the pixel size 200×50 μm^2 the cell is rotated by 90° with respect to the long side of the module.

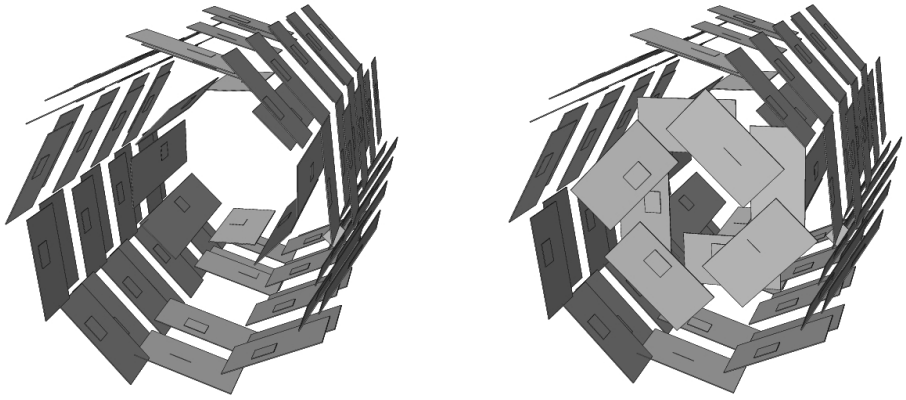

Figure 5.11: Artists view of the inner two pixel barrel layers (left) and together with the first two pixel disc layers (right). Only the silicon detectors are shown here leaving out the support and the beam and target pipes.

Moreover the orientation of the module itself with respect to the beam axis is not the same for both pixel barrel layers. This is illustrated in Figure 5.11, were only the two inner pixel layers in the barrel section are shown (left) and in a combined view with the first two pixel disc structures included (right). The modules of the second pixel layer are turned by 90° with respect to the beam axis. Each disc structure is build by four pixel modules and both are tilted by an angle of 45° in order to avoid to large acceptance gaps close to the interaction point. This complex arrangement was chosen initially to compensate the worse resolution in the direction of the long pixel dimension for the ATLAS pixel detector design, which features a asymmetric pixel size of 50×400 μm^2. For this highly asymmetric design the next layer had to compensate the loss in resolution in beam direction by turning the sensor by 90° (second pixel layer in Figure 5.11). At present a re-design of the MVD pixel part is

under way to optimized for the use of smaller pixel sizes, which came accessible in recent years.

5.4.1 Variation of the Pixel Cell Size

The reaction $\bar{p}p \rightarrow \pi^+\pi^-$ has been analyzed at the highest beam momentum of 15 GeV/c. The analysis was already explained in section 5.2. This channel is suitable for the investigation of the vertex resolution with the forward part of the tracking system, in particular the MVD discs close to the interaction zone. Most of the pions from this channel are confined to polar angle cone of $\theta = 40°$ around the beam pipe. Therefore the resolution in the plane perpendicular to the beam axis can be constrained over the full momentum range and is better than $\sigma_{d_0} = 40$ μm. The resolution in beam direction is worse since both particles are boosted in forward direction due to the large beam momentum. Again the best resolution is obtained in the symmetric case, where both pions carry almost half the beam momentum and stay at around $\theta \approx 20°$. For higher momenta one pion track is more aligned to the beam axis and the vertex position of the two-pion system is defined only by the resolution of the low-momentum partner. This slower partner goes to larger polar angles.

Figure 5.12 shows the change of the transverse vertex resolution $\sigma(d_0)$. The upper row gives the uncertainty against the pion momentum, whereas in the lower row the lateral vertex resolution as function of the pion angle is shown. For a better display the four sets of pixel sizes have been separated into two columns. Figure 5.13 shows the appropriate figures for the resolution in beam direction $\sigma(z_0)$.

The best resolution in both components is obtained by quadratic 100×100 μm^2 large pixels over the full phase space of the $\pi^+\pi^-$ reaction. Compared to 200×200 μm^2 large pixels the gain in resolution is about 30 %. The decrease of resolution is almost constant over the full momentum range, as shown in Figure 5.12 (upper left).

The histogram in the upper right of Figure 5.12 shows the momentum dependence of d_0 for rectangular shaped pixels with sizes of 200×50 μm^2 and 50×200 μm^2, respectively. For 50×200 μm^2 the shape of the distribution follows in principle the curve for 100×100 μm^2 large pixel cells. The minimum at $p_\pi = 8$ GeV/c is defined to be better than 30 μm.

The decrease in resolution towards larger momenta, and respectively lower momenta, since both pions are kinematical coupled, comes from the poor coverage by the first pixel discs close to the interaction zone. There are two local maxima in the $\sigma(d_0)$ distributions, which corresponds to polar angles for the pions of $\theta_1 \approx 18°$ and $\theta_2 \approx 37°$, respectively. For these solutions the trajectories miss the first pixel layers and are than defined by the next measurement in the second barrel layer, where the pixel is turned by 90° and the long side would be responsible for the lateral measurement. This degrades the resolution almost by a factor of two. The other option

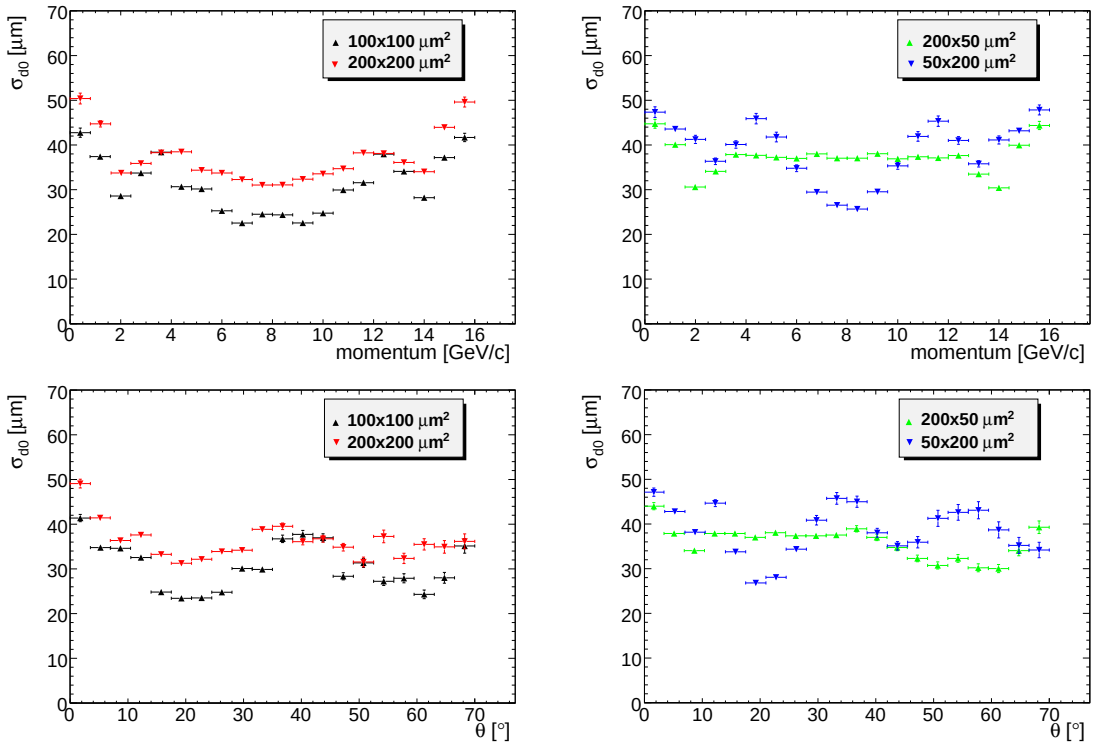

Figure 5.12: Vertex resolution $\sigma(d_0)$ perpendicular to the beam axis for different pixel cell sizes in the hit reconstruction for two-pion vertices from the reaction $\bar{p}p \rightarrow \pi^+\pi^-$ at highest $\overline{\text{PANDA}}$ beam momentum (see text for details).

for the pixel size of 200×50 μm^2 shows the opposite behavior, as expected. It has been shown that asymmetric pixel dimensions and acceptance gaps in the first pixel layer can generate larger excesses in the resolution function.

The accuracy of the vertex position in beam direction $\sigma(z_0)$ and its change with momentum, or polar angle, respectively, is shown in Figure 5.13. Again, the best resolution of the vertex component is obtained with 100×100 μm^2 quadratic pixels. The longitudinal component can be reconstructed almost with the same accuracy with 200×50 μm^2 large cells (Figure 5.13, green curve, upper right), where the short pixel dimension points in radial direction in the pixel disc plane. In the transverse plane at the MVD disc positions the radial hit position is well reconstructed in this case. The improvement is however only marginal compared to the quadratic 100×100 μm^2 large pixels. To determine the radial position as accurately as possible helps to restrict the vertex position along the beam axis for tracks going in forward direction. Increasing the pixel size drastically to 200×200 μm^2 large pixels reduces the resolution by more than a factor of two for pions with half the beam momentum. A reduction to 50×200 μm^2 large pixels would only slightly change the resolution

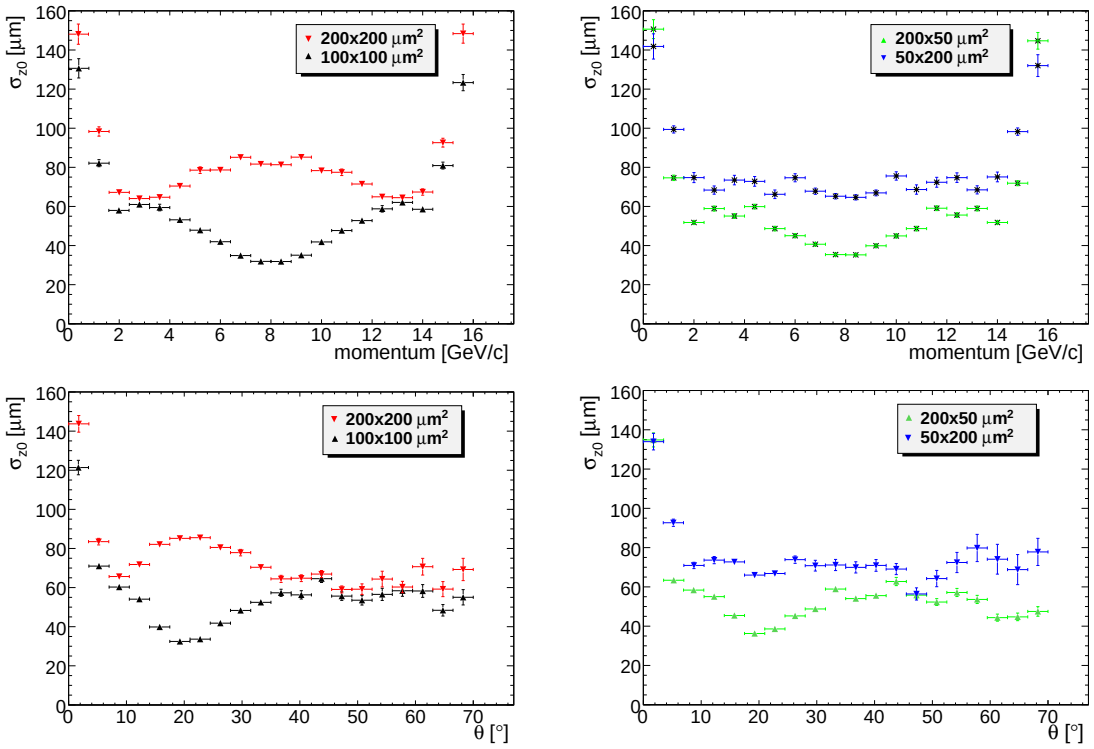

Figure 5.13: Vertex resolution $\sigma(z_0)$ in beam direction for different pixel cell sizes for the reaction $\overline{\mathrm{p}}\mathrm{p} \rightarrow \pi^+\pi^-$.

of the longitudinal component compared to the 200×200 $\mu\mathrm{m}^2$ large pixels.

The channel $J/\psi\gamma$ was analyzed at an intermediate beam momentum of $p_{beam} = 5.55$ GeV/c. The variation in the vertex resolution by the influence of different pixel dimensions is expected to be less prominent. Since the muons have lower energies as compared to the hard pions from the previously discussed two-pion channel $\overline{\mathrm{p}}\mathrm{p} \rightarrow \pi^+\pi^+$, the small angle scattering is the dominating aspect here. Therefore not much difference can be seen in Figure 5.14 by comparing the reconstruction of the J/ψ decay position with 100×100 $\mu\mathrm{m}^2$ large pixels and 200×200 $\mu\mathrm{m}^2$ large pixels, respectively. For the other two sets of digitization schemes the results are the same. The transverse impact parameter resolution $\sigma(d_0)$ is approximately the same for both sets. A small change in the resolution of the longitudinal component can be seen by increasing the pixel cell size. The deviation is mostly within 10 μm and only at lower and higher momenta the deviation gets larger. This is partly due to the poorer statistics.

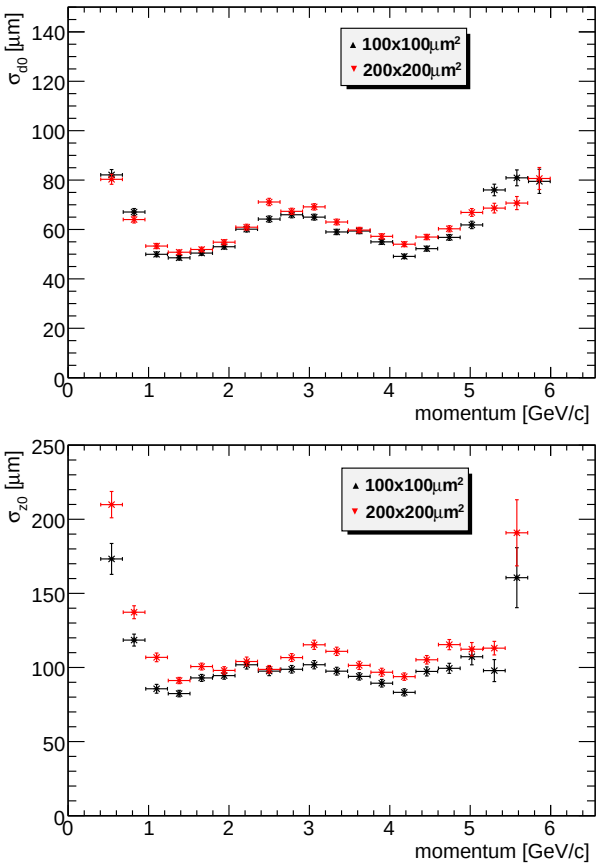

Figure 5.14: Momentum dependence of the vertex resolution transverse (left) and along (right) the beam axis for the leptonic J/ψ decay. Shown are only the resolutions for 100 $\times$ 100 μm^2 large pixels (black) and 200 $\times$ 200 μm^2 large pixels (red), respectively. Other variation have been omitted in the figure, which are within the errors identical to the black symbols.

5.4.2 Variation of the Strip Sensor Readout Pitch

The MVD disc part is mainly covered by pixel detectors. The first four discs are build completely from pixel detectors and only in the outermost layers strip sensors are employed in order to reduce the material budget and the number of readout channels. A variation of the strip readout pitch would not change the vertex resolution of the MVD setup. There are up to four hit measurements in pixel sensors for tracks traversing the last two disc structures. Figure 5.15 shows the reconstructed vertex position of the two-pion production vertex for two sets of strip readout sizes. For events having only tracks in the forward region and therefore only hits in the MVD discs, the ability to reconstruct the production vertex does not change if the size of the readout pitch of the strip detectors in the forward discs is varied. The small deviation at lower pion momenta at $p \approx 2$ GeV/c comes from two-pion combinations, where one track remains in the forward MVD part at higher momentum of $p \approx 14$ GeV/c and the corresponding partner track enters the barrel section. In the barrel section the third and fourth layer are intended to be constructed from strip detectors. Since the number of pixel layers in front of the strip barrel layers is only two, the strip detector hits contribute to the vertex resolution. In a modified design of the MVD

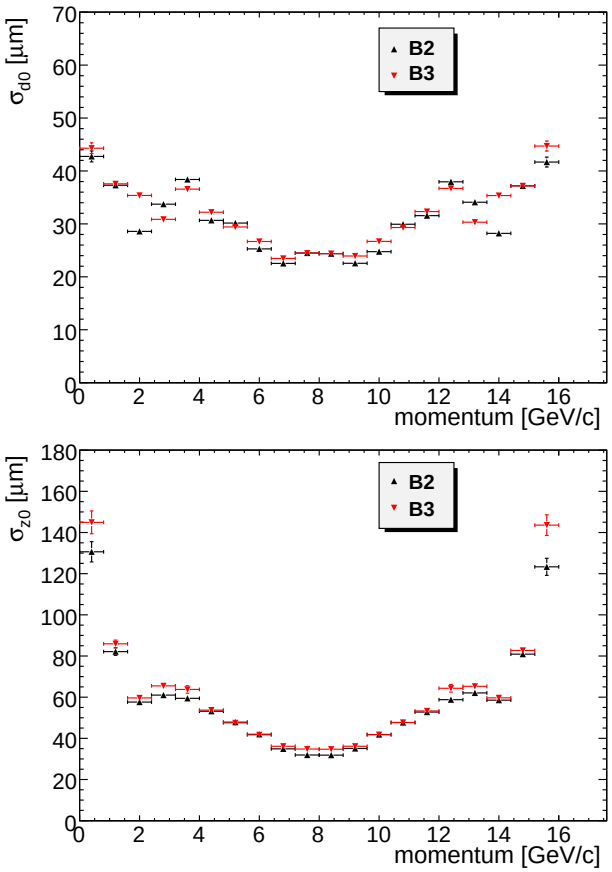

Figure 5.15: Vertex resolution of the two-pion production vertex of the reaction $\bar{p}p \rightarrow \pi^+\pi^-$ at highest beam momentum. According to Table 5.2 only the sets B2 and B3 are shown for a clear view. There is only a small deviation at lower momenta in the transverse component, which is caused by tracks entering the barrel section, for which the resolution becomes slightly reduced. The resolution along the beam axis $\sigma(z_0)$ remains the same for different strip readout dimensions.

strip part the sensors in the discs have been replaced by wedge-shaped sensors with a slightly worse hit resolution. According to these simulations the vertex resolution will not suffer by increasing the strip readout pitch slightly beyond 150 μm, but will have the advantage of a reduced material budget in the forward domain. The size of the readout pitch in the barrel should be kept below 150 μm in order to contribute to a good vertex resolution.

For the channel $\bar{p}p \rightarrow J/\psi\gamma$ the vertex resolution is shown in Figure 5.16. Again, the upper frame shows the transverse, whereas the lower frame shows the longitudinal component separately. All three considered subsets have been included to the figure, but within the statistics the resolution is practically the same. At a beam momentum of $p_{beam} = 5.55$ GeV/c the muons have momenta of around one GeV/c only (see Figure 5.8 for the available phase space). Slower particles are distorted by small angle scattering in the material in front of the strip sensor layers. Therefore an increase in the readout pitch in the strip detector part does not degrade the vertex resolution. The usage of larger readout dimensions would allow to save readout channels and readout electronics at the same time. This would have a positive effect on the overall material budget. Less readout channels are required to cover the solid

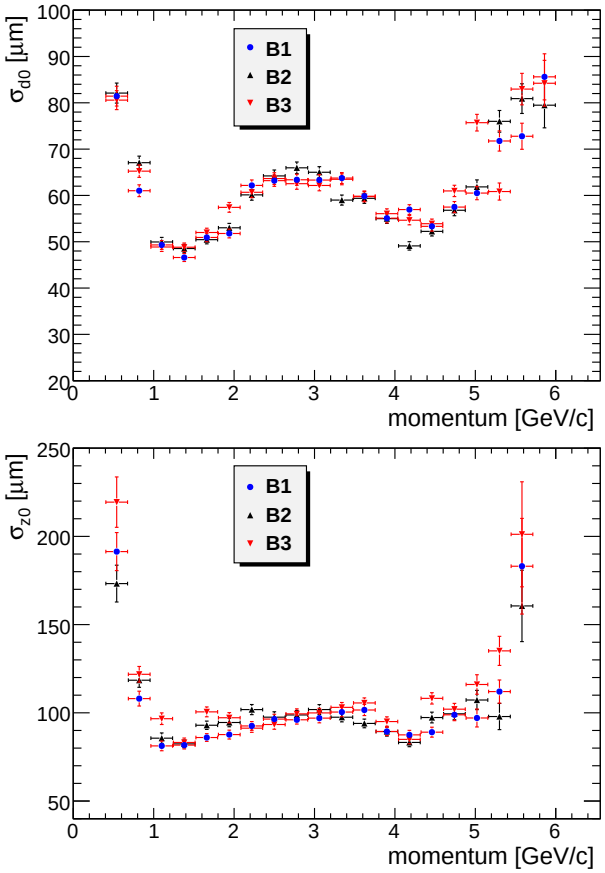

Figure 5.16: Two-muon vertex resolution of the J/ψ decay in the reaction $\bar{p}p \rightarrow J/\psi\gamma$. All three subsets are shown here, according to Table 5.2. There are only small deviations, which in general stay within the error bars. The errors are growing at the ends of the momentum range due to the limited statistics.

angle per layer with less frontends, which are usually located near the sensors. The frontend electronics must be cooled in order to keep them at constant temperature. The cooling effort could be decreased for the outer strip layers, which would have again a positive impact on the overall MVD material budget.

6 Physics Performance for Charmed Meson Channels

6.1 Motivation

The $\overline{\text{P}}$ANDA detector will provide an excellent experimental tool to investigate channels including short-lived particles in the final state. To demonstrate the physics performance of the experimental setup, two reaction channels with D mesons in the final state have been investigated. This is of particular importance for investigations of charmonium states above the $D\overline{D}$ threshold, e.g. the charmonium states $\psi(3770)$ and $\psi(4040)$, for which the knowledge about their properties is rather poor compared to other $c\bar{c}$ states (see Section 1.2.2 for a brief overview). Furthermore, it is speculated that hybrid states might exist above the $D\overline{D}$ threshold and can be addressed in $\overline{\text{p}}$p annihilations [5], which may decay into open charm channels.

In general the knowledge about the mass region above the $D\overline{D}$ threshold is rather poor. The Particle Data Group lists only the higher ψ states in their listings, for which the decay into $D\overline{D}$ has been observed (see Section 1.2.2 for details). Some of the higher $c\bar{c}$ resonances can decay into $D\overline{D}$, if not forbidden by some selection rules. The dominant strong decays are into open charm channels through production of a $q\bar{q}$ pair, which can be modeled via the $^3P_0$ model[1] [115]. Table 6.1 lists predictions about some higher $c\bar{c}$ states, their decay into open charm channels and the calculated with for the particular transitions. Only those states are listed here, for which some experimental evidence for decays to open charm channels exists. Ref. [115] gives also model predictions for the calculated states $3S$, $4S$, $2P$, $3P$, $1D$, $2D$, $1F$, $2F$ and $1G$, respectively. The model expectations for the total width are in good agreement with experimental findings. The experimental knowledge about the partial width of higher $c\bar{c}$ states is missing, either the particular resonance had not been identified so far, or the obtained event samples are to low in order to arrive at conclusions about the nature of reported resonances in the charmonium mass region (see Section 1.2.2 for a brief overview of the experimental knowledge about $c\bar{c}$ states above the open charm threshold).

[1] This model assumes that the $q\bar{q}$ pair is produced with quantum number corresponding to a $^3P_0$ state (see [115] and references therein for details).

$c\bar{c}$	state	decay mode	Γ_{th} [MeV/c^2]	Γ_{exp} [MeV/c^2]
$\psi(3770)$	1^3D_1	$D\bar{D}$	43	23.6 ± 2.7
$\chi_2(3930)$	2^3P_2	$D\bar{D}$	42	-
		DD^*	32	-
		total	80	29 ± 10
$\psi(4040)$	3^3S_1	DD^*	33	-
		$D^*\bar{D}^*$	33	-
		$D_s\bar{D}_s$	7.8	-
		total	74	80 ± 10
$\psi(4160)$	2^3D_1	$D\bar{D}$	16	-
		DD^*	0.4	-
		$D^*\bar{D}^*$	35	-
		$D_s\bar{D}_s$	8	-
		total	74	103 ± 8
$\eta_c(4043)$	3^1S_0	DD^*	47	-
		$D^*\bar{D}^*$	33	-
		total	80	-
$\psi(4415)$	4^3S_1	DD^*	2.3	-
		$D^*\bar{D}^*$	16	-
		$D\bar{D}_2^*$	23	-
		$D_s\bar{D}_s$	1.3	-
		$D_s\bar{D}^*_s$	2.6	-
		total	78	62 ± 20

Table 6.1: Selection of calculated widths for $c\bar{c}$ states above the $D\overline{D}$ threshold and their decay to various open charm channels [115]. If possible, the experimental total widths are given for comparison from [15].

Only a few model calculations are available [116][117], which allow an estimate of the production cross sections for open charm processes in $\overline{\text{p}}$p annihilations. In Section 6.2.1 an estimate is given based on a Breit-Wigner approach via a charmonium resonance as basis for the discussion on the $D\overline{D}$ reaction channels in this chapter. Since the initial state is composed of heavy hadrons, the background of light hadronic channels to the charmed reaction channels is expected to be several orders of magnitudes larger. To clearly identify the physics signal and to reduce the hadronic background sufficiently, a very precise tracking system for momentum and vertex reconstruction together with a good particle identification system will be essential. The following sections will show the good performance to clearly identify channels containing $D\overline{D}$ in the final state via its delayed decays and allow to suppress the large hadronic background sufficiently to extract the charmed signal events. The

main focus of this benchmark study is to exploit the ability to separate the charmed signal from the huge hadronic background.

In previous attempts [118][119] to investigate the physics performance of the $\overline{\text{P}}$ANDA detector, and in particular the reconstruction of open charm channels, the simulation made simplistic assumptions in the reconstruction stage of the expected detector response. Many aspects of the general detector design have been changed, e.g. there is a completely redesigned MVD used in the new simulations. The previous version of the MVD was defined to use only silicon pixel detectors and was not optimized in terms of number of layers and their positions. The results presented in the next sections make use of a detailed detector description and sophisticated analysis tools. This includes the MVD as important part with a realistic digitization procedure of the expected signals from the detector response. This allows the development of reconstruction algorithm at an early stage as needed input for a realistic track reconstruction. It is not only important for the expected physics performance of the detector setup, but also for the investigation of properties of the inner tracking detector itself, such as vertex and momentum resolution. The development of MVD related reconstruction algorithms and the adaption and evaluation of track reconstruction tools were prerequisites for the detailed simulation studies and a major part of this work. In Section A a more detailed description of the used detector software is given.

For the studies presented here, a detailed background study have been performed. This includes not only generalized $\overline{\text{p}}$p background reactions via the DPM model compared to previous simulations [118], but also the investigation of specific reaction channels, which will be major background sources for the analysis presented in Section 6.3.

6.2 Definition of the $D\overline{D}$ Benchmark Channels

The reconstruction of delayed decays caused by the weak decay of the charm quark is crucial for many aspects of the $\overline{\text{P}}$ANDA physics program. In order to demonstrate the physics performance of the proposed detector setup, two open charm channels $\overline{p}p \to D\overline{D}$ have been defined, for which the precise reconstruction of the secondary vertex is essential. The $D\overline{D}$ channels have been chosen with a focus on the tracking and PID reconstruction abilities of $\overline{\text{P}}$ANDA. They contain only charged particles in the final state.

The reaction channel $\overline{p}p \to D^+D^-$ has been investigated at a beam momentum of $p_{beam} = 6.57$ GeV/c, which corresponds to the charmonium resonance $\psi(3770)$ and is approximately 40 MeV above the $D\overline{D}$ threshold. The production mechanism has been assumed to directly proceed into a D^+D^- pair. The channel $\overline{p}p \to D^{*+}D^{*-}$ was produced at a beam momentum of $p_{beam} = 7.70$ GeV/c slightly above the $D^{*+}D^{*-}$ threshold, which corresponds to the charmonium resonance $\psi(4040)$. Both reaction channels and the considered charged D meson decays are given in Table 6.2. For

channel	D^+D^-	$D^{*+}D^{*-}$
decay	$D^+ \to K^-\pi^+\pi^+$ (9.2%)	$D^{*+} \to D^0\pi^+$ (67.7 %) $D^0 \to K^-\pi^+$ (3.8 %)

Table 6.2: Definition of the $D\overline{D}$ channels and their decays into charged final states.

both channels the signature in the detector is similar and therefore the analysis is rather similar. The selection of the charmed signal is discussed in Section 6.3.

6.2.1 Reaction Cross Sections

The charm production cross section close to threshold in $\overline{\mathrm{p}}$p annihilations is so far unknown. To estimate the $D\overline{D}$ production cross section, a Breit-Wigner approach can be used to calculate the resonant cross section of the $\psi(3770)$ resonance via

$$\sigma_R(s) = \frac{4\pi\hbar^2c^2}{s - 2m_p^2c^4} \frac{B_{in}B_{out}}{1 + (2(\sqrt{s} - M_Rc^2)/\Gamma_R)^2}, \tag{6.1}$$

where B_{out} is the branching ratio $\psi(3770) \to D^+D^-$ and B_{in} the decay branching ratio $\psi(3770) \to \overline{p}p$. Γ_R and M_R are resonance parameters and m_p the mass of the proton. For B_{in} there is no measurement at all and therefore this ratio has to be estimated. This can be approximated by using the known branching ratio of the J/ψ resonance, with its value $B(J/\psi \to \overline{p}p) = 2.12 \cdot 10^{-3}$ [15], and scaling the individual width of both charmonium states [119]. This results in a ratio of:

$$\begin{aligned} B_{in} &= B(\psi(3770) \to \overline{p}p) = B(J/\psi \to \overline{p}p) \times \frac{\Gamma_{J/\psi}}{\Gamma_{\psi(3770)}} \\ &= 2.12 \cdot 10^{-3} \times \frac{93.2\mathrm{keV}}{27.3\mathrm{MeV}} \\ &= 7.24 \cdot 10^{-6} \end{aligned} \tag{6.2}$$

Using a decay branching of $B_{out} = B(\psi(3770) \to D^+D^-) = 36.1$ % and the resonance parameters $\Gamma_{\psi(3770)} = 27.3$ MeV/c^2 and $M_{\psi(3770)} = 3772.9$ MeV/c^2, the resonance cross section can be calculated to:

$$\sigma(\overline{p}p \to \psi(3770) \to D^+D^-) = 1.02\,nb. \tag{6.3}$$

for the D^+D^- channel.

For the second channel $D^{*+}D^{*-}$ the same estimation of the cross section can be made using the Breit-Wigner approach given in Equation (6.1). The $\psi(4040)$ resonance parameters [15] $\Gamma_{\psi(4040)} = 4040 \pm 1$ MeV/c^2 and $M_{\psi(4040)} = 80 \pm 10$ MeV/c^2 and the decay branching of the $\psi(4040)$ into $\overline{\mathrm{p}}\mathrm{p}$ are needed. The later can be calculated again by scaling to the J/ψ branching ratio and yields:

$$B_{in} = B(\psi(4040) \to \overline{p}p) = 2.47 \cdot 10^{-6} \tag{6.4}$$

By using the branching into open charm of $B_{out} = B(\psi(4040) \to D^{*+}D^{*-}) \approx 33$ % [120] this leads to a cross section of:

$$\sigma(\overline{\mathrm{p}}\mathrm{p} \to \psi(4040) \to D^{*+}D^{*-}) = 0.30\,nb \tag{6.5}$$

The production cross section of continuum $D\overline{D}$ production close to threshold in $\overline{\mathrm{p}}\mathrm{p}$ production is unknown, but it can be assumed to be in the same order as for the corresponding charmonium production cross sections. This assumption might be valid, since the $D\overline{D}$ production is close to threshold and the relative branching $c\overline{c} \to D^+D^-$ is relatively large. For the following considerations to calculate the relative branching of the expected $D\overline{D}$ signals to the total cross section the values obtained in Equation (6.3) and Equation (6.5) have been rescaled to account for the missing contribution from continuums production and the decay of the $c\overline{c}$ resonance into $D\overline{D}$ has been set to 100%. This gives the cross section of:

$$\sigma(\overline{p}p \to D^+D^-) = 2.83\,nb \tag{6.6}$$

and for the second channel

$$\sigma(\overline{p}p \to D^{*+}D^{*-}) = 0.90\,nb \tag{6.7}$$

For the $D^\pm$ decay only one prominent charged decay $D^\pm \to K^\mp\pi^\pm\pi^\pm$ was used in the analysis, which has a branching ratio of 9.2 %. Taking the considered $D^\pm$ meson decay branchings into account the ratio to the total cross section can be calculated to

$$R = \frac{\sigma(\overline{p}p \to D^+D^-)}{\sigma(\overline{p}p \to X)} = \frac{2.83nb \cdot (0.092)^2}{60mb} = 4.0 \cdot 10^{-10} \tag{6.8}$$

by using a total inelastic cross section of $\sigma(\overline{p}p \to X) = 60$ mb [15].

For the $D^{*+}D^{*-}$ channel the subsequent D meson decay has to be taken into account and the relative branching can be calculated to be

$$R = \frac{\sigma(\overline{p}p \to D^{*+}D^{*-})}{\sigma(\overline{p}p \to X)} = \frac{0.90nb \cdot (0.677)^2 \cdot (0.038)^2}{60mb} = 1.0 \cdot 10^{-11} \tag{6.9}$$

The values for the expected branching ratios given in Equations 6.8 and (6.9) can only be approximate values. The strength of the ψ-resonance decay into $\overline{\text{p}}$p is completely unknown and in addition there are only a few predictions concerning the production of $D\overline{D}$ at threshold, but they do not provide a consistent picture. One model calculation [116] gives a wide range for the $D\overline{D}$ production cross section in $\overline{\text{p}}$p annihilation of $10 - 100$ nb in the $\overline{\text{P}}$ANDA energy range. In a second attempt, using a quark-gluon string model [QGSM] [117] a cross section of 20 nb at threshold were predicted for the channel $\overline{p}p \to D^+D^-$. These models extrapolate from channels with strange quark content to the charm region, e.g. as shown in Figure 6.1 and have no experimental confirmation.

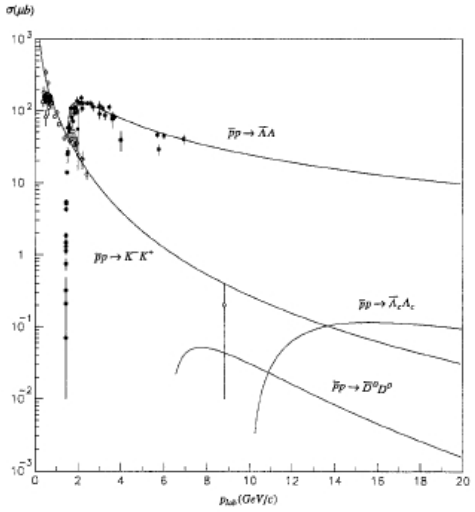

Figure 6.1: Prediction of the $\overline{p}p \to D^0\overline{D}^0$ cross section at threshold derived from a quark-gluon string model [QGSM] (figure from [117]). The model gives the same cross section for the D^+D^- channel.

This shows that the knowledge of the reaction dynamics is rather poor at threshold and the production mechanism and production strength are unknown and needs detailed investigations. The following paragraph will show that even the major background contributions to these channels are not well measured.

6.2.2 Hadronic Background Reactions

Compared to the total $\overline{\text{p}}$p cross section of 60 mb the $D\overline{D}$ production cross section will be suppressed at least by ten orders of magnitude as explained in Section 6.2.1. For this analysis the event pattern in the detector will be six charged tracks. Therefore background reactions leaving a similar signature can fake the physics signal.

Figure 6.2 gives an overview of channels which are considered to be major background sources. The cross sections have been derived from data samples mainly from

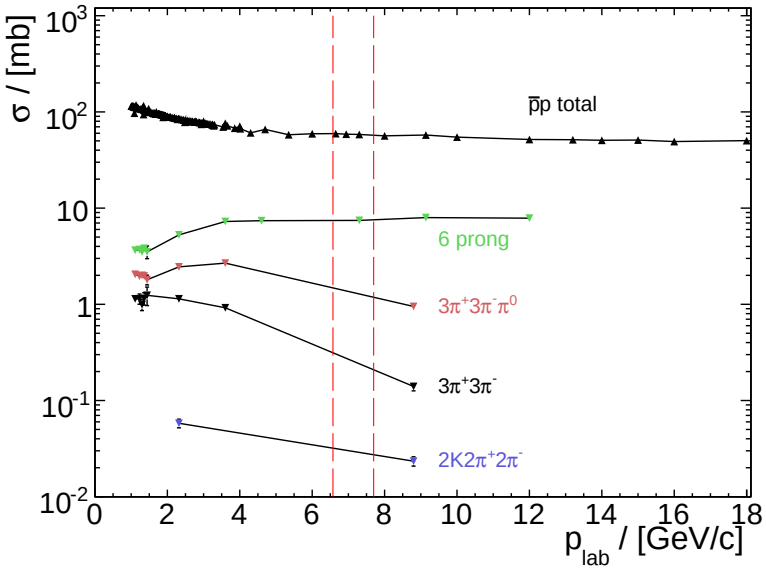

Figure 6.2: Overview about possible background reactions and their total cross section compared to the total $\overline{\text{p}}$p cross section.

bubble chamber experiments. The six-prong events are those, which have six charged tracks in the final state ([121][122][123][124][125][126]). The next two channels containing only pions, either with one additional pion $3\pi^+3\pi^-\pi^0$, or exactly six charged pions $3\pi^+3\pi^-$ ([122][123][127][128]). For the later the cross section is one order of magnitude smaller. These channels have a rather high cross section and therefore a good PID within $\overline{\text{P}}$ANDA is necessary to suppress the pions sufficiently compared to kaons to detect the D mesons via their decay into charged kaons and pions.

The channel $K^+K^-\pi^+\pi^+\pi^-\pi^-$ may be the largest background source. This channel is still six to seven orders of magnitudes above the $D\overline{D}$ cross section estimates from Section 6.2.1, but the experimental signature in the detector and the kinematics are similar. Only a precise tracking system, which allows to clearly identify the secondary vertices from the delayed D meson decays will allow to reduce this channel

sufficiently in order to extract the pair of charmed mesons from the huge background level.

As illustrated in Figure 6.2 even the knowledge of these basic multi-charged channels is rather poor. To obtain values for cross sections at the $c\bar{c}$ positions (indicated as red lines in Figure 6.2) an interpolation between the available data points was used.

reaction	cross section [mb]	fraction to $p\bar{p}$	fraction to D^+D^-
$3\pi^+3\pi^-\pi^0$	1.5	$2.5 \cdot 10^{-2}$	$6.25 \cdot 10^7$
$3\pi^+3\pi^-$	0.32	$5.0 \cdot 10^{-3}$	$1.25 \cdot 10^7$
$2K^{\mp}4\pi^{\pm}$	0.033	$5.0 \cdot 10^{-4}$	$1.25 \cdot 10^6$

Table 6.3: Cross sections for prominent background channels relevant for the $D\overline{D}$ benchmark channels. Additionally the fractions compared to the total $\overline{p}p$ and the D^+D^- channels are given.

To evaluate the ability to reduce the background to a sufficient level, a large scale simulation study was performed. In a general approach the Dual Parton Model (DPM) [96] was used to produce background coming from $\overline{p}p$ annihilations. The DPM model can describe $\overline{p}p$ interactions at intermediate energies, where $\overline{\text{P}}$ANDA will operate, reasonable well. This model includes the description of elastic hadronic events. Elastic events were filtered out before the detector simulation was performed, to reduce the simulation needs. The inelastic events include multi prong events, which could be interpreted as signal events.

Technically it was not possible to simulate $10^{10} - 10^{11}$ DPM events in a full detector simulation. Therefore, a two step approach has been followed. The DPM event generator has been used to study 10^7 events to test the analysis, e.g. for the acceptance of events containing charged track multiplicities equal or larger than six and for possible detector effects.

In a second approach a study with specific background reactions was performed for the channels, which are listed in Table 6.3. Channels containing six charged pions are abundant enough to eventually fulfil the kinematic requirements for the considered $D\overline{D}$ channels. Additionally, the channel with two charged kaons and four charged pions has exactly the same signature in the detector. With only kinematic constraints events coming from this background reaction may remain in the D meson mass region.

6.3 Reconstruction of Signal Events

The reconstruction of the $D\overline{D}$ channels is characterized by the delayed weak decay of the D mesons. Therefore, in the analysis the decay position of the D meson has to be found by combining stable tracks to a common vertex. Both D candidates are reconstructed separately and are combined and fitted again to a common vertex position. This position marks the primary interaction point. The displacement of both reconstructed vertices can be used for background suppression. As discussed in the previous section the charmed signal is several orders of magnitude smaller compared to other hadronic background channels. In this analysis the limiting factors are the resolution of the tracking system and the extension of the primary interaction zone. In these simulations an extended beam-target interaction region has been used, since it defines a worst-case scenario for the the $D\overline{D}$ benchmark channel analysis, which focus on the tracking abilities of the $\overline{\text{P}}$ANDA setup. If the target zone diameter would be known to less than 100 μm, the suppression of background events can be assumed to be much stronger and the displacement of the D meson decay position from the beam-target spot would allow a much better separation of background events.

6.3.1 The Signal Channel $\bar{p}p \rightarrow D^+D^-$

The channel $\bar{p}p \rightarrow D^+D^-$ has been defined to be investigated at the mass of the $\psi(3770)$ charmonium state, which is approximately 40 MeV/c^2 above the D^+D^- threshold. This corresponds to a beam momentum of $p_{beam} = 6.57$ GeV/c. Since the excess energy for the production of the D^+D^- pair is small, both $D^{\pm}$ mesons will most likely carry half of the beam momentum and remain at small angles close to the beam pipe. The reconstruction of this channel relies on the ability to reconstruct all three decay particles from the prominent $D^{\pm} \rightarrow K^{\mp}\pi^{\pm}\pi^{\pm}$.

Since the momentum transfer to the $D^{\pm}$ mesons is rather large, the resolution of the primary vertex position along the z axis is expected to be worse, compared to the transverse component. Both charmed mesons are bound to small opening angles close to the beam pipe. Therefore the opening angle between the trajectories is small, which is shown in Figure 6.3, where the distribution of the $D^{\pm}$ meson opening angle is given. The resolution of both vertex positions, the uncertainty of the production vertex and the decay position of the $D^{\pm}$ mesons, are given in Figure 6.4. The upper row shows the difference of the reconstructed primary interaction point compared to its simulated value. All three spatial coordinates are given separately. The identification of the interaction point in the transverse plane can be achieved with an uncertainty of $\sigma_{x,y} \approx 30$ μm, whereas the definition of the z coordinate, the position in beam direction, is rather poor and the uncertainty cannot be obtained to better than $\sigma_z \approx 500$ μm. Table 6.4 gives an overview of the resolution of the primary and secondary vertex (note the different scale on the x-coordinate for the z

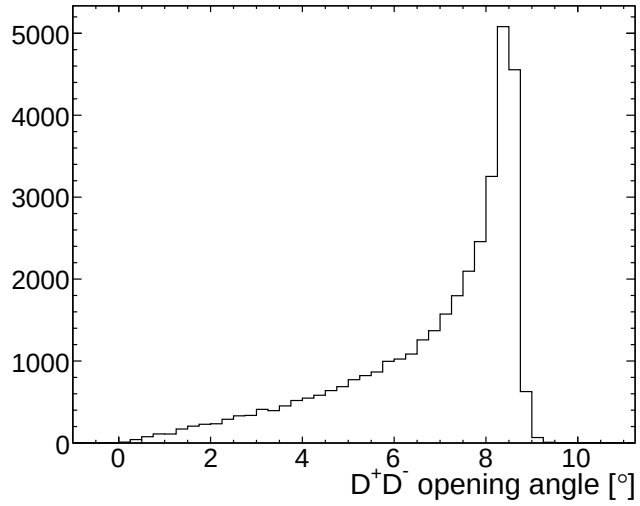

Figure 6.3: Opening angle in the laboratory frame between the reconstructed D meson candidates.

component of the vertex positions).

The D^+D^- channels has been investigated at a beam energy corresponding to the $\psi(3770)$ resonance position. This is about 40 MeV/c^2 above the D^+D^- threshold. At higher beam momenta the transverse momentum of the $D^\pm$ mesons becomes larger and the opening angle between the two charmed mesons increases. The accuracy to reconstruct the z-component of the production vertex increases, as can be seen in Table 6.4. The reconstruction has been done at higher incident beam energies at $p_{beam} = 7.5$ GeV/c and $p_{beam} = 8.5$ GeV/c, respectively. The opening angle between the two D mesons becomes larger, which is advantageous to reconstruct the production vertex along the beam axis. Going to higher initial beam momenta means to go to higher excess energies. This shall illustrate, that the definition of the primary

momentum	vertex resolution [μm]					
GeV/c	primary			secondary		
	$\sigma_{prim,x}$	$\sigma_{prim,y}$	$\sigma_{prim,z}$	$\sigma_{sec,x}$	$\sigma_{sec,y}$	$\sigma_{sec,z}$
6.57	30.7	30.7	493.6	35.4	35.2	77.1
7.50	30.4	30.3	208.5	37.1	36.4	84.0
8.50	30.0	29.0	157.4	36.7	36.2	92.4

Table 6.4: Production and decay vertex resolution for $D^\pm$ mesons. Due to kinematic restrictions the resolution in z direction improves with higher beam momenta.

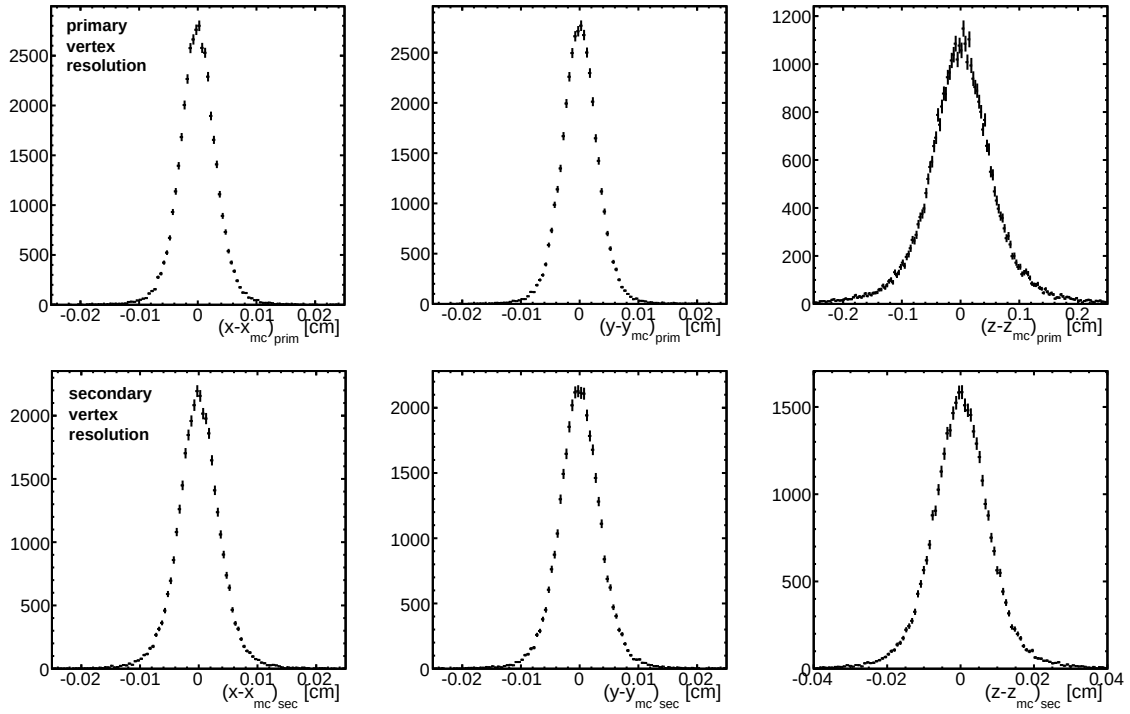

Figure 6.4: Deviation of the reconstructed vertex position from the generated value. The upper row shows the deviation of the primary vertex position, whereas the lower row shows the secondary vertex resolution (note the different scale in the z coordinate).

vertex position strongly depends on the reaction kinematics. The resolution of the $D^{\pm}$ decay vertex is much better and is additionally given in Table 6.4. In the plane transverse to the beam the resolution is comparable to the resolution of the impact parameter and in the order of $\sigma_{x,y}(sec) \approx 35$ μm.

As discussed in Section 5.1.1 in the simulation an extended target zone was defined. Unlike the pellet target scenario, where the definition of the z coordinate of the interaction point is basically defined by the size of the pellet, the cluster jet target produces a much larger extended interaction zone. In case of the pellet target the size of the frozen droplets will be around 50 μm [119]. The beam spot at the target position is usually larger and the uncertainty of the primary interaction point is then limited by the ability to calibrate the position of the pellets with respect to the $\overline{\mathsf{P}}$ANDA coordinate system. In case of the cluster jet target the interaction zone is defined by the size of the beam and the profile of the much more extended gas jet crossing the beam. The profile can be up to a few millimeter broad, since a distance of about 1.5 m has to be covered. Since the target type for the use in $\overline{\mathsf{P}}$ANDA is not defined up to now, an extended target zone has been defined with an Gaussian

width of $\sigma_i = 1.6$ mm (see Section 5.1.1 for details). In the transverse plane this is more extended than the expected width of the beam profile at the target position. The defined interaction zone in the simulations models more likely the extended cluster jet target option. The precision of the vertex position measurement then only depends on the track reconstruction alone. The decay position of the $D^{\pm}$ mesons can be reconstructed with an uncertainty of $\sigma_{x,y} \approx 35$ μm in the transverse plane at the decay vertex position and about a factor of two worse in the beam direction, $\sigma_z \approx 80$ μm.

Before the vertex fit is applied a loose mass window is set for the $D^{\pm}$ meson candidates. The defined mass region ranges from $m_{D^{\pm}} = 1.5$ GeV/c^2 to $m_{D^{\pm}} = 2.1$ GeV/c^2. The corresponding $K\pi\pi$ invariant mass distribution, obtained after the decay vertex is found, is shown in Figure 6.5. The blue distribution reflects the mass resolution without kinematic fit, whereas the narrow mass distribution shows the improvement with kinematic fit. The improvement is in the order of 50 %. The invariant mass distribution can be well described by two Gaussian components with the individual widths of $\sigma_1 = 11.2$ GeV/c^2 and $\sigma_2 = 7.4$ GeV/c^2.

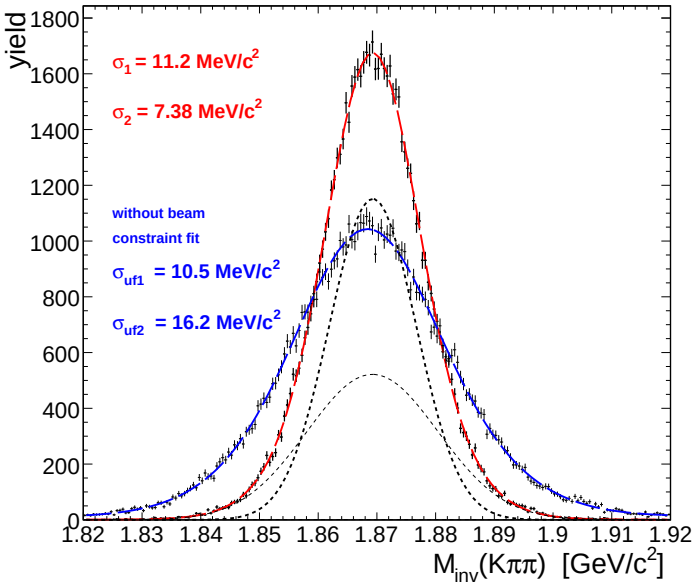

Figure 6.5: Invariant mass distribution of the $D^{\pm}$ candidates. The broader histogram described by the blue fit curve shows the mass distribution without 4C-fit, compared to the narrow distribution, followed by the red curve with additional kinematic fit.

To reconstruct the $D^{\pm}$ candidates no further restriction has been made on the in-

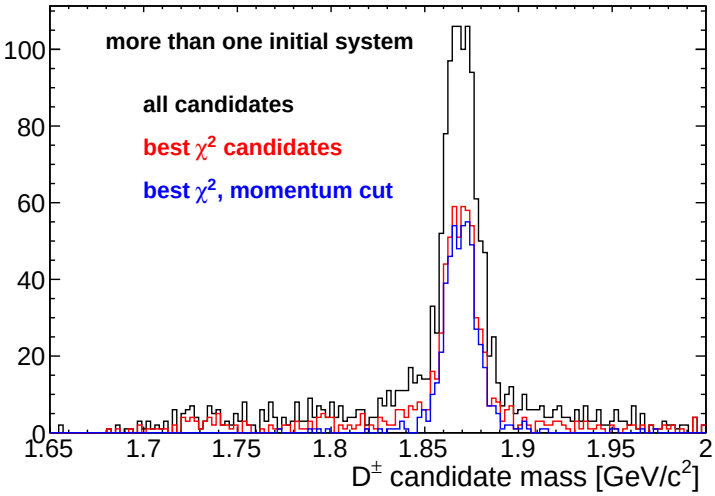

Figure 6.6: $D^{\pm}$ candidate invariant mass if more than two candidates are found. The best candidate is selected according to its confidence level and χ^2 value (blue histogram).

formation about the particle type. To obtain a clean sample without combinatorial combinations, the kinematic constraints on the beam four-momentum are already good enough to select the appropriate combination of $D^{\pm}$ candidates. In 392 out of 39890 reconstructed events, there are more candidates for the initial $\overline{\mathrm{p}}\mathrm{p}$ system found, which fit kinematical to the initial $\overline{\mathrm{p}}\mathrm{p}$ system. This corresponds to less than one percent of all reconstructed events and less than 0.4% of all generated events. The combinatorial background is caused by wrong combinations of the stable tracks to $D^{\pm}$ candidates. For those events having more $D^{\pm}$ candidates left after all selections, the invariant mass distribution is shown in Figure 6.6. The black histogram shows combinations for $D^{\pm}$ candidates, whereas the red distribution shows the candidates coming from the initial system with the best χ^2 from the primary vertex fit. Furthermore, candidates have been rejected which are not within an elliptical area, defined by the kinematical allowed region for the real $D^{\pm}$ candidates. This region is shown in Figure 6.7 together with the topological cut in the plane defined by the longitudinal and transverse components of the $D^{\pm}$ candidates. This restriction on the momentum rejects nearly all candidates which do not have a mass between 1.83 GeV/c^2 and 1.92 GeV/c^2. The remaining events are additional shown in Figure 6.6 as blue histogram.

For this signal channel $1 \cdot 10^5$ events have been simulated and 39890 events survive the selection criteria described above. The efficiency of the signal selection using the four-constraint kinematic fit is $\epsilon = 39.9\%$

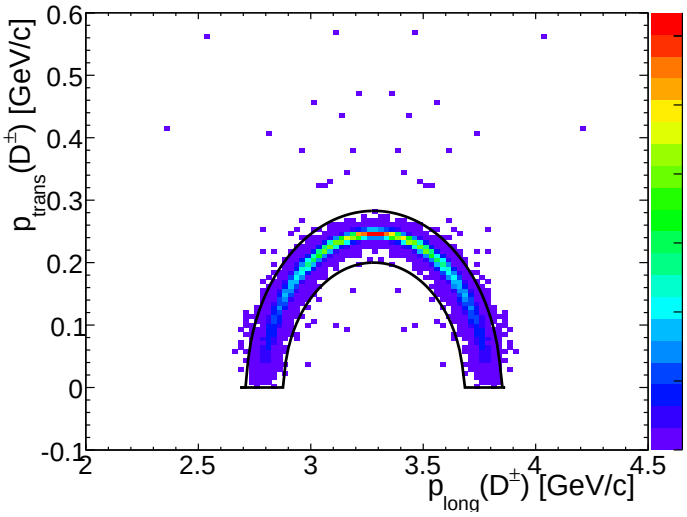

Figure 6.7: Longitudinal vs. transverse momentum distribution of the reconstructed $D^{\pm}$ mesons. Since the excess energy for the channel $\bar{p}p \to D^{+}D^{-}$ is small, the transverse momentum component is small compared to the longitudinal component. This reflects the large beam boost to the $D^{\pm}$ mesons.

6.3.2 The Signal Channel $\bar{p}p \to D^{*+}D^{*-}$

For the second $D\overline{D}$ channel, there are more kinematic constraints due to the subsequent D meson decays. The D^{*+} decays into $D^{0}\pi^{+}$ and the neutral D meson into a charged $K\pi$ pair, as defined in Section 6.2 for this channel. The signature in the detector will be similar for this analysis compared to the $D^{+}D^{-}$ channel discussed in the previous paragraph (Section 6.3.1). For the defined decay channels there are six charged tracks in the detector, in particular two kaons and four pions. The phase space for the reconstructed charged tracks in the final state is shown in Figure 6.8. The daughter tracks from the D^{0} decay will traverse the detector to higher angles. The pions can have polar angles of $\theta_{max} = 150°$, whereas the heavier kaons are confined to the forward direction with a maximum angle of $\theta_{max} = 80°$. This shows again, that a good coverage of the solid angle is important, in particular of the inner tracking detector, the MVD. A good vertex reconstruction is only possible if even low momentum particles at large angles in the backward hemisphere can be measured close to the interaction point.

Due to the two-body decay of the $D^{*\pm}$ and the large mass difference between the decay products, the heavier D^{0} carries most of the $D^{*\pm}$ boost. The pion from this decay is low in momentum and its momentum distribution is visible in Figure 6.8 as spot in the lower picture.

The trajectory gets reconstructed mainly by the forward part of the MVD. This

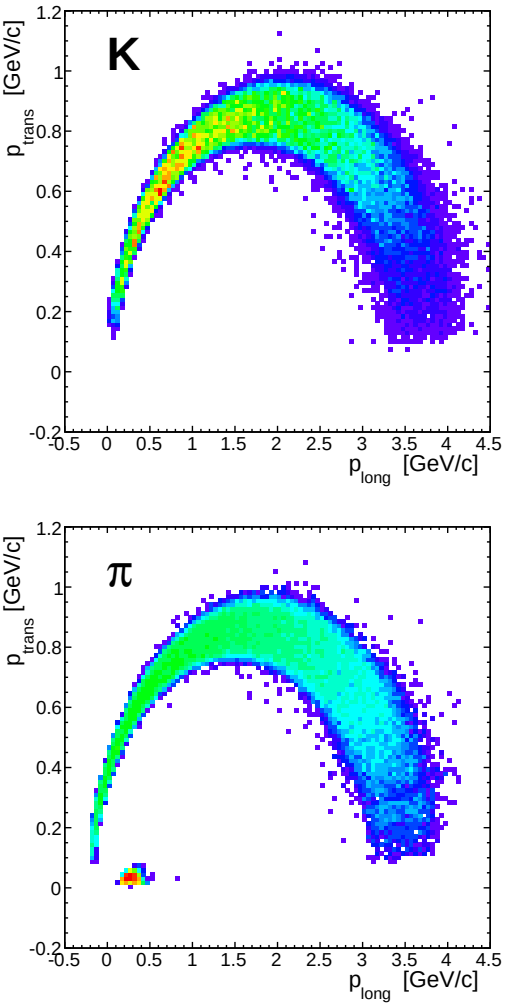

Figure 6.8: Available phase space of stable tracks from the subsequent D meson decays. The upper frame shows the kaons from the D^0 decay, whereas the lower frame shows the pions from the $D_s^{\pm}$ decay (low momentum spot) together with the relatively high momentum pion (band) from the D^0 decay. Both components are well separated.

low-momentum pion is difficult to reconstruct, since it has a very small phase space limited by the mass difference of the $D^{*\pm}$ decaying into $D^0\pi$. The blue histogram in Figure 6.9 shows the Monte Carlo truth information and the black histogram the reconstructed momentum of the $\pi^{\pm}$. Both histograms are in good agreement. A slight shift to smaller values can be seen between the reconstructed pion momentum and its corresponding generated value. The systematic shift towards smaller values for the slow pion momentum is below one percent. The right hand side of Figure 6.9 shows the error of the momentum reconstruction for the slow pion, which is approximately $\Delta p = 3.5\%$. The gray shaded histogram on the left-hand side shows the momentum distribution at event generator level. This illustrates the good coverage of the tracking system and in particular of the MVD, which is most important to measure the slow pion contribution.

The D^0 is found by combining a kaon and a pion track to a common vertex.

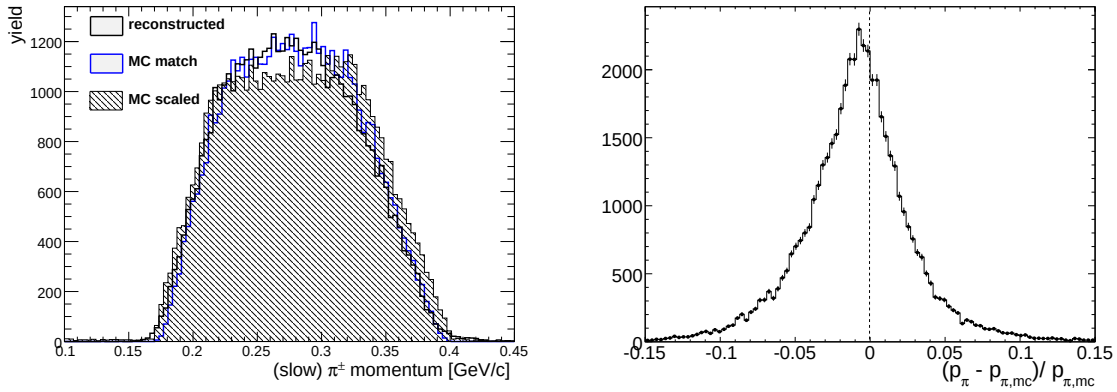

Figure 6.9: Momentum distribution of the pion from the $D^{*\pm}$ decay (left, black histogram). The blue curve shows the corresponding distribution for the Monte Carlo value of the pion momentum, the shaded histogram the momentum distribution on event generator level. The picture to the right shows the error of the reconstructed low-momentum pions.

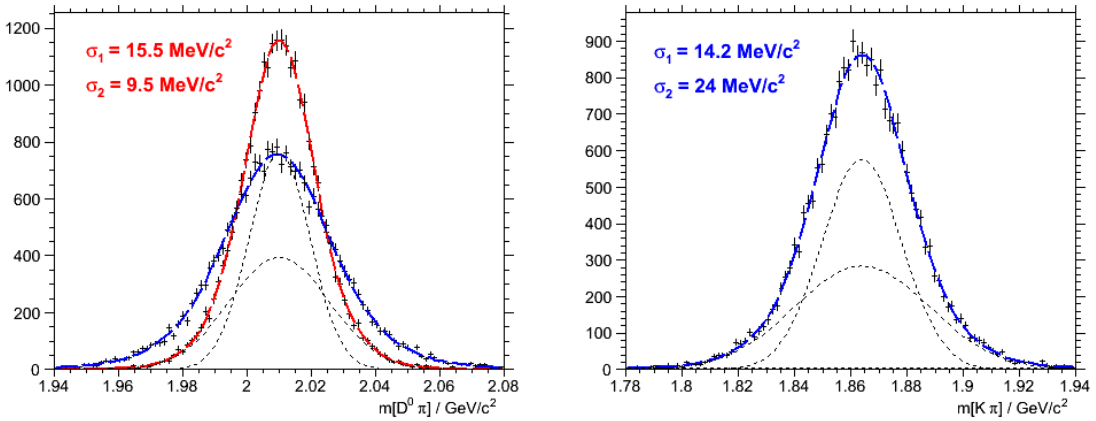

Figure 6.10: Invariant mass distribution of the D^0 candidate (left) and the invariant mass of the D^* candidate (right) for a four-constraint kinematic fit.

By adding the low momentum pion, the corresponding $D^{*\pm}$ candidate is fitted to a common vertex. The corresponding invariant masses of the D mesons are shown in Figure 6.10. The whole decay tree has to meet the four-momentum of the initial $\overline{\mathrm{p}}\mathrm{p}$ system. The left panel of Figure 6.10 shows the $D^{*\pm}$ invariant mass, whereas the right panel shows the D^0 invariant mass. In addition to the resulting $D^{*\pm}$ mass resolution the distribution obtained without the kinematic constraint on the initial

beam momentum is shown in comparison (blue curve). The improvement in mass resolution is approximately 50%. The mass distribution can be well described in a combined fit with two Gaussian components with the individual widths of $\sigma_{D^*,1} = 9.50$ MeV/c^2 and $\sigma_{D^*,2} = 15.5$ MeV/c^2. Both contributions are additionally shown as dashed curves.

The whole decay tree is reconstructed by its subsequent $D^{*\pm}$ decays. In the $D^{*\pm}$ reconstruction the previously found D^0 candidate can be set to its known PDG[2] mass value, instead of using the reconstructed value. This introduces an additional constraint on the $D^{*\pm}$ candidates. Its mass is set to the value of $m(D^0) = 1.8645$ GeV/c^2. By using this five-constraint kinematic fit the invariant mass distribution improves strongly as shown in Figure 6.11.

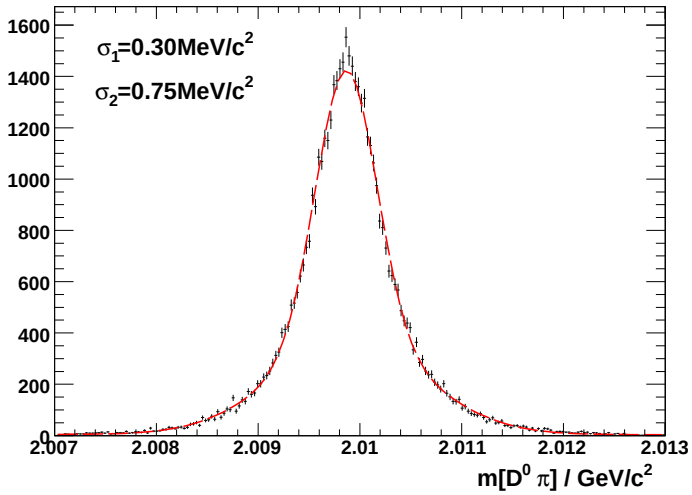

Figure 6.11: Invariant mass distribution after applying the additional D^0 mass constraint in the kinematic fit.

The overall efficiency for the whole tree does only get slightly reduced from $\epsilon_{signal,4C} = 27.4\%$ to $\epsilon_{signal,5C} = 24.0\%$ The improvement of the mass resolution is given in Figure 6.11, where its width is well below $\sigma_{D^*} < 1$ MeV/c^2.

[2]Particle Data Group, see ref. [15] for details. The simulations used the values from the particle listings of the year 2006. Currently an improved value for the D^0 mass is given by the PDG group: $m(D^0) = 1864.84 \pm 0.17$ MeV/c^2 [15].

6.4 Suppression of Hadronic Backgrounds

6.4.1 Simulation Demands

As explained in Section 6.2.1 the assumption was made that the physics signal will be hidden under a huge hadronic background and the suppression factor of the physics signal compared to the total $\overline{\text{p}}$p cross section is in the order of 10^{10}. The previous section has shown the good performance of the proposed $\overline{\text{P}}$ANDA detector setup, and in particular of the inner tracking detector. In the $\overline{\text{P}}$ANDA spectrometer the interaction rate will be large, around $1\text{–}2 \cdot 10^7$ interactions per second, depending on the used luminosity mode. To reconstruct the $D\overline{D}$ channels by their charged tracks, a large suppression factor of several 10^7 is needed to suppress the large hadronic background. In the following paragraphs the ability to suppress different reaction channels, relevant for the analysis of the investigated $D\overline{D}$ channels, will be examined.

As explained in Section 6.2.2, the investigation of major background components for the analysis presented here follows a two-step approach. Since it was technically not possible to reach the amount of background events by using the full DPM [96] model, which describes the $\overline{\text{p}}$p annihilation process reasonably well, only part of the general $\overline{\text{p}}$p background was generated. To test the analysis 83×10^7 DPM events have been simulated, omitting the elastic scattering.

In a second step selected hadronic channels have been simulated, which were already discussed in Section 6.2.2. Table 6.5 lists all channels and the corresponding simulation demands.

channel	D^+D^-	$D^{*+}D^{*-}$
	number of events $[\times 10^6]$	
DPM	83	-
$3\pi^+3\pi^-\pi^0$	50	43
$3\pi^+3\pi^-$	10	14
$2K^\mp 4\pi^\pm$	1	10

Table 6.5: Simulated events for selected background channels in millions.

For the second benchmark channel $\bar{p}p \to D^{*+}D^{*-}$ the expected cross section is a factor of 3 smaller. In this specific analysis, which considers only the charged decay channels given in Table 6.2, this results in a relative suppression factor of 40 compared to the D^+D^- channel (see section Section 6.2.1 for details). To estimate the signal to noise ratio for this channel and to reach the expected signal cross section, the events for the considered background channels have been produced by

using a prefilter before pass on the background events to the transport code, which simulates the full detector. The filter calculates the invariant mass for the D meson candidate and sets its mass to a loose window from 1.7–2.1 GeV/c^2 for the D^0 and 1.7–2.3 GeV/c^2 for the D^* candidate. These mass windows are exactly the same as in the event analysis. The borders of the mass windows have been tested and do not appear to be very restrictive. More limiting is the request for finding a D^* candidate consisting of a previously selected D^0 and a pion candidate which accounts for the good preselection of the filter. This gives an reduction factor of six. Table 6.5 lists the number of simulated events for the $\overline{\mathrm{p}}\mathrm{p} \to D^{*+}D^{*-}$ channel by using this preselection.

6.4.2 Background Analysis for the $\overline{p}p \to D^+D^-$ Channel

6.4.2.1 The $\overline{p}p \to K^+K^-2\pi^+2\pi^-$ Background Channel

A major contribution to the background of the $D\overline{D}$ channels may come from the non-resonant channel $\overline{p}p \to K^+K^-2\pi^+2\pi^-$, which has exactly the same signature in the detector as the charmed $D\overline{D}$ channels. To show the sufficient suppression of this channel, the non-resonant production of $2K^{\mp}4\pi^{\pm}$ has been analyzed, which has a 10^6 higher branching than the $D\overline{D}$ production at threshold. An additional cut on the kaon probability will not help to reduce the amount of background. Applying the kinematic cuts, such as the loose mass window before vertex fitting and especially the restriction on the momentum of the D meson candidates, will select those background events, which have similar kinematics compared to real $D\overline{D}$ events. However, since events from the charmed physics channels are characterized by a delayed decay, this information can be used to suppress the non-resonant $K^+K^-2\pi^+2\pi^-$ channel, where all particles originate in the primary interaction point.

Figure 6.12 shows the the longitudinal vs. the transverse momentum component of the $D^{\pm}$ meson candidates for signal (left side) and background events (right side). All kinematic constraints have been applied. Although the four-constraint kinematic fit was demanded, in total 19785 of the produced 10^6 events survived the selection criteria and remain in the $D^{\pm}$ mass region. Constraining the momentum via an elliptical cut in the two dimensional plane gives an additional reduction factor $\epsilon(mom, D^{\pm})$ of:

$$\epsilon(mom, D^{\pm}) = \frac{767}{19785} = 25.8 \tag{6.10}$$

This cut has been tested for different variations of used cuts, e.g. the cut on the $D^{\pm}$ vertex probability, and its suppression factor appears to be rather stable around $\epsilon(mom, D^{\pm}) = 26$.

Selection cuts in the phase space distribution of the background events are always dangerous, since this kind of selection enhances background in the expected signal

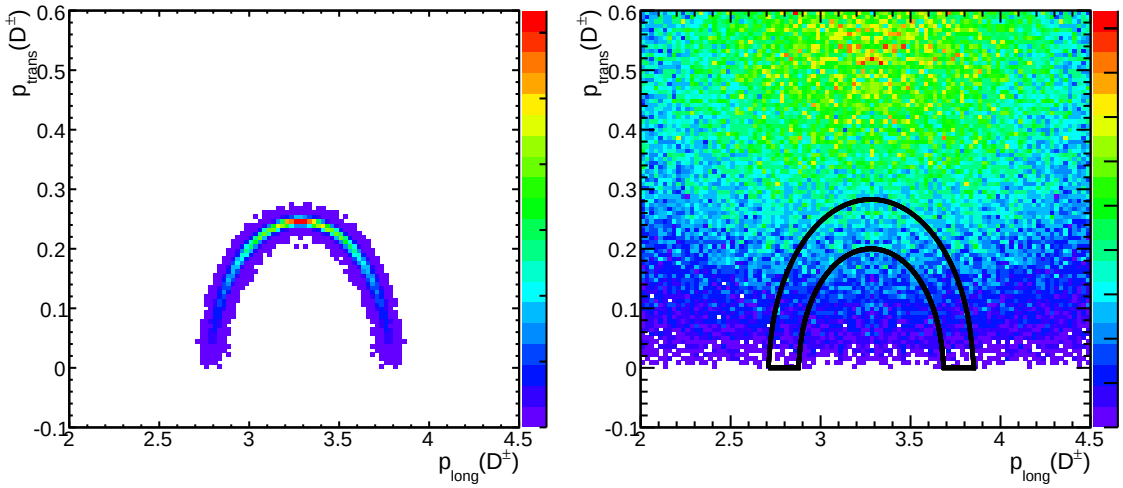

Figure 6.12: Momentum components of $D^{\pm}$ candidates for signal events (left panel) and for non-resonant $K^+K^-2\pi^+2\pi^-$ background (right panel). The surrounded region shows the restriction applied to the $D^{\pm}$ candidate momentum.

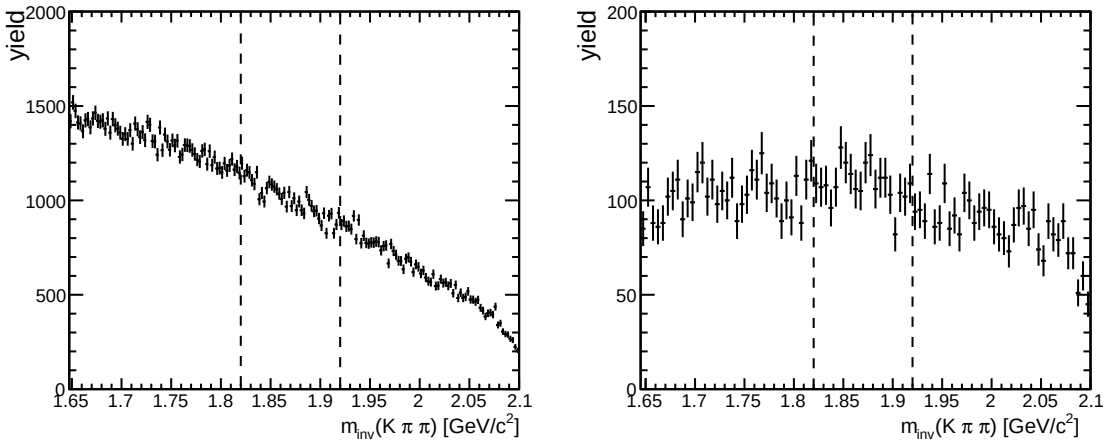

Figure 6.13: Invariant mass distribution for $D^{\pm}$ candidates from the background channel $\overline{\mathrm{p}}\mathrm{p} \rightarrow K^+K^-2\pi^+2\pi^-$ without kinematic fit (left) and with kinematic fit to the beam four-momentum (right). The signal region is indicated by the dashed lines.

region. The distribution of the momentum for reconstructed $D^{\pm}$ candidates from background events shows a major fraction with too large transverse momentum. A momentum reconstructed too large for the $D^{\pm}$ candidate is equivalent to a corre-

sponding invariant mass which is too small, due to energy conservation. Figure 6.13 shows the invariant mass distribution of the $K\pi\pi$ system, which corresponds to a $D^{\pm}$ candidate. The left part shows the remaining background of the $K^+K^-2\pi^+2\pi^-$ channel after vertex finding and kinematic fit, whereas the right side shows the reduction of the background with the restricted $D^{\pm}$ candidate momentum, indicated in Figure 6.12. The background remains flat in the signal region, indicated by the vertical lines. The shape of the distribution changes, since entries with too small invariant masses are suppressed by the limitation of the momentum of the $D^{\pm}$ candidate. The remaining background of 767 events in the $D^{\pm}$ mass signal region will behave kinematical similarly to signal events and cannot be separated further by kinematic constraints. A significant background contribution remains in the mass region of the $D^{\pm}$ signal.

Background will be produced promptly at the interaction point and can be in principle separated by finding the $D^{\pm}$ decay vertices located outside the interaction region. Since the boost at threshold will be large and will be distributed among the stable particles in the outgoing channel, the vertex resolution along the beam axis will be limited as discussed in Section 6.3.1. Since for this analysis an extended primary interaction zone was assumed, the decay vertex of the $D^{\pm}$ candidate is usually found within the primary interaction region. Thus, the uncertainty of the primary vertex in beam direction close to the $D\overline{D}$ threshold is large, which enlarges the probability to misidentify background events.

The reconstruction of the $D^{\pm}$ decay vertex has a resolution of $\sigma_{x,y} \approx 35$ μm in the transverse and of $\sigma_z \approx 75$ μm in beam direction (according to Table 6.4), whereas the longitudinal component of the primary interaction point can be reconstructed with a resolution around $\sigma_{prim,z} \approx 500$ μm. The D^+D^- channel was studied close to threshold and both $D^{\pm}$ mesons are confined to a narrow forward cone by kinematic limits. The small opening angle between the mesons limits the resolution in beam direction. However, only the good secondary vertex resolution can be used to calculate the distance Δz between the decay vertices of both $D^{\pm}$ mesons. The projection on the difference vector to the beam axis is shown in Figure 6.14. In addition to the distribution of signal events (black histogram) the distribution for the remaining background events is shown (blue histogram). Applying a cut on Δz rejects the remaining background events. Due to the delayed decays of the $D^{\pm}$ the slope of the Δz distribution is less steep compared to background events. Table 6.6 lists for different cut values the remaining background events in the signal region and the signal efficiency.

The simulations are demanding for the $D\overline{D}$ channels and the amount of simulated background events was chosen in a way to meet the level of signal generation with a relative branching ratio of 10^6 with the estimated signal cross sections discussed in Section 6.2. If the analysis is able to reject all background events this would result in a signal to background ratio of 1:1, if the signal efficiency is 100 %. Another factor of 10^5 background events was out of scope within this analysis and a growth in

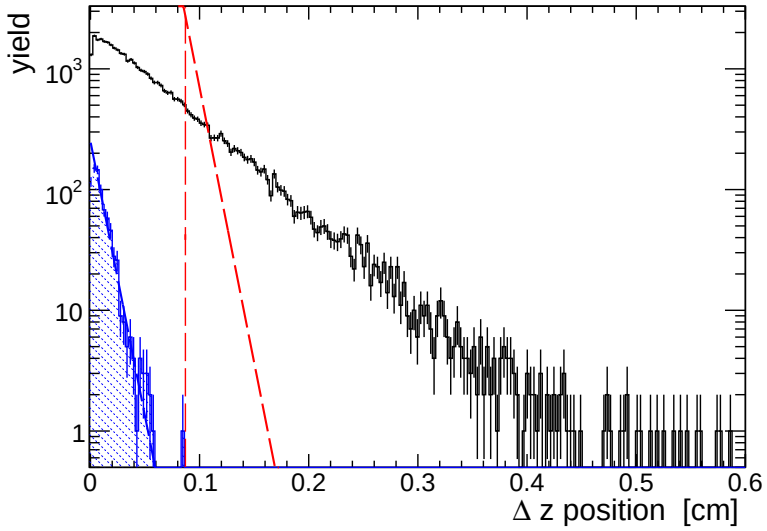

Figure 6.14: Distribution of the difference of the reconstructed $D^{\pm}$ meson decay vertices Δz in beam direction (black) and remaining background events (blue). The dashed red curve symbolizes the expected scaled background and the vertical dashed line the cut value to get a signal to background ratio of about one (see text for details).

Δz cut [cm]	background events 10^6	D^+D^- events 10^5	D^+D^- efficiency ϵ [%]
0.0	1534	72152	36.1
0.01	595	61534	30.8
0.02	185	51681	25.8
0.04	30	36171	18.1
0.06	2	25258	12.6
0.088	-	15116	7.6
0.175	-	3152	1.6

Table 6.6: Progression of signal and background efficiency with respect to the vertex cut.

background events was estimated by scaling the background distribution to a higher level.

To estimate the suppression of signal events in order to get an estimate on the cut level for Δz the shape of the remaining background distribution has been determined and scaled by a factor 10^5. The shape of the background distribution can be assumed

to be the same like the blue shaded region since only vertex constraints would change the slope of the distribution. The vertical dashed red line in Figure 6.14 symbolizes the cut level needed to get a signal to noise ratio of one. In this case the integral for both distributions is equal. To obtain a really background free sample a cut of $\Delta z = 0.175$ cm has to be applied. The remaining signal efficiency will then be in the order of $\epsilon_{signal}(D^+D^-) = 1.6\%$.

6.4.2.2 Multi-Pion Background Channels

The signal is analyzed by reconstructing the charged decays of the D mesons and therefore background channels with multiple charged tracks can sometimes overcome the restrictions made by the analysis. Channels containing six charged pions in the final state, such as $3\pi^+3\pi^-(\pi^0)$, have been investigated for which two pions can be misidentified as kaons. The relative branching of charged multi-pion channels is still high enough to fake a physics signal.

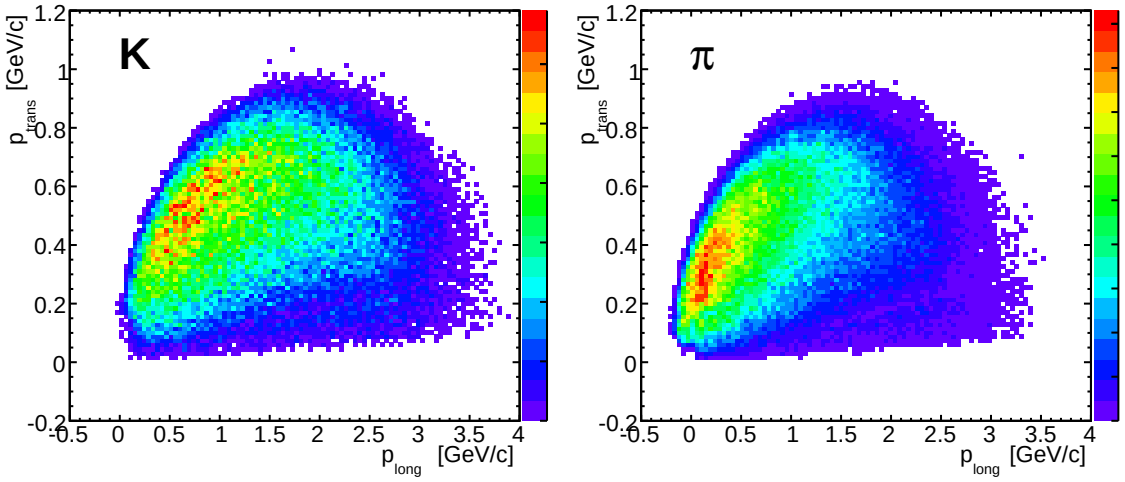

Figure 6.15: Momentum components of the stable tracks from the $D^{\pm}$ decay (kaons left, pions to the right).

If kinematic restrictions to the final state are not strong enough to reject background from these channels, the particle identification must be able to clearly distinguish between kaons and pions over a wide momentum range while retaining as much as possible of the signal events. Especially in the low momentum range a good PID to classify pions and kaons is needed. To illustrate this requirement, Figure 6.15 shows the available phase space of the $D^{\pm}$ decay products from signal events of the reaction channel $\overline{p}p \to D^+D^-$. A major component of the stable particles traverses

the solenoid part of the $\overline{\text{P}}$ANDA spectrometer with low momenta. Important for a good kaon/pion separation at low energies are the dE/dx informations from the tracking detectors. In Section 4.4 the contribution of the PID information obtained with the MVD was discussed. In general, the tracking system of the target spectrometer provides a good combined energy loss signal which can contribute to the global PID reconstruction[3]. This is essential, since the central Cherenkov detector (DIRC) is only sensitive to particles with momenta larger than $p \geq 800$ MeV/c.

$3\pi^+3\pi^-$ background channel The cross section for the reaction $\overline{\text{p}}\text{p} \rightarrow 3\pi^+3\pi^-$ is a factor of ten larger compared to the $K^+K^-2\pi^+2\pi^-$ channel and the relative suppression ratio to the D^+D^- channel is still a factor of 10^7. Thus, an amount of $10 \cdot 10^6$ background events has been studied to estimate the expected signal to background ratio for this channel.

Using the selection cuts explained in Section 6.3.1, no event survived the analysis and was misidentified as a D^+D^- event. This would correspond to an efficiency of spuriously finding a D^+D^- event of:

$$\epsilon_{3\pi^+3\pi^-} \leq 1 \cdot 10^{-7} \tag{6.11}$$

An estimate of the signal to background level would than yield to:

$$\begin{aligned} \frac{S}{B} &\geq \frac{\sigma(\overline{p}p \rightarrow D^+D^-) \times BR}{\sigma(\overline{p}p \rightarrow 3\pi^+3\pi^-)} \cdot \frac{\epsilon_{D^+D^-}}{\epsilon_{3\pi^+3\pi^-}} \\ &\geq \frac{2.82nb \cdot (0.092)^2}{0.32mb} \times \frac{0.399}{1 \cdot 10^{-7}} > 0.29 \end{aligned} \tag{6.12}$$

This null-result is only an approximate value. To investigate the influence of the various cuts, which are necessary to reject unphysical background, some cuts have been relaxed and the influence of individual cuts have been studied. Omitting the restriction on the momentum of the $D^\pm$ candidate for background events, in total 14 events are found by the analysis. These events have a larger transverse momentum of $p_{trans}(D^\pm) > 0.3$ GeV/c and have invariant masses for the $D^\pm$ candidates lower than the real $D^\pm$ mass. Since this number is not significant enough, because all those events are usually rejected by the analysis, the influence of the restriction on the momentum of the $D^\pm$ candidate was estimated by analyzing the background without the kinematic fit, which constraints on the beam four-momentum. Without kinematic fit and no restriction on the $D^\pm$ momentum, 26835 events pass the analysis and only 210 are within the allowed momentum window for the $D^\pm$ candidates. This gives an suppression factor of

$$\epsilon_{D^\pm_{mom}} = \frac{210}{26835} \approx 7.8 \cdot 10^{-3} \tag{6.13}$$

[3]Global PID reconstruction refers to the combination of information from different subsystems of the detector setup. Probabilities from all PID sub-system are combined for all possible hypotheses. For the MVD contribution see Section 4.4.

In a similar way the influence of the kinematic fit has been determined to

$$\epsilon_{4C} = \approx 2.6 \cdot 10^{-4} \tag{6.14}$$

Without both cuts the analysis requires only two reconstructed vertices and a converging vertex fit for the initial system. The probability for the fit has to be larger than $p(\chi^2) > 0.01$. This results in an efficiency of wrongly identified background as signal events of:

$$\epsilon_{vertex} = \approx 5.4 \cdot 10^{-3} \tag{6.15}$$

Altogether this yield an efficiency for the $3\pi^+3\pi^-$ channel of

$$\epsilon_{3\pi^+3\pi^-} = \epsilon_{vertex} \cdot \epsilon_{4C} \cdot \epsilon_{D^{\pm}_{mom}} \approx 1.1 \cdot 10^{-8} \tag{6.16}$$

which is sufficient in order to clearly identify the D^+D^- signal. This results in a signal to background ratio of better than:

$$\begin{aligned} \frac{S}{B} &= \frac{\sigma(\overline{p}p \to D^+D^-) \times BR}{\sigma(\overline{p}p \to 3\pi^+3\pi^-)} \cdot \frac{\epsilon_{D^+D^-}}{\epsilon_{3\pi^+3\pi^-}} \\ &= \frac{2.82nb \cdot (0.092)^2}{0.32mb} \times \frac{0.399}{1.1 \cdot 10^{-8}} = 2.7 \end{aligned} \tag{6.17}$$

For this estimate no information from the particle identification has been used, which means that there was no discrimination between the kaon and pions from the $D^{\pm}$ decay. If a higher cut on the kaon probability[4] of 30% is used, the background events can be suppressed by an additional factor of ≈ 4. This requirement reduces the signal events by a factor of two, but further improves the signal to background ratio. Table 6.7 gives an overview of various cuts and their influence on the signal to background ratio.

$3\pi^+3\pi^-\pi^0$ background channel The reaction $\overline{\mathrm{p}}\mathrm{p} \to 3\pi^+3\pi^-\pi^0$ is still challenging for simulation, since the relative branching ratio compared to the assumed cross section for direct D^+D^- production is at least 1.6×10^{-8}, taking the charged decay branching of the $D^{\pm}$ into account. For this channel a total amount of $5 \cdot 10^7$ events has been investigated. Using the signal selection criteria described in Section 6.3.1

[4] If no restriction on the particle probability is imposed, all five different particle hypotheses (proton, kaon, pion, muon, electron) get the same probability of 20 %.

selection	efficiency			signal/background	
	D^+D^-	$3\pi^+3\pi^-$	$3\pi^+3\pi^-\pi^0$	$\frac{D^+D^-}{3\pi^+3\pi^-}$	$\frac{D^+D^-}{3\pi^+3\pi^-\pi^0}$
preselection	0.43	$5.4 \cdot 10^{-3}$	$9.6 \cdot 10^{-4}$	-	-
4C-fit	0.40	$1.4 \cdot 10^{-6}$	$4.2 \cdot 10^{-7}$	0.02	0.015
$D^\pm$ momentum	0.40	$< 1.1 \cdot 10^{-8}$	$< 3.6 \cdot 10^{-9}$	> 2.7	> 1.8
K LH > 0.3	0.23	$< 1.8 \cdot 10^{-9}$	$< 1.7 \cdot 10^{-9}$	> 9.5	> 2.2

Table 6.7: Expected signal to background ratios for pionic background channels.

no events pass this analysis. This corresponds to an efficiency to wrongly identify $3\pi^+3\pi^-\pi^0$ background as signal of better than:

$$\epsilon_{3\pi^+3\pi^-\pi^0} < (5 \cdot 10^7)^{-1} = 2 \cdot 10^{-8} \tag{6.18}$$

This results in a signal to background ratio according to equation 4.16 of better than:

$$\begin{aligned} \frac{S}{B} &\geq \frac{\sigma(\overline{p}p \to D^+D^-) \times BR}{\sigma(\overline{p}p \to 3\pi^+3\pi^-)} \cdot \frac{\epsilon_{D^+D^-}}{\epsilon_{3\pi^+3\pi^-\pi^0}} \\ &\geq \frac{2.82nb \cdot (0.092)^2}{1.5mb} \times \frac{0.399}{2 \cdot 10^{-8}} > 0.32 \end{aligned} \tag{6.19}$$

In a similar manner as for the $3\pi^+3\pi^-$ background channel the influence of the different cuts has been investigated. In general the kinematic suppression of this channel is better, since the additional neutral pion is not reconstructed and its energy is missing. Therefore the use of the kinematic fit gives an even better suppression for this channel. Finally the efficiency to misidentify a $3\pi^+3\pi^-$ background event as D^+D^- signal can be given to

$$\begin{aligned} \epsilon_{3\pi^+3\pi^-\pi^0} &= \epsilon_{vertex} \times \epsilon_{4C} \times \epsilon_{D^\pm_{mom}} \\ &= 0.96 \cdot 10^{-3} \times 4.4 \cdot 10^{-4} \times 8.5 \cdot 10^{-3} = 3.6 \cdot 10^{-9} \end{aligned} \tag{6.20}$$

This results in a signal to background ratio of approximately

$$\frac{S}{B} = \frac{\sigma(\overline{p}p \to D^+D^-) \times BR}{\sigma(\overline{p}p \to 3\pi^+3\pi^-)} \cdot \frac{\epsilon_{D^+D^-}}{\epsilon_{3\pi^+3\pi^-\pi^0}} = 1.8 \tag{6.21}$$

A summary of the influence of single cuts was already given in table 6.7 together with the channel $\overline{\mathrm{p}}\mathrm{p} \to 3\pi^+3\pi^-$ for comparison.

For both background channels, which contain only pions, no restriction on the $D^\pm$ vertex position was needed to enhance the signal against pionic background.

Although the channel $3\pi^+3\pi^-\pi^0$ is approximately a factor five more abundant compared to the $3\pi^+3\pi^-$ background channel, the reduction is of the same order of magnitude.

6.4.2.3 General DPM background

In order to understand the general features of the analysis the Dual Parton Model (DPM) was used to produce background coming from $\overline{\mathrm{p}}\mathrm{p}$ annihilations. Only inelastic collisions including multi-prong events have been simulated. Because of the small ratio between the $D\overline{D}$ cross section and the total $\overline{\mathrm{p}}\mathrm{p}$ cross section, a very large number of events needs to be generated. For this reason this general study was carried out only for the D^+D^- channel: $8.3{\cdot}10^7$ events were produced to test the analysis, *e.g.* for the acceptance of events containing charged track multiplicities equal or larger than six and to check for possible detector-related effects. Only 11 events pass the analysis for the D^+D^- channel, if no constraint on the decay vertex position of the two $D^{\pm}$ candidates is applied . These events contain two charged kaons and four pions in the event. Since the DPM model generates the reaction channel $\overline{\mathrm{p}}\mathrm{p} \to K^+K^-2\pi^+2\pi^-$ as a subset, the number of remaining events corresponds within the statistics with the suppression efficiency of the $K^+K^-2\pi^+2\pi^-$ background channel.

6.4.3 Background Analysis for the $\overline{p}p \to D^{*+}D^{*-}$ Channel

6.4.3.1 The Background Channel $\overline{p}p \to K^+K^-2\pi^+2\pi^-$

For the analysis of the $K^+K^-2\pi^+2\pi^-$ background to the $D^{*+}D^{*-}$ channel a total of 10^7 events has been studied. The events have been produced by using a prefilter on the event generator output, which selected only those events with two $D_s^{\pm}$ candidates in the event in a wide window of $\Delta m = 300$ MeV/c^2 around the mass of the $D_s^{\pm}$. Only 15 % of the generated events survived the preselection on the $K^+K^-2\pi^+2\pi^-$ background events, which amounts to an equivalent of $6.7 \cdot 10^7$ generated events.

In the analysis the subsequent D^0 meson decay can be used as an additional kinematic constraint. Using the selection cuts explained in section 6.3.2, all background events could be suppressed. All produced background events could be suppressed completely by the selection criteria of the analysis. The efficiency of the analysis to reject background event is better than:

$$\epsilon_{K^+K^-2\pi^+2\pi^-} = (6.7 \cdot 10^7)^{-1} = 1.5 \cdot 10^{-8} \tag{6.22}$$

The efficiency for $D^{*+}D^{*-}$ events is $\epsilon = 24.0\%$ and the signal to noise ratio $\frac{S}{N}$ for this background channel can be calculated to:

$$\begin{aligned} \frac{S}{N} &\geq \frac{\sigma(\overline{p}p \to D^{*+}D^{*-}) \times BR}{\sigma(\overline{p}p \to K^+K^-2\pi^+2\pi^-)} \cdot \frac{\epsilon_{D^{*+}D^{*-}}}{\epsilon_{K^+K^-2\pi^+2\pi^-}} \\ &\geq \frac{0.9nb \cdot (0.038)^2 \cdot (0.67)^2}{0.033mb} \times \frac{0.24}{1.5 \cdot 10^{-8}} = 1/3 \end{aligned} \tag{6.23}$$

The suppression of the $K^+K^-2\pi^+2\pi^-$ background channel is better than the envisaged 10^{-8} needed in order to reconstruct the physics channel. In the analysis no vertex restriction on the D^0 decay position was necessary to suppress the background. Figure 6.16 shows the distance of both D^0 decay vertices along the beam axis. The D^0 has a mean flight distance in the detector larger than the resolution of the decay vertex.

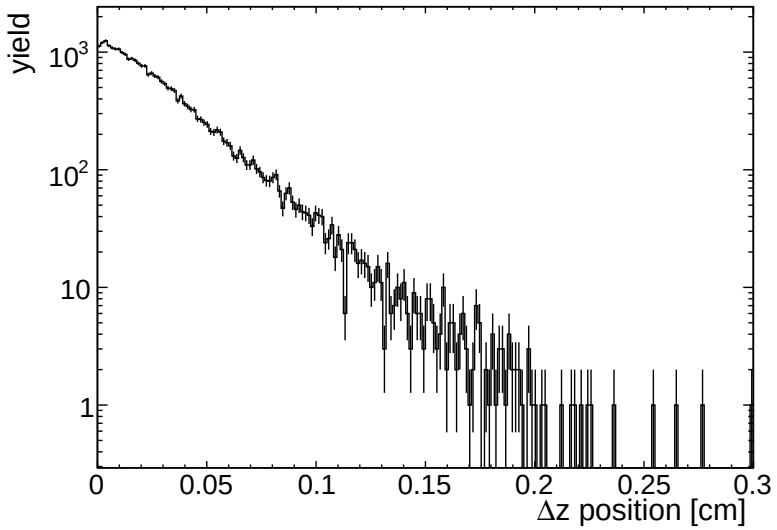

Figure 6.16: Distribution of the difference of the reconstructed D^0 meson decay vertices Δz in beam direction.

According to the analysis of this background channel for the D^+D^- signal, an additional suppression factor of 10 could be obtained by applying a cut on the difference of the D^0 decay vertices of $\Delta z = 200$ μm. This cut would reduce the signal efficiency from $\epsilon = 24.0\%$ to $\epsilon = 12.7\%$ and the signal to noise ratio $\frac{S}{N}$ can be estimated according to equation (6.23) to:

$$\frac{S}{N} = \frac{0.9nb \cdot (0.038)^2 \cdot (0.67)^2}{0.033mb} \times \frac{0.12}{1.5 \cdot 10^{-9}} = 1.4 \tag{6.24}$$

This ratio may be further improved by shifting the Δz cut to a larger value. This will, of course, reduce the $D^{*+}D^{*-}$ signal, but could eventually stronger reduce the background level. To prove this, much more data has to be simulated to study the slope of remaining background events.

6.4.3.2 The Background Channel $\overline{p}p \to 3\pi^+3\pi^-$

For this particular background channel $14{\cdot}10^6$ background events have been analyzed. This corresponds to a total amount of $93 \cdot 10^6$ events, since a prefilter was used to reject events with wrong kinematics (see Section 6.4.3.1 for details). No events pass the selection cuts and the efficiency to reduce this background is therefore larger than:

$$\epsilon_{3\pi^+3\pi^-} \leq 1.1 \cdot 10^{-8} \tag{6.25}$$

In order to estimate the influence of the kinematic fit, this background channel has been investigated without the five-constraint kinematic fit. This means, that the analysis makes use only of vertex fitting of the D^0 and D^* candidates and of loose mass windows of $\Delta m_{D^*} = \pm 200$ MeV/c^2 and $\Delta m_{D^*} = \pm 150$ MeV/c^2, respectively. Only few events pass the loose selection and the rejection efficiency drops to

$$\epsilon_{3\pi^+3\pi^-,loose} \approx 5.0 \cdot 10^{-7} \tag{6.26}$$

At this stage, the suppression of the $3\pi^+3\pi^-$ background channel for the $D^{*+}D^{*-}$ channel is already four orders of magnitude better than for the same background contribution to the D^+D^- signal (see Table 6.7). Assuming at least an additional suppression factor of 10^{-4} for the kinematic fit, an estimate on the expected signal to background ratio can be given to

$$\frac{S}{N} \geq \frac{0.9nb \cdot (0.038)^2 \cdot (0.67)^2}{0.32mb} \times \frac{0.27}{5.0 \cdot 10^{-11}} \geq 9.8 \tag{6.27}$$

The suppression of the $\pi^+3\pi^-$ background contribution is sufficient to reject this particular background channel. No additional PID information and no further constraint on the vertex position of the D^0 candidate is necessary. Table 6.8 gives an overview of the expected signal to background ratios for the pionic background channels to the $D^{*+}D^{*-}$ channel.

6.4.3.3 The Background Channel $\overline{p}p \to 3\pi^+3\pi^-\pi^0$

The contribution of the channel $\overline{p}p \to 3\pi^+3\pi^-\pi^0$ to the background of the signal channel $\overline{p}p \to D^{*+}D^{*-}$ is expected to be smaller compared to the $3\pi^+3\pi^-$ channel. As given in Section 6.4.3.2 the six-charged pionic channel can be suppressed sufficiently already with loose kinematic cuts. The reduction factor for the $3\pi^+3\pi^-\pi^0$ channel can be expected to be larger. The neutral pion is not considered by the analysis and its missing energy leads to a very good suppression by using a kinematic fit to the beam four-momentum.

selection	efficiency			signal/background	
	$D^{*+}D^{*-}$	$3\pi^+3\pi^-$	$3\pi^+3\pi^-\pi^0$	$\frac{D^{*+}D^{*-}}{3\pi^+3\pi^-}$	$\frac{D^{*+}D^{*-}}{3\pi^+3\pi^-\pi^0}$
preselection	0.27	$5.0 \cdot 10^{-7}$	$7.5 \cdot 10^{-8}$	-	-
5C-fit	0.24	$5.0 \cdot 10^{-11}$	$7.5 \cdot 10^{-12}$	> 8.8	12.4

Table 6.8: Expected signal to background ratios for multi-pion background to the $D^{*+}D^{*-}$ signal channel.

For this channel a total of $4.3 \cdot 10^7$ events have been investigated and not a single event passes the analysis. Again, a prefilter has been used to reduce simulation demands, which corresponds to $3.1 \cdot 10^8$ background events. If the background is analyzed without kinematic fit of the whole decay tree, a few background events pass the selection which leads to an efficiency of

$$\epsilon_{3\pi^+3\pi^-\pi^0,loose} \approx 7.5 \cdot 10^{-8} \tag{6.28}$$

The number of events is too small to estimate the influence of the kinematic fit to the background suppression. According to the analysis of the same background channel to the D^+D^- signal channel, at least an additional factor of 10^{-4} can be assumed. For the $D^{*+}D^{*-}$ channel the suppression due to the kinematic fit might be even stronger, since an additional constraint on the D^0 mass is made. Therefore, an efficiency for this channel to spuriously contribute to the signal can be given to be smaller than:

$$\epsilon_{3\pi^+3\pi^-\pi^0,5C-kin} \approx 7.5 \cdot 10^{-12} \tag{6.29}$$

This conservative estimate is sufficient to reject background from this contribution and a signal to background ration can be calculated to be larger than:

$$\frac{S}{N} \geq \frac{0.9nb \cdot (0.038)^2 \cdot (0.67)^2}{1.5mb} \times \frac{0.27}{7.5 \cdot 10^{-12}} \geq 14.0 \tag{6.30}$$

The expected signal to background ratio will be much higher, since no further constraints on the momentum of the $D^{*\pm}$ candidate and no vertex restrictions on the D^0 candidates are made. The obtained values for the efficiency of the analysis and the background ratio to the signal are compared to the $3\pi^+3\pi^-$ channel in Table 6.8.

6.5 Expected $D\overline{D}$ Data Rates

The analysis of the major background sources has shown the good suppression of multi-charged channels. Non-resonant channels containing strangeness in the final

state will be the strongest background contribution. Even under the conservative cross section estimate, given in Section 6.2.1, the extraction of the charmed physics signal from the huge hadronic background will be possible. Figure 6.17 shows the expected D^+D^- signal on the remaining background, which is dominated by the $K^-K^+2\pi^-2\pi^+$ channel, as discussed in Section 6.4.2.1. The background distribution was scaled by the use of the obtained suppression factors. The distribution corresponds roughly to one year of data taking. It is obvious that the proposed $\overline{\text{P}}$ANDA detector setup provides an excellent tracking system and a good particle identification system which reaches the needed suppression of hadronic background channels.

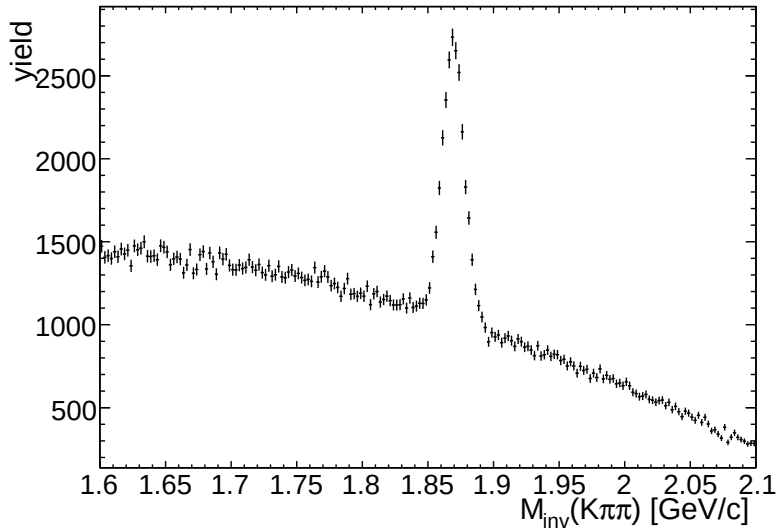

Figure 6.17: Expected signal to background ratio for the $D^{\pm}$ channel. The background below the prominent signal is smaller than the signal itself and the signal is sitting on a smooth background.

Assuming values for the reaction cross sections of open charm production above the $D\overline{D}$ threshold to be in the order of 3 nb for the D^+D^- signal channel and 1 nb for the $D^{*+}D^{*-}$ channel, the expected numbers of reconstructed events per year of $\overline{\text{P}}$ANDA operation are 1.5×10^4 and 1.4×10^3, respectively. For these estimations signal efficiencies of $\epsilon_{D^+D^-} = 7.1\,\%$ for the D^+D^- channel and $\epsilon_{D^{*+}D^{*-}} = 24.0\,\%$ have been used.

These values are obtained by using only the dominant charged decays of the D mesons. Including further decay channels, such as semi-leptonic decay modes, should significantly improve the expected charmed signal yield. Furthermore, the real production cross sections of $D\overline{D}$ may be a factor of ten or even more larger as predictions

suggest, which would drastically increase the charmed signal yield. The $\overline{\mathsf{P}}$ANDA detector in its given setup will be able to contribute to investigate various physics topics in the charmonium mass region.

Conclusive Remarks

The $\overline{\text{P}}$ANDA detector becomes more and more mature in design and ongoing R&D projects investigate detailed solutions for the use in the experiment. Also the design of the MVD starts to tend to an optimum solution, for which a good coverage of the solid angle can be achieved. Moreover, the used detector types, silicon pixel and strip detectors, provide a very good intrinsic hit resolution and the frontend electronics will provide a signal which is proportional to the deposited energy left by a particle in the detector. The signal can be used to weight the individual contributions of single channels to a hit cluster information and result in a hit resolution of better than $\sigma_{hit} < 30$ μm (see Section 4.2 Figures. 4.6 and 4.8). It was noticed that quadratic pixels of the size 100×100 μm^2 provide the best hit resolution compared to asymmetric dimensions (Table 4.3).

It became also clear that the vertex reconstruction ability decreases towards lower momenta (see Sections 4.3.2-4.3.3 and Figure 4.3.3) and will be the limiting factor for the vertex reconstruction of particles with momenta below 1.5 GeV/c.

In this context two basic channels at different incident beam momenta have been investigated. The two-pion production vertex of the reaction $\overline{p}p \to \pi^+\pi^-$ at the highest $\overline{\text{P}}$ANDA beam momentum of $p_{beam} = 15$ GeV/c can be reconstructed with lateral resolution of $\sigma_{d0} < 40$ μm and a longitudinal resolution of at least $\sigma_{d0} < 60$ μm, but with much stronger momentum dependence. The good resolution can be reached over the full momentum range between a few hundreds of MeV/c and up to 15 GeV/c. (Figure 5.6) This particular channel at the highest beam momentum tests the forward part of the MVD and demonstrates a good vertex reconstruction performance. The $\pi^+\pi^-$ channel may be of interest also for calibration purposes, because it provides a clean signal which is abundant enough to serve as calibration channel for the pellet target tracking and would allow a precise beam spot determination for a single droplet.

At intermediate energies the channel $\overline{p}p \to J/\psi\gamma$ has been investigated at a beam momentum of $p_{beam} = 5.55$ GeV/c. This channel is more related to physics, since higher charmonium states can undertake transitions to lower laying $c\bar{c}$ states. The J/ψ was reconstructed via its prominent two-muon decay, which provides a clean signature in the detector. Again, the focus of this analysis was the study of the vertex resolution of the J/ψ decay position. Although the momenta of the outgoing muons are smaller compared to the fast pions from the $\pi^+\pi^-$ channel a lateral vertex resolution of the J/ψ decay position of $\sigma_{d0} < 80$ μm was found. The longitudinal

vertex component along the beam axis can be given to be better than $\sigma_{z0} < 100$ μm (Chapter 5.3.2, Figure 5.10). For both channels the best resolution was obtained with symmetric 100×100 μm^2 large pixel cells and it has been found that the readout structure size of the strip detector plays a minor role and can be kept around 150 μm (Section 5.4.2).

In Chapter 6 it was demonstrated that the proposed $\overline{\mathsf{P}}$ANDA setup will be able to investigate the charmonium system above the $D\overline{D}$ threshold, e.g. via the decay of higher $c\bar{c}$ states to open charm channels. Special emphasis was given to the question to reduce the large hadronic background which covers the expected charmed signal. In Section 6.4 it was discussed that the background can be suppressed sufficiently and by using a conservative estimate for the cross section for open charm production at $\overline{\mathsf{P}}$ANDA energies an expected signal to background ratio of at least $S : N = 1 : 1$ can be achieved for both considered $D\overline{D}$ channels (see Section 6.4). Furthermore, the experimental resolution of the tracking system, and in particular of the MVD, allows the reduction of background by vertex constraints to enhance the signal yield over background (Section 6.4.2.1). For the D meson decay vertex a lateral resolution of $\sigma_d < 40$ μm and a longitudinal resolution of $\sigma_d < 90$ μm can be achieved.

The investigation of this particular region in the charmonium spectrum is interesting, since recent findings of new states does not fit particularly well into the charmonium spectrum. The $\overline{\mathsf{P}}$ANDA detector is a unique tool to investigate the charmonium system above the open charm threshold with high precision.

This work provides detailed results towards further optimization of the Micro Vertex Detector for the use in a hight rate hadronic experiment – the $\overline{\mathsf{P}}$ANDA detector.

A Structure of the Reconstruction Software of the Micro Vertex Detector

A.1 Overview

The results presented in this work were obtained with the $\overline{\text{P}}$ANDA-framework, which based in parts on the simulation framework developed by the BaBar collaboration [105] and were adopted to $\overline{\text{P}}$ANDA needs [10]. The use of the BaBar-based framework combined different advantages. The detector concept is very similar, although the BaBar detector was used at a collider, where beams of different energies were brought to collisions. This transfers part of the beam momentum to the $B\bar{B}$ pair, which elongates the observed decay length in the laboratory frame. The detector setup is similar to the $\overline{\text{P}}$ANDA approach with the exception of the additional forward spectrometer part at $\overline{\text{P}}$ANDA. The tracking systems are comparable and the sophisticated track reconstruction and track fitting algorithms [114] were adopted for the use within the $\overline{\text{P}}$ANDA framework. Results using the track reconstruction algorithms have been reported in Chapters 4–5

Figure A.1 shows a general overview about the major applications in the software framework. Detector relevant input is given to all major tasks of the simulation procedure. The detector simulation package (Bogus) is based on the widely used Geant4 package [106]. This part simulates the interaction of the particles with the detector materials. Inside sensitive elements, e.g. the silicon sensors of the MVD, detector specific information are collected, such as the hit position and the deposited energy. These data are input for the digitization process, which generates a data output, which is comparable to real data. This is important in order to develop realistic reconstruction algorithms as basis for the physics analysis of the simulated data much earlier before real data become available. Furthermore, for the detector development many basic questions can only be addressed with a realistic detector response and reconstruction algorithms.

The digitization procedure is realized in a separate application *SimApp*, which produces the digitized data format. After this stage in principle the data format from the real experiment should be exactly the same as produced in the Monte-

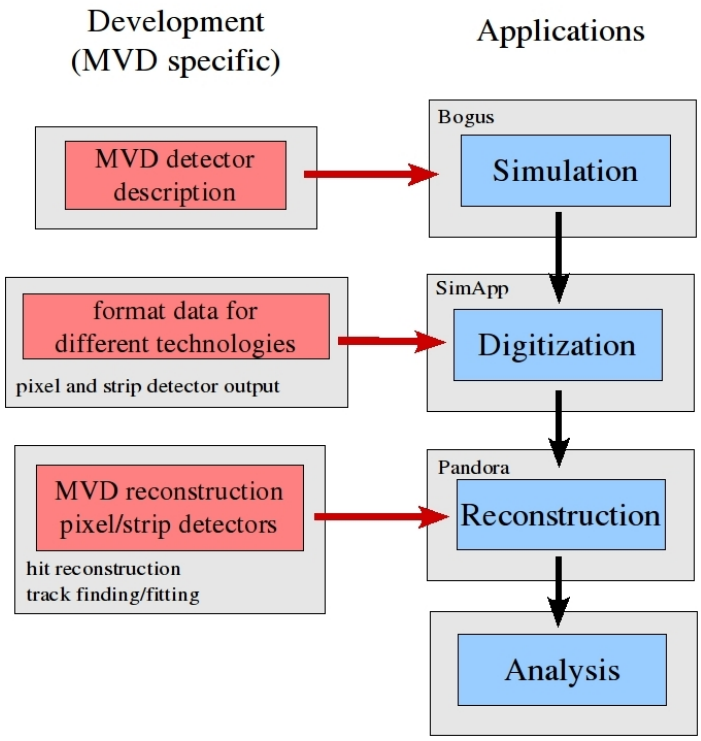

Figure A.1: General overview of the simulation procedure and the MVD specific input (see text for details).

Carlo simulations. This allows the study of typical detector effects in the physics analysis, such as missing detector channels or the influence of pile-up and noise.

The reconstruction of the digitized data format is realized in *Pandora*, the reconstruction application. In case of the MVD the cluster finding is processed before a reconstructed hit information in space is calculated. The hit information and the hit uncertainty is the basis for the track fitter, which allows the combination of relevant information from all tracking sub-detectors. Furthermore, in this last reconstruction phase the PID information from all detectors are collected and a global decision based on individual likelihoods from different sub-detectors is calculated. The track fit and the PID information is used to construct a physics candidate which is the basis for later physics analysis.

The $\overline{\mathrm{P}}$ANDA collaboration has started a joint-venture in the development of a next-generation software framework for FAIR experiments called FAIRroot, for which the $\overline{\mathrm{P}}$ANDA specific developments are a component called PANDAroot [129]. This allows to use synergy effects in the development of framework specific task like data storage for simulated and (later on) experimental data or common reconstruction tools.

Details about the structure, technical aspects and implementation details of the simulation software are described in [130]. Since the inner tracking detector is still

under development, the following sections will give only an overview about the MVD simulation software and are a snapshot of the current status.

A.2 Detector Implementation

The first ideas for an inner tracking system were based only on silicon pixel detectors [118] and the setup was rather compact with an outer radius of 6 cm. Figure A.2 shows a comparison of the only pixel setup (left) and the hybrid MVD design, which used strip detectors at the outer layers..

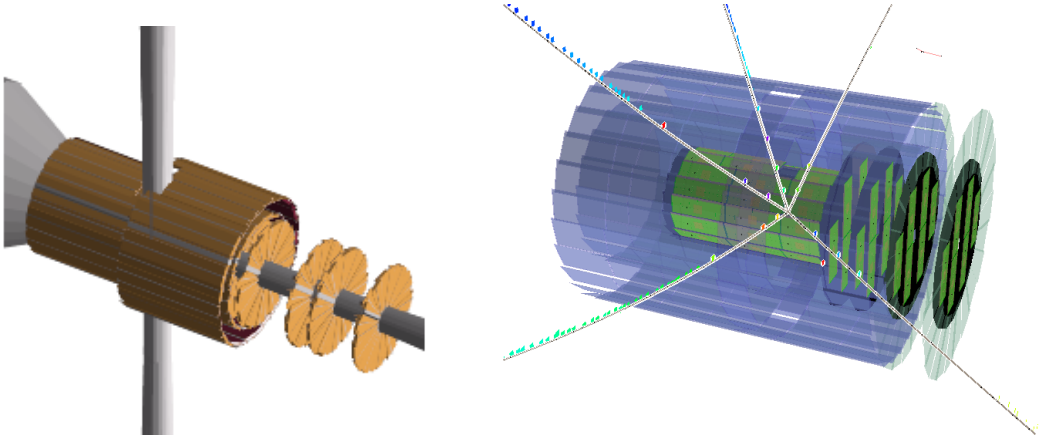

a) only pixel b) hybrid setup

Figure A.2: Comparison of different MVD designs, one with only pixel detector layers (left)[118] and the current hybrid detector setup with modified strip detector part (right)[131].

On the left side of Figure A.2 a scheme of the only-pixel detector based setup is shown. Meanwhile, silicon strip detectors were introduced to the design and there are major modifications towards a more realistic detector layout:

- **Barrel layer modifications**: The space between beam pipe and outer tracking detector is from 1–15 cm. The hybrid design with pixel and strip detectors fills the gap almost uniform with four detector layers in the barrel section.
- **Forward disc design:** Constructing wedged-shaped pixel detectors might be possible in principle but not attempted in previous experiments. The CMS collaboration constructed a forward pixel wheel but with rectangular pixel sensor shapes [101] and with larger inner radius. The current MVD design uses still rectangular shaped pixel sensors for closing the gap between the outer strip sensor disc and the beam pipe. Overlap between adjacent pixel modules can

not be avoided, but is less critical in the forward direction since most particles in this region will have higher energies. The outer strip sensor ring in the forward discs will be made out of wedge-shaped sensors.

- **Different detector technologies:** In the current MVD design the outer barrel layers are considered to be build of micro strip detectors. This has the advantage of a reduced material budget per layer and a much lower number of readout channels by keeping the same spatial and timing resolution.
- **Modified beam pipe setup:** The upstream part of the MVD changed because of necessary modifications in the beam pipe. In general the MVD setup strongly depends on the beam and target pipe cross design. The beam pipe opens in backward direction at the interaction point to stabilize the beam vacuum.

The geometry description in the BaBar-based $\overline{\text{P}}$ANDA software framework was realized with a flexible software tool called `DetectorModel` developed by the CMS collaboration [104]. The definition of all detector components is done in XML and automatically processed to the transport code at run-time. The detector model provides classes, which allow the handling of grouped objects, e.g. a set of detector elements combined to a layer. A specialized detector class uses the framework connection to access the geometry information if needed:

```
const MvdDetector* detector = gblEnv->getMvd()->getDetector();
```

A user defined detector description class can then easily load tcl parameters which are necessary e.g. in the digitization procedure. This can be done in all applications, if detector relevant data are needed. This common procedure assures the consistency of the detector description and the processing of detector parameters.

Nowadays a CAD converter program can be used to convert the layout definitions to a format which can be used in the framework and processed to the transport code [130],[132]. This converter was developed for the new PANDARoot framework and enables an easy way to compare different sub-settings in the simulations.

A.3 Generation of the Digitized Data Formats

Based on the detector simulation the digitization is performed as a prerequisite for the reconstruction process. Silicon pixel and strip detector technologies are widely used in HEP experiments and a design for the pixel part of the MVD were incorporated from the ATLAS pixel detector. As starting point the data format from the ATLAS frontend chip was used as digitization scheme [133]. The digitized data format was defined in a more general way since the electronics standard for $\overline{\text{P}}$ANDA is not defined up to now. In the digitization step the readout structures on the sensor surfaces are modeled. Parameters like the pixel dimensions or number of channels per frontend

can be changed at runtime to test different readout schemes in the simulations. This is done by TCL parameters, which are evaluated by the MVD digitization sequence as part of the global digitization application of the software framework. The sequence is schematically shown in Figure A.3

At run-time basic parameters can easily be changed by setting proper values to a set of parameter:

```
module talk MvdDigiModule
  ....
  pixCellX set 50
  pixCellY set 200
  pitchRPhi set 100
  pitchZ set 100
  ....
exit
```

where the MvdDigiModule corresponds to the Mapping stage in Figure A.3

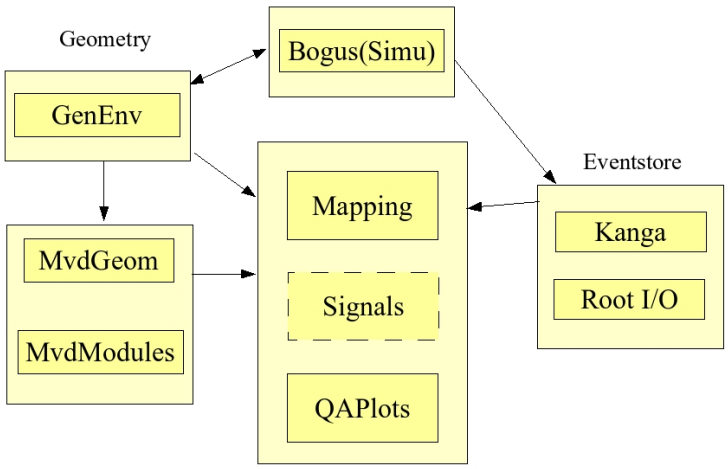

Figure A.3: Scheme for the MVD digitization sequence. The building block in the middle stores MVD relevant algorithms. As input information about the used geometry (MvdGeom) provided by the global environment. The storage to disc is realized via Kanga event store [105].

As an result of the digitization sequence the pixel matrix from an arbitrary frontend

is shown in Figure A.4. The upper frame corresponds to a pixel size of 50×200 μm^2 large pixels, whereas the lower figure shows the original ATLAS pixel size of 50×400 μm^2.

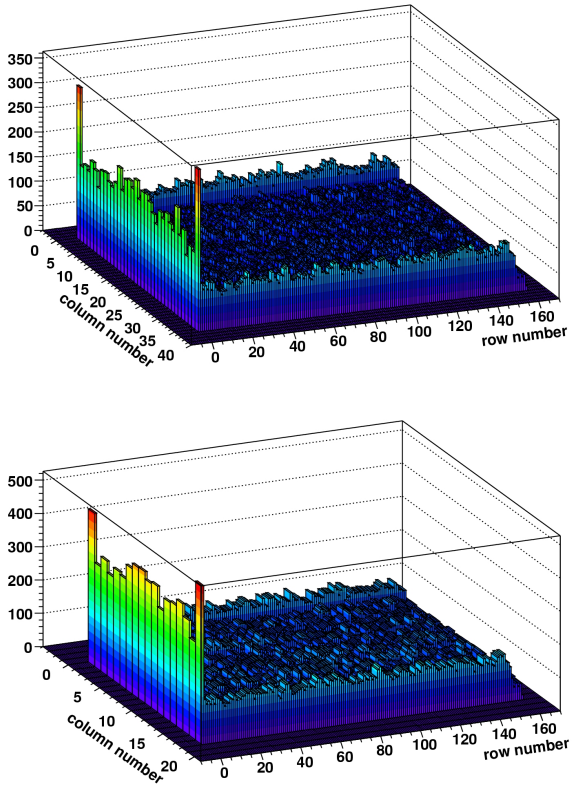

Figure A.4: Visualization of different pixel matrices after the digitization step. The upper picture shows the column and row information for a pixel size of 50×200 μm^2 and the lower frame the readout matrix for the ATLAS pixel size of 50×400 μm^2 for comparison.

The MVD design used for most simulations in this work were based on the ATLAS pixel sensors [134]. The sensor is read out by two columns of eight frontends, which are bump bonded to the sensor surface to connect the sensor pixel matrix to the frontend electronics. For the bump bonding process and for the positioning of the frontends on the sensor surface some additional space is required, which is compensated by larger pixel cells at the borders of each frontend region. This can be seen in Figure A.4 in both frames for channels in the first and last column and the first row. The number of entries corresponds to the size of enlarged pixel cells, e.g. for the ATLAS frontend the edge pixels are enlarged by 200 μm to a pixel size of 50×600 μm^2.

A.4 Cluster Reconstruction

The reconstruction algorithms for both silicon detector types are processed in the global reconstruction application (Pandora). The cluster finder sorts all channels which originate from the same sensor into an ordered list. Afterwards to a selected channel all neighboring channels are searched and stored to a temporary list. The procedure continues with the previously found member until no further states can be found. The local position on the sensor is calculated by taking the energy information of the individual channels into account. In case of the pixel detector the channels are treated as strip detectors, where only one dimension is considered. If all clusters are found a merging towards the missing coordinate is performed and all basic parameters are recalculated.

The cluster finder is able to select different algorithms, a charge weighting method or a simple geometric calculation of the mean position. At the end an global time information is calculated and a cluster position and energy is determined. Together with the known position of the sensor module the position in space can be calculated.

Bibliography

[1] GSI Helmholtzzentrum für Schwerionenforschung. FAIR - An International Accelerator Facility for Beams of Ions and Antiprotons. Technical report, FAIR-GSI, 2006. available via: http://www.gsi.de/fair/reports/btr.html.

[2] H. Fritsch and M. Gell-Mann. Current algebra: Quarks and what else? In *Proceedings of the XVI International Conference on High Energy Physics*, volume 2, page 135, 1972. available via: hep-ph/0208010v1.

[3] A. Donnachie. Low-energy hadronic physics. *Physics Reports*, 403-404:281–301, 2004.

[4] PANDA collaboration. Letter of Intent for: PANDA - Strong Interaction Studies with Antiprotons. Technical report, FAIR-ESAC, 2004.

[5] K. Peters. Charmed hybrids in proton antiproton annihilation. *Nuclear Instruments and Methods in Physics Research B*, 214:60–64, 2004.

[6] D. Bettoni and R. Calabrese. Review: Charmonium spectroscopy. *Progress in Particle and Nuclear Phyics*, 54:615–651, 2005.

[7] K. Brinkmann, P. Gianotti, and I. Lehmann. Exploring the Mysteries of Strong Interactions - The PANDA Experiment. *Nucl. Phys. News*, 16:15–18, 2006.

[8] C.T.H. Davies (HPQCD and UKQCD Collaborations). High-Precision Lattice QCD Confronts Experiment. *Phys. Rev. Lett.*, 92:022001, 2004.

[9] MILC collaboration. Recent Results. http://physics.indiana.edu/sg/milc.

[10] PANDA collaboration. Physics Performance Report for: PANDA Strong Interaction Studies with Antiprotons. Technical report, FAIR-GSI, 2009. available online: http://www-panda.gsi.de/auto/_home.htm.

[11] K.K. Seth. Experimental review of charmonium spectroscopy. *Eur.Phys. J. A*, 18:563–565, 2003.

[12] Burton Richter. From the Psi to Charm – The Experiments of 1975 and 1976. Nobel Lecture, December 1976. http://nobelprize.org/nobel_prizes/physics/laureates/1976/richter-lecture.html.

[13] Samuel C.C. Ting. The Discovery of the J Particle: A Personal Recollection. Nobel Lecture, December 1976. http://nobelprize.org/nobel_prizes/physics/laureates/1976/ting-lecture.html.

[14] B.J. Bjørken and S.L. Glashow. Elementary particles and SU(4). *Phys. Lett.*, 11(3):255–257, 1964.

[15] C. Amsler. Review of Particle Physics. *Phys. Lett. B*, 667(1-5):1, September 2008.

[16] G.S. Adams. Measurement of $\Gamma_{ee}(J/\psi)$, $\Gamma_{tot}(J/\psi)$, and $\Gamma_{ee}[\psi(2S)]/\Gamma_{ee}(J/\psi)$. *Phys. Rev. D*, 73:051103R, 2006.

[17] B. Aubert et al. Measurements of the mass and width of the η_c meson and of an $\eta_c(2S)$ candidate. *Phys. Rev. Lett.*, 92:142002, 2004.

[18] R.E. Mitchell. An Experimental Review of Charmonium. *arXiv:hep-ex/0810.3231v1*, October 2008. 34th International Conference on High Energy Physics, Philadelphia, 2008.

[19] M. Andreotti et al. Results of a search for the $h_c\,{}^1P_1$ state of charmonium in the $\eta_c\gamma$ and $J/\psi\pi^0$ decay modes. *Phys. Rev.*, D72:032001, 2005.

[20] J. L. Rosner et al. Observation of the $h_c{}^1P_1$) State of Charmonium. *Phys. Rev. Lett.*, 95(10):102003, Aug 2005.

[21] S. Dobbs et al. Precision Measurement of the Mass of the $h_c{}^1P_1$ State of Charmonium. *Phys. Rev. Lett.*, 101, October 2008.

[22] Kamal K. Seth. Alternative analysis of the r measurements: Resonance parameters of the higher vector states of charmonium. *Phys. Rev. D*, 72(1):017501, Jul 2005.

[23] C. Amsler (Particle Data Group). Review of Particle Physics - New Charmonium-like States. *Phys. Lett. B*, 667, 2008. http://pdg.lbl.gov.

[24] Stephen Godfrey. The XYZ's of $c\bar{c}$: Hints of Exotic New Mesons. *arXiv:hep-ph/0605152v1*, May 2006. Flavor Physics and CP Violation Conference, Vancouver, 2006.

[25] S. K. Choi et al. Observation of a new narrow charmonium state in exclusive $B+ \to K^+pi^+ + pi^-J/\psi$ decays. *Phys. Rev. Lett.*, 91:262001, 2003.

[26] B. Aubert et al. Study of the $B \to J/\psi K^- \pi^+ \pi^-$ decay and measurement of the $B \to X(3872) K^-$ branching fraction. *Phys. Rev. D*, 71:071103, 2005.

[27] Darin E. Acosta et al. Observation of the narrow state $X(3872) \to J/\psi \pi^+ \pi^-$ in $\bar{p}p$ collisions at $\sqrt{s} = 1.96$ TeV. *Phys. Rev. Lett.*, 93:072001, 2004.

[28] V. M. Abazov et al. Observation and properties of the $X(3872)$ decaying to $J/\psi \pi^+ \pi^-$ in $p\bar{p}$ collisions at $\sqrt{s} = 1.96$ TeV. *Phys. Rev. Lett.*, 93:162002, 2004.

[29] A. Abulencia et al. Analysis of the quantum numbers J^{PC} of the X(3872). *Phys. Rev. Lett.*, 98:132002, 2007.

[30] S. Uehara et al. Observation of a χ'_{c2} candidate in $\gamma\gamma \to D\overline{D}$ production at Belle. *Phys. Rev. Lett.*, 96:082003, 2006.

[31] Nils A. Törnqvist. Isospin breaking of the narrow charmonium of Belle at 3872 MeV as a deuson. *Phys. Lett. B*, 590:209–215, 2004.

[32] G. Gokhroo et al. Observation of a near-threshold $D^0 \overline{D}^0 \pi^0$ enhancement in $B \to D^0 \overline{D}^0 \pi^0 K$ decay. *Phys. Rev. Lett.*, 97:162002, 2006.

[33] K. Abe et al. Observation of a Charmoniumlike State Produced in Association with a J/ψ in e^+e^- Annihilation at $\sqrt{(}s) \approx 10.6$ GeV. *Phys. Rev. Lett.*, 98:082001, 2007.

[34] K. Abe et al. Observation of a near-threshold $\omega J/\psi$ mass enhancement in exclusive $B \to K \omega J/\psi$ decays. *Phys. Rev. Lett.*, 94:182002, 2005.

[35] B. Aubert et al. Observation of $Y(3940) \to J/\psi\omega$ in $B \to J/\psi\omega K$ at BABAR. *Phys. Rev. Lett.*, 101:082001, 2008.

[36] B. Aubert et al. Observation of a broad structure in the $\pi^+\pi^- J/\psi$ mass spectrum around 4.26-GeV/c^2. *Phys. Rev. Lett.*, 95:142001, 2005.

[37] Q. He et al. Confirmation of the Y(4260) resonance production in initial state radiation. *Phys. Rev. D*, 74:091104, 2006.

[38] C.-Z. Yuan et al. Measurement of the $e^+e^- \to \pi^+\pi^- J/\psi$ Cross Section Via Initial-State. *Phys. Rev. Lett.*, 99:182004, 2007.

[39] Felipe J. Llanes-Estrada. Y(4260) and possible charmonium assignment. *Phys. Rev. D*, 72(3):031503, Aug 2005.

[40] T. E. Coan et al. Charmonium decays of Y(4260), $\psi(4160)$, and $\psi(4040)$. *Phys. Rev. Lett.*, 96:162003, 2006.

[41] P. Lacock, C. Micheal, P. Boyle, and P. Rowland. Hybrid mesons from quenched QCD. *Phys. Lett. B*, 401(1-2):308 – 312, 1997.

[42] T. Barnes, F. E. Close, and E. S. Swanson. Hybrid and conventional mesons in the flux tube model: Numerical studies and their phenomenological implications. *Phys. Rev. D*, 52(9):5242–5256, Nov 1995.

[43] B. Aubert et al. Evidence of a broad structure at an invariant mass of 4.32 GeV/c^2 in the reaction $e^+e^{\rightarrow}\pi^+\pi^-\psi(2S)$ measured at BaBar. *Phys. Rev. Lett.*, 98:212001, 2007.

[44] X. L. Wang et al. Observation of Two Resonant Structures in $e^+e^- \rightarrow \pi^+\pi^-\psi(2S)$ via Initial State Radiation at Belle. *Phys. Rev. Lett.*, 99:142002, 2007.

[45] D.M. Asner et al. Physics at BES-III. *arXiv:hep-ex/0809.1869v1*, 2008.

[46] E. Klempt and A. Zaitsev. Glueballs, hybrids, multiquarks - Experimental facts versus QCD inspired concepts. *Phyics Reports*, 454:1–202, 2007.

[47] C.J. Morningstar and M. Peardon. Glueball spectrum from an anisotropic lattice study. *Phys. Rev. D*, 60:034509, 1999.

[48] C. Edwards et al. Observation of a pseudoscalar state at 1440MeV in j/ψ radiative decays. *Phys. Rev. Lett.*, 49:259, 1982.

[49] E. Klempt. GLUEBALLS, HYBRIDS, PENTAQUARKS: Introduction to Hadron Spectroscopy and Review of Selected Topics. *arXiv:hep-ph/0404270v1*, 2004.

[50] T. Barnes, F.E. Close, P.R. Page, and E.S. Swanson. Higher quarkonia. *Phys. Rev. D*, 55:1457, 1997.

[51] G.S. Bali et al. A comprehensive lattice study of SU(3) glueballs. *Phys. Lett. B*, 309:378–384, 1993.

[52] L. Faddeev et al. Glueballs, closed fluxtubes, and $\eta(1440)$. *Phys. Rev. D*, 70:114033, 2004.

[53] F.E. Close. Implications of the Glueball-$q\bar{q}$ filter on the 1^{++} nonet. *Z. Phys. C*, 76:469–474, 1997.

[54] S.J. Brodsky, A.S. Goldhaber, and J. Lee. Hunting for glueballs in electron-positron annihilation. *Phys. Rev. Lett.*, 91:112001, 2003.

[55] K. Abe et al. Observation of Double $c\bar{c}$ Production in $e + e-$ Annihilation at $s \approx 10.6GeV$. *Phys. Rev. Lett.*, 89(14):142001, Sep 2002.

[56] Michael S. Chanowitz and Stephen R. Sharpe. GLUEBALL AND MEIKTONS WHICH DECAY TO MULTI-KAON FINAL STATES. *Phys. Lett.*, 132B(4,5,6):413–418, December 1983.

[57] A. Abele et al. Evidence for a $\pi\eta$ P-wave in $\bar{p}p$ annihilations at rest into $\pi^0\pi^0\eta$. *Phys. Lett. B*, 446:349–355, 1999.

[58] A. Abele et al. Exotic $\eta\pi$ state in anti-p d annihilation at rest into $\pi^-\pi^0\eta p(spectator)$. *Phys. Lett. B*, 423:175–184, 1998.

[59] G. S. Adams et al. Confirmation of a π_1^0 Exotic Meson in the $\eta\pi^0$ System. *Phys. Lett.*, B657:27–31, 2007.

[60] S. U. Chung et al. Exotic and $q\bar{q}$ resonances in the $\pi^+\pi^-\pi^-$ system produced in π^-p collisions at 18 GeV/*c*. *Phys. Rev. D*, 65(7):072001, Mar 2002.

[61] C. A. Baker, C. J. Batty, K. Braune, D. V. Bugg, N. Djaoshvili, W. Dünnweber, M. A. Faessler, F. Meyer-Wildhagen, L. Montanet, I. Uman, S. Wallis-Plachner, and B. S. Zou. Confirmation of $a0(1450)$ and $\pi_1(1600)$ in $\bar{p}p \to \omega\pi^+\pi^-\pi^0$ at rest. *Phys. Lett. B*, 563(3-4):140 – 149, 2003.

[62] A. R. Dzierba et al. A partial wave analysis of the $\pi^-\pi^-\pi^+$ and $\pi^-\pi^0\pi^0$ systems and the search for a $J^{PC} = 1^{-+}$ meson. *Phys. Rev. D*, 73:072001, 2006.

[63] S. U. Chung and E. Klempt. Vector mesons in systems. *Phys. Lett. B*, 563(1-2):83 – 86, 2003.

[64] C. Amsler (Particle Data Group). Review of Particle Physics - Note on non-$q\bar{q}$ mesons. *J. Phys. G*, 33, 2006. Review by C. Amsler, Note on non-$q\bar{q}$ mesons, via URL: http://pdg.lbl.gov.

[65] K. J. Juge, J. Kuti, and C. J. Morningstar. Ab *Initio* Study of Hybrid $\bar{b}gb$ Mesons. *Phys. Rev. Lett.*, 82(22):4400–4403, May 1999.

[66] K. Jimmy Juge, Julius Kuti, and Colin Morningstar. Fine Structure of the QCD String Spectrum. *Phys. Rev. Lett.*, 90(16):161601, Apr 2003.

[67] Frank E. Close and Philip R. Page. Gluonic charmonium resonances at BaBar and Belle? *Phys. Lett. B*, 628:215–222, 2005.

[68] PANDA collaboration. PANDA - Antiproton Annihilation at Darmstadt, 2009. http://www-panda.gsi.de/auto/_home.htm.

[69] M. Di Pierro and E. Eichten. Excited heavy-light systems and hadronic transitions. *Phys. Rev. D*, 64(11):114004, Oct 2001.

[70] H. Albrecht et al. PRODUCTION AND DECAY OF THE F MESON IN e+ e- ANNIHILATION AT 10-GeV CENTER-OF-MASS ENERGY. *Phys. Lett. B*, 153:343, 1985.

[71] G. Blaylock et al. OBSERVATION OF $e^+e^- \to D_s^\pm D_s^{*\pm}$ AT $\sqrt{s} = 4.14$ GeV. *Phys. Rev. Lett.*, 58:2171, 1987.

[72] H. Albrecht et al. OBSERVATION OF A NEW CHARMED - STRANGE MESON. *Phys. Lett.*, B230:162, 1989.

[73] Y. Kubota et al. Observation of a new charmed strange meson. *Phys. Rev. Lett.*, 72:1972–1976, 1994.

[74] B. Aubert et al. A study of the $D_{sJ}^{*+}(2317)$ and $D_{sJ}^{+}(2460)$ mesons in inclusive c anti-c production near $\sqrt{s} = 10.6$ GeV. *Phys. Rev.*, D74:032007, 2006.

[75] D. Besson et al. Observation of a narrow resonance of mass 2.46-GeV/c^2 decaying to $D_s^{*+}\pi^0$ and confirmation of the $D_{sJ}^{*}(2317)$ state. *Phys. Rev.*, D68:032002, 2003.

[76] Stephen Godfrey and Nathan Isgur. Mesons in a relativized quark model with chromodynamics. *Phys. Rev. D*, 32(1):189–231, Jul 1985.

[77] T. Barnes, F. E. Close, and H. J. Lipkin. Implications of a DK molecule at 2.32 GeV. *Phys. Rev. D*, 68(5):054006, Sep 2003.

[78] G. E. Brown and Mannque Rho. Scaling effective lagrangians in a dense medium. *Phys. Rev. Lett.*, 66(21):2720–2723, May 1991.

[79] K. Tsushima, D. H. Lu, A. W. Thomas, K. Saito, and R. H. Landau. Charmed mesic nuclei: Bound D and $\overline{D}$ states with ^{208}Pb. *Phys. Rev. C*, 59(5):2824–2828, May 1999.

[80] B. Alessandro et al. Charmonium production and nuclear absorption in p-A interactions at 450 GeV. *Eur.Phys. J. C*, 33:31, 2004.

[81] C. Sanarta et al. Generalized mass formula for non-strange and hypernuclei with SU(6) symmetry breaking. *J. Phys. G: Nucl. Part. Phys.*, 32:363–373, 2006.

[82] S. Barsov et al. ANKE, a new facility for medium energy hadron physics at COSY-Jülich. *Nuclear Instruments and Methods in Physics Research Section A: Accelerators, Spectrometers, Detectors and Associated Equipment*, 462:364–381, 2001.

[83] M. Büscher et al. The Moscow-Jülich Frozen-Pellet Target. In A. Reis, C. Göbel, J. D. S. Borges, and J. Magnin, editors, *Hadron Spectroscopy*, volume 814 of *American Institute of Physics Conference Series*, pages 614–620, February 2006.

[84] Chr. Bargholtz et al. Properties of the WASA pellet target and a stored intermediate-energy beam. *Nuclear Instruments and Methods in Physics Research A*, 587:178–187, 2008.

[85] ATLAS collaboration. ATLAS Inner Detector Technical Design Report. Technical report, CERN LHCC, 1997.

[86] D. Calvo, P. De Regimis, R. Wheadon, S. Martoiu, and A. Rivetti. TOPIX: the first prototype of pixel readout for PANDA experiment. *Nuclear Instruments and Methods in Physics Research A*, 596:96–99, 2008.

[87] B. Ketzer. Micropattern gaseous detector in the COMPASS tracker. *Nuclear Instruments and Methods in Physics Research A*, 494:142–147, 2002.

[88] I. Adam et al. The DIRC particle identification system for the BaBar experiment. *Nucl. Instrum. Meth.*, A538:281–357, 2005.

[89] PANDA collaboration. Technical Design Report for: PANDA Electromagnetic Calorimeter (EMC). Technical report, FAIR-PANDA, 2008. to be found at: arXiv:0810.1216v1.

[90] ATLAS collaboration. ATLAS TDR Part8 - Muon identification and measurements. Technical report, ATLAS, May 1999.

[91] ATLAS collaboration. ATLAS Muon Spectrometer Home Page, 2009. https://twiki.cern.ch/twiki/bin/view/Atlas/MuonSpectrometer.

[92] P. Abbon et al. The compass experiment at cern. *Nuclear Instruments and Methods in Physics Research Section A: Accelerators, Spectrometers, Detectors and Associated Equipment*, 577(3):455 – 518, 2007.

[93] H.E. Jackson. The hermes dual radiator rich–performance and impact. *Nuclear Instruments and Methods in Physics Research Section A: Accelerators, Spectrometers, Detectors and Associated Equipment*, 553(1-2):205 – 209, 2005. Proceedings of the fifth International Workshop on Ring Imaging Detectors.

[94] H Terrier and I Belyaev. Particle identification with LHCb calorimeters. Technical Report LHCb-2003-092, CERN, Geneva, Sep 2003.

[95] G. Bonomi. Light hypernuclei in FINUDA. *Few-Body Systems*, July 2008.

[96] A. Capella, U. Sukhatme, C.-I. Tan, and J. Tran Thanh Van. Dual parton model. *Phys. Rept.*, 236:225–329, 1994.

[97] M. Bleicher et al. Relativistic hadron hadron collisions in the ultra- relativistic quantum molecular dynamics model. *J. Phys.*, G25:1859–1896, 1999.

[98] S. A. Bass et al. Microscopic models for ultrarelativistic heavy ion collisions. *Prog. Part. Nucl. Phys.*, 41:225–370, 1998.

[99] ZEUS collaboration. ZEUS MVD material budget. `http://www.nikhef.nl/pub/departments/mt/projects/zeus/vertex/MATERIAL/budget/index.html`. Mechanical Design of the ZEUS Micro Vertex Detector.

[100] Thobias Stockmanns. The micro-vertex-detector of the PANDA experiment at FAIR. *Nuclear Instruments and Methods in Physics Research A*, pages 106–112, 2006.

[101] CMS collaboration. The Tracker Project Technical Design Report. Technical Report 98-6, CERN/LHCC, April 1999.

[102] T. Würschig. Utilization of Double-Sided Silicon Strip Detectors within the PANDA Micro-Vertex-Detector. *IEEE Nuclear Science Symposium Conference Record*, N30-140:2215–2219, 2008.

[103] Joseph R. Incandela. Life on the critical path: Constructing silicon detectors for hadron colliders. *Nuclear Instruments and Methods in Physics Research A*, 579:712–717, 2007.

[104] P. Arce et al. Simulation framework and XML detector description for the CMS experiment. *Nucl. Instrum. Meth.*, A502:687–688, 2003.

[105] BaBar collaboration. Workbook for BaBar users - online documentation. http://www.slac.stanford.edu/BFROOT/www/doc/workbook/workbook.html.

[106] S. Agostinelli et al. Geant4: A simulation toolkit. *Nucl. Instrum. Meth.*, A506:250–303, 2003.

[107] Gerhard Lutz. *Semiconductor Radiation Detectors - Device Physics*. Springer Verlag Berlin Heidelberg, 2nd edition edition, 2001.

[108] D.N. Brown, E.A. Charles, and D.A. Roberts. The babar track fitting algorithm, proc. computing in high energy physics conference. In *Proc. Computing in High Energy Physics Conference*, Padova, 2000.

[109] W.D. Hulsbergen. Decay chain fitting with a kalman filter. *arXiv:physics/050319v1*, 2005.

[110] R. Frühwirth. Application of Kalman filtering to track and vertex fitting. *Nuclear Instruments and Methods in Physics Research Section A: Accelerators, Spectrometers, Detectors and Associated Equipment*, 262(2-3):444 – 450, 1987.

[111] W.R. Leo. *Techniques for Nuclear and Particle Physics Experiments*. Springer Verlag, 1994.

[112] O. Reinecke and R. Jäkel. Parametrization of the energy loss distribution of fast charged particles. Technical report, IKTP TU Dresden, 2008.

[113] A. Khoukaz. private communication.

[114] BaBar collaboration. Babar track parameter proposal. BaBar technical documentation, October 1995.

[115] T. Barnes, S. Godfrey, and E. S. Swanson. Higher charmonia. *Phys. Rev. D*, 72(5):054026, Sep 2005.

[116] P. Kroll, B. Quadder, and W. Schweiger. Exclusive production of heavy flavours in proton-antiproton annihilation. *Nuclear Physics B*, 316:373–390, 1989.

[117] A.B. Kaidalov and P.E. Volkovitsky. Binary reactions in $\bar{p}p$ collisions at intermediate energies. *Z. Phys. C*, 63:517–524, 1994.

[118] A. Sokolov. *Development of proportional chamber detectors and simulations to measure charm hadrons in antiproton-proton annihilation.* PhD thesis, Justus Liebig Universität Giessen, July 2005.

[119] PANDA collaboration. PANDA Technical Progress Report. Technical report, FAIR-ESAC, 2005.

[120] G. Goldhaber and J.E. Wiss. D and D^* Meson Production near 4 GeV in e^+e^- Annihilation. *Phys. Lett.*, 69B(4), August 1977.

[121] D. Everett, P. Grossmann, P. Mason, and H. Muirhead. Cross-Sections and Multiplicity Distributions for anti-p p Annihilations at 4.6-GeV/c. *Nucl. Phys.*, B73:449, 1974.

[122] J. B. Gay et al. The Reaction anti-p p $\rightarrow$ 3 pi- 3 pi+ Between 1.09-GeV/c and 1.44-GeV/c and the Effect of pi pi Phase Shifts. *Nuovo Cim.*, A31:593, 1976.

[123] C. K. Chen, T. Fields, D. S. Rhines, and J. Whitmore. anti-p p Interactions at 2.32-GeV/c. *Phys. Rev. D*, 17:42, 1978.

[124] P. S. Gregory et al. Cross-Sections of Annihilation and Inelastic Final States for anti-p p Interactions at 9.1-GeV/c. *Nucl. Phys.*, B119:60–76, 1977.

[125] G. D. Patel et al. GENERAL FEATURES OF ANTI-P P INTERACTIONS AT 7.3-GEV/C. *Z. Phys.*, C12:189–202, 1982.

[126] P. Johnson et al. GENERAL FEATURES OF THE anti-p p INTERACTION AT 12- GeV/c. *Nucl. Phys.*, B173:77, 1980.

[127] D. R. Ward et al. EXCLUSIVE ANNIHILATION PROCESSES IN 8.8-GEV ANTI-P P INTERACTIONS AND COMPARISONS BETWEEN ANTI-P P NONANNIHILATIONS AND P P INTERACTIONS. *Nucl. Phys.*, B172:302, 1980.

[128] H. W. Atherton et al. General characteristics of the annihilation reaction $pp \rightarrow 3pi^+3pi^-(pi^0)$ at 3.6 Gev/c. *Nucl. Phys.*, B18:221–245, 1970.

[129] S. Spataro. Simulation and event reconstruction inside the PandaRoot framework. *Journal of Physics: Conference Series*, 119:032035, 2008.

[130] PANDA computing wiki
. http://panda-wiki.gsi.de/cgi-bin/view/Computing/WebHome.

[131] R. Kliemt. MVD geometry in PANDAroot. priv. communication.

[132] Thobias Stockmanns. A CAD converter for detector geometries. priv. communication.

[133] ATLAS collaboration. ATLAS MCC module and data specifications. information available via web access: http://icwiki.physik.uni-bonn.de/twiki/bin/view/Systems/UsbPix.

[134] M.S. Salam et al. The ATLAS silicon pixel sensors. *Nuclear Instruments and Methods in Physics Research A*, 456:217–232, 2001.

List of Figures

1.1 QDC coupling constant 5
1.2 Recent LQCD results 6
1.3 Charmonium System 7
1.4 Formation of charmonium in e^+e^- and $\overline{\mathrm{p}}\mathrm{p}$ collisions 8
1.5 Level scheme for the eight charmonium states below the $D\overline{D}$ threshold 9
1.6 Cross section of hadron production in e^+e^- collision above the $D\overline{D}$ threshold 10
1.7 Glueball spectrum from lattice calculations 15
1.8 Charmonium potentials and hybrid spectrum from LQCD 18
1.9 Predicted mass spectrum for the heavy-light $c\overline{s}$ system 20
1.10 Predicted in-medium modification of the D meson 22
1.11 Nuclear hyper chart and production of double-hypernuclei at $\overline{\mathrm{P}}$ANDA 23

2.1 Schematic view of the $\overline{\mathrm{P}}$ANDA apparatus 26
2.2 Side view of the $\overline{\mathrm{P}}$ANDA target spectrometer 27
2.3 Artists view of the Micro Vertex Detector 30
2.4 Schematic view of the Time Projection Chamber 32
2.5 Schematic view of the Straw Tube Tracker 33
2.6 Schematic view of the target spectrometer EMC 35
2.7 Side view of the $\overline{\mathrm{P}}$ANDA forward spectrometer 37
2.8 Modified experimental setup of hypernuclear physics at $\overline{\mathrm{P}}$ANDA . . . 39

3.1 Phase space distribution of hadronic reactions in $\overline{\mathrm{p}}\mathrm{p}$ and $\bar{p}A$ collisions 45
3.2 Artists view of the MVD and the target and beam pipe cross, which defines the primary interaction region. 47
3.3 Momentum components for kaons and pions from the decay $D^{\pm} \rightarrow K^{\mp}\pi^{\pm}\pi^{\pm}$ 48
3.4 Momentum dependent distribution of the mean deflection angle $\bar{\Theta}$. . . 48
3.5 Mean number of MVD hits per track 50
3.6 Mean number of hit points by the MVD per track 50
3.7 Part of the radiation length X_0 in the materials within the MVD volume as function of polar angle 53
3.8 Resolution of the primary vertex position for single pion tracks reconstructed in the barrel section of the MVD 54

3.9 Number of particles per event for $\overline{\mathrm{p}}$p and $\overline{\mathrm{p}}$N collisions 55
3.10 Layout of the Micro Vertex Detector 58
3.11 Readout concept of the ATLAS pixel detector 61
3.12 MVD strip part concept study 63
3.13 MVD geometry definition in the simulation 64

4.1 Momentum uncertainty obtained by the track fit without and with MVD contributions 65
4.2 Track parameter for single pion tracks 66
4.3 Visualization of the readout structure sizes and their orientation with respect to the beam direction 69
4.4 Pixel cluster size 70
4.5 Strip cluster size 70
4.6 Pixel hit resolution 71
4.7 Two-dimensional pixel hit resolution 72
4.8 Resolution of the reconstructed position on the strip detectors 73
4.9 Influence of the material dependent corrections on the primary vertex resolution along the beam 75
4.10 Momentum Resolution of a combined track fit 76
4.11 Vertex resolution for pions with momentum of $p = 1$ GeV/c 77
4.12 Momentum dependence of the vertex reconstruction for single pion tracks 78
4.13 Angular dependence of the transverse vertex component 78
4.14 Primary vertex resolution with respect to polar angle 79
4.15 Proton energy loss in the Mvd silicon. 81
4.16 Energy loss distribution for protons 82
4.17 dE/dx versus track momentum in the MVD for different particle species 83
4.18 Deviation of the mean energy loss from the Bethe-Bloch expectation . 84
4.19 Gaussian and Landau widths 85
4.20 Separation power for dE/dx measurement with the MVD 86
4.21 Normalized proton likelihood from MVD PID information 87

5.1 Primary vertex region defined by the event generator 90
5.2 Angular and momentum distribution of the reaction $\bar{p}p \rightarrow \pi^+\pi^-$ at 15 GeV/c 92
5.3 Angular distribution for pions from the reaction $\bar{p}p \rightarrow \pi^+\pi^-$ with respect to momentum 93
5.4 Difference of reconstructed and generated vertex position as a function of particle momentum for the reaction $pbarp \rightarrow \pi^+\pi^-$ 94
5.5 Transverse and longitudinal impact parameter resolution for pions from the reaction $\bar{p}p \rightarrow \pi^+\pi^-$ 95
5.6 Dependence of the primary vertex resolution on momentum 96
5.7 Resolution of the $\pi^+\pi^-$ production vertex 97

5.8 Illustration of the allowed phase space for the two muons coming form the J/ψ decay . . . 98
5.9 Two-muon invariant mass of the J/ψ . . . 99
5.10 Vertex resolution of the two-muon J/ψ . . . 100
5.11 Artists view of the inner pixel layer of the MVD layout . . . 102
5.12 Vertex resolution in the transverse plane with respect to the beam pipe for different pixel cell sizes . . . 104
5.13 Vertex resolution in beam direction for different pixel cell sizes . . . 105
5.14 Momentum dependence of the vertex resolution transverse and along the beam axis for the leptonic J/ψ decay . . . 106
5.15 Vertex resolution of the two-pion production vertex . . . 107
5.16 Two-muon vertex resolution of the J/ψ decay in the reaction $\bar{p}p \rightarrow J/\psi\gamma$ for different strip dimensions . . . 108

6.1 $D^{\pm}$ cross section prediction . . . 114
6.2 Cross sections for major background sources for $D\overline{D}$ channels. . . . 115
6.3 Invariant $D^{\pm}$ candidate mass . . . 118
6.4 Production and decay vertex resolution of the D meson decay for the $\overline{\mathrm{p}}\mathrm{p} \rightarrow D^{+}D^{-}$ channel . . . 119
6.5 Invariant $D^{\pm}$ candidate mass . . . 120
6.6 Combinatorial background and its invariant $D^{\pm}$ mass for signal events 121
6.7 $D^{\pm}$ momentum components . . . 122
6.8 Phase space for the decay production of the $D^{\pm}$ decay . . . 123
6.9 Pion momentum distribution from the $D_s^{\pm}$ decay . . . 124
6.10 Invariant masses of the D^0 and D^* after four-constraint kinematic fit 124
6.11 $D^{*\pm}$ invariant mass distribution after 5C-kinematic fit . . . 125
6.12 Momentum components of $D^{\pm}$ candidates for signal and $K^+K^-2\pi^+2\pi^-$ background events . . . 128
6.13 Invariant mass distribution for $D^{\pm}$ candidates from the $\overline{\mathrm{p}}\mathrm{p} \rightarrow K^+K^-2\pi^+2\pi^-$ background channel. . . . 128
6.14 Difference of both $D^{\pm}$ decay vertices . . . 130
6.15 Momentum distributions of the $D^{\pm}$ decay products. . . . 131
6.16 Difference of both D^0 decay vertices . . . 136
6.17 Expected signal to background ratio for the $D^{\pm}$ channel . . . 139

A.1 General overview of the simulation procedure . . . 144
A.2 Comparison of different MVD designs . . . 145
A.3 Scheme for the MVD digitization sequence . . . 147
A.4 Visualization of different pixel matrices after the digitization process . 148

List of Tables

1.1 Recently found states above the $D\overline{D}$ threshold and their observed mass and width parameters 11

3.1 Decay length and prominent decays of hadrons with strange and charm quark content 52
3.2 Particle multiplicity per event for $\overline{\mathrm{p}}$p and $\overline{\mathrm{p}}$-Au collisions 56
3.3 Expected maximum count rates 57
3.4 MVD layer and disc parameters 59

4.1 Mean and σ values for the error distribution of the transverse and total momentum for the full $\overline{\mathsf{P}}$ANDA tracking 66
4.2 Various readout dimensions of the silicon detectors for resolution studies 68
4.3 Radial resolution on the pixel sensors 72
4.4 Fit parameters for the energy loss distribution obtained by the MVD for protons 82

5.1 Two pion reconstruction efficiency 91
5.2 Various readout dimensions of the silicon detectors for resolution studies 101

6.1 Calculated width for $c\bar{c}$ states above the $D\overline{D}$ threshold 110
6.2 Definition of the $D\overline{D}$ channels and the decays considered in the reconstruction 112
6.3 Cross sections for possible $D\overline{D}$ background reactions 116
6.4 Resolution of the production and decay vertex of the $D^{\pm}$ mesons . . . 118
6.5 Number of simulated events for $D\overline{D}$ background studies 126
6.6 Progression of the efficiency decrease with respect to vertex cut . . . 130
6.7 Signal to background ratios for pionic background channels 134
6.8 Expected signal to background of the pionic backgrounds to the $D^{*+}D^{*-}$ signal channel 138

Danksagung

An erster Stelle möchte ich meiner kleinen Familie danken, dass sie immer für mich da waren und mir Rückhalt boten. Und ganz besonders möchte ich Katrin dafür danken, dass Du mich immer unterstützt und begleitet hast, auch wenn es nicht immer einfach war! Du hast Dich auch immer liebevoll um unseren größten Schatz Timi gekümmert, der mich auch oft genug in letzter Zeit entbehren mußte!

Besonders danke ich Prof. Dr. H. Freiesleben für die freundliche Übernahme der Betreuung und des Gutachtens, sowie für alle kleinen und großen Hilfestellungen.

Ganz besonderen Dank möchte ich Prof. Dr. Kai-Thomas Brinkmann aussprechen für die große Unterstützung und fachliche Betreuung meiner Arbeit sowie für die Geduld, die er mit mir hatte (auch wenn ich bei unserem Dauerschachspiel wiedereinmal vergessen hatte zu ziehen!)

Allen PANDA's aus Bonn und Dresden möchte ich meinen Dank aussprechen, besonders den "Älteren": Hans-Georg, Ralf und Thomas, für die vielen Tipps und Korrekturen, aber auch den aufstrebenden "Jungpandas": Robert, Oscar, Felix und Lars!

Den TOF'lern Martin, Wolfgang und nicht zu vergessen Solomon danke ich für das andauernde gute Miteinander und die vielen freundschaftlichen Diskussionen. Besonders einige unserer hitzigen Debatten beim Mittagstisch werde ich wohl nie vergessen!

Den Bochumern Matthias Steinke, Bertram Kopf, Marc Pelizäus und Jan Zhong gilt mein Dank für die gute Zusammenarbeit bei der Erstellung der Simulationssoftware und für viele erhellende und klärende Gespräche und auch für so manch lustige Runde auf langen PANDA-Meetings. Besonders möchte ich dabei Marc danken, der sich immer hingebungsvoll um die Datenproduktion gekümmert hat.

Ganz besonderer Dank geht auch an meine Eltern und Schwiegereltern, die mich immer bestärkt und an mich geglaubt haben!

Versicherung

Hiermit versichere ich, dass ich die vorliegende Arbeit ohne unzulässige Hilfe Dritter und ohne Benutzung anderer als der angegebenen Hilfsmittel angefertigt habe; die aus fremden Quellen direkt oder indirekt übernommenen Gedanken sind als solche kenntlich gemacht. Die Arbeit wurde bisher weder im Inland noch im Ausland in gleicher oder ähnlicher Form einer anderen Prüfungsbehörde vorgelegt.

Ich erkenne die Prüfungsordnung der Fakultät Mathematik und Naturwissenschaften der TU Dresden uneingeschränkt an.

Dresden, den 06.04.2009 Dipl.-Phys. René Jäkel